Compact Microstructured Reactors for Decentralized Methanation of CO_2

Zur Erlangung des akademischen Grades einer

DOKTORIN DER INGENIEURWISSENSCHAFTEN

von der KIT-Fakultät für
Chemieingenieurwesen und Verfahrenstechnik
des Karlsruher Instituts für Technologie (KIT)

genehmigte

DISSERTATION

von

M. Sc. Sarvenaz Farsi
aus Tehran, Iran

Tag der mündlichen Prüfung: 11.10.2021

Erstgutachter/-in: Prof. Dr.-Ing. Roland Dittmeyer
Zweitgutachter/-in: Prof. Dr.-Ing. Robert Güttel

"*I am a forest, and a night of dark trees*:
but he who is not afraid of my darkness, will find banks full of roses under my cypresses"
- Friedrich Nietzsche

Acknowledgements

First of all, I would like to express my most sincere gratitude to Prof. Dr.-Ing. Roland Dittmeyer, for providing me with the opportunity to conclude my doctoral study on this engaging project at the Institute for Micro Process Engineering (KIT). His priceless expertise and insightful feedback pushed me to promote my scientific perspectives and led my work to a higher level.

I am deeply thankful to my group leader and supervisor, Prof. Dr.-Ing. Peter Pfeifer for all his valuable guidance and consistent support throughout my time at IMVT. Our fruitful discussions, his exceptional knowledge, and most importantly his trust helped me to develop my scientific skills.

Moreover, I would like to thank Prof. Dr.-Ing. Robert Güttel for acting as the second reviewer of my work. I would like to thank Prof. Dr.-Ing. Steffen Grohmann, and Prof. Dr. Reinhard Rauch for undertaking to be examiners.

The three and half years at IMVT would have never been the same without my colleagues. Your unique cooperative spirit together with exemplary friendliness made these challenging years much easier. I would like to thank Dipl.-Ing. Heinz Lambach, Matthias Schoeffler, Georg Rabsch, Cornelia Schorle and Dipl.-Ing. Robin Duerrschnabel for their technical assistance on the design and maintenance of reactors and laboratory test rigs. I am grateful to Dr. Oliver Goerke for his support, especially during the first year of my PhD. I would also like to thank Dipl.-Ing. Uta Gerhards for her help with SEM measurements. Keeping this short, I appreciate the support, knowledge and, motivation I got from every single IMVT staff, who dedicated much to the successfulness of this work.

My students; Sebastian Leopoldus, Wolfgang Olbrich, Shengzhi Liang, Youna Zhang, Donghee Son, Emre Turan, Kay Gebhardt and, Jonas Bretz contributed a great deal to this work and I would like to thank them for their engagement and commitment.

I am grateful to my colleagues, Marcel Loewert, Michael Belimov, Sahba Sadir, Francisco Vidal Vazquez, Elvia Valadez-Sanchez, Hannah Kirsch, Giulia Baracchini, Sara Claramunt, Tabea Stadler, Chenghao Sun, and Alexander Stroh for their advice and thoughtful recommendations.

The support of Prof. Dr. Jan-Dierk Grunwaldt and Marc-Andre Serrer as well as INERATEC GmbH for providing the Ni_3Fe catalyst and the promoted mono-metallic Nickel catalyst respectively, is gratefully appreciated. I am thankful to the Institue of Nanotechnology (INT), especially Charlotte Neidiger and Dr. Di Wang for running the TEM measurements.

Funding of this research by the German Ministry for Education and Research (BMBF) within the Kopernikus Project Power-to-X (P2X) is sincerely acknowledged.

Last but not least, I would like to say thanks to my family, in particular my parents, grandmother, and my partner Manfred for their unconditional support and eternal love throughout my life.

Abstract

This dissertation, defined in the scope of the Kopernikus project Power-to-X, is devoted to kinetic and reaction engineering aspects for the catalytic methane generation from carbon dioxide (CO_2) and hydrogen (H_2). In this respect, microstructured reactors are presented as a key component to compact, modular, and decentralized Power-to-Gas processes with exceptionally high space-time yield and dynamic operability.

A microstructured packed bed reactor with an internal cross-flow cooling channel was developed specifically for methanation kinetic studies. The reactor made short-contact time measurements for the highly exothermic methanation feasible. The kinetic measurements were done on two promising catalyst systems (primarily on a bimetallic Ni_3Fe/γ-Al_2O_3 and for comparison on a mono-metallic Ni catalyst) under technical operation conditions. The collected data for the Ni_3Fe catalyst were fitted to three appropriate literature models and additionally, a refined CO_2 methanation model was developed in this work. The model was expressed upon LHHW rate formalism, with consecutive reaction pathway and applying a non-isothermal reactor model. Discrimination among different models was done using various statistical methods. The refined model in this work was shown to provide an enhanced description of the reaction for the catalysts of interest.

Long-term stability tests for a duration of over 300 hours showed that the mono-metallic Ni catalyst deactivates much slower compared to the bimetallic catalyst. Upon this observation, it was concluded that despite the lower initial activity, the mono-metallic Ni catalyst is a better candidate for industrial applications and pilot plant tests on methanation.

In another working package, an advanced microstructured packed-bed reactor operated with high-pressure evaporation cooling was examined thoroughly. This reactor offers the advantage of overall process efficiency increase when coupled with a steam electrolyzer, by utilizing the reaction heat generated during methanation in the form of steam. The axial temperature profile and product quality under various process conditions and different modes of operation such as start-up, steady-state and transient were analyzed in detail and a safe operation strategy for a stable reactor performance was established. For reactor simulation purposes, a non-isothermal heterogeneous cascade model of ideally

mixed CSTRs was implemented. Via this method, the overall heat transfer coefficient was estimated locally. Applying the axial heat transfer coefficient profile, the experimental temperature profile data and the product composition can be predicted very well.
As an outlook for the scale-up implementation of the power-to-gas concept, a brief introduction on the design and early tests on a modular and scaled-up methanation microstructured reactor for 100 kW methane generation in container-based plants is provided. The reactor is to be operated applying the evaporation cooling strategy in a large-scale research infrastructure; Energy Lab 2.0.

Kurzfassung

Die vorliegende Dissertation, entstanden im Rahmen des Kopernikus Projekts Power-to-X, widmet sich der Aufklärung der kinetischen und reaktionstechnischen Aspekte der katalytischen Methanerzeugung über Kohlenstoffdioxid (CO_2) and Wasserstoff (H_2). In diesem Zusammenhang werden mikrostrukturierte Reaktoren als Schlüsselkomponente zu kompakten, modularen und dezentralen Power-to-Gas-Prozessen mit aussergewöhnlich hoher Raum-Zeit-Ausbeute und dynamischer Bedienbarkeit vorgestellt.
Speziell für die kinetischen Untersuchungen der katalytischen Methanisierung wurde im Rahmen der Arbeit ein mikrostrukturierter Festbettreaktor mit internem Kreuzstrom-Kühlkanal ausgelegt und eingesetzt, welcher auch Kurzzeitmessungen für die stark exotherme Methanisierung ermöglicht. Die kinetischen Messungen wurden an zwei vielversprechenden Katalysatorsystemen (primär an einer bimetallischen Legierung Ni_3Fe/γ-Al_2O_3 und im Abgleich mit monometallischem Nickel) unter technischen Betriebsbedingungen durchgeführt. Die mit dem Ni_3Fe Katalysator erfassten Daten wurden einerseits mit drei in der Literatur beschriebenen Modellen gefittet, sowie zusätzlich mittels eines im Rahmen dieser Arbeit entwickelten verfeinerten CO_2-Methanierungsmodells auf Basis des LHHW-Ratenformalismus mit konsekutivem Reaktionspfad und unter Anwendung eines nicht-isothermen Reaktormodells. Ein Abgleich des verfeinerten Modells mit den Literaturmodellen erfolgte anhand statistischer Methoden. Hierbei konnte gezeigt werden, dass das verfeinerte Modell eine verbesserte Beschreibung der Reaktion für die Katalysatoren von Interesse liefert.
Vergleichende experimentelle Langzeitstabilitätstests über eine Dauer von >300 Stunden an beiden Katalysatortypen zeigten, dass der mono-metallische Katalysator im Vergleich zum bimetallischen Katalysator signifikant langsamer degradiert. Aus dieser Beobachtung wurde gefolgert, dass der monometallische Ni-Katalysator trotz geringerer anfänglicher Aktivität einen bessereren Kandidaten gerade für industrielle Anwendungen und Pilotanlagentests zur Methanisierung darstellt.
In einem weiteren Arbeitspaket wurde ein fortschrittlicher mikrostrukturierter Festbettreaktor, der mit Hochdruck-Verdampfungskühlung betrieben wird, eingehend untersucht. Dieser Reaktortyp bietet den Vorteil der Gesamtprozesseffizienz-Steigerung bei Kopp-

lung mit einem Dampfelektrolyseur durch Nutzbarmachung der während der Methanisierung generierten Reaktionswärme in Form von in der Kühlung erzeugtem Wasserdampf. Hierfür wurden das axiale Temperaturprofil und die Produktqualität bei verschiedene Prozessbedingungen und unterschiedlichen Betriebsarten wie Anfahren, stationärem sowie dynamischem Betrieb des Reaktors evaluiert und eine sichere Betriebsstrategie für eine stabile Reaktorleistung wurde festgelegt. Für die Reaktorsimulation wurde ein heterogenes nicht-isothermes Kaskadenmodell von ideal durchmischten CSTRs implementiert. Mit dieser Methode wurde der Gesamtwärmeübergangskoeffizient lokal abgeschätzt. Unter Anwendung des axialen Wärmeübergangs-Koeffizientenprofils ist es möglich experimentelle Temperaturprofildaten und die Produktzusammensetzung sehr gut vorherzusagen.

Als Ausblick der Arbeit für die hochskalierte Umsetzung des Power-to-Gas Konzepts gibt es eine Einführung in das Design und erste Tests eines modularen und skalierten Methanisierungsreaktors für die Erzeugung von 100 kW-Methan in containerbasierten Anlagen. Der Reaktor soll unter Anwendung der Verdampfungskühlstrategie in einer grosstechnischen Forschungsinfrastruktur, dem Energy Lab 2.0, betrieben werden.

Table of Contents

List of symbols and abbreviations

Abbreviations

BIC	Bayesian information criterion
BJH	Barrett, Joyner, and Halenda
Bo	Bodenstein number
Ca	Carberry number
CSTR	Continuous stirred tank reactor
DEN	Denominator
DME	dimethyl ether
DRIFTS	Diffuse reflectance infrared Fourier transform spectroscopy
EBI	Engler-Bunte Institute
EDX	Energy dispersive X-ray spectroscopy
EFTEM	Energy filtered transmission electron microscopy
FID	Flame ionization detector
FTIR	Fourier-transform infrared spectroscopy
GC	Gas chromatograph
GHG	Greenhouse gas
GHSV	Gas hourly space velocity
HAADF	High angle annular dark-field
HRTEM	High resolution transmission electron microscopy
INT	Institute of Nanotechnology

IPCC	Intergovernmental panel on climate change
IMVT	Institut für Mikroverfahrenstechnik
KIT	Karlsruher Institut für Technologie
LFC	Liquid mass flow controller
LHHW	Langmuir-Hinshelwood-Hougen-Watson
LOHC	liquid organic hydrogen carrier
LNG	Liquefied natural gas
MFC	Mass flow controller
Nu	Nusselt number
ODE	Ordinary differential equation
PDE	Partial differential equation
PFR	Plug flow reactor
Pe	Peclet number
$\mathbf{Pe}_{ax}$	Axial Peclet number
PtX	Power to X
PtG	Power to gas
PtL	Power to liquid
Re	Reynolds number
$\mathbf{Re}_{p}$	Particle Reynolds number
RSS	Sum of least square residuals
rWGS	Reverse water gas shift
SAED	Selected area electron diffraction
Sc	Schmidt number
SEM	Scanning electron microscope
SNG	Synthetic natural gas

STEM	Scanning transmission electron microscopy
STP	Standard temperature and pressure
TCD	Thermal conductivity detector
TEM	Transmission electron microscopy
TOS	Time on stream
TPD	Temperature programmed desorption
TPRx	Temperature programmed reaction
WGS	Water gas shift
WHSV	Weight hourly space velocity

Latin Symbols and Variables

A_{rel}	relative activity
ΔA_{cool}	cooling area in one control volume [m^2]
a	thermal diffusivity [$m^2\,s^{-1}$]
$a(t)$	activity factor
C_i	concentration of component i [$mol\,m^{-3}$]
C_p,$C_{p,m}$	heat capacity [$J\,kg^{-1}\,K^{-1}$]
$C_{p,n}$	mole based heat capacity [$J\,mol^{-1}\,K^{-1}$]
D_{ax}	axial dispersion coefficient [$m^2\,s^{-1}$]
D_{eff}	effective diffusion coefficient [$m^2\,s^{-1}$]
D_i	diffusion coefficient of component i [$m^2\,s^{-1}$]
d	diameter [m]
d_h	hydraulic diameter [m]
dm_{cat}	catalyst mass in one control volume [kg]

d_{pore}	catalyst pore diameter [nm]
E_A	activation energy [kJ mol^{-1}]
G	mass flux [kg m^{-2} s^{-1}]
ΔH	adsorption energy [J mol^{-1}]
$\Delta_R H_{298\,\mathrm{K}}$	specific reaction enthalpy at standard conditions [J mol^{-1}]
J_M	diffusive molar flux [mol m^{-2} s^{-1}]
J_H	heat flux [W m^{-2} s^{-1}]
K_i	adsorption constant of component i a.u.
K_{eq}	equilibrium constant a.u.
k_a	deactivation factor [h^{-1}]
k_{eff}	overall heat transfer coefficient [W m^{-2} K^{-1}]
k_i	reaction rate constant a.u.
k_0	pre-exponential factor a.u.
L	length [m]
L/L_0	reactor axial position
m	mass [kg]
m_a	order of deactivation
$\dot{m}$	mass flow [kg s^{-1}]
$N_{reaction}$	Number of the reactions
n	cell number
n_{DP}	number of data points
n_P	number of independent parameters in a model
$\dot{n}$	molar flow [mol s^{-1}]
$\dot{n}_i$	molar flow of component i [mol s^{-1}]
P	perimeter of a channel [m]
p	pressure [bar]

p_i	partial pressure of component i [bar]
$\dot{Q}_{reac.}$	heat of the reaction [J mol^{-1}]
$\dot{q}$	heat flow [kJ s^{-1}]
R	Universal gas constant [J mol^{-1} K^{-1}]
$R_{m,i}$	catalyst mass specific net reaction rate of component i [mol s^{-1} kg^{-1}]
R^2	coefficient of determination
R^2_{adj}	adjusted coefficient of determination
r	radius, radial coordinate [m]
r_i	observable reaction rate [mol s^{-1} m^{-3}]
S_{CH_4}	CH_4 selectivity
ΔS_{cat}	catalyst surface area in one control volume [m^2]
s	thickness of the wall separating reaction and cooling channel [m]
T	temperature [K]
δ_T	thickness of thermal boundary layer [m]
t	time [h] or [s]
$t_{Diffusion}$	Diffusion time constant [s]
$t_{Thermal}$	heat transfer time constant [s]
u	superficial velocity [m s^{-1}]
U	perimeter of catalytic bed in heat exchange with coolant [m]
$\dot{V}$	volumetric flow [m^3 s^{-1}]
X_{CO_2}	CO_2 conversion
$X(t)$	conversion at time of t
Y_i	yield of component i [mol m^{-3}]
Y_{CO}	CO yield
ΔY_i	experimental error of component i
y_i	mole fraction

z	axial coordinate [m]

Greek Symbols and Variables

α	reaction exponent of CO_2
α_c	coolant side heat transfer coefficient [$W\,m^{-2}\,s^{-1}$]
α_{pb}	packed bed heat transfer coefficient [$W\,m^{-2}\,s^{-1}$]
β	rate exponent of H_2 in rWGS and CO_2 methanation
γ	reaction exponent of CO
Δ	difference
ϵ_{cat}	Catalyst porosity
λ	solid thermal conductivity [$W\,m^{-1}\,K^{-1}$]
ν	reaction exponent for compound i
ρ	density [$kg\,m^{-3}$]
τ_{cat}	Catalyst tortousity
τ_{mod}	modified contact time [$mg\,min\,mm^{-1}$]
φ	reaction exponent of H_2 in CO methanation

Indices

A	activation
a	activity factor
abs	absolute
ads	adsorbed
air	cooling air
ax	axial
bed	catalyst bed
CO – Meth	CO methanation

c	cooling
cat	catalyst
cool	cooling
cross	cross-section
diffusion	diffusion
eff	effective
eq	equilibrium
exp	experimental
fluid	fluid
H	heat
h	hydraulic
i	component i
in	inlet
j	reaction j
M	mass
Meth	methanation
mod	modified
m	mass-based
n	mole-based
out	outlet
pore	catalyst pore
R	reactor
reac	reaction
rel	relative
rWGS	reverse water gas shift
sim	simulation

T	temperature
tot	total
wall	reactor wall
w	water
x	x axis

1 Introduction

1.1 Motivation

The ongoing anthropogenic climate change in the form of global warming is a palpable phenomena and is one of our hugest challenges in the 21st century. This issue is essentially due to greenhouse gas (GHG) emissions, of which carbon dioxide conveys the highest share among all (Fig. 1.1-c) [1]. In the case that no massive actions for reducing the CO_2 emission rate be taken, the anticipated global heating rate will be about 100 times more than the historic and naturally occurring climate change [2]. The fifth assessment report provided by the 'Intergovernmental Panel on Climate Change (IPCC)' states that the 0.9 °C increase in the average earth surface temperature in the years from 2006 to 2015 compared to the 1800s (Fig. 1.1-a) and its conspicuous imprint, is solid evidence of the upcoming impacts of 1.5 °C temperature increase on living organisms, ecosystems, and human systems. The adverse consequences of risking to surpass the 1.5 °C are made clear in this report: regional and seasonal severe weather phenomenon, increase in the frequency, intensity and duration of marine heat-waves, extreme rainfalls and wildfires, acidification of the oceans, sea-level rise up to 90 cm by the year 2100 (Fig. 1.1-b), and dramatic melting of the snow and polar ice. These are only a few examples that call for urgent attention to the severity of the human-triggered global warming outcomes [3].
As a result of the united nations climate change conference (UNFCCC) in December 2015, the Paris agreement was signed by 174 countries. This agreement imposes new policies to eliminate or limit the activities which breed human-induced global warming and to control the temperature growth to well below 2 °C. Therefore, all the participating countries are committed to drastically reducing their GHG emissions [4]. For retaining the Paris agreement goals, the CO_2 emission must be restrained to below 25 Gt per year by 2030, while the current strategy will leave us with 56 Gt till then. This value is more than twice the target and demands 7.6% emission reduction each year in the upcoming decade [5]. Since two-third of the released CO_2 are a result of fossil fuel consumption (Fig 1.1-d), development of and investment in sustainable energy technologies gain tremendous importance. Such a far-reaching task is not feasible without the cooperation of

different sectors and great political support.

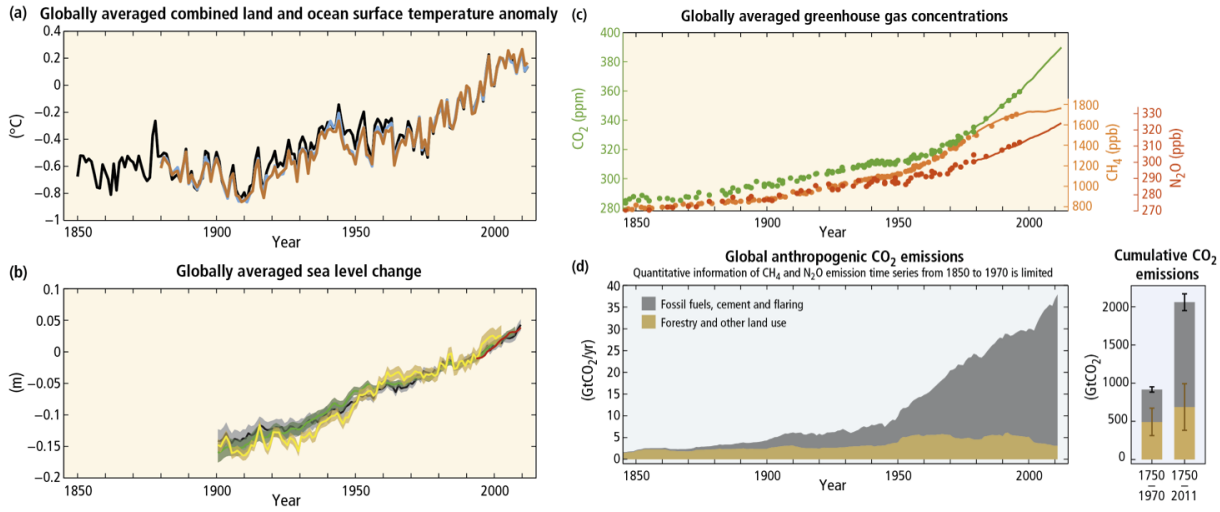

Figure 1.1: ”Observations and other indicators of a changing global climate system. Observations: a) Annually and globally averaged combined land and ocean surface temperature anomalies relative to the average over the period 1986 to 2005. b) Annually and globally averaged sea-level change relative to the average over the period 1986 to 2005 in the longest-running dataset. All datasets are aligned to have the same value in 1993, the first year of satellite altimetry data (red). c) Atmospheric concentrations of the greenhouse gases carbon dioxide (CO_2, green), methane (CH_4, orange), and nitrous oxide (N_2O, red) determined from ice core data (dots) and direct atmospheric measurements (lines). Indicators: d) Global anthropogenic CO_2 emissions from forestry and other land use as well as from burning of fossil fuel, cement production and flaring. Cumulative emissions of CO_2 from these sources and their uncertainties are shown as bars and whiskers, respectively, on the right-hand side.” Taken from: [3].

In Germany, the transition from fossil energy carriers to renewable energies gained momentum in the year 2010 which is referred to as ’Energiewende’. Since fossil energy carriers are the backbone of almost all industrial sectors, the Energiewende compels tremendous transformation in the infrastructure and technologies [6]. Therefore, the journey to expanding the renewable sources share in the energy supply is divided into definite milestones. For example, in January 2019, Germany decided upon phasing out coal power plants by the year 2038. In line with the aforementioned environmental ambitions, Germany plans to cut GHG emissions to 80-95% by the year 2050 [1]. Although Germany has been successful in some sectors like electricity generation via increasing the share of renewable energies (from 7% in the year 2000 to 45% in 2019) [7], the overall CO_2 emissions have still an increasing rate and seem to fall behind the ambitious

[1] https://www.iea.org/reports/germany-2020, last accessed: 02.03.2020

targets noted [8].

Fulfilling the climate change policies on both national and international levels and the global energy demand call for intelligent strategies to efficiently increase the share of renewable energy sources. The major drawback of green energies such as wind and solar energy is the spatial and temporal mismatch between their generation and demand. This issue can only be resolved with energy storage systems and a dense H_2 network for energy distribution on a different scale. New policies concentrate on technologies which transit power generation from central to decentral, from point to area, and from direct energy consumption to energy storage.

Power-to-X (PtX) stands for all processes that propose sector-coupling for storage and conversion of the surplus generated renewable electrical energy [9,10]. Electrical, electrochemical, mechanical, thermal, electromagnetic and chemical technologies are popular subjects under study for short- or long-term storage of the green energies in stock and their integration into the energy system [9].

Batteries are one of the promising energy storage systems which may be implemented for supporting a flexible power grid and are expected to increase their share in the upcoming decade (from 11 GW h in 2017 to 167 GW h in 2030) [11]. Mechanical energy storage technologies that apply compressed air or flywheel energy storage are alternative means for short-term energy storage. The largest developed flywheel can supply 340 MW for 30 seconds [12].

Another process scheme is using the surplus green energy for water electrolysis into H_2 and O_2. Having the highest gravimetric energy density among gases (33.3 kW h kg^{-1}), hydrogen can be used as an energy carrier itself (Power-to-Gas or PtG, hydrogen). The generated H_2 can be either used directly or energetically. On the other hand, storage and transportation of H_2 due to its low volumetric energy density (0.003 kW h l^{-1} at 25 °C and 1 bar) is a challenging task and H_2 liquefaction is an energy-consuming process. Therefore, at the current stage, a widespread H_2 infrastructure as the main energy source is assessed economically infeasible and can be only taken into consideration for special regions with very high H_2 requests [9]. Several projects work on technical and economical aspects of a H_2 network for both short- and long-term green H_2 applications[2]. A PtG-H_2 system can be integrated into an industrial plant with high H_2 demand such as NH_3 and methanol synthesis or hydro-cracking. The high renewable power generation potential for such locations is a decisive factor to provide a continuous H_2 stream. The energetic implementation of H_2 can be realized via injecting this renewable gas into present natural gas lines, which covers a very good and massive infrastructure. According to DVGW

[2] https://www.hypos-eastgermany.de/das-innovationsprojekt/hypos-strategie/, last accessed: 18.04.2021

[3], apart from methane, CO_2, N_2 and higher hydrocarbons (e.g. Propane and Butane), a maximum H_2 concentration of 1.5% can be added to the current natural gas pipeline in Germany. The addition of higher H_2 concentrations calls for detailed evaluation and customization of system components [9].

Further catalytic processing of hydrogen with carbon dioxide into diverse chemicals such as methane (Power-to-Gas, methane), hydrocarbon-based liquid fuels via Fischer-Tropsch synthesis, methanol or dimethyl ether (Power-to-Liquid) are other prospects for seasonal energy storage and decentralization of the industrial and transport sectors [9]. Fischer-Tropsch products could be directly used in the mobility sector via the existing distribution network. Methanol and Dimethyl ether (DME) could be used as base chemicals in various applications [13, 14].

Green synthetic methane could be stored or injected in the existing gas grid and used in different sectors such as heating, transport, or simply reconverted into electricity via gas turbines. In this context, methane is viewed as a preferred long-term energy storage option (up to 100 TWh storage capacity) due to its existing infrastructure and versatile applications [9]. The natural gas pipeline in Germany is 511,000 Kilometer long, and 51 large storage tanks with 24.6 Mrd.m^3 volume already exist [4], [5]. Europe's excellent infrastructure of 2,210,677 kilometers with 113 natural gas import locations, ease the energy supply to multiple economy sectors [15]. Another aspect speaking for PtG plants is the carbon-neutrality of the generated fuel. There are several sources for CO_2 supply: large point sources include iron, steel, or cement industries (gray carbon). Bio-gas and biomass-gasification plants are the next options for CO_2 capture (green carbon). Direct air capture is another technology that assures a closed carbon cycle (green carbon) [9,16]. The complications in this scheme are mainly of economic nature. Industrial purification, storage, and transport of CO_2 is technically feasible, though high investment costs stand against this process scheme. Throughout water electrolysis, methanation, and storage, a substantial part of the energy is lost. The energy efficiency after these steps falls to 54-65%, while after electrolysis it is around 67-81% [17]. Smart utilization of the exothermic methanation heat can help to balance this energy loss and improve the overall efficiency. This energy can be utilized, e.g. for the CO_2 capture step, for steam generation in a steam power cycle, or fed to a high-temperature steam electrolyzer [16]. For example,

[3] The German association for gas and water.

[4] Bundesministerium für Wirtschaft und Energie (BMWi), "Erdgasversorgung in Deutschland", https://www.bmwi.de/Redaktion/DE/Artikel/Energie/gas-erdgasversorgung-in-deutschland.html, last accessed: 04.03.2020

[5] Bundesministerium für Wirtschaft und Energie (BMWi), "Instrumente zur Sicherung der Gasversorgung", https://www.bmwi.de/Redaktion/DE/Artikel/Energie/gas-instrumente-zur-sicherung-der-versorgung.html, last accessed: 04.03.2020

the schematic drawing of the PtG process depicted in Fig. 1.2 proposes the utilization of the reaction heat of the exothermic methanation reaction in the form of high-pressure steam in combination with a high-temperature electrolyzer.

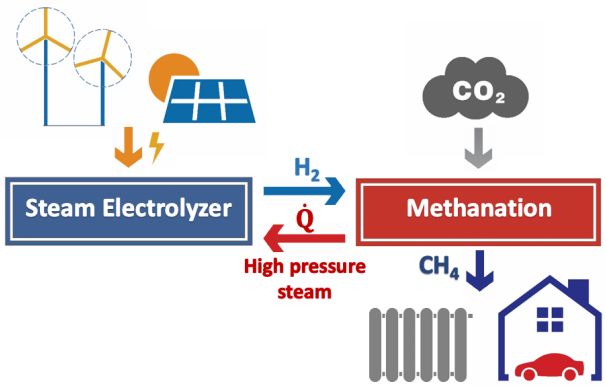

Figure 1.2: Power-to-Gas process scheme: generation of high pressure steam by the reaction heat of methanation and coupling with a steam electrolyzer

In conclusion, anthropogenic climate change enforces a transition of the current fossil-based energy supply infrastructure to green sustainable energy supply. Future technologies are moving toward decentral and flexible power supply integrated with high capacity energy storage and grid expansion. Methanation of CO_2 and H_2 in the context of a PtG process is one of the feasible routes. In this definition, the CO_2 neutral methane is solely observed as a chemical energy carrier. Renewable energy sources have a fluctuating nature, which imposes operability under transient conditions on the electrolyzer. In order to avoid building massive H_2 buffer tanks and meet the goal of delocalized renewable energy storage, the methanation reactors must as well be capable of operating under fluctuating reaction conditions and integrating into decentral infrastructures. The state-o-the-art methanation reactors are mainly designed for massive infrastructures and operated adiabatically under steady-state conditions, which makes them improper candidates for realizing PtG process requirements.

The current work aims to introduce compact microstructured reactors for storing intermittent power from renewable energy sources by hydrogen generation and further methane generation as substitute natural gas for grid injection or liquefied natural gas (LNG) applications.

1.2 Objectives of this dissertation

This doctoral study was defined within the BMBF funded project Kopernikus P2X [6]. The first phase of this project started in September 2016 and took three years. As the P2X title implies, the project aimed to identify novel routes for converting electricity into chemical energy. Two main focus areas of the Kopernikus P2X project were firstly H_2 production via various electrolysis technologies and further storage (e.g. liquid organic hydrogen carriers or LOHC) and/or direct use in various sectors (e.g. road transport, polymer components, etc.). The second part of the project was dedicated to H_2 conversion together with CO_2 derived from different sources. Among other things, this research package pursued the development of intensive, modular, and scalable technologies which are suited for decentral e-fuels production.

The objective of this PhD thesis, prescribed by Kopernikus P2X requirements, was studying the catalytic methanation of CO_2 in compact and scalable methanation reactors. The focus was on both fundamental reaction aspects like kinetics of the reaction and long-term stability tests of the catalyst, as well as on reactor development, investigation, and modelling.

The **second chapter** of this dissertation delivers a comprehensive overview of the methanation reaction fundamental and technological aspects available in the literature to date. This overview covers thermodynamics, catalyst systems, kinetics, as well as mechanistic aspects and deactivation phenomena. In addition, state-of-the-art reactors for decentralized methane generation are surveyed and rated by their strengths and limitations. Finally, the chapter reveals the striking advantages of microreactors for fast reactions with special heat management requirements.

The **third chapter** is concerned with kinetic studies in a microstructured cross flow-cooled reactor. The underlying aspects of the consecutive CO_2 methanation reaction were revealed experimentally. It was shown that water is the major kinetically inhibiting species. Based on the experimental insights and the relevant literature rate models, a refined kinetic rate model was developed and statistically validated. The recommended model was shown to be capable of reflecting the experimental data with very good accuracy and predicting the course of intermediate CO formation and consumption. The kinetic model was evaluated for two promising catalyst systems. Both catalysts were subject to long-term tests for a total duration of 300 hours.

Chapter four presents high-pressure evaporation cooling as a highly efficient mechanism for temperature control in a compact and novel microstructured packed bed reactor

[6] https://www.kopernikus-projekte.de/projekte/p2x. Accessed on: 14.04.2021

prototype. The experiments were successfully concluded under different modes of operation (i.e. start-up, steady-state and transient) and varied operational conditions. For a better understanding of the involved effects in the tested reactor, a non-isothermal heterogeneous reactor model was developed. The mass and energy conservation equations were represented as an algebraic set of equations by dividing the reactor in n ideally mixed CSTRs. In this context, the kinetic model recommended in chapter three was implemented and verified.

Chapter five is a short presentation of the scaled-up prototype of the evaporation cooled microstructured reactor with methane output of 100 kW.

Chapter six provides a summary of the work and gives an outlook for future studies.

2 Theoretical and technological background

2.1 Chemistry and thermodynamics of CO_2 methanation

The catalytic hydrogenation of CO_2 was first discovered by Paul Sabatier in 1902 [18]. Ever since, this reaction has gained profound technical relevance in different fields such as gas purification for synthesis gas, and adjustment of H_2/C ratio in biomass or coal gasification processes [19–21]. The latest studies on methanation are orchestrated by PtG targets and specifications. The reaction of hydrogen and carbon dioxide to methane is a highly exothermic reaction, limited by thermodynamic equilibrium and is accompanied by volume reduction, as given in Eq. 2.1. According to Le Chatelier's principle, high pressures and low temperatures act in favor of product formation. However, reducing the temperature to below a certain degree slows down the reaction rate and is therefore not economically desired. The upper-pressure limit needs to be justified as well due to safety concerns and maintenance costs of high-pressure reactors.

$$CO_2 + 4\,H_2 \rightleftharpoons CH_4 + 2\,H_2O \quad \Delta_R H_{298\,\mathrm{K}} = -165\,kJmol^{-1} \tag{2.1}$$

The catalytic CO_2 methanation can be written as a two-step reaction with reverse water gas shift (rWGS, Eq. 2.2), followed by CO methanation (Eq. 2.3).

$$CO_2 + H_2 \rightleftharpoons CO + H_2O \quad \Delta_R H_{298\,\mathrm{K}} = 41\,kJmol^{-1} \tag{2.2}$$

$$CO + 3\,H_2 \rightleftharpoons CH_4 + H_2O \quad \Delta_R H_{298\,\mathrm{K}} = -206\,kJmol^{-1} \tag{2.3}$$

For determination of the favorable temperature and pressure window in absence of kinetic and transport limitations, thermodynamic studies were carried out using the total Gibbs free energy minimization method, described thoroughly by Gautam et al. in [22]. Gao et al. provides a comprehensive thermodynamic analysis on both CO and CO_2 methanation [23].

At equilibrium, the total Gibbs energy of a system reaches its minimum. By defining all the individual species of interest in a reaction system (here CH_4, CO_2, CO, H_2, H_2O,

O_2, N_2 and solid carbon), the composition of the products under specific conditions (i.e., temperature, pressure and composition) for the minimum value of Gibbs free energy can be calculated. The atomic elements carbon (C), hydrogen (H), oxygen (O), and nitrogen (N) must meet the mass balance constraints.

In the present work, the minimization procedure was carried out in Matlab® applying `fmincon` solver for computing the equilibrium mole fraction of the involved species. The details of this minimization problem are provided in the dissertation of Belimov [24], which was the basis of the thermodynamic analysis presented within this work. Tab. 2.1 gives an overview of 8 possible reaction pathways in CO_2 methanation.

Table 2.1: Overview of the reaction pathways relevant in the thermodynamic analysis of CO_2 methanation

No.	Reaction equation	$\Delta_R H_{298\,K}$ [kJ mol^{-1}]	Reaction type
1	$CO_2 + 4\,H_2 \rightleftharpoons CH_4 + 2\,H_2O$	-165	CO_2 methanation
2	$CO + H_2O \rightleftharpoons CO_2 + H_2$	-41	WGS
3	$CO + 3\,H_2 \rightleftharpoons CH_4 + H_2O$	-206	CO methanation
4	$2\,H_2 + 2\,CO \rightleftharpoons CH_4 + CO_2$	-247	Reverse dry methane reforming
5	$2\,CO \rightleftharpoons C + CO_2$	-172	Boudouard reaction
6	$CH_4 \rightleftharpoons C + 2\,H_2$	75	Methane cracking
7	$2\,H_2 + CO_2 \rightleftharpoons C + 2\,H_2O$	-90	CO_2 reduction
8	$H_2 + CO \rightleftharpoons C + H_2O$	-131	CO reduction

Natural gas is a mixture of different gaseous hydrocarbons and its exact composition and specifications depend on the location of methanation facilities. Based on the methane content, natural gas is divided into two main types: *type L* (low; with methane content of approximately 85%) or *type H* (high; with methane content of 89%-98%). This varied composition influences the physical properties of the natural gas mixture in terms of e.g. the heating value. Several criteria are used for comparing the quality of natural gas. Wobbe index is a measure for characterization of fuel gases, such as natural gas and sets the limit for interchangeability of fuels. Methane number is another indicant which is a measure of the knock resistance of natural gas for burning in combustion engines and is similar to the octane number for liquid fuels. In this definition, pure methane is assigned to a methane number of 100 and pure H_2 retains a methane number of zero.

Tab. 2.2 provides an overview of the main components of different natural gases distri-

buted in Germany from various geographical origins [15]. This table shows the absence of CO in natural gas sources and thus emphasizes the importance of methane selectivity during methane generation reaction. In addition, it can be grasped that most of the natural gas facilities do not include H_2. Injection of H_2 into current natural gas infrastructure demands detailed studies and feasibility analysis since technical adaptations must be implemented. Studies of Altfeld et al. hint that up to 10 Vol.% hydrogen can be blended in some natural gas systems [25]. However, in many regions, this issue remains open. The investment costs of such maintenance projects depend highly on the respective pipelines, operational conditions and hydrogen concentrations of interest [15].

Table 2.2: Region-based natural gas composition and specifications [15]

Compound	Unit	Russia (*H*)	North sea (*H*)	Denmark (*H*)	Netherlands (*L*)	Germany (*L*)
CH_4	mol.%	96.96	88.71	90.07	84.84	84.46
CO_2	mol.%	0.18	1.94	0.60	1.68	2.08
N_2	mol.%	0.86	0.82	0.28	10.21	10.24
Ethane	mol.%	1.37	6.93	5.68	3.56	1.06
Propane	mol.%	0.45	1.25	2.19	0.61	0.11
Butane	mol.%	0.15	0.28	0.90	0.19	0.03
Pentane	mol.%	0.02	0.05	0.22	0.04	0.01
Hexane and higher hydrocarbons	mol.%	0.01	0.02	0.06	0.07	0.01
Total sulfur	$mg\,m^{-3}$	<3	<5	<3	<3	<3
Calorific value	$MJ\,m^{-3}$	40.3	41.9	43.7	36.8	35.4
Standard density	$kg\,m^{-3}$	0.74	0.81	0.81	0.83	0.81
Wobbe index	$MJ\,m^{-3}$	53.1	52.9	55.0	46.0	44.7
Methane number	-	90	79	72	88	97

In the present work, thermodynamic studies were carried out on a mixture of CO_2 and H_2 with H_2/CO_2 stoichiometric ratio of 4. The parameters discussed include CO_2 conversion, CH_4 selectivity, CO yield, and mole fraction of the involved species. The methanation reactor introduced in Cha. 4 can be operated at a maximum absolute pressure of 6 bar. This pressure was kept constant during all the parameter variation tests (see Sec. 4.1.3). Thus, for the sake of better comparability, the pressure of 6 bar was used in thermodynamic studies when addressing the effect of temperature or composition. Due to the importance of pressure increase effect and variation of pressure in kinetic studies of Cha. 3, the influence of pressure increase on CO_2 conversion and methane selectivity are discussed in detail as well.

Fig. 2.1 left pictures the equilibrium composition of the involved species in CO_2 me-

thanation in the temperature range from 100 °C to 700 °C. The minimum mole fraction of CO_2 is at temperatures below 300 °C. This value reaches its maximum at around 600 °C and is relatively constant between 550 °C-700 °C. The CH_4 mole fraction has a decreasing trend over the entire temperature window, which sharpens above 450 °C. The increase in CO mole fraction with temperature magnifies at temperatures higher than 550 °C. In the entire temperature range, the solid carbon fraction (C_s) is very close to zero. Therefore, deactivation due to coking in CO_2 methanation for a stoichiometric (and over-stoichiometric) feed ratio is not foreseen by thermodynamics.

Fig. 2.1 right shows that CO_2 conversion changes from 100% to 70% in the studied temperature window. This conversion drop is steepest between 400 °C to 550 °C and afterward reaches a constant level due to increased values of the equilibrium constants of other side reactions such as CO_2 reduction at higher temperatures [23]. Additionally, CO yield starts to gain weight above 500 °C, since the equilibrium constant of CO methanation has the lowest value at higher temperatures compared to the other involved reactions. Accordingly, CH_4 selectivity drops considerably above 500 °C; i.e., from 98% at 500 °C to 57% at 700 °C. According to this information and the fact that below 200 °C the kinetics are extremely slow, the temperature window of interest can be confined to 200-500 °C and is used for further thermodynamic calculations.

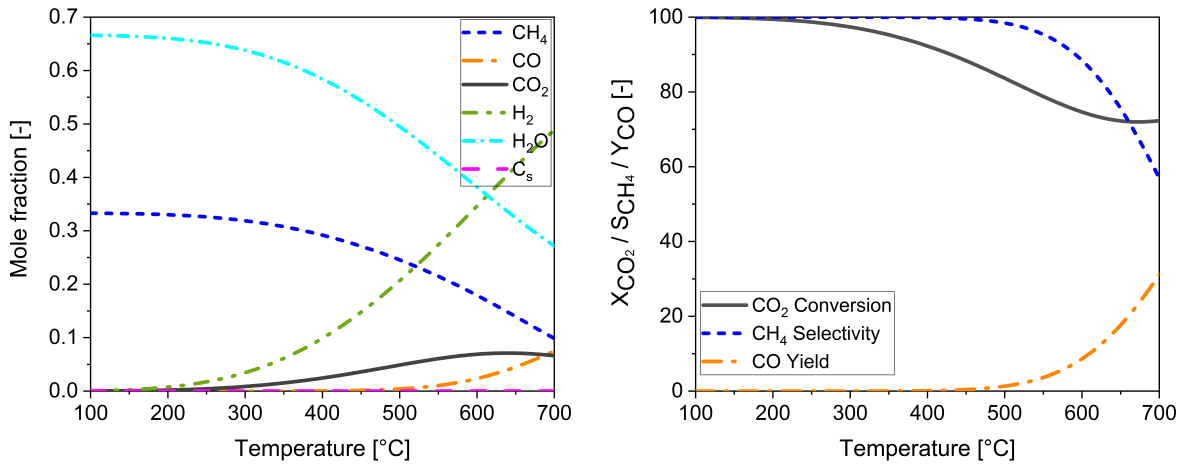

Figure 2.1: Temperature effect on thermodynamic equilibrium. Left: Mole fraction of CO_2 methanation components. Right: CO_2 conversion, CH_4 selectivity and CO yield. $H_2/CO_2 = 4$, $p_{abs} = 6$ bar.

The influence of pressure increase on CO_2 conversion, CH_4 selectivity and CO yield in the range of 1-20 bar, at 400 °C and stoichiometric feed ratio is presented in Fig. 2.2.a. By increasing the pressure from 1 bar to 5 bar, the CO_2 conversion improves by about

7% (from 85% to 92%). With further increase of pressure, CO_2 conversion approaches a plateau. Raising the pressure further to 20 bar results in only 3% conversion improvement. In the case of higher CH_4 selectivity, the positive effect of pressure is less evident. At 1 bar, the selectivity equals to 98.5% and with slight enhancement in the pressure (only 1 bar), it surpasses 99%. The same applies to the CO yield which varies between 0.4% and 0.04% under the studied conditions.

Fig. 2.2.b and c show the pressure and temperature effects on equilibrium conversion and selectivity, respectively. In the lower temperature regime (<350 °C), the CO_2 conversion and the selectivity to CH_4 are hardly affected by pressure. Higher temperatures, which are indeed industrially relevant, show a higher sensitivity toward pressure. Increased CO_2 conversion from 71% to 89% at 500 °C by pressure enhancement from 1 bar to 20 bar supports operation at higher pressures in fixed-bed reactors. However, the extent of this improvement levels off beyond 5 bar. The same applies to methane selectivity; elevation of pressure above 5 bar has a very small influence on increasing this value.

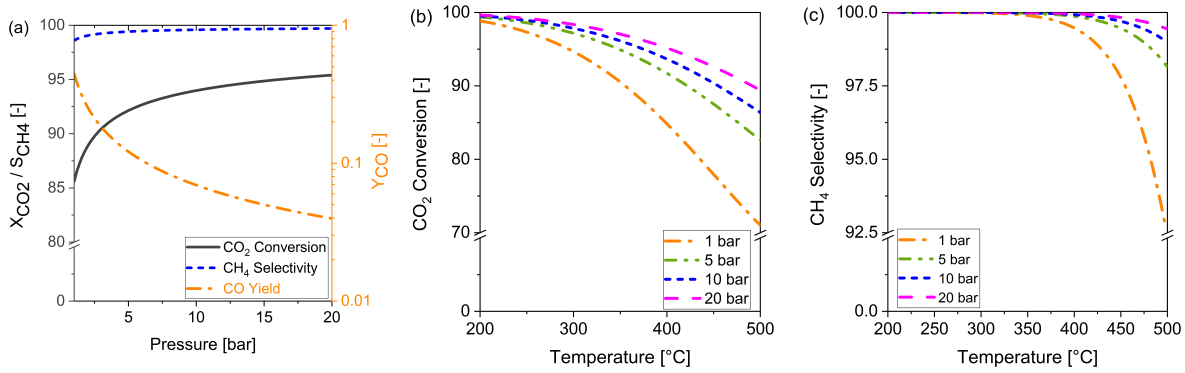

Figure 2.2: Pressure effect on thermodynamic equilibrium. (a): CO_2 conversion, selectivity to CH_4 formation and CO yield at T=400 °C. (b): CO_2 conversion at T = 200-500 °C. (c): CH_4 selectivity at T = 200-500 °C. H_2/CO_2 = 4.

Apart from temperature and pressure, the quality of the methanation product may be adjusted by the H_2/CO_2 ratio in the feed. It is of importance to note that in a steady-state methanation unit, a feed ratio < 4 is uncommon due to the increased probability of carbon formation. However, from a research perspective, it is necessary to study the under-stoichiometric ratios.

Fig. 2.3 demonstrates the equilibrium CO_2 conversion and CH_4 selectivity with varied feed ratio (3-6), at a temperature range of 200-500 °C and a pressure of 6 bar. H_2 deficiency influences the conversion more pronounced than its surplus. For example, at

stoichiometric H_2/CO_2 ratio (p = 6 bar, T = 400 °C) the equilibrium CO_2 conversion is equal to 92%. Cutting back this ratio to 3.5 results in 10% conversion decline, while increasing the ratio to 5 and higher improves the conversion to 99%. The equilibrium CH_4 selectivity is less sensitive to the feed ratio. This parameter is equal to 96.7% in the worst case (T = 500 °C, H_2/CO_2 ratio = 3). Although for injection in the gas grid only traces of CO_2 are desired, increasing the feed ratio results in considerable unreacted H_2 share. As discussed earlier, this unreacted H_2 would require separation and recycling in case of incompatibility with the natural gas system.

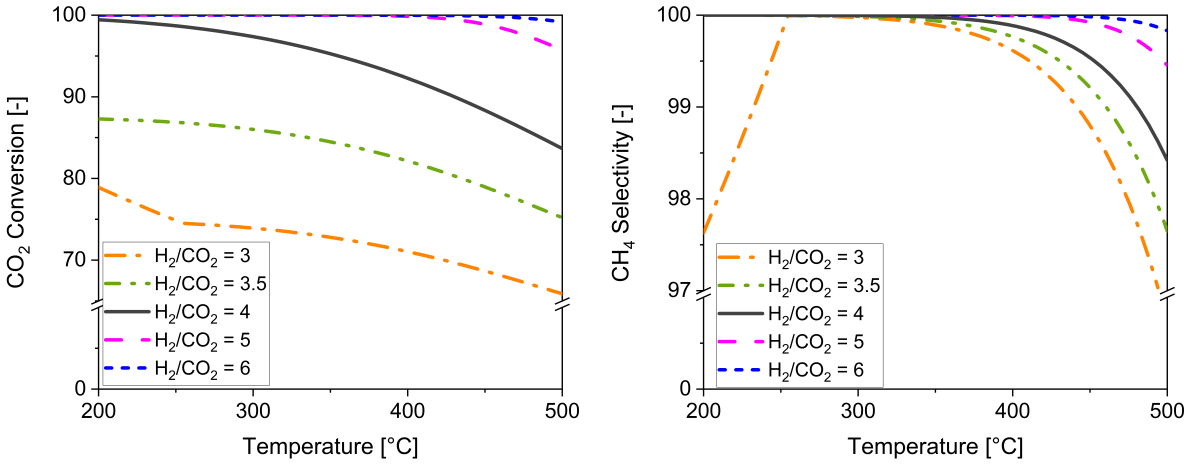

Figure 2.3: H_2/CO_2 ratio effect on thermodynamic equilibrium. Left: Conversion of CO_2. Right: Selectivity to CH_4. p_{abs} = 6 bar, T = 200-500 °C

2.2 Catalyst systems

About two decades after the famous discovery of Sabatier on the catalytic reaction of CO_2 and H_2 on Ni catalysts in 1902; Fischer, Tropsch, and Dilthey identified the order of methanation activity for different metals [26]. Vannice was the first scientist who conducted an analytical study on the catalytic activity of the metals Fe, Co, Ni, Ru, Rh, Pd, Ir, and Pt for the methanation reaction [27]. In their follow-up research, they confirmed the decisive influence of the support on the activity and selectivity of Ni catalysts [28]. The concluding studies in the next years proved that the list of important metals for this reaction can be shortened and classified as [29]:

Activity: Ru > Fe > Ni > Co > Mo

Selectivity: Ni > Co > Fe > Ru

There is a huge number of research papers and many reviews which give an overview of different catalytic systems for CO and/or CO_2 methanation [30–38]. The metallic active components, the applied support [39], the promoter, and the preparation method [40] are the optimization points that are studied based on the desired application and the studied parameter range.

Nickel and ruthenium are the two leading methanation catalysts that are extensively studied. Comparing the activities of commercial 3% Ru-Al_2O_3 to a 20% Ni-Al_2O_3 proved the enhanced performance of ruthenium compared to nickel. Gabarino et al. [41] showed that by applying the Ru catalyst at 15 000 h^{-1} gas hourly space velocity (GHSV) and excess of H_2, 96% CH_4 yield at 573 K is obtainable. Whereas for Ni, the maximum 80% CH_4 yield is achieved at a higher temperature of 673 K and is, therefore, it is outperformed by the Ru-based catalyst. Additionally, in the case of using Ru, no CO in the byproduct was measured, which was not the case in experiments on Ni catalyst. Quindimil et al. [42] conducted detailed studies on the effect of metal loading on Al_2O_3 supported Ni and Ru catalysts. Their most important results are that increasing the temperature diminishes the Ru dispersion on Al_2O_3 due to the formation of agglomerates. In the case of Ni, higher temperatures promote the formation of Ni phases which are highly interacting with the Al_2O_3 support and are therefore inactive for CO_2 methanation. Furthermore, in contrast to Ru, the dispersion of Ni on Al_2O_3 is highly sensitive to its loading amount. The authors designated 4% Ru-Al_2O_3 and 12% Ni-Al_2O_3 as the optimally prepared catalysts and confirmed the superior activity of the 4% Ru-Al_2O_3, especially at lower temperatures.

According to these studies and many more which investigate the catalytic methanation activity of Ru and Ni individually, ruthenium is the most active and stable methanation catalyst. The high low-temperature activity of Ru makes this catalyst especially attractive [43–45]. However, the high costs of this noble metal argue against its prominent application in industry. Therefore, undoubtedly nickel is highlighted as the most commonly applied methanation catalyst. The high activity, enhanced selectivity, low cost, and availability make Ni much more interesting for commercial practices [32, 33, 35].

Despite being the standard methanation catalyst, Ni has some serious problems. Sintering, carbon deposition, and sulfur poisoning are the main barricades that hinder a stable and long-term methanation operation [46]. Aftermath of utilizing renewable H_2 for methanation is the fluctuating reaction conditions. Deficient H_2 conditions can be crucial for Ni catalyst, since it may go under irreversible structural mutations under different

operational conditions. A great deal of studies attempt to address these issues [47].
In this respect, the second most important optimization parameter after the active phase in a methanation catalyst is the choice of support. High surface area support plays an important role in the morphology and dispersion of the active metal and its adsorption properties. γ-Al_2O_3 is the classic support for Ni [39, 41, 48–64]. Nonetheless, there are many studies on other support materials such as SiO_2 [39, 40, 49, 50, 65–73], TiO_2 [39, 50, 56, 74, 75], ZrO_2 [59, 76–82], CeO_2 [59, 83–89], CeO_2-ZrO_2 mixed oxide [90–95], hydrotalcite [96–101] and etc.
Generally speaking, direct comparison of the different supports is rather speculative due to the different operational conditions under study, varied metal loading, different preparation methods, and addition of promoters. Tada et al. [83] derived an analogy between 10 wt.% Ni loaded on various supports of α-Al_2O_3, CeO_2, MgO and TiO_2. The activity of Ni supported on α-Al_2O_3 and CeO_2 was confirmed to be superior to the two other supports. CO_2-TPD (temperature-programmed desorption) studies showed that the CO_2 adsorbed on the Ni-CeO_2 surface was much higher compared to Ni-Al_2O_3, which explains the better activity of Ni-CeO_2 catalyst in the temperature range of 250-450 °C. The in-situ infrared investigations of Muroyama et al. [59] on Ni catalysts supported on various metal oxides proved the formation of different intermediate species on the catalyst surface, depending on the applied support. One explanation was that supports with modest basic sites are desired for the high catalytic activity of methanation catalysts, verified by the CO_2 desorption behavior on different tested supports.
The synergy between the promoter and the active metal and/or support can also be used for improving a number of catalyst properties such as: the electron mobility [71, 102], dispersion degree [103, 104], the thermal stability [105–107], resistance to carbon deposition and coke formation [53, 107], Ni sintering [70, 105, 108–110] and catalyst reducibility [51, 103, 104, 110].
The addition of a second metal is another approach that can modify the activity, selectivity, and stability of methanation catalysts [52, 81, 111–115]. The investigations of Hwang et al. [112] and Ren et al. [81] on adding a second metal (M) to Ni (in [112] M = Fe, Zr , Y and Mg, and in [81] M = Fe, Co, and Cu) proved an enhanced activity of Ni catalysts when doped with Fe. Upcoming researches demonstrated that a Ni to Fe ratio of 3 is highly desired in order to optimize the Ni dispersion [116–118].
Mutz et al. [119] proved the outstanding activity of a 17 wt.% Ni_3Fe catalyst supported on γ-Al_2O_3 compared to a mono-metallic Ni reference catalyst. In addition, their experimental tests in a microstructured packed bed reactor for 45 hours proved the higher activity and selectivity of the Ni_3Fe/γ-Al_2O_3 compared to a commercial Ni catalyst.

Serrer et al. [120] carried out detailed operando investigations on a monometallic Ni catalyst and a bimetallic Ni_3Fe/γ-Al_2O_3 in over- and under-stoichiometric hydrogen-dosed cycles. They showed that under H_2-deficient conditions, the monometallic Ni catalyst is more prone to irreversible surface oxidation. Whereas in the case of Ni_3Fe catalyst, a preferential and reversible FeO formation is observed which protects the active Ni sites from oxidation. In this respect, iron is confirmed to play a protective role by preserving the catalytic activity under fluctuating operational conditions.
These studies certify that new catalyst materials for CO_2 methanation are a dynamic topic in the research community. Nevertheless, for improving the catalytic activity still, much work on new materials and the underlying reaction mechanism is required, and to this date, no all-inclusive formula is at hand.

2.3 Mechanistic aspects

For revealing the mechanism of a reaction, the knowledge from experimental surface science, i.e., in-situ spectroscopy techniques, and theoretical surface i.e., computational modelling must be brought and examined together. This is usually an elaborate and challenging task [121].
Although the methanation reaction of CO_2 and H_2 is known for over a century, the research community did not converge to a single reaction mechanism. The true mechanistic course of CO_2 hydrogenation to methane is not yet fully understood or agreed upon.
The proposed mechanistic pathways for CO_2 methanation can be divided into two categories. The first pathway is via CO_{ads} formation from CO_2 dissociation through the rWGS reaction (Eq. 2.2). The subsequent hydrogenation of the adsorbed CO follows the same course as methanation of CO (Eq. 2.3, the *dissociative* route, Fig. 2.4.b) [66,67,122–126]. The second scheme is without CO intermediate and via direct adsorption of CO_2 and H_2. In this respect, formate, carbonate or methanol species have been reported as intermediate species (the *associative* route, Fig. 2.4.a) [76, 84, 127–131].
The same controversial discussions on two mechanistic pathways apply to the mechanism of CO methanation. The first premise was introduced by Araki and Ponec [132] and is known as the "carbon theory". According to the carbon theory, molecular adsorption and successive dissociation of CO leads to surface carbon formation. This adsorbed carbon reacts further with H_2 to form CH_4 (Fig. 2.4-d) [123, 124, 133–135]. The second mechanism presumes the formation of an oxygenated compound as the intermediate (e.g. carbon hydroxyl COH_x) in presence of H_2 due to its lower activation energy for breaking

the C-O bond (Fig. 2.4-c) [136–139]. For each pathway, differing rate-determining steps (RDS) for both CO and CO_2 methanation is suggested. An overview of the details of these studies can be found in literature [30, 32, 140–142].

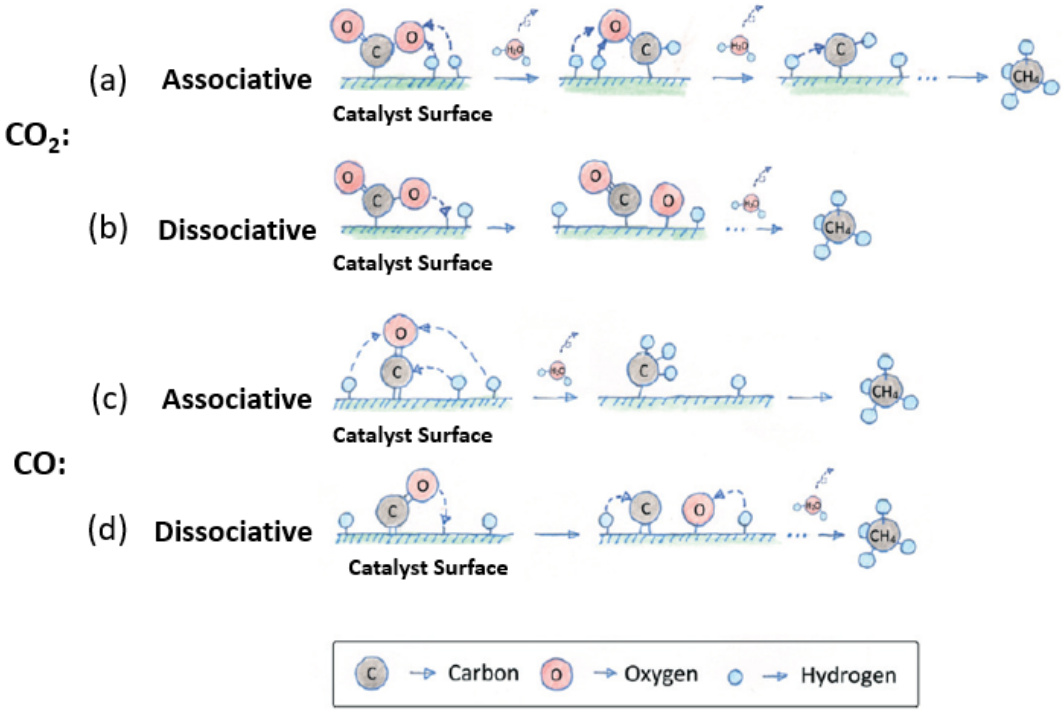

Figure 2.4: CO_2 and CO methanation mechanistic pathways: (a) associative CO_2 hydrogenation, (b) dissociative CO_2 hydrogenation, (c) associative CO hydrogenation and (d): dissociative CO hydrogenation. Adapted from [141].

Vogt et al. [143] carried out detailed investigations on well-defined Ni/SiO_2 catalysts with particle sizes in the range of 1-7 nm and identified two particle size-dependent mechanisms. They showed that the intensity of the CO_{ads} peak in FTIR (Fourier-transform infrared spectroscopy) measurements can be used as an indirect way for diagnosing the Ni particle size. In samples with higher Ni dispersion, gaseous CO and less CO_{ads} species were observed. Whereas no gaseous CO was measured for samples with larger Ni nanoparticles and the peaks correlated to more stable adspecies containing CO (such as bridged carbonyl or carboxylate) were more pronounced. In this respect, three particle size-dependent intermediates are reported: 1. CO_{ads} (dominant on larger particles, dissociative pathway), 2. gaseous CO, and 3. surface formate (dominant in smaller Ni nanoparticles, associative pathway). The conclusion made by Vogt et al. is that a moderate adsorption strength of the intermediate CO (realized by 2-3 nm particles) is desired

for an optimal methanation catalyst.
Similar work on sensitivity of methanation mechanism on active metal particle size was published by Wu et al. in [144]. The H_2/CO_2 ratio [141] and the effect of the support material [59, 84, 130] are some of the other parameters which have a great influence on the methanation mechanism.
In conclusion, it is of importance to realize that there is solid evidence for both mechanistic pathways and that declaring a specific reaction scheme without stating the details of the system under study may lead to premature judgments.

2.4 Reaction kinetics

Earliest publications on methanation kinetics were done in the 1950s [65, 145]. Further developments on the models for application in gas purification and methane steam reforming were mainly carried out in the 1980s [67, 146, 147].
The developed rate models can be divided in two main groups of power law and Langmuir-Hinshelwood-Hougen-Watson (LHHW) type kinetics [148]. While the first one is rather simple and has few parameters for estimation, it fails to apply to a wide reaction parameter range. The general form of these two rate model types is presented in Eq. 2.4 and 2.5, respectively. As Eq. 2.5 indicates, the fundamental difference between them is the integration of an inhibition term in the denominator of the kinetic equation.

$$r_{CO_2 \rightarrow CH_4} = k_i \cdot p_{CO_2}^{\alpha} \cdot p_{H_2}^{\beta} \cdot (equilibrium\ term) \tag{2.4}$$

$$r_i = \frac{(rate\ constant) \cdot (driving\ force) \cdot (equilibrium\ term)}{adsorption\ term} \tag{2.5}$$

The dependency on temperature of the rate constant is included via the Arrhenius relation:

$$k_i = k_0 \exp(\frac{E_A}{RT}) \tag{2.6}$$

The kinetic model published by Xu and Froment [147], who studied methane steam reforming on an aged 15.2 wt.% $Ni/MgAl_2O_4$ catalyst in a tubular reactor can be understood as a pioneering work for further investigations on methanation kinetics. In their work, a set of reaction rate coefficients for the reversible reactions (CO and CO_2 methanation and rWGS reaction) are suggested. A summary of accompanied and following studies can be found elsewhere [35, 142].
Despite a considerable number of developed rate equations and studies delivering rate constants for the methanation of CO and/or CO_2, only a few deliver data under relevant

operating conditions [142]. For example, most of the studies are carried out under very low reaction temperature and pressures. Whereas, the typical operation regime in technical plants is a temperature window of 300-500 °C and a pressure of 5-20 bar [35]. In the following, three of the most pertinent literature kinetic rate models to the targets set in this study are reviewed shortly:

The model developed by Koschany et al. [61] was developed for PtG applications of Ni catalysts with pure CO_2 in the feed. Process parameters had been varied between 180 °C-340 °C, 1-15 bar and H_2/CO_2 ratio of 0.25 to 8. The measurements were carried out in a lab-scale fixed bed reactor on Ni-based catalysts. Prior to the kinetic data collection, the catalyst was aged for 300 h at 380 °C and 7 bar under a feed containing H_2, CO_2, CH_4, and H_2O to reach a constant level of activity during the kinetic measurements. Koschany et al. could show that a power-law rate equation can be applied to describe the experimental data fairly well; however, it systematically overestimated the reaction when approaching the thermodynamic equilibrium. The authors solved this problem by developing a model with inhibition term based upon the LHHW formalism. The LHHW model was derived assuming hydrogen-assisted carbon-oxygen bond cleavage. The rate-determining step of the reaction was assumed to be the formyl formation. The model fails to describe methane selectivity, and can be only used for the description of CO_2 conversion since it completely ignores CO formation and simulates direct CO_2 to CH_4 conversion.

Kopyschinski [149] studied CO methanation together with the WGS reaction. He applied a spatially resolved wall-coated plate reactor for data collection using a commercial nickel catalyst. The reaction conditions applied are characterised by temperature window of 280-360 °C, pressure of 1 bar and H_2/CO_2 ratio of 5-6. One of the important conclusions made was that below 300 °C, the WGS reaction can be neglected. According to Kopyschinski, CH_4 and CO_2 do not inhibit the reaction rate, in contrast to water, which clearly contributes to the rate inhibition. Three models postulated from this reaction mechanism were found to be equally good in describing the experimental data. Unfortunately, no equilibrium term was included in these models, which could make them tricky to apply them for the description of technical reactors.

Zhang et al. [150] investigated the methanation reaction using biomass-based synthesis gas, that is with mixtures of CO and CO_2 in the feed. The experimental data of this work are fitted to CO methanation and WGS. They investigated the methanation reaction under industrially relevant conditions in a tubular milli-fixed bed reactor on a commercial Ni catalyst. Temperature and pressure were varied from 275 to 360 °C and 1 to 5 bar. The kinetic rate models used were adapted from the work of Xu and Froment [11] and fitted

to the collected data. Essential insights achieved by Zhang et al. are that CO_2 does not influence on the rate of CO methanation and that a higher H_2/CO ratio improves the methane selectivity significantly. All other species taking part in the reaction (H_2, CO, CH_4 and H_2O) are included in the inhibition term.
In Tab. 2.3 the mathematical description of the models after Koschany, Kopyschinski and Zhang are presented according to Eq. 2.5. The equations are adapted to the further notation in this work.

Table 2.3: Overview of LHHW kinetic rate models in literature for industrial operating conditions

Model	Reaction	Kinetic term	Inhibition term	Equilibrium term
Koschany [61]	$r_{(CO_2 \rightarrow CH_4)}$	$k p_{CO_2}^{0.5} \; p_{H_2}^{0.5}$	$\frac{1}{(1+K_{OH} \frac{p_{H_2O}}{p_{H_2}^{0.5}} + K_{H_2} p_{H_2}^{0.5} + K_{mix} p_{CO_2}^{0.5})^2}$	$(1 - \frac{p_{CH_4} p_{H_2O}^2 p_{tot}^2}{p_{CO} p_{H_2}^4 K_{CO_2Meth.}})$
Kopyscinski [149]	$r_{(CO_2 \rightarrow CO)}$	$k_1 p_{CO_2} p_{H_2}^{0.5}$	$\frac{1}{(1+K_C p_{CO} + K_{OH} \frac{p_{H_2O}}{p_{H_2}^{0.5}})^2}$	$(1 - \frac{p_{CO} p_{H_2O}}{p_{CO_2} p_{H_2} K_{rWGS}})$
	$r_{(CO \rightarrow CH_4)}$	$k_2 p_{CO}^{0.5} p_{H_2}^{0.5}$		-
Zhang [150]	$r_{(CO_2 \rightarrow CO)}$	$k_1 \cdot p_{CO_2}$	$\frac{1}{(1+K_C p_{CO} + K_{H_2} p_{H_2} + K_{CH_4} p_{CH_4} + K_{H_2O} \frac{p_{H_2O}}{p_{H_2}})^2}$	$(1 - \frac{p_{CO} p_{H_2O}}{p_{CO_2} p_{H_2} K_{rWGS}})$
	$r_{(CO \rightarrow CH_4)}$	$k_2 \cdot p_{CO} p_{H_2}^{0.5}$		$(1 - \frac{p_{CH_4} p_{H_2O} p_{tot}^2}{p_{CO_2} p_{H_2}^3 K_{COMeth.}})$

2.5 Considerations on catalyst deactivation

The methanation reaction like many other catalytic processes is prone to deactivation over time. According to Bartholomew [46], the catalyst deactivation mechanisms can be divided into three major categories: chemical, mechanical and thermal. These three categories may be classified into several subdivisions such as poisoning, fouling, thermal degradation, vapor-solid reactions, and so on. As already mentioned in Sec. 2.2, the main issues in Ni catalyzed methanation are: poisoning, coking, and sintering. In the following, a summary of each of these processes is provided.

2.5.1 Poisoning

The chemisorption of a compound on the catalyst surface, which in turn affects the catalytic activity is called poisoning. Irreversible and strong chemisorption of H_2S on Ni surface is one of the chief methanation problems, especially when coal or biomass gasification plants are the syngas resources. Apart from sulfur poisoning, exposure to

oxygen changes the oxidation state of the catalyst. Under reaction conditions and in presence of the educts such alterations can have negative effects on catalyst activity [46]. This deactivation source is more feasible for a PtG process scheme since temporary H_2 deficient conditions may induce irreversible changes of the Ni oxidation state and therefore activity [70, 114, 120].

2.5.2 Fouling

Bartholomew defines fouling as the "physical deposition of species from the fluid phase onto the catalyst surface, which results in activity loss due to blockage of sites and/or pores. In its advanced stages, it may result in the disintegration of catalyst particles and plugging of the reactor voids. Important examples include mechanical deposition of carbon and coke in porous catalysts" [46].
All reactions which involve CO and hydrocarbons are susceptible to carbon or coke deposition. The industrially famous reaction which leads to formation of surface-carbon is the Boudouard reaction (equation 5 in Tab. 2.1).
Unlike CO methanation, thermodynamic studies on CO_2 methanation indicate that carbon deposition is not favorable in this reaction (see Sec. 2.1). Since the rWGS reaction is the first step of CO_2 hydrogenation to methane, the formation of CO is accompanied by water evolution which plays a protective role regarding restraining carbon deposition [23]. However, operating under conditions with a temporary under-stoichiometric ratio of H_2/CO_2 or directing biogas as the methanation reactor feed can lead to carbon formation during CO_2 methanation too [35, 151, 152].
Intensive studies on coking mechanism were done by [153–156]. Tab. 2.4 shows the different carbon species which tend to deposit on Ni surfaces and the relevant temperatures for their formation and reaction. This points out that the carbon and coke formed on Ni surfaces convey varied morphology and adsorption strengths. Thus, removing them or suppressing their formation requires detailed knowledge on the reaction conditions, catalyst type, and surface chemistry.

Table 2.4: Temperature range for formation of different carbon species on Ni surfaces [46]

Surface carbon sort	Temperature of formation [°C]	Peak temperature for reaction with H_2 [°C]
Surface carbide: adsorbed, atomic (C_α)	200-400	200
Polymeric, amorphous films (C_β)	250-500	400
Vermicular fibers and whiskers (C_ν)	300-1000	400-600
Bulk Ni_3C (C_γ)	150-250	275
Graphitic films (C_c)	500-550	550-850

2.5.3 Sintering

Sintering is referred to as the loss of active surface area, mainly occurring due to thermal processes. Generally speaking, sintering in supported catalysts is observed to have two main mechanisms: one is the coalescence and migration of crystallites along the support surface resulting in a collision of the crystallites. The second mechanism is the migration of atoms from a metal crystallite across the support surface and collision with another crystallite. Due to the stability of larger metal crystallites, the smaller crystallites tend to reduce in size in favor of larger crystallites [157]. Structural distortion of the support e.g. loss of support area or support collapse due to thermal processes affects the catalytic activity in a similar way. A number of parameters affect the sintering rate in supported metallic catalysts, such as temperature, atmosphere, active metal type, and its dispersion degree, the addition of promoters and support characteristics (e.g. surface area, morphology, porosity, and metal-support interactions) [46]. For example, many industrial reactive gases such as O_2, H_2, CO and H_2O increase the sintering rate of metallic particles (e.g. Ni, Pt, Pd, and Co) by decreasing the particles diffusion barrier through surface modification or formation of mobile species [46, 158].
Fig. 2.5 presents the transmission electron microscopy (TEM) images of 15% Ni/Al_2O_3 catalyst before (2.5 left) and after sintering in H_2 at a temperature of 1023 K. The TEM images show a clear increase in the active metal size. In addition, the Ni particles in the sintered sample indicate an uneven size distribution [159].
Sintering is seen as one of the crucial problems in catalytic methanation practised in fixed bed reactors due to high operating temperatures [35]. Some studies report that Ni sintering is accelerated in presence of steam in the reacting mixture [160]. Therefore, it is much more efficient to apply materials and methods which are sintering resistant, rather

than dealing with its consequences. The addition of a promoter to improve the metallic dispersion, alloying via a noble metal to increase the sintering resistance, or a second base metal to enhance the nano-alloy properties are some of the practiced methods in the research community [161–163].

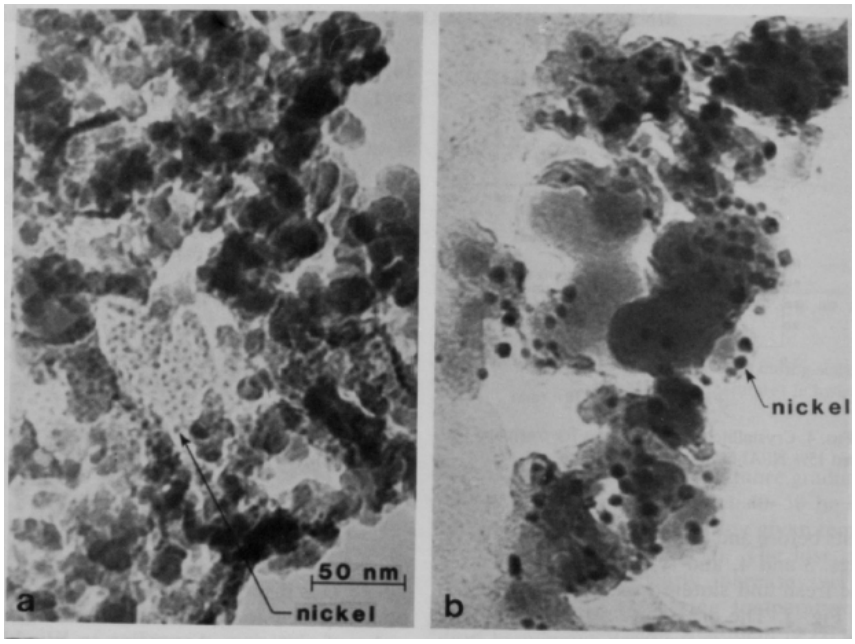

Figure 2.5: Electron micrographs of catalysts before and after sintering in H_2 at 1023 K. Left: Fresh 15% Ni/Al_2O_3, right: sintered 15% Ni/Al_2O_3 (taken from [159])

2.6 State-of-the-art methanation reactors

Methanation of CO_2 and H_2 in the context of a Power-to-Gas technology has caught great attention in the last decade, as already pointed out in Cha. 1. There is a considerable number of research articles as well as pilot plant and industrial projects proceeding in this field. A detailed description of these projects is given in references [16, 21, 35, 152]. In the following, the most common methanation reactor concepts with a special focus on technologies applicable to decentralized methanation plants are summarized.

2.6.1 Methanation reactor concepts

The main complication in the design of methanation reactors is temperature control (see Sec. 2.1). Therefore, the optimization point in the design of methanation reactors

is concentrated on enhancing the heat removal strategy. In this respect, state-of-the-art methanation reactors can be divided into three major types: 1. adiabatic reactors, 2. isothermal reactors, and 3. polytropic reactors.

The most industrially established and simple concept is a cascade of fixed bed reactors together with intermediate cooling stages, usually with gas recycling [164–167], as shown in Fig. 2.6. In adiabatic reactors, the operational temperature can go as high as 700 °C. Although this is connected to a high reaction rate, it limits the conversion due to thermodynamics and enforces high thermal-stress resistance on the catalyst [46]. Feed recirculation systems are tangled with high investment and operational costs and a complex operational infrastructure [35]. Another important factor highlighted by Goetz et al. [16] is that reducing the hydrogen storage by enabling dynamic operation of the methanation reactor can cut back the total PtG plant investments by up to 8%. Adiabatic fixed bed reactors show very poor load flexibility and therefore, they are impractical for decentralized PtG applications.

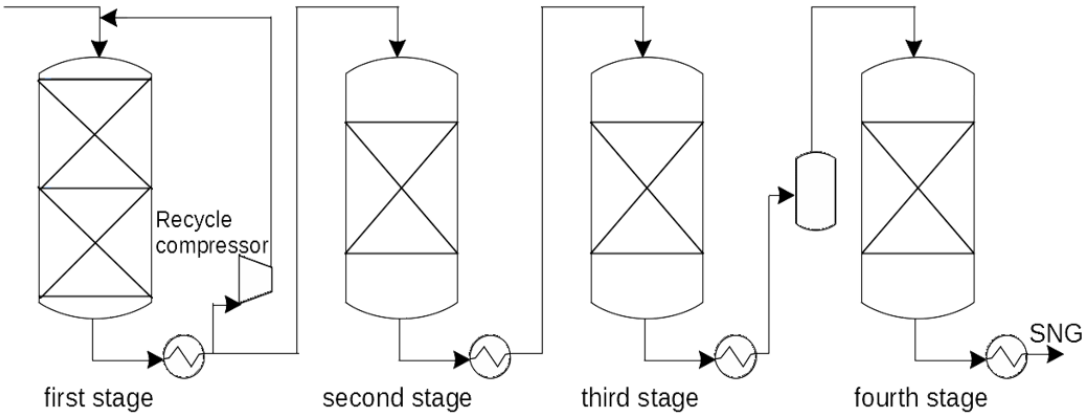

Figure 2.6: Adiabatic methanation using multi-stage fixed bed reactors together with intermediate cooling and recycling (the TREMP process, process scheme adapted from [165])

Fluidized bed reactors are another class of methanation reactors that are intensively studied due to their enhanced heat transfer characteristics. Near isothermal conditions and uniform temperature gradients prevail owing to a continuous flow of gas through a bed of fine catalyst particles [168]. The major drawback of fluidized bed reactors is the erosion of the reactor walls and internal parts and loss of catalyst that result in massive maintenance costs [169, 170].

Three-phase methanation is an attractive alternative concept which also guarantees isothermal operation by suspending the catalyst particles in a liquid with high heat capacity,

in so-called slurry bubble column reactors. The main disadvantage of three-phase reactors is catalyst attrition and decomposition of the liquid phase. In addition, the complex mass and heat transfer phenomena and hydrodynamics of the system are not yet fully understood. This impedes the prediction of the system behavior and makes the scale-up from lab to pilot and industrial-scale a challenging task [171, 172].

The third class of methanation reactors which combines advantages of high reaction rate and good temperature control is structured reactors with a polytropic temperature profile. Honey-comb reactors [173–176], reactors filled with structured foams [60, 177, 178], micro-channel reactors [179–184] and 3D printed reactors [63] are operated in milder temperatures compared to adiabatic reactors (below 500 °C) and provide an enhanced heat removal.

Recently Schollenberger et al. [175] showed the potential of a honeycomb reactor surrounded with a heat transfer oil jacket to meet the requirements of PtG plants. The authors work further on the scale-up of this technology for 1 MW feed, as proposed in the EU-funded project Store & Go. Frey et al. [178] research is dedicated to detailed research on the intensification of mass and heat transfer and control of the reaction conditions in a structured bed reactor filled with coated open-cell foams. Neubert et al. [183] suggested a new methanation reactor with heat pipe integration into a structured reactor. Their initial experimental tests confirmed that in a 5 kW prototype, the hotspot temperature can be well-controlled. Extending the process to a second stage via a fixed bed reactor shows promising product quality for injection in the SNG grid.

Based on CFD Simulations, Alarcon et al. [185] proposed a reactor applying a multitabular design for achieving a high methane yield in elevated space velocities. It was shown that in order to lower the hotspot temperature and operate in a thermodynamically controlled reaction regime, the reacting media must be cooled via a cooling media of medium temperature. In the optimal design suggested by Alarcon et al., 1000 tubes were necessary for a medium-size biogas plant.

Giglio et al. [186] studied the optimized reactor parameters, plant efficiency, and SNG quality when coupling a high-temperature electrolyzer with a methane generation unit. Their work showed that thermal management is the main hurdle for the design of multitube fixed bed methanation reactors, although having very high heat transfer coefficients when using the evaporation of water as the cooling system. Optimization of the methanation unit (e.g. number of the fixed bed tubes, the water coolant temperature, and CO_2 flow inlet) had to fulfill several constraints such as the maximum reaction temperature (<550 °C) and outlet CH_4 concentration (95%). The process simulations showed that via integration of the optimized methanation unit and the electrolyzer, an efficiency of 86%

(HHV [1]-based) is realizable.
Although the structured reactors offer superior properties regarding heat transfer and pressure drop, the low amount of catalyst that can be inserted via coating in the reactor imposes space velocity limits, when aiming to approach the thermodynamic conversion. The coating process on its own is a challenging task and in case of catalyst deactivation, the reactor is to be replaced. The other reactor types that have been studied for the methanation are membrane [87, 187–191], sorption-enhanced [192, 193] and non-thermal plasma reactors [192, 194]. However, all these systems are yet in the research and development stage and are far from industrial maturity.
The microstructured reactors are one of the most promising generations of reactors that are lately catching a great deal of attention in decentralized applications [195]. In the following chapter, the main characteristics of this technology are summarized.

2.6.2 Process intensification by microstructured reactors

One of the most generic definitions of process intensification, construed by Hessel et al. [196] is as follows:
"Process intensification encompasses both novel apparatus and techniques which are designed to bring dramatic improvements in manufacturing and processing. As a result, safe, cheap, compact, environmentally friendly, and energy-efficient technologies are obtained."
Microstructured technology is one of the most appealing concepts to achieve the target of going one step beyond conventional chemical systems. The initial idea for designing micro-devices was reducing investment costs by building a compact-size plant and scaling down the size and number of pipelines and peripheral equipment for an identical production rate [197]. However, chemical micro-engineering is not always confined to the implementation of small-scale devices. But as the above definition implies, it also serves for improvement of the process conditions such as enabling novel operational windows, increased process safety, and unique process control methods [198].
As a rule of thumb, the implementation of microreactors is recommended for reactions with a reaction enthalpy higher than 50 kJ mol^{-1} and a characteristic reaction time below 1 second. The specific wall area of microstructured devices is typically between 10.000 to 50.000 $m^2\,m^{-3}$, while this value is usually at most 100 $m^2\,m^{-3}$ for conventional devices. This high ratio together with fast heat transfer and mixing due to these fluid structures give rise to superior heat and mass transfer properties. The overall heat transfer coefficient in

[1] Higher heating value.

microreactors can be as high as 25.000 W m^{-2} K^{-1} in gas-liquid chemical reactions [199]. Mass transfer is often a limiting factor in fast catalytic reactions. It may diminish the overall performance of a process in a conventional reactor. The Einstein-Smoluchovski equation (Eq. 2.8) derives a relationship for estimation of the time (t) and length (r) scale of mass transfer processes:

$$t_{diffusion} = \frac{r^2}{D_{eff}} \tag{2.7}$$

Where D_{eff} is the effective diffusion coefficient and is about 10^{-5} – 10^{-6} m^2 s^{-1} for gases and 10^{-9} – 10^{-10} m^2 s^{-1} for low viscosity liquids. Presuming conventional reactors to encompass dimensions in the centimetre range, the fluid structure limits to 100 µm-1 mm and the corresponding diffusion time is estimated to be <1 ms in gases and 1 s in liquids. Whereas in microstructured reactors, the geometry is typically downsized to 100 µm-1 mm, generating 1 µm fluid structure. Such low fluid structure is highly beneficial in reducing the mixing time (100 µs for gases and 1 ms in liquids). The superior mass transport characteristics of microstructured reactors can promote the productivity considerably. In addition, the controlled residence time in the reactor plays a vital role in suppressing consecutive reactions that reduce the selectivity [200].

A similar relationship can be derived for the heat transfer time constant as the following:

$$t_{thermal} = \frac{r^2}{a} \tag{2.8}$$

Where a is the thermal diffusion and is defined as (λ = thermal conductivity, ρ = density and C_p = specific heat capacity):

$$a = \frac{\lambda}{\rho \times C_p} \tag{2.9}$$

The higher specific wall area in microstructured reactors enhances the heat transfer time constant considerably compared to conventional systems.

Fig. 2.7 shows the heat transport across a solid wall for a general case, where two fluids are separated with a solid wall. The thermal boundary layer with a thickness of δ_T represents the distance from the wall with T_{wall} to the point that the temperature is equal to bulk fluid temperature (T_{fluid}). The thickness of this layer increases in the direction of the flow. In conventional technologies, the reactor-heat exchangers are typically operated in a turbulent regime due to reduction of the δ_T thickness and superior heat transfer properties caused by flow turbulence. The improved heat transfer in turbulence flows is attributed to the intensive exchange of momentum and internal energy between neighboring fluid particles. This improved heat exchange aids in boosting the heat transfer characteristics

of a heat exchanger system. In microstructured technologies due to reduced geometry, the classic constant bulk temperature and thermal boundary layer is no more a limitation for heat transfer. Thus by overcoming the thermal boundary layer effect, the heat transfer is considerably improved and operation in laminar flow regimes becomes feasible [201].

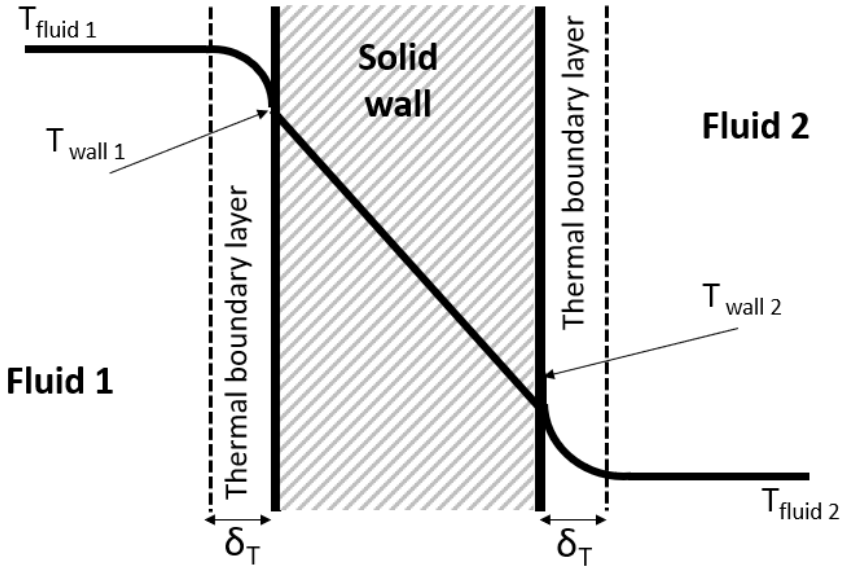

Figure 2.7: Heat transfer profile across a solid wall in a general problem and formation of the thermal boundary layer (adapted from [201]).

Another leverage in the application of microreactors is process safety. Small dimensions of these reactors allow operation of the reactor in aggressive temperatures and pressures, which are usually a limiting factor in conventional reactors due to safety issues. The good heat transfer properties of the reactor allow for the prevention of hotspot occurrence, which is usually accompanied by safety risks due to incidental development of side-reactions, in the case that side reactions have a higher activation energy than the main reaction. In emergency conditions, the well-controlled material and system can be swiftly treated owing to the small process scales [199].

The differing scale-up strategy in microstructured reactors compared to conventional reactors is another factor in favor of their implementation. In order to keep the promising high specific wall area of microstructured reactors, a numbering-up approach is pursued for their scale-up. The two leading scale-up strategies for the microstructured reactors include internal numbering-up and external numbering-up.

In the external numbering-up approach, the reactor unit which is verified in lab-scale

is kept consistent and a number of these units are operated parallel to each other (Fig. 2.8 left). The drawbacks of this scale-up concept are high maintenance and economic costs [199].

Internal numbering-up pursues to design a system with larger outer dimensions, but with reaction channels identical to those of the lab-system (see Fig. 2.8 right). In such a device, the flow is distributed in a mixing zone before entering the reaction chamber. Internal numbering-up is more economically interesting due to the reduced number of equipment. The main challenge in such designs is achieving a well-distributed flow in all reaction channels, which in reality sets certain limits on the number of the units stacked on top of each other [199].

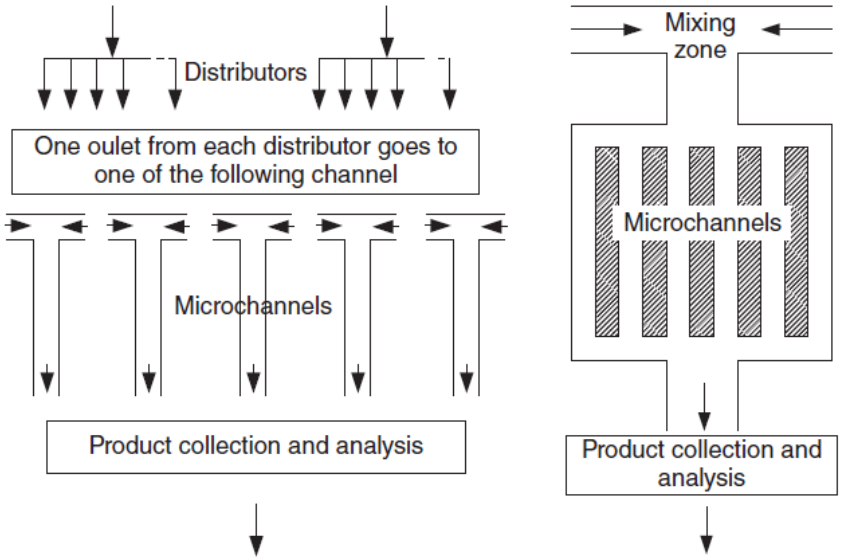

Figure 2.8: Schematic representation of Scale-up approach in microstructured reactors. Left: external numbering, right: external numbering-up (taken from [199]).

The numbering-up approach in microstructured devices benefits from the fact that no pilot plant reactor design and examination is necessary which saves much time and effort. Therefore, the time interval between demand and supply shrinks. Additionally, the size of the reactor can be adjusted according to the specific customer requests [198].

In summary, dictated by the fast and exothermic nature of methanation reaction and the specifications of decentralized PtG processes, microstructured technology is one of the most promising reactor concepts, which also has exceptional industrial potential.

3 Kinetic studies in a microstructured packed bed reactor

This chapter presents reaction kinetics of CO_2 methanation on a 17 wt. % Ni_3Fe/γ-Al_2O_3 catalyst under technical operation conditions of Power-to-Gas processes. A short-contact time microstructured packed bed reactor with internal cross-flow cooling was designed particularly for kinetic studies of the highly exothermic methanation reaction. The catalyst under study is a state-of-the-art methanation catalyst and was provided by the project partners within the Kopernikus P2X project. To the knowledge of the author and within the project time-line, no other kinetic study on a Ni-Fe catalyst system was known. The influence of temperature, pressure, reactant, and product composition as well as contact time on the product composition and conversion of the reactants was carefully studied. In total 166 data points were collected and fitted to three literature models applying a non-isothermal reactor model. Based on state-of-the-art kinetic models (for CO methanation and direct CO_2 methanation) and the experimental observations, a modified LHHW rate equation for the consecutive CO_2 methanation reaction was developed. This refined model has a lower number of parameters and improves the description of the reaction compared to literature models with regard to the Ni_3Fe catalyst system. Special attention was paid to the selectivity behavior and the influence of carbon monoxide and water on the reaction. A long-term stability test on the catalyst for a total duration of 300 h was carried out. The deactivation causes were analyzed via relevant catalyst characterization methods. Finally, the possibility of applying the developed kinetic model to a mono-metallic nickel catalyst was investigated by fitting the model to data from kinetic tests on a representative monometallic Ni catalyst.

3.1 Experimental methodology

3.1.1 The short-contact time microstructured reactor

The kinetic measurements were performed in a microstructured packed bed reactor with an internal cross-flow cooling structure illustrated in Fig. 3.1, designed and fabricated at the Institute for Micro Process Engineering (IMVT). The general reactor concept has already been successfully tested for other applications such as methanol, DME and Fischer-Tropsch synthesis [202–204]. Mutz et al. [119] used this general reactor design for CO_2 methanation catalyst performance tests, but compared to the present study with a much longer packed bed length. Based on the results achieved in the former studies, the reactor applied in this work was optimized for kinetic studies in the exothermic methanation reaction. The enhanced reactor possesses a shorter bed length (20 mm compared to 60 mm in the previous applications) and a different stacking scheme of the microstructured plates to be able to measure the temperature directly adjacent to the reaction zone. In the center of the reactor body, two structured metal plates stacked face to face form the reaction slit with dimensions of 20 mm (length) × 9 mm (width) × 1.5 mm (depth). On the backside of these plates, a slotted hole with a diameter of 1 mm is used for measuring the metal surface temperature 1.5 mm away from the catalyst on the left and right side of the bed at half-length using K-type thermocouples (marked as P1 and P2 in Fig. 3.1). The short bed length allows for operating at short-contact time conditions, without requiring extreme dilution of the catalyst or feed to reach the low or intermediate conversion. Also, the shorter bed length is beneficial regarding keeping the pressure drop low. The bed temperature or rather the metal surface temperature near the bed, in order to be precise, was used for setting the operational boundaries (to avoid the formation of hotspots).

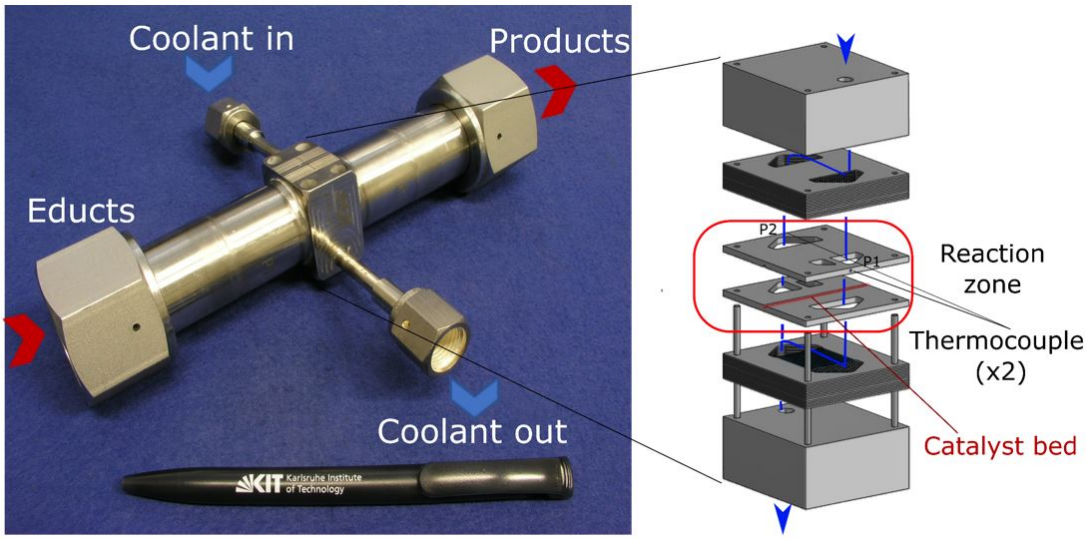

Figure 3.1: The microstructured packed bed reactor used for kinetic measurements

Above and under the reaction zone, 16 microstructured metal foils with a thickness of 400 µm are stacked on each other as the cooling structure. Each of these foils contains 19 semicircular channels of 250 µm depth, 500 µm width, and 25 mm length, which are arranged perpendicular to the flow direction of the reaction zone. The foil stack is sandwiched between two 16 mm thick metal plates, in which in total four holes are drilled for inserting heating cartridges to heat up the reactor to reaction temperature. The material used for the reactor is an austenitic high temperature-resistant alloy (Nicrofer® 3220) to guarantee reactor endurance under carburizing, oxidizing, and reducing conditions, as well as negligible blank activity [205].

3.1.2 Experimental setup for kinetic studies

The schematic drawing of the experimental setup used for kinetic measurements is displayed in Fig. 3.2. This test-rig is composed of three major parts:

I. Gas supply: In the gas supply part, five SLA 5800 series mass flow controllers (MFCs) from Brooks Instruments and one liquid flow controller (LFC) from Bronkhorst® were integrated. Water dosage was carried out by applying a nitrogen pressurized water tank followed by the LFC and an evaporation pipeline.

II. Reactor: The catalyst was fixed in the reaction bed from both sides by glass wool. All the tubing before the reactor was heated up to reaction temperature. The lines after the reactor were kept at 200 °C in order to avoid water condensation. Pressure

regulation was done using a pressure sensor and an automated Flow-serve® needle valve after the reactor. The pressure drop along the reactor was measured with a pressure difference sensor from DL-Systeme GmbH. Pressurized air was used as the cooling medium to keep the reaction temperature gradient-free in the catalytic bed. The flow rate of the air was adjusted at 40 l min^{-1}. The air was always pre-heated to the reaction temperature. For air pre-heating, a micro heat-exchanger built at IMVT with 15 heating cartridges, 225 W each, and electrically heated lines were installed.

III. Analytics: The reaction gases were analyzed by an online Gas chromatograph 7890B from Agilent Technologies. The gas chromatograph was equipped with two columns, HP-Plot/Q 19095P-Q04 and 5A-Mole sieve 19095P-MS6, and two detectors, a flame ionization detector (FID) and a thermal conductivity detector (TCD). The online data were used for quantification of CO_2, CO, H_2, H_2O, and N_2 (using TCD) and CH_4 (using FID).

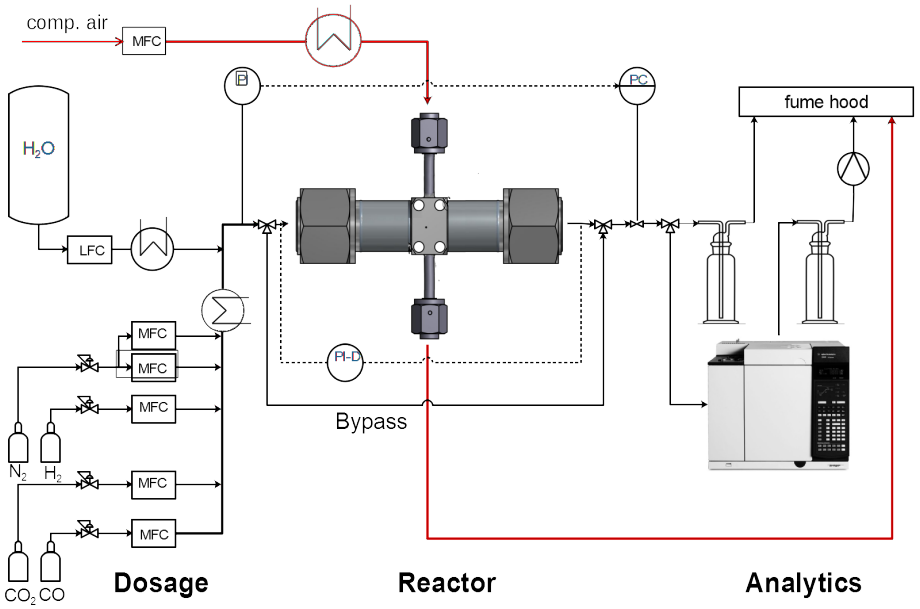

Figure 3.2: Schematic drawing of the methanation test-rig for kinetic studies

3.1.3 Experimental conditions and procedure

The kinetic data used for the modelling were collected in the first 50 hours of time on stream (TOS), where the activity was proven to be stable (see Sec. 3.3.5). The catalyst was replaced when an activity loss of around 3-5% was measured; for this, the reactor was opened and newly loaded. In total 5 reactor loadings were used for collecting the data and to reproduce data points. After each reactor loading, a reference point (T = 350 °C, H_2/CO_2 = 4, p_{abs} = 4 bar and τ_{mod,CO_2} = 0.38 mg min ml^{-1}) was measured which was used for calculation of the standard deviation. Consequently, for all data points, the uncertainty of the measured data was estimated using this standard deviation.
The kinetic measurements were carried out at nine different temperatures varied between 300 °C and 450 °C. The pressure ranged from 2 to 18 bar. The modified contact time, which is defined as the mass of the catalyst divided by the volumetric flow rate of CO_2 (at standard temperature and pressure), was varied between 0.09 and 0.72 mg min ml^{-1}. These parameters were varied under a constant stoichiometric ratio of H_2/CO_2 (= 4) and 50 % feed dilution with N_2. The known volumetric flow rate of inert N_2 in the feed was used as an internal standard for the calculation of the volume increase due to the reaction. The tested stoichiometric ratio of H_2/CO_2 was varied between 2 and 8. In this regard, two sets were examined: in the first set, p_{H_2} was kept constant at 1.6 bar and p_{CO_2} was changed. In the second set, p_{CO_2} was kept at 0.4 bar and with p_{H_2} variation, different H_2/CO_2 ratios were achieved. In this analysis, the modified contact time of CO_2 was kept constant at 0.38 mg min ml^{-1} for the sake of comparability. Finally, the influence of water and CO addition in the feed in relevant concentrations on the product formation/inhibition was investigated. A detailed overview of the experimental plan and parameters for kinetic studies is provided in Appendix A.1.
In all experiments, the catalytic bed was diluted with γ-Al_2O_3 (1/8 in. pellets, Alfa Aesar), crushed to the desired particle size fraction, in order to guarantee a homogeneous distribution of the catalyst in the bed and to avoid temperature deviations higher than +10 °C between the measured temperature inside the foil stack and the set-point. The mass ratio of catalyst to γ-Al_2O_3 was 2 to 1 when loading the bed with 76 mg catalyst, and 0.7 to 1 at reduced catalyst loading of 47 mg. The catalyst loading had to be reduced (diluted) in order to be able to measure short contact times and higher temperatures (over 400 °C) without forming a hotspot. Both catalyst and γ-Al_2O_3 were fractionated between 200 and 300 µm to avoid segregation of the particles while being filled in the reactor due to their different physical properties. The Ni_3Fe catalyst was provided by the Institute of Catalysis Research and Technology (IKFT-KIT) and prepared by Marc-Andre Serrer

in the framework of the Kopernikus P2X project. The synthesis of the catalyst and its detailed characteristics can be found elsewhere [119].
For reduction, the catalyst was heated to 500 °C with 5 K min^{-1} ramp under a gas flow of a 1:1 mixture of H_2 and N_2 with a total volumetric flow of 900 Nml $g_{cat}^{-1} min^{-1}$. The temperature was kept for two hours at 500 °C. The absolute pressure during the reduction was set to 2.5 bar. Between experiments, the reactor was kept at 300 °C in a reducing atmosphere under a flow identical to the reduction procedure to keep the catalyst in the reduced state. For each experimental point, the catalyst was operated over 120 minutes reaction run under a particular condition, and 5 gas chromatograph (GC) measurements were averaged to ensure reproducibility of the data. The reference point was measured every 15 hours of reaction run to check for possible catalyst deactivation. Every single data point used for the kinetic modelling was controlled for internal and external mass and heat transport limitation by calculating the Weisz modulus, Carberry number and Mears criterion [206]. The detailed description of these criteria are given in Appendix A.2. The requirements of Carberry and Weisz-Prater were fulfilled. The film and particle overheating criteria for some of the data points exceeded the criteria by a factor of 1.1-1.7, which was still considered acceptable for including them in the modelling of the reaction kinetics, given the approximative character of these criteria and the underlying simplifying assumptions.

3.1.4 Catalyst characterization methods

Electron microscopy investigations were performed on the fresh catalyst (before reduction), freshly reduced catalyst samples and on the catalyst sample after 300 hours TOS in order to investigate the cause of activity drop. The measurements were carried out at KIT, Institute of Nanotechnology (INT) by Ms. Charlotte Neidiger and Dr. Di Wang. The powder samples were directly dispersed on copper grids covered with a Lacey carbon film (TEM film support). The morphology and structure of the catalysts were characterized by high-resolution transmission electron microscopy (HRTEM) and high angle annular dark-field (HAADF) STEM in a FEI Titan 80-300 microscope (aberration corrected) operating at 300 kV. Some STEM (scanning transmission electron microscopy) and EDX (energy dispersive X-ray spectroscopy) images of the fresh and used samples were taken on a Tecnai microscope (FEI Tecnai F20 at 200 kV). The composition of the samples was evaluated via EDX with an EDAX S-UTW EDX detector. Quantification of the EDX spectra and STEM-EDX spectrum imaging were accomplished by applying TEM Image and Analysis Version 4.15 software. Evaluation of the HRTEM, selected

area electron diffraction (SAED), and energy-filtered transmission electron microscopy (EFTEM) images were carried out with the Digital Micrograph Version 3.22.1461.0 software. The size of the supported metal nanoparticles was estimated using the ImageJ software fitting the particles with ellipsoid shapes.

3.2 Mathematical methods

3.2.1 Product analysis

For calculation of the reactants' degree of conversion, selectivity and yield of the products, the mole flow of each participating species before and after the reaction must be measured. The bypass measurements served for recording the actual feed flow composition. Estimation of the species mole flows in the product was possible by means of dosing N_2, which remains inert throughout the reaction and therefore served as an internal standard:

$$\dot{n}_i = \dot{n}_{N_2} \frac{y_i}{y_{N_2}} \tag{3.1}$$

Or, assuming ideal gas behavior and identical temperature and pressure on the feed and product side:

$$\dot{V}_{i,STP} = \dot{V}_{N_2,STP} \frac{y_i}{y_{N_2}} \tag{3.2}$$

The flow rates of the species in this chapter were all recorded in $\mathrm{ml\,min^{-1}}$ at standard temperature and pressure (STP). Therefore, the CO_2 conversion (X_{CO_2}), CH_4 selectivity (S_{CH_4}), and CO yield (Y_{CO}) can be calculated as follows:

$$X_{CO_2} = (1 - \frac{\dot{V}_{CO_2,out,STP}}{\dot{V}_{CO_2,in,STP}}) \cdot 100\% \tag{3.3}$$

$$S_{CH_4} = \frac{\dot{V}_{CH_4,out,STP} - \dot{V}_{CH_4,in,STP}}{\dot{V}_{CO_2,in,STP} - \dot{V}_{CO_2,out,STP}} \cdot 100\% \tag{3.4}$$

$$Y_{CO} = X_{CO_2} \cdot (100\% - S_{CH_4}) \tag{3.5}$$

Finally, for examination of the consistency of the measured species concentrations, the elemental balance for the three elements of carbon, hydrogen and oxygen was checked. For instance, the percentage error of the elemental balance for carbon reads:

$$\Delta C = \frac{[\dot{V}_{CO_2,in,STP} + \dot{V}_{CO,in,STP} + \dot{V}_{CH_4,in,STP}] - [\dot{V}_{CO_2,out,STP} + \dot{V}_{CO,out,STP} + \dot{V}_{CH_4,out,STP}]}{\dot{V}_{CO_2,in,STP} + \dot{V}_{CO,in,STP} + \dot{V}_{CH_4,in,STP}} \cdot 100\% \tag{3.6}$$

This error typically was within a tolerance range of ±5% based on the dosed flow rates (via MFCs) and the measured compositions via GC. In case this limit was surpassed, the GC calibration/MFC calibration and/or the measurement was repeated.

3.2.2 The reaction rate model

The rate equations developed and tested in this work are formulated based on the Langmuir-Hinshelwood-Hougen-Watson (LHHW) approach. The general form of a LHHW rate equation is:

$$r_{LHHW} = \underbrace{k \cdot \Pi_j p_j^{\nu_i}}_{\textit{kinetic term}} \underbrace{\frac{1}{\left(1 + \sum_i K_i p_i^{\nu_i}\right)^2}}_{\textit{adsorption term}} \cdot \underbrace{\left(1 - \frac{p_{abs}^{\Delta\nu}}{K_{eq}} \Pi_k p_k^{\nu_k}\right)}_{\textit{equilbrium term}} \tag{3.7}$$

The general approach for deriving a LHHW rate equation is applying the assumption of a rate-determining step to a given reaction mechanism and deducing the rate formula based on elementary steps [207].
In the present work, several prerequisites were desired for the final kinetic model:

1. The formation of methane from CO_2 occurs through two consecutive reactions with the formation of CO as an intermediate product: the first reaction is the so-called rWGS reaction followed by CO methanation. Therefore, the model should be capable of describing the CO yield and the selectivity to methane formation.
2. The thermodynamic equilibrium of all reactions should be considered in the model.
3. The total effective order of the reaction for both reactions must be greater than zero.
4. The potential inhibition of the reaction rate by H_2, CO, CH_4 and H_2O should be verified by means of the modelling and/or experiments.

3.2.3 Reactor model: non-isothermal PFR

The catalytic reactor was modelled as a non-isothermal, pseudo-homogeneous plug flow reactor (PFR, the Bodenstein number was estimated to be around 60). The mathematical description was based on a 1D steady-state material balance, neglecting axial dispersion.

Since the pressure drop measured along the reactor was always below 10% of the absolute pressure, no momentum balance was solved. The material balance reads:

$$\frac{d(uC_i)}{dz} = \rho_{bed} R_{m,i} = \rho_{bed} \sum_{j=1}^{N_{reaction}} \nu_{i,j} \cdot r_{m,j} \tag{3.8}$$

Beside the material balance, an energy balance was solved for the reactor, since all the kinetic constants are temperature-dependent and the assumption of an isothermal bed can induce substantial error in data evaluation. In this regard, all temperatures i.e., gas temperature in the inlet of the reactor, cooling air and the reactor body temperature were adjusted by electrical heating to the actual setpoint. The catalyst bed temperature was measured with the internal thermocouples (see Fig. 3.1). The solved energy balance (Eq. 3.9) includes the convective heat transport in axial direction, the released reaction heat, and the heat transfer from the catalyst bed of the reaction zone towards the coolant air.

$$\frac{dT}{dz} = \frac{1}{\sum_i \dot{n}_i C_{p,n,i}} \left(-\frac{m_{cat}}{L_{bed}} \sum_{j=1}^{N_{reaction}} r_{m,j} \Delta_R H_j - k_{eff} U (T - \overline{T_c}) \right) \tag{3.9}$$

The parameters ρ_{bed}, m_{cat}, L_{bed} represent the packed bed density, mass of the catalyst and the bed length, respectively. The heat transfer coefficient k_{eff} includes all individual resistances between the reaction zone and the cooling channel. The value of the coefficient was taken from [208] (500 W m^{-2} K^{-1}), where the same reactor concept had been applied and checked based on experimental data. The parameter U is the perimeter of the catalytic bed which exchanges heat with the coolant medium.

The temperature in the catalyst bed (T) is considered gradient-free in radial direction, and $\overline{T_c}$ is an estimated average coolant temperature (i.e., the numerical mean value of the coolant temperature between its inlet and outlet). It is derived by adding half of the temperature increase of the air along the reactor (ΔT_c) to the coolant temperature at the inlet $T_{c,in}$:

$$\overline{T_c} = T_{c,in} + \frac{1}{2} \Delta T_c \tag{3.10}$$

The temperature increase of the air can be calculated by Eq. 3.11, when assuming zero heat loss to the surroundings:

$$\Delta T_c = \frac{\dot{q}_{air}}{\dot{m}_{air} C_{p,m,air} / L_{bed}} \tag{3.11}$$

$$\dot{q}_{air} = k_{eff} U (T - \overline{T_c}) \tag{3.12}$$

Inserting Eq. 3.10 and 3.11 in Eq. 3.12, an equation based on the known parameters $T_{c,in}$ and $\dot{m}_{air}$ is derived:

$$T - \overline{T_c} = \frac{T - T_{c,in}}{1 + \frac{k_{eff} U L_{bed}}{2\dot{m}_{air} C_{p,m,air}}} \tag{3.13}$$

By substituting Eq. 3.13 into Eq. 3.9, we get:

$$\frac{dT}{dz} = \frac{1}{\sum_i \dot{n}_i C_{p,n,i}} \left(-\frac{m_{cat}}{L_{bed}} \cdot \sum_{j=1}^{N_{reaction}} r_{m,j} \Delta_R H_j - k_{eff} U \left(\frac{T - T_{c,in}}{1 + \frac{k_{eff} U L_{bed}}{2\dot{m}_{air} C_{p,m,air}}} \right) \right) \tag{3.14}$$

The boundary conditions are defined as:

$$T(z = 0) = T_{in} \qquad and \qquad \dot{n}_i(z = 0) = \dot{n}_{i,in} \tag{3.15}$$

The numerical solution of the material and energy balances was carried out in Matlab® applying `ode15s` as the solver.

The simulated temperature profile in the reactor for temperature setpoints of 300 to 450 °C at p_{abs} = 4 bar and τ_{mod,CO_2} = 0.38 mg min ml^{-1} is provided in Fig. 3.3, while the corresponding experimental values are provided in Tab. 3.1. Position 1 (marked as P1 in Fig. 3.1) refers to the thermocouple which measures the temperature at half of the bed length near the catalytic bed on the inlet side of the cooling air, while position 2 is measured at the same bed length (axial position) but on the outlet side of the cooling air (marked as P2 in Fig. 3.1). Due to the design of the cooling channels, an axial temperature profile measurement in the reactor was not technically feasible. For better comparison, modelled temperature values at the center of the reactor are provided in Tab. 3.1. The experimental temperature at P1 was always very close to the inlet temperature of the feed/coolant air. The temperature values at P2 however indicate a slight increase due to exothermic reaction. The modelled temperature values at half of the reactor length are somewhat higher (about 2 to 3 °C) than the experimentally measured data. However, note that the measured values could be obscured by the air flow temperature which is close to the thermocouple measuring position and that they do not reflect the precise catalyst temperature. Thus assigning a higher temperature inside the catalyst bed is a reasonable assumption. In summary, comparison of the measured temperatures to the modelled temperature profiles confirms that the model assumptions are suitable and capable of reproducing the experimental trends.

Table 3.1: Experimental versus modelled temperatures at half of the bed length at temperature set-points of 300 to 450 °C, p_{abs} = 4 bar and τ_{mod,CO_2} = 0.38 mg min ml^{-1}.

T_{in} [°C]	Exp. T at P1 [°C]	Exp. T at P2 [°C]	Modelled T at bed center [°C]
300	300	301	302
320	320	322	324
335	335	341	346
350	350	356	358
385	385	392	396
400	401	408	412
450	452	458	462

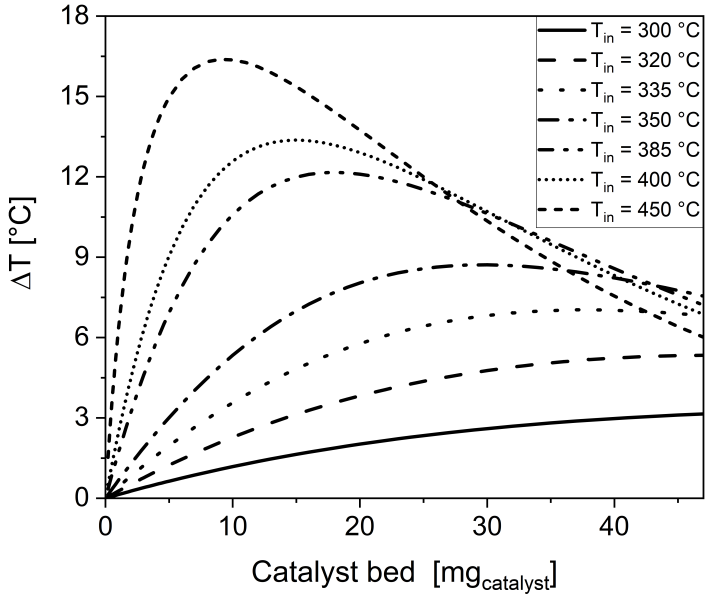

Figure 3.3: Modelled temperature profile along the catalyst bed for different temperature set-points of 300 to 450 °C, p_{abs} = 4 bar and τ_{mod,CO_2} = 0.38 mg min ml^{-1}.

3.2.4 Parameter estimation

The parameters of the different tested models were estimated by solving a minimization problem. For that, the sum of least square residuals (*RSS*) of the yield of all carbon-containing species (CO_2, CO and CH_4) can be defined as:

$$RSS = \sum_i (Y_{i,sim} - Y_{i,exp})^2 \tag{3.16}$$

For a more accurate representation, the deviation ($Y_{i,sim} - Y_{i,exp}$) can be scaled with an estimation of the experimental error $\Delta Y_{i,exp}$ to take into account the true information content of each component measurement in relation to the measurements of the other components. Through summing the weighted deviations for all individual data points over the rest, a normalized sum or least squares is obtained. Applying this method, the sum of least square residuals reads:

$$RSS = \sum_i \left[\frac{(Y_{i,sim} - Y_{i,exp})}{\Delta Y_{i,exp}} \right]^2 \tag{3.17}$$

Where $\Delta Y_{i,exp}$ is an estimate of the experimental error. The experimental error can be estimated by calculating the standard deviation for a reference point. In the present study, the first method corresponding to Eq. 3.16 was used for *RSS* estimation for different kinetic models to be compared to the performance of the Ni_3Fe catalyst. The significance of using the second method will be discussed in Sec. 3.3.2. This method was tested for parameter estimation for the mono-metallic Ni catalyst, presented in Sec. 3.3.7.
Nonlinear regression was used for the determination of the kinetic parameters, applying an iterative procedure [209]. Minimization was done applying the `lsqnonlin` function and using Levenberg-Marquardt algorithm in Matlab®. For each experimental data point, the corresponding material and energy balances (Eq. 3.8 and 3.14) were solved to determine the *RSS* value. For solving the differential equations during the parameter estimation procedure, the `ode15s` solver was implemented. The choice of this solver instead of the commonly applied solver `ode45` was due to the stiffness of the problem for some parameter considerations, the robustness of this solver against numerical instabilities, and for saving computation time, i.e., faster convergence. `ode15s` is a variable-order and variable-step solver based on the numerical differentiation formulas (NDFs) (occasionally the backward differentiation formulas (BDFs)). The major advantage of this solver compared to `ode45` is that it requires a much fewer number of steps in stiff regions in order to meet the required accuracy for integration. A comparative study

on the choice of ODE solver for various problems is provided in [210, 211]. Through the iterative procedure of the `lsqnonlin` routine, optimal kinetic parameter estimates were obtained, and the *RSS* value was calculated.

Discrimination among several competing models with a different number of parameters was accomplished applying the Bayesian information criterion (*BIC*) proposed by Schwarz [212]. For *BIC* identification, the maximum likelihood function, the number of independently adjusted parameters within the model (n_P) and the number of data-points (n_{DP}) are required. In a simplified form of this criterion and under the assumption that the model errors and disturbances are independent and equally distributed, the sum of squares of the residuals (*RSS*) is equivalent to the maximum likelihood function [213]. When comparing two models, the one having a lower value of the (*BIC*) is preferred. A lower (*BIC*) value signifies either fewer variables, better fit, or both.

$$BIC = n_{DP} \ln(\frac{RSS}{n_{DP}}) + n_P \ln(n_{DP}) \tag{3.18}$$

For the evaluation of the fit between the model and experimental data, the adjusted coefficient of determination R^2_{adj} was compared. This parameter is a modified linear coefficient of determination R^2 that also takes the number of parameters in a complex model into account. It allows judging the necessity of applying more parameters for improving the description of the experimental data. The maximum value for R^2_{adj} is one, which corresponds to a perfect consistency between the data points and the model. In contrast to R^2, the value of R^2_{adj} can also be negative which indicates the model has too many parameters [214]. In this work, for each carbon-containing species, CO, CO_2 and CH_4 an individual R^2_{adj} was calculated to assess the accuracy of different kinetic models with regard to predicting CO_2 conversion as well as selectivity towards the formation of CH_4 and CO.

To evaluate the accuracy and reliability of the model parameters, the 95% confidence intervals of the parameter estimates were determined, i.e., the interval within which the true parameter value should be found with 95% certainty or confidence level.

Finally, to evaluate the interdependency of pairs of variables, the correlation matrix was determined. A value of zero implicates that there is absolutely no correlation between two chosen parameters. +1 or −1 indicate perfect linear correlation. Although in an ideal model all parameter estimates are uncorrelated, in reality often correlations are observed in particular in highly non-linear models. In this situation, a model showing a correlation matrix with moderate values well below 0.9 is accurate. Models for which some parameter estimates are correlated with +1 or −1 must be over thought. This either indicates that

one parameter can be expressed as a linear function of another and therefore could be removed from the model. Alternatively the correlation is due to non-linearity and may be reduced by a suitable re-parametrisation. In an adequate model, each parameter has its own well-defined function without influencing the others.

3.3 Results and discussion

3.3.1 Development of the kinetic model

As explained in Sec. 3.2.2, all rate equations tested in this work are based on a LHHW model. The general form of the tested equation for the two reactions of interest, i.e., rWGS and CO methanation is as follows:

$$r_{rWGS} = \frac{k_1 p_{CO_2}^{\alpha} p_{H_2}^{\beta}}{(inhibition\ term)^2} \cdot (1 - \frac{p_{CO} p_{H_2O}}{p_{CO_2} p_{H_2} K_{rWGS}}) \tag{3.19}$$

$$r_{CO-methanation} = \frac{k_2 p_{CO}^{\gamma} p_{H_2}^{\varphi}}{(inhibition\ term)^2} \cdot (1 - \frac{p_{CH_4} p_{H_2O} p_{abs.}^2}{p_{CO} p_{H_2}^3 K_{CO-meth.}}) \tag{3.20}$$

The reaction rate models are derived from postulations on the reaction mechanism, therefore values of zero, 0.5 and 1 are proposed for the reaction orders (here: α, β, γ and φ). A value of 1 stands for direct adsorption whereas a value of 0.5 indicates dissociative adsorption on the surface. CO can also adsorb in bridged mode on the surface of a Ni catalyst (reaction order equal to 0.5). However according to literature, this adsorption mode is a much more stable conformation and is therefore associated with a poisoning influence on the Ni surface if the hydrogen ion is not effective [124, 143]. It is therefore not considered here. Zero is also a possible value which would mean that this species has no influence on the reaction rate. Based on the experimental observation (see Sec. 3.3.4.3) an exponent of zero for hydrogen was considered infeasible and therefore not included in the parameter estimation. In this work, 36 combinations of the reactant exponents as shown in Eq. 3.21 were tested.

$$\begin{pmatrix} \alpha = \\ 0; \frac{1}{2}; 1 \end{pmatrix} \times \left(\beta = \ \frac{1}{2}; 1 \right) \times \begin{pmatrix} \gamma = \\ 0; \frac{1}{2}; 1 \end{pmatrix} \times \begin{pmatrix} \varphi = \\ \frac{1}{2}; 1 \end{pmatrix} \tag{3.21}$$

The method of least squares described in Sec. 3.2.4, proved that $\alpha = 0.5$, $\beta = 0.5$, $\gamma = 1$ and $\varphi = 0.5$ yielded the most suiting reaction orders.

The inhibition term of the model was assessed both experimentally (see Sec. 3.3.4.6 and 3.3.4.5) and with modelling. The reaction hindrance by CO and/or H_2 was considered a plausible scenario considering the high affinity of Ni catalysts to CO. H_2 could be adsorbed on the catalyst surface in molecular and dissociative way. 6 combinations of H_2 and CO exponents in the inhibition term as shown in Tab. 3.2 were tested:

Table 3.2: CO and H_2 tested terms combinations in inhibition term of Eq. 3.19 and 3.20.

Inhibition by H_2 / Inhibition by CO	0	$K_{H_2} p_{H_2}^{0.5}$	$K_{H_2} p_{H_2}$
0	0 ; 0	0 ; $K_{H_2} p_{H_2}^{0.5}$	0 ; $K_{H_2} p_{H_2}$
$K_{CO} p_{CO}$	$K_{CO} p_{CO}$; 0	$K_{CO} p_{CO}$; $K_{H_2} p_{H_2}^{0.5}$	$K_{CO} p_{CO}$; $K_{H_2} p_{H_2}$

The modelling results indicated that inhibition by CO and/or H_2 does not help to reduce the *RSS* value. For most of the combinations, the adsorption constant was close to zero, and therefore CO and H_2 were confirmed to have no inhibiting effect. Hindrance by CO_2 was found only relevant for the rWGS reaction. Since the *RSS* value was observed to increase with a factor of 10 when applying CO_2 in the inhibition term, the hindrance was rejected. The experimental tests on CO, H_2 and CO_2 influence on CO_2 methanation and rWGS reactions are presented in Sec. 3.3.4.6 and are in accordance with the modelling results.

The inhibition of the reaction by the products was assessed by testing two terms for CH_4: no adsorption and simple adsorption, and four terms for water: 1. no adsorption, 2. direct adsorption, 3. adsorption as a hydroxyl group, and 4. adsorption as oxygen on the catalyst surface. Hence, in total 8 cases as in Tab. 3.3 were analyzed:

Table 3.3: CH_4 and H_2O tested terms combinations in Eq. 3.19 and 3.20.

inhibition by H_2O / inhibition by CH_4	0	$K_{H_2O} p_{H_2O}$	$K_{OH} \frac{p_{H_2O}}{p_{H_2}^{0.5}}$	$K_O \frac{p_{H_2O}}{p_{H_2}}$
0	0;0	0; $K_{H_2O} p_{H_2O}$	0; $K_{OH} \frac{p_{H_2O}}{p_{H_2}^{0.5}}$	0; $K_O \frac{p_{H_2O}}{p_{H_2}}$
$K_{CH_4} p_{CH_4}$	$K_{CH_4} p_{CH_4}$; 0	$K_{CH_4} p_{CH_4}$; $K_{H_2O} p_{H_2O}$	$K_{CH_4} p_{CH_4}$; $K_{OH} \frac{p_{H_2O}}{p_{H_2}^{0.5}}$	$K_{CH_4} p_{CH_4}$; $K_O \frac{p_{H_2O}}{p_{H_2}}$

Without an inhibition term (resulting in a simple power law) the model was unable to reproduce conversions over 60%, as already found by Koschany et al. [61]. When only CH_4 was considered in the inhibition term, the higher conversion regime could be modelled, but not the effect of water addition in the feed (see Sec. 3.3.4.5). Combinations of CH_4 and water inhibition delivered only values close to zero for the methane adsorption constant K_{CH_4}. Therefore, water was conceived as the only factor inhibiting the reaction progress. In contrast to literature models, in which inhibition by water has been mainly modelled as oxygen or hydroxyl groups on the catalyst surface [61, 149], in this study a simple water adsorption resulted in the best fit. The final model identified as the most suitable one for the description of the experimental data is provided in Eq. 3.22 and 3.23.

$$r_{rWGS} = \frac{k_1 p_{CO_2}^{0.5} p_{H_2}^{0.5}}{DEN^2} \cdot (1 - \frac{p_{CO} p_{H_2O}}{p_{CO_2} p_{H_2} K_{rWGS}}) \tag{3.22}$$

$$r_{CO-methanation} = \frac{k_2 p_{CO} p_{H_2}^{0.5}}{DEN^2} \cdot (1 - \frac{p_{CH_4} p_{H_2O} p_{abs}^2}{p_{CO} p_{H_2}^3 K_{CO-meth.}}) \tag{3.23}$$

The inhibition term is defined as:

$$DEN = 1 + K_{H_2O} p_{H_2O} \tag{3.24}$$

For the reaction rate and adsorption constants, the classical Arrhenius and Van't Hoff approaches were used, respectively:

$$k_i = k_{i,555\ K} \exp\left(\frac{E_{A,i}}{R}\left(\frac{1}{555K} - \frac{1}{T}\right)\right) \tag{3.25}$$

$$K_{H_2O} = K_{H_2O,555\ K} \exp\left(\frac{\Delta H_{H_2O}}{R}\left(\frac{1}{555K} - \frac{1}{T}\right)\right) \tag{3.26}$$

The reference temperature was left at 555 K for better comparability with literature models [61].

The equilibrium constant of the rWGS reaction was calculated from a correlation used in literature (Eq. 3.27) [215]. The CO methanation equilibrium constant was fitted using a polynomial function, applying the data from thermodynamic analysis (see Cha. 2, Sec. 2.1). The goodness of these fits was validated by direct comparison to the thermodynamic data as well as other literature correlations, such as the relationship provided by Swikrath

et al. [216]. The correlations used for the equilibrium constants of the rWGS reaction and CO methanation are as follows:

$$K_{rWGS} = \frac{1}{10^{-2.4198+3.855\cdot10^{-4}T+\frac{2180.9}{T}}} \tag{3.27}$$

$$K_{CO-meth.} = 10^{4.1002\cdot10^{-5}T^2-0.08025T+39.6039} \tag{3.28}$$

The estimated parameters and their 95% confidence intervals are given in Tab. 3.4. The confidence intervals for all parameters are relatively small, except for the water adsorption enthalpy. The activation energy of the CO methanation reaction in this work is calculated to be 60.98 ± 4.54 kJ mol^{-1}. Kopyscinski estimated a value of 74.1 kJ mol^{-1}. Also, other works reported similar values: Gardner und Bartholomew 72-78 kJ mol^{-1} [48], McCarty und Wise 71 kJ mol^{-1} [156] and Hayes et al. 78 kJ mol^{-1} [217]. A possible reason for the lower activation energy derived in this work could be a change of the active site between Ni in literature studies and the Ni_3Fe catalyst in our study. The estimation of the activation energy of the rWGS reaction for our model is 166.55 ± 8.48 kJ mol^{-1}. In literature, a wide spectrum of estimates of the activation energy of the WGS reaction (opposite reaction pathway) on diverse catalysts are reported [218, 219]. For Ni/Al_2O_3 catalysts, literature values are around 85 kJ mol^{-1}, while for Fe-Oxide catalyst about 150-160 kJ mol^{-1} are cited. The fitted models of Zhang and Kopyscinski provided 108 kJ mol^{-1} and 202 kJ mol^{-1} respectively. Therefore, the estimated activation energy for the rWGS in this model for the Ni_3Fe catalyst appears to be in a meaningful range.

Table 3.4: Parameter estimates for the rWGS (1) and CO methanation (2) reaction rate models and their corresponding 95% confidence intervals for the Ni_3Fe catalyst

Parameter	Value	Confidence interval	Unit
$k_{1,555\,k}$	0.144	± 0.030	mol(kg s bar)$^{-1}$
$E_{A,1}$	166.55	± 8.48	kJ mol^{-1}
$k_{2,555\,k}$	11.541	±0.785	mol(kg s bar$^{1.5}$)$^{-1}$
$E_{A,2}$	60.98	± 4.54	kJ mol^{-1}
$K_{H_2O,555\,k}$	0.678	± 0.038	bar^{-1}
ΔH_{H_2O}	11.44	± 4.96	kJ mol^{-1}

Tab. 3.5 shows the correlation matrix of the parameter estimates. As described in Sec.3.2.4, values closer to zero are indicative of low interdependency between a pair of estimates. Half of the values are in the range of 0 to 0.5. A quarter of the values are between 0.5 and 0.65 and the rest are between 0.65 and 0.75. Since all the correlation coefficients are well below 0.9, the estimates overall display low correlation. It is concluded that although there are some moderate dependencies, all estimated parameters are well-defined and have their explicit function in the model.

Table 3.5: Correlation matrix of the parameters in the suggested model

	$k_{1,555\,k}$	$k_{2,555\,k}$	$K_{H_2O,555\,k}$	$E_{A,1}$	$E_{A,2}$	ΔH_{H_2O}
$k_{1,555\,k}$	1	-	-	-	-	-
$k_{2,555\,k}$	-0.554	1	-	-	-	-
$K_{H_2O,555\,k}$	0.474	-0.745	1	-	-	-
$E_{A,1}$	0.127	-0.082	-0.403	1	-	-
$E_{A,2}$	-0.540	0.660	-0.412	-0.530	1	-
ΔH_{H_2O}	-0.003	0.222	0.054	-0.686	0.669	1

3.3.2 Evaluation of the developed rate model

The consistency between the experimental data and the new model can be analyzed with parity plots (see Fig. 3.4). The parity plots for the three literature models of interest are presented in Appendix A.4. The calculated volumetric flow rates at the reactor exit applying the kinetic rate model are compared to the experimentally measured values for all 166 experimental data points. The majority of the data are in the range of ±25% deviation from the model. Careful evaluation of the data shows that the inconsistent points are mainly in the range of smaller flow rates (< 100 $ml\,min^{-1}$). The data points corresponding to the CO concentration have the highest scattering of all. However, there is no systematic error recognizable in the CO parity plot, and the scattering seems to be of statistical nature. The CO concentrations in the product gas were always much smaller compared to CO_2 and CH_4, (0.1-1% for CO compared to 10-20% for CO_2 and CH_4 and/or 1-15 $ml\,min^{-1}$ for CO vs. 20-500 $ml\,min^{-1}$ for CO_2 and CH_4) which results in a larger relative deviation and thus larger scattering. The standard and relative deviation estimated using the reference measurement point for CO_2 conversion was equal to ± 2.74 and 4.7% respectively. For CH_4 selectivity, an absolute error of ± 0.65 and a relative

error value of 0.7% was approximated. For the case of CO, the absolute error was ± 0.35, which yielded a relative error of 15.3%. These values are provided in Tab. 3.6. Apart from the low flow rate range, the detection limit of the GC for measurement of CO was about 500 ppm, which is the main reason for the high relative error for CO data points.

Table 3.6: Standard and relative deviation values for the reference measurement point (T = 350 °C, H_2/CO_2 = 4, p_{abs} = 4 bar and τ_{mod,CO_2} = 0.38 mg min ml^{-1})

Compound	Standard deviation	Relative deviation
CO_2 conversion	± 2.74	4.7%
CH_4 selectivity	± 0.65	0.7%
CO yield	± 0.35	15.3%

In order to account for such error sources for less accurate data (e.g. CO concentrations), the application of weighting factors during parameter estimation as described in Sec. 3.2.4 is recommended. This method should lead to a uniform scattering among all components.

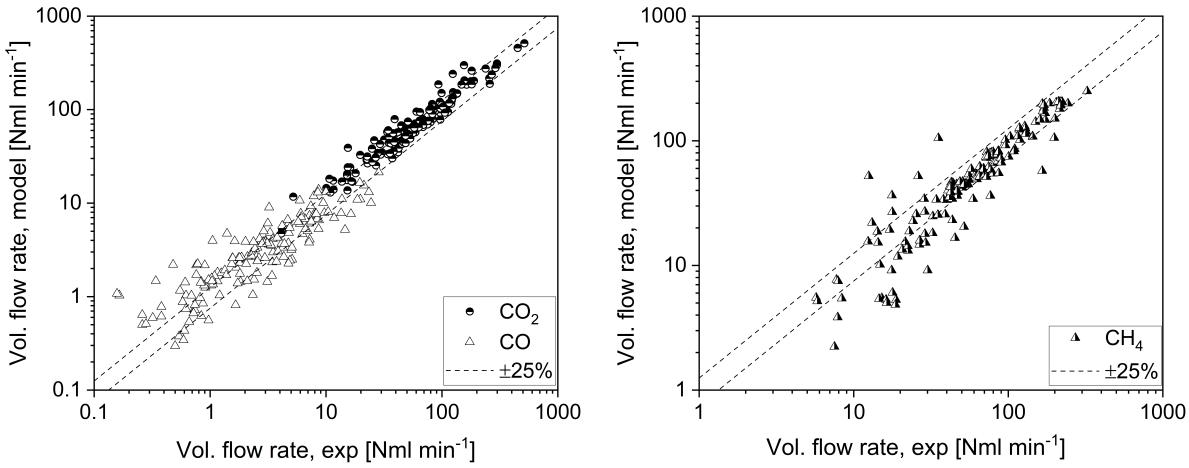

Figure 3.4: Parity plots for comparison of the experimental data to the recommended LHHW rate model for CO and CO_2 volumetric flows (left), and CH_4 volumetric flow (right).

In order to analyze the model fit over the entire tested temperature window, the course of CO_2 conversion and CH_4 selectivity were studied in detail. Fig. 3.5 shows the CO_2

conversion (left) and CH_4 selectivity (right) as a function of temperature at 4 bar for three modified CO_2 contact times of 0.72, 0.38 and 0.16 mg min ml^{-1} in comparison to the predicted values from the developed kinetic model. Fig. 3.5 left shows that CO_2 conversion increases with raising the temperature up to 380 °C, according to the Arrhenius law. After around 380 °C, the conversion approaches a plateau, which could be explained in various ways: 1. Inhibition by the reaction products, 2. reaching the equilibrium, and 3. transport limitations. The first two are covered by this work, and hence the model can simulate this behavior. The possibility of transport limitations has been theoretically ruled out, as mentioned in Sec. 3.1.3. It is of importance to note that these criteria do not guarantee that these limitations are absent, especially at higher temperatures where the kinetics are very fast [220]. Methane selectivity experimental data displayed in Fig. 3.5 right, show also a positive trend by temperature increase up to 380 °C for CO_2 residence times of 0.38 and 0.72 mg min ml^{-1}. This positive trend stops at around 380 °C and reaches a constant level. For the residence time of 0.16 mg min ml^{-1}, the methane selectivity drops at a temperature above 385 °C, which is presumably due to the fact that the catalyst started to show deactivation signs (see Sec. 3.1.3 and 3.3.5).

The recommended kinetic model shows a good agreement to the experiment for all three residence times up to a temperature of 400 °C. Above this temperature level, it is expected for the model to approach the equilibrium curve. However, above 400 °C, the model has a degrading trend with a steeper slope compared to the one for the thermodynamic equilibrium. The same trend and a weak drop in methane selectivity at high temperatures is detectable for the case of modelled CH_4 selectivity as well. The thermodynamic curve in Fig. 3.5 is plotted using the Gibbs energy minimization used in Cha. 2. At very long contact times, CO_2 conversion and CH_4 selectivity deliver identical values via the kinetic model compared to that of the Gibbs minimization method. Hence, the inaccuracy of the equilibrium constant correlations in simulating the approach to equilibrium can be excluded. Sec. 3.3.4.5 verifies that the inhibition term has a similar trend for the entire temperature range of 300 to 450 °C. However, the experimental data for water inhibition effect on the reaction rate were gathered solely at 350 °C. Overestimation of the rate inhibition at higher temperatures could refer to some changes in the inhibiting effect of water or other reaction components such as CO at T > 420 °C. The addition of more terms in the inhibition term, could assist in reducing the impact of water inhibition and care for these additional effects when increasing the reaction temperature. This assumption is further discussed in Sec. 3.3.3 when comparing the developed model to literature models. Another reason between inconsistency between the model and experimental data (at high

temperatures and modified contact times of 0.38 and 0.16 mg min ml^{-1}) can be related to the early catalyst deactivation signs.

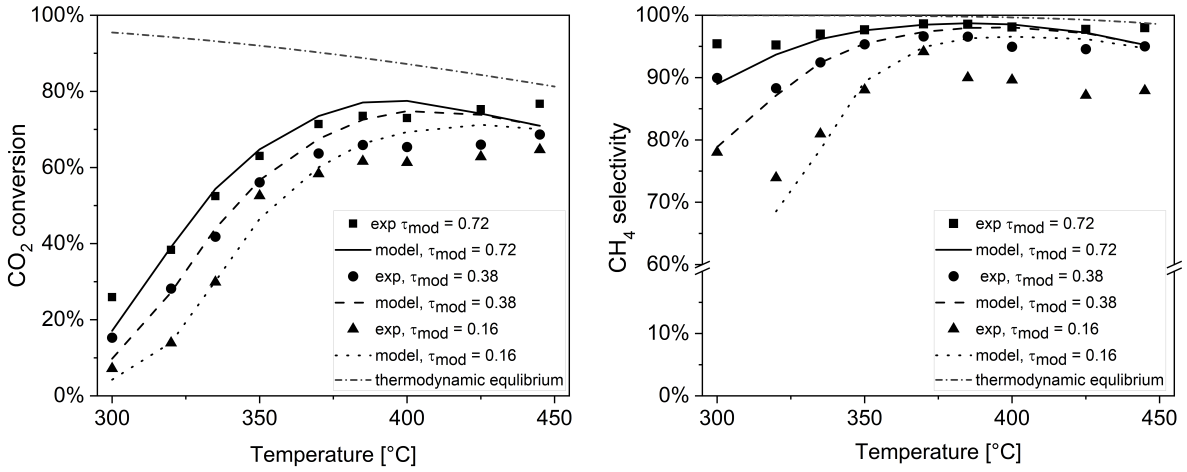

Figure 3.5: Comparison of CO_2 conversion (left) and CH_4 selectivity (right) for experimental data versus model prediction (p_{abs} = 4 bar) for temperature range of 300 to 450 °C.

3.3.3 Comparison to literature models

Some features of the kinetic model of this work against the literature models can be best compared when having a closer look at CO_2 conversion and CH_4 selectivity versus temperature, as plotted in Fig. 3.6. The experimental data points are marked with their corresponding standard deviation bar that is calculated as clarified in Sec. 3.1.3 and provided in Sec. 3.3.2. The predictions made by the literature models are presented with newly fitted parameters using the experimental data of this work since otherwise, they failed to describe the trends observed for the Ni_3Fe catalyst used in this work. In previous studies carried out by Mutz et el., similar observations were made [119]. The parameters were estimated applying the same method as described in Sec. 3.2 and are provided in Appendix A.4.

Fig. 3.6 left shows that the model of this work displays the best fit to the experimental data for CO_2 conversion among all studied literature models. Its trend looks similar to the one obtained by the Koschany model, which is due to the fact that the same reaction orders for CO_2 and H_2 were applied. However, the Koschany model overestimates the conversion in the temperature range of 330 °C up to 450 °C, and the equilibrium is already reached at a lower temperature of 400 °C. At higher conversions, the product inhibition obviously plays a more important role than predicted by the Koschany model. The different form of

the inhibition term of the model of this work compared to that of Koschany apparently helps to avoid such overestimation.

The models of Zhang and Kopyscinski fit the data of this work only in the middle-temperature range (350-400 °C) very well. In the high and low conversion regions, they both overestimate the conversion. The model of Kopyscinski crosses the thermodynamic equilibrium conversion at 430 °C, which is clearly due to neglecting the thermodynamic term in the CO-methanation model. Despite CO_2 conversion overestimation in a wide temperature range, the models of Zhang and Koschany provide a better description of the CO_2 conversion trend at high temperatures. These models describe the approach to the thermodynamic curve as it is expected at temperatures close to 450 °C. The different form of the inhibition term in these models (inhibition through H_2, CO, CO_2, etc.) and application of more parameters, which in return scales down the impact of individual parameters, can be deduced as the most feasible explanation. For future references, before adding to the complexity of the model, it is recommended to run complementary experiments at high temperatures in presence of water, CO, etc. to win a deeper understanding of the factors inhibiting the reaction and further refine the model.

Fig. 3.6 right shows that the lowest selectivity measured is 95% at 300 °C. It reaches a maximum of 98% at 350 °C and decreases to 97% at higher temperatures. The model of this work is able to reproduce the trend of a maximum between 335 °C and 425 °C; however, it still underestimates the selectivity especially in the lower temperature range ($T < 320$ °C). The models of Zhang and Kopyscinski show increasing selectivity with increasing temperature which is not quite the case as the experimental data indicate. The model of Zhang exhibits a maximum at 430 °C due to the equilibrium, and the Kopyscinski model misses such a trend completely. Overall, similar to CO_2 conversion, the model of Zhang shows the most reasonable trend at $T > 420$ °C. The model of Koschany cannot be applied for selectivity prediction, since it simulates direct CO_2 methanation.

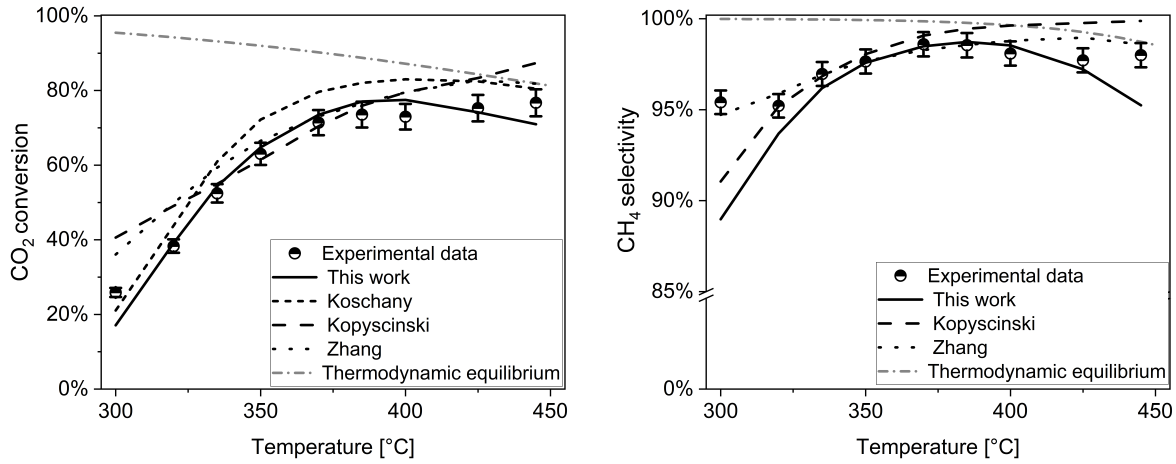

Figure 3.6: Comparison of CO_2 conversion (left) and a CH_4 selectivity (right) as a function of temperature for experimental data versus prediction by the developed model and the literature models (p_{abs} = 4 bar and τ_{mod,CO_2} = 0.72 mg min ml^{-1})

The sum of squares of the residuals of the yield of carbon-containing species $RSS(Y_{c,i})$ as well as the adjusted coefficient of determination R^2_{adj} between modelled and experimentally observed molar flow rates of CO_2, CH_4, and CO at the reactor exit were used for evaluation of the three literature models versus the new model (see Tab. 3.7). The *RSS* values for all three literature models after being fitted to the experimental data are up to a factor of three higher than for the new model. This is the first indication of a better description of the experimental data with the new model. The R^2_{adj} (CO_2) for all literature models is below 0.9, whilst the new model reaches a value of 0.93 which is the closest to one. For the case of CH_4, the R^2_{adj} is equal to 0.89 and is superior compared to other models as well. An improvement in R^2_{adj} (CO) can be grasped compared to the Zhang model with 0.42 versus 0.48 for the new model. The model of Kopyscinski resulted in a negative value of R^2_{adj} (CO), and for the Koschany model, no R^2_{adj} (CO) could be estimated since it does not consider CO formation at all.

In conclusion, the model of Koschany, which applied the same reaction exponents as in this work, can simulate the CH_4 and CO_2 product flow rates best amongst the literature models. The model of Zhang, nevertheless, was the only proper literature model for simulating CO formation as an intermediate.

Another advantage of the new model is reflected by the *BIC* factor. It has the smallest value (highest negative number). The modest number of parameters used in this model together with an accurate description of the formation/consumption of species led to this favorable *BIC* value. Therefore, it is confirmed that 6 applied parameters are statistically

advantageous and sufficient for a wide parameter range in comparison to complex models of Kopyscinksi and Zhang, in which 12 parameters are applied.

Table 3.7: Statistical comparison of the new two-step CO_2 methanation rate model with literature models

Model	*BIC*	*RSS*	$R^2_{adj}(CO_2)$	$R^2_{adj}(CH_4)$	$R^2_{adj}(CO)$
Koschany [61]	-426.5	9.94	0.891	0.832	-
Zhang [150]	-371.3	12.25	0.852	0.755	0.424
Kopyscinski [149]	-379.5	11.66	0.836	0.774	-0.015
The new suggested model	-636,7	2.98	0.927	0.889	0.483

3.3.4 Influence of experimental conditions on reaction rate

3.3.4.1 Temperature

For a better discussion of the observed effects on intermediate CO, the yield of CO formation over CO_2 conversion for different temperatures is plotted in Fig. 3.7. For 300 °C, only small amounts of CO were formed, and the maximum value for the CO yield is only 2%. At higher temperatures (350 °C and 400 °C), much higher CO yield (up to 7%) was observed; at high CO_2 conversion (>70%), the CO yield drops quickly to below 2%. The shape of the Y-X curve for T = 300 °C suggests that CO is an intermediate product of CO_2 hydrogenation to CH_4. At T > 350 °C, when the required contact time is much shorter, substantial amounts of CO were measured at intermediate CO_2 conversions. By increasing the contact time, CO_2 conversion improves, and therefore the intermediate CO reacts further to CH_4. In between 300 °C and 350 °C, there is a continuous transition, indicated by data collected at 335 °C, which connects the low-temperature-regime to the high-temperature-regime. Having a look at the estimated values for the rWGS and CO methanation in Tab. 3.4 illustrates that the activation energy for the rWGS reaction is much higher than for CO methanation (166.55 versus 60.98 kJ mol^{-1}). This means the rWGS reaction gets faster compared to CO methanation at a higher temperature. As Fig. 3.7 illustrates, this transition is simulated accurately with the model of this work.

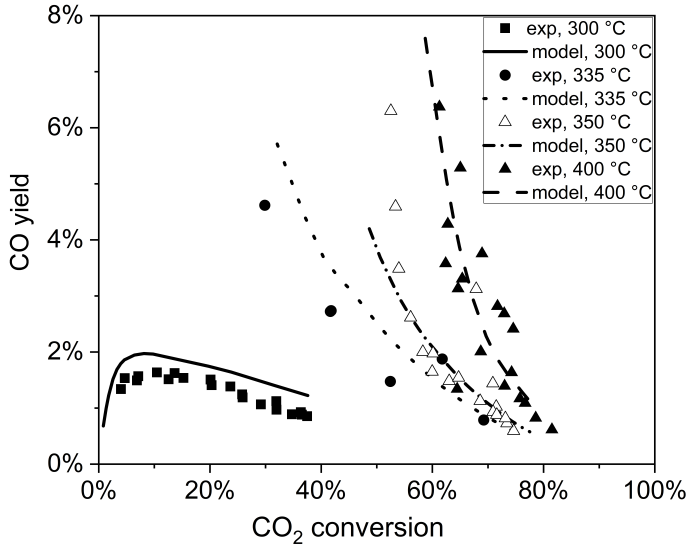

Figure 3.7: Y_{CO} versus X_{CO_2} diagram for CO formation from CO_2 derived from different temperatures, contact times and pressures.

3.3.4.2 Pressure

The impact of a pressure increase from 2 to 18 bar on conversion and selectivity is shown in Fig. 3.8. The measurements were carried out at 350 °C for $\tau_{mod,CO_2} = 0.38$ mg min ml^{-1}, and at 300 °C for $\tau_{mod,CO_2} = 0.72$ mg min ml^{-1}. Pressure proves to have a positive influence on CO_2 conversion and selectivity to CH_4 formation. However, after 5 bar this influence becomes less pronounced. There are again two explanations for such behavior: the pressure dependency of the thermodynamic equilibrium (see Cha. 2, Sec. 2.1) and the inhibition effect of water on the reaction rate at higher conversion levels. Since both terms are included in the kinetic model of this work, a very good consistency between the simulation and the measured points is recognizable.

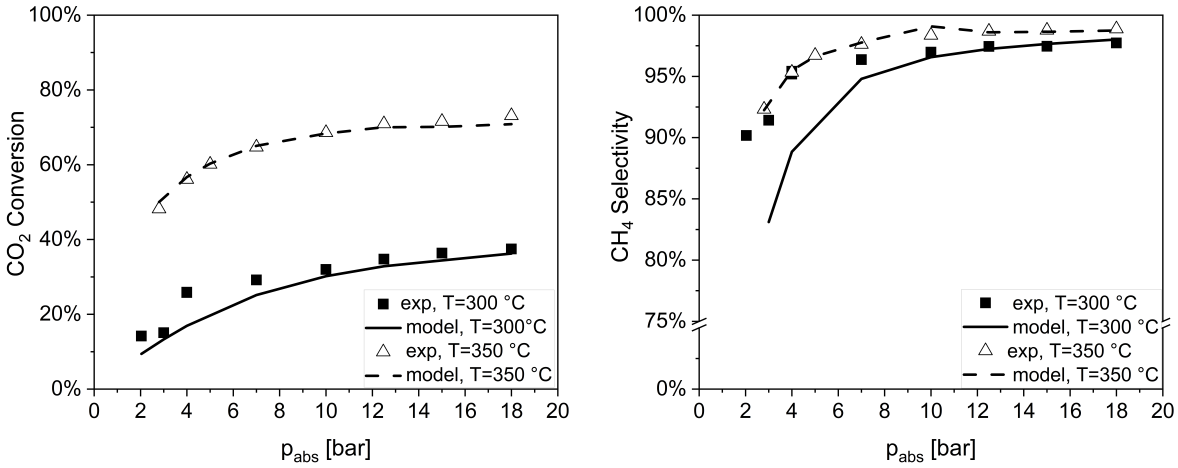

Figure 3.8: Experimental and simulated CO_2 conversion (left) and CH_4 selectivity (right) from 2 to 18 bar (T = 300 °C for $\tau_{mod,CO_2} = 0.72\,mg\,min\,ml^{-1}$ and T = 350 °C for $\tau_{mod,CO_2} = 0.38\,mg\,min\,ml^{-1}$)

3.3.4.3 H_2:CO_2 ratio

The H_2/CO_2 ratio was varied from 2 to 8 with two different measurement series as already clarified in Sec. 3.1.3. In all measurements, the modified contact time for CO_2 was kept constant (= $0.38\,mg\,min\,ml^{-1}$) in order to be able to conclude on the integral reaction rate. Fig. 3.9 indicates that the H_2/CO_2 has a pronounced positive influence on CO_2 conversion for both measurement series, although slightly weaker for the case of p_{H_2} = constant. The conversion drops from 60% in H_2/CO_2 = 4 to 30% for a H_2/CO_2 ratio of 2. Doubling this ratio to 8 increases the conversion to 90%.

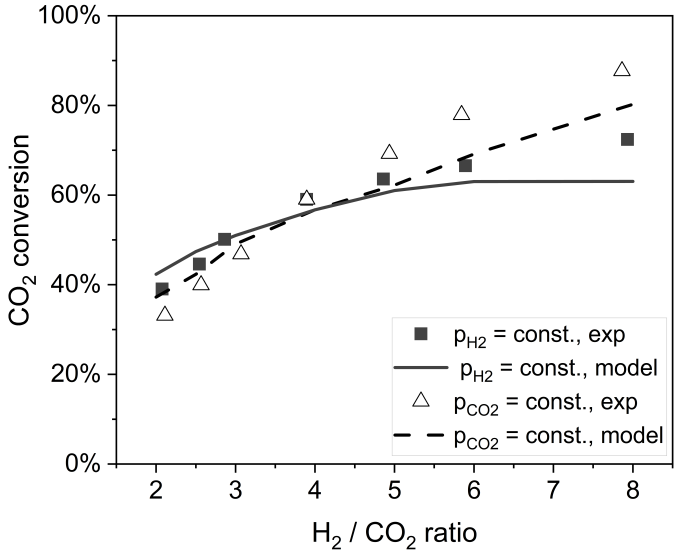

Figure 3.9: CO_2 conversion for different values of the H_2/CO_2 ratio between 2 and 8 for two series of experiments (T = 350 °C for τ_{mod,CO_2} = 0.38 mg min ml^{-1})

Valuable information can be discerned by having closer look at the reactants ratio imprint on selectivity. The influence of H_2/CO_2 variation on CH_4 selectivity is completely different for the two studied scenarios and demands special attention. Thus, for better understanding of the involved effects on the reaction rate in the H_2/CO_2 variation tests, CH_4 selectivity in the experiments with p_{H_2} variation is also compared to experiments where the total pressure was varied for constant H_2/CO_2 (= 4) ratio. CO_2 and H_2 conversion and CH_4 selectivity in dependence of the varied p_{H_2} are plotted in Fig. 3.10 (left: CO_2 and H_2 conversion, right: CH_4 selectivity). Fig. 3.10 left exhibits that in the beginning the H_2 conversion is constant ($\approx$ 60%, p_{H_2} = 0.8-1.6 bar), where CH_4 selectivity is rising considerably from its lowest level (= 91%, Fig. 3.10 right) with increasing p_{H_2}. With further increase in p_{H_2} (p_{H_2} > 2 bar), H_2 conversion starts to drop with an accelerating trend. Such behavior can be interpreted in a way that in lower p_{H_2} region, the added H_2 is consumed instantaneously to products with the overall increasing rate. At p_{H_2} > 1.6 bar, the stoichiometry is reached and additional dosed H_2 remains unreacted, which leads to a drop in H_2 conversion. According to Fig. 3.10 left, CO_2 conversion has a positive trend in the whole range of p_{H_2} increase, so that more CO could appear through the rWGS reaction. However, further conversion of CO to methane is rather depending on the H_2 concentration and not on the CO_2 amount present (see Sec. 3.3.4.6), so with higher H_2 concentration, its conversion to CH_4 is guaranteed, and this explains the enhancing trend for CH_4 selectivity in Fig. 3.10 right. The CH_4 selectivity for data with constant H_2/CO_2

= 4 has the same trend as when CO_2 is kept constant. Since the increased methane selectivity (Fig. 3.10 right) and the increased CO_2 conversion (Fig. 3.10 left) have very similar trends, an identical reaction order is plausible for CO_2 and H_2 in both, the rWGS and the CO methanation reaction.

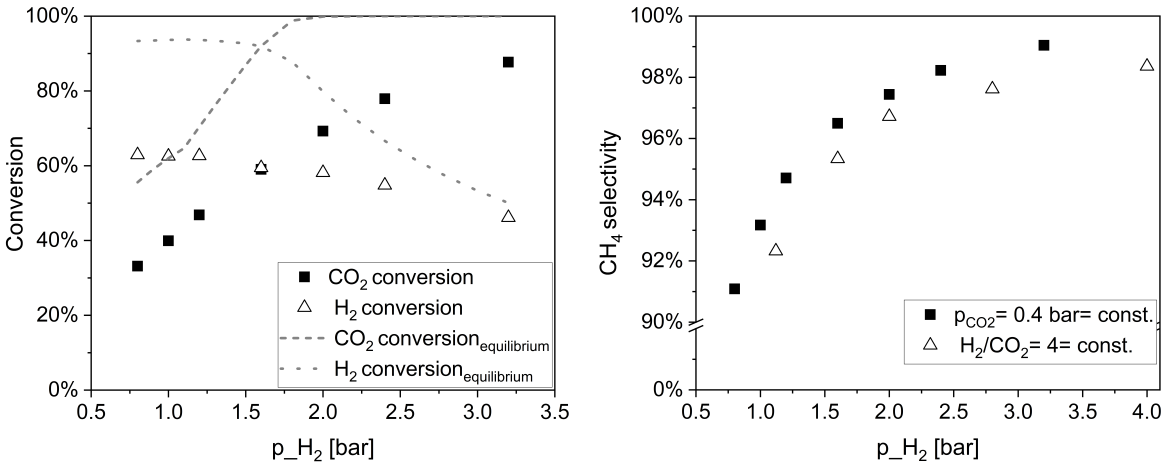

Figure 3.10: CO_2 and H_2 conversion (left) and CH_4 selectivity (right) in dependence of the H_2 partial pressure (p_{CO_2} = 0.4 bar = const., T = 350 °C and τ_{mod,CO_2} = 0.38 mg min ml^{-1}). In the right figure a plot of CH_4 selectivity is added for variation of the total pressure at H_2/CO_2 = 4 = const. (T = 350 °C and τ_{mod,CO_2} = 0.38 mg min ml^{-1})

Fig. 3.11 depicts the results of the case where p_{H_2} is kept at 1.6 bar and p_{CO_2} is varied. In Fig. 3.11 left, CO_2 conversion shows a linear drop with increasing p_{CO_2} and extra dosed CO_2 remains unreacted. Even though the graph starts at over-stoichiometric H_2-conditions, this trend is continuously valid over the whole range of p_{CO_2} which leads to the assumption that the surface is already saturated with CO_2 species. On account of the CO_2 saturated surface, the produced CO through the rWGS reaction should also stay constant. As p_{H_2} is kept constant, the following CO methanation reaction has also a constant rate, which is supported from the finding of a relatively constant selectivity for CH_4 formation (Fig. 3.11 right). Experimental points with H_2/CO_2 = 4 prove this argument, in which for example for the data points with p_{H_2} < 1.6 bar (p_{CO_2} < 0.4 bar) the methane selectivity is lower than the corresponding points with p_{H_2} = 1.6 bar = const. (92% versus 96%). When H_2/CO_2 < 4 (and so p_{CO_2} > 0.4 bar), the CH_4 selectivity stays below the corresponding value for the stoichiometric mixture (97.8% versus 96%). This supports the assumption that the CO_2 concentration has no influence on the selectivity and on the CO methanation reaction.

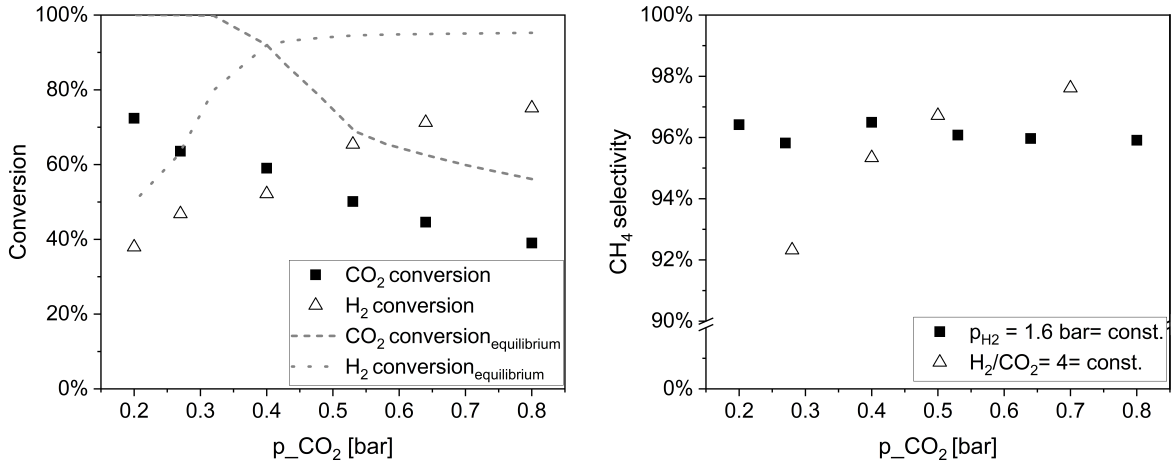

Figure 3.11: CO_2 and H_2 conversion (left) and CH_4 selectivity (right) in dependence of the CO_2 partial pressure (p_{H_2} = 1.6 bar = const., T = 350 °C and τ_{mod,CO_2} = 0.38 mg min ml^{-1}). In the right figure a plot of CH_4 selectivity is added for variation of the total pressure at H_2/CO_2 = 4 = const. (T = 350 °C and τ_{mod,CO_2} = 0.38 mg min ml^{-1})

3.3.4.4 Modified contact time

The modified contact time was varied from 0.1 to 0.72 mg min ml^{-1}. In Fig. 3.12 left, the effect of contact time on conversion for five different temperatures between 300 to 400 °C is demonstrated. For all temperatures, the increase in contact time is associated with higher conversion, however, this is more pronounced at lower temperatures. In total, good agreement between the model and the experimental data is realized.

In Fig. 3.12 right, the CO yield for temperatures of 300 °C, 320 °C and 350 °C and different contact times is plotted. The CO yield change for different contact times can be interpreted as the temporal progress of the reaction. Although experimental data at 300 °C show constant CO when varying the contact time, the measurements at 320 °C exhibit a gradual approach to the formation of a maximum for CO formation throughout the time. For experiments at 350 °C, a continuous CO yield drop with time is observable. The kinetic model suggests the existence of a maximum in CO yield at the beginning of the reaction, which sharpens and moves forward at higher temperatures. Unfortunately, residence times below 0.1 mg min ml^{-1} are not possible due to technical limitations of the setup, so that this trend cannot be fully confirmed. What is clear in the model and the data points as well is that for all temperatures, the CO yield drops to about 2% at contact times above 0.6 mg min ml^{-1}.

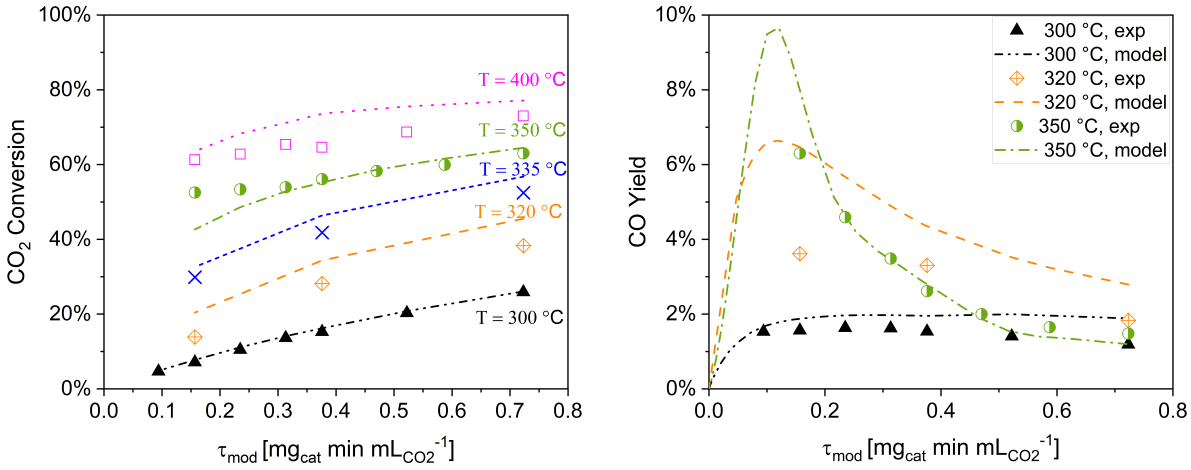

Figure 3.12: CO_2 conversion (left) and CO Yield (right) in dependence of the modified contact time for different temperatures (p_{abs} = 4 bar)

3.3.4.5 Water addition

The effect of adding water in the feed is depicted in Fig. 3.13 left. After adding 10 vol.% water in the feed, the conversion drops from 23% to 9%. With a further increase in the water flow rate, the conversion drops further. The experiment proves that water has a significant retarding impact on the reaction rate, which, as given in Eq. 3.22 and 3.23, is included in the rate equation through the water adsorption term. Fig. 3.13 left exhibits that the model precisely simulates the rate drop for different water concentrations added to the feed.

In this context, the value of the inhibition term is calculated for different temperatures and water partial pressures and plotted in Fig. 3.13 right. When trivial fractions of water are present in the gas mixture, *DEN* approaches 1, and the reaction rate is not affected. By adding small amounts of water to the feed, the rate decreases sharply. For example, for p_{H_2O} = 0.2 bar, the reaction rate is reduced to about 50% of its initial value. The plot indicates that this reduction is weakly temperature-dependent. Fig. 3.13 reveals further that the conversion drop during an increase of the water partial pressure (left plot) has exactly the same trend as the inhibition term (right plot). This proves that the reduction in conversion in presence of water is not affected by the rWGS reaction equilibrium, but explicitly by the presence of water in the reaction mixture.

Several literature works have reported an inhibiting effect of water on the rate of the methanation reaction [149]. Theofanidis et al. [221] have shed some light on the most important mechanistic concerns of CO_2 activation on Ni-Fe catalyst. Based on their study, CO_2 is dissociated on the Fe sites to surface CO and iron oxide (Eq. 3.29). It is well

known that H_2 is strongly attracted by Ni and adsorbs dissociatively on a Ni surface [222]. Through an alternating pulse experiment over a Fe promoted Ni catalyst, they could show that a redox reaction occurs, in which H_2 reduces the oxidized Fe sites (Eq. 3.30). A possible explanation for the inhibition effect of water observed in the experiments is that, by increasing the water concentration, the CO_2 activation sites are blocked with water leading to competing adsorption of water and CO_2 over the free sites. Furthermore, water can adsorb on the oxidized iron sites and can compete with hydrogen to reduce iron, thus, the rate of CO_2 conversion is slowed down.

$$Fe + CO_2 \longleftrightarrow FeO_x + x\,CO \tag{3.29}$$

$$H_2 + FeO_x \longleftrightarrow Fe + x\,H_2O \tag{3.30}$$

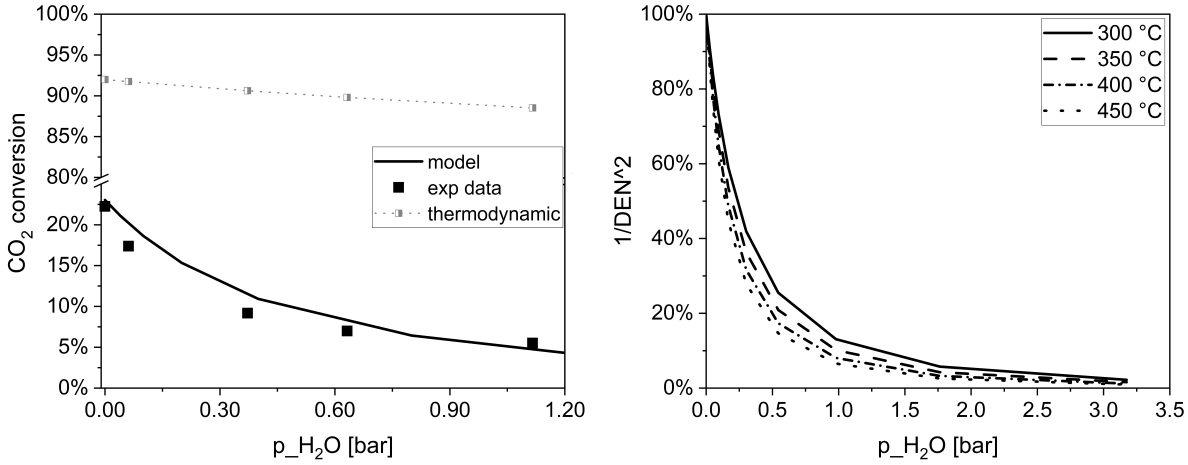

Figure 3.13: Influence of water addition on CO_2 conversion at T = 350 °C for τ_{mod,CO_2} = 0.38 mg min ml^{-1} and p_{abs} = 4 bar together with the corresponding thermodynamic conversion (left), illustration of the water inhibition term for different temperatures as a function of the water pressure (right).

3.3.4.6 CO addition

The experimental results of CO/CO_2 mixture methanation experiments are usually reported as the consumed amount of CO and CO_2 to provide an integral reaction rate. In addition, it is impossible to calculate CO conversion and methane selectivity explicitly from CO_2. Only the CO consumption and formation can be discussed with balance equations and comparison to a reference point. These experiments were performed at a temperature of 350 °C and absolute pressure of 4 bar. In Fig. 3.14 left the results of

converted CO and CO_2 in $ml\,min^{-1}$(in normal conditions) are shown for different flows of CO (0-11.4 $ml\,min^{-1}$) added in the feed. By increasing the CO amount from 0 to 11.4 $ml\,min^{-1}$, the CO_2 consumption decreases from 64 $ml\,min^{-1}$ to 61 $ml\,min^{-1}$. It may seem that CO can have a slightly negative influence on CO_2 consumption. However, this may also be due to the thermodynamic equilibrium, the additional H_2 consumption or inhibition due to extra water produced from the added CO. Since the model describes the experimental data accurately (the solid line in Fig. 3.14 left), it is concluded that no further CO inhibition term for the rWGS reaction is necessary and water serves as the only retarding species. Another interesting conclusion made from this experiment is that the CO methanation rate is not influenced by CO_2 in the feed, since the values for CO consumption in the case of mixed methanation and pure CO methanation (dotted line, Fig. 3.14 left) fall on a straight line with an identical slope.

Fig. 3.14 right demonstrates the changes in reactant consumption for variable CO_2 in the feed (0-115 $ml\,min^{-1}$) with constant CO (6 $ml\,min^{-1}$) added to the feed. The first impression is that CO consumption reduces with increasing the CO_2 flow rate in the feed (dashed line, Fig. 3.14 right). Therefore, four experiments with CO_2 flow rate variation, this time without CO in the feed were performed (pointed line, Fig. 3.14 right), to add the CO formed from CO_2 in the balance. It can be seen that the CO consumption remains constant at 5.6 $ml\,min^{-1}$. Thus, the reaction hindrance due to CO_2 addition in CO methanation can be ruled out. This result is coherent with the observations made for various H_2/CO_2 ratios (Sec. 3.3.4.3). In this test, reacted CO_2 is only slightly influenced by the added CO and the deviation is less than 3%. This difference can be due to the increased H_2 consumption, thermodynamic effects, or additionally formed water from the added CO, which is also correctly reflected by the model (solid and pointed lines, Fig. 3.14 right).

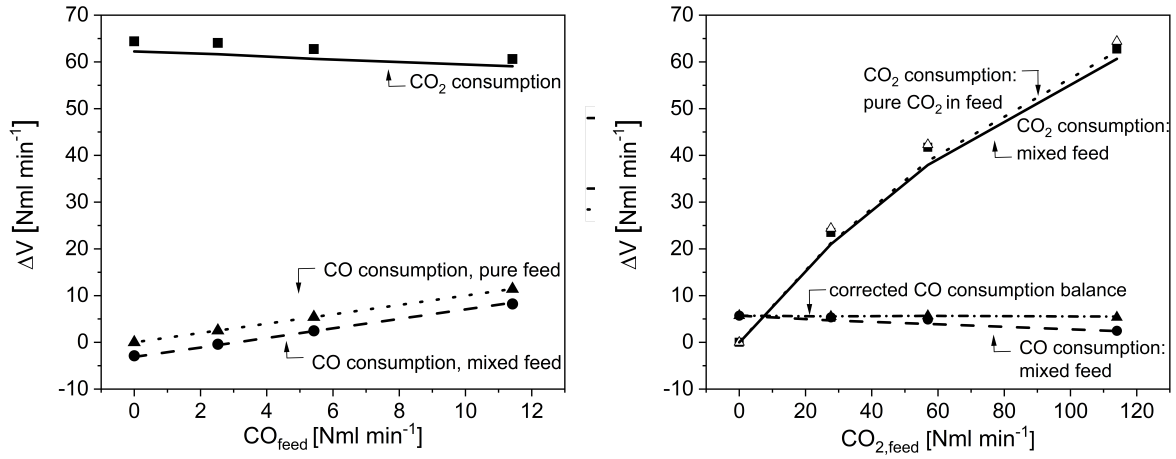

Figure 3.14: Variable CO addition to a constant CO_2 volumetric flow and influence on CO and CO_2 consumption (left), variable CO_2 addition to a constant CO volumetric flow and influence on CO and CO_2 consumption (right). (T = 350 °C and p_{abs} = 4 bar)

3.3.5 Long-term tests

Under reference reaction conditions (T = 350 °C, p_{abs} = 4 bar and $\tau_{mod,CO_2} = 0.38$ mg min ml^{-1}) a long-term test for 300 h was carried out. The kinetic data used for the modelling were collected in the first 50 h and due to varied reaction parameters, they are not included in Fig. 3.15 left to avoid confusion. The gaps in the TOS of 85-100 h and 200-220 h are due to technical stops of the gas chromatograph. The reaction was not interrupted in these periods. In the first 50 h, CO_2 conversion drops by about 5%, however selectivity to methane remains quite constant. With time, the decrease in conversion and selectivity gets steeper. In order to describe the temporal change of the intrinsic activity of the catalyst, an activity factor $a(t)$ between 0 and 1 is defined which serves to correct the reaction rate.

$$r_i(t) = a(t) \cdot r_i(t = 0) \tag{3.31}$$

This representation of the time dependence of the activity is without any speculation on the mechanism or the reasons for deactivation. For calculation of $a(t)$, a variable in the final kinetic model was defined and then adjusted based on the whole data from the long-term experiment. The results of this fit are given in Fig. 3.15 right. This trend could be fitted to a linear function, with which the average deactivation rate could be read out from the slope of this function: 0.32% h^{-1}. This value indicates that on average, in every 3 hours, the catalyst loses about 1% of its initial activity. It should be notified however that this is a very rough estimation of the activity loss for this catalyst and the trend is

not perfectly linear.
For comparison with literature, an exponential approach which is often adopted in literature was applied. The relative activity (A_{rel}) was obtained from the conversion, and the deactivation factor k_a as well as the deactivation order m_a were calculated. The model describes a catalyst-aging phenomenon due to structural changes or sintering processes, without any dependence on the composition of the reactants. Tab. 3.8 summarizes the values estimated for k_a and m_a for two self-prepared (i.e., non-commercial) Ni-based catalysts from literature [223] as well as the Ni_3Fe catalyst used in this work.

$$A_{rel} = \frac{X(t)}{X(t=0)} \tag{3.32}$$

$$\frac{d}{dt}A_{rel} = -k_a \cdot A_{rel}^{m_a} \tag{3.33}$$

Table 3.8: Comparison of the deactivation factor and order of the Ni_3Fe catalyst to those of Ni catalysts from literature [223]

Catalyst	k_a [h^{-1}]	m_a
Ni (Al-doped)	8.61 10^{-4}	5.69
Ni (Fe-doped)	7.13 10^{-4}	34.1
Ni_3Fe	14.9 10^{-4}	-1.34

The k_a value estimated for Ni_3Fe compared to the literature values has the same order of magnitude and is about a factor two higher. The deactivation factor can be interpreted as the tendency of a catalyst to lose its activity and thus for the Ni_3Fe catalyst no improvement compared to other Ni catalysts is detectable. The major difference between the Ni_3Fe catalyst used in this work compared to the catalyst used in literature is comprehended from the value of deactivation order m_a, which is an indication of the temporal dynamics of the deactivation. In this context, an order of zero stands for a linear deactivation or a constant deactivation rate over the entire runtime. A deactivation order bigger than zero means an exponential trend for deactivation in which the activity falls faster in the beginning and then slows down with time. For the case of Ni_3Fe catalyst, the deactivation order is estimated smaller than zero. A negative value implicates that in the beginning the deactivation is slower and after a certain time it grows faster, which can be deduced from

Fig. 3.15 left. Based on these observations, the main disadvantage of the Ni_3Fe catalyst is strong and non-linear activity loss throughout long operational hours. Future studies on this catalyst would call for modification of the catalyst formula and/or preparation method to avoid such deactivation behavior.

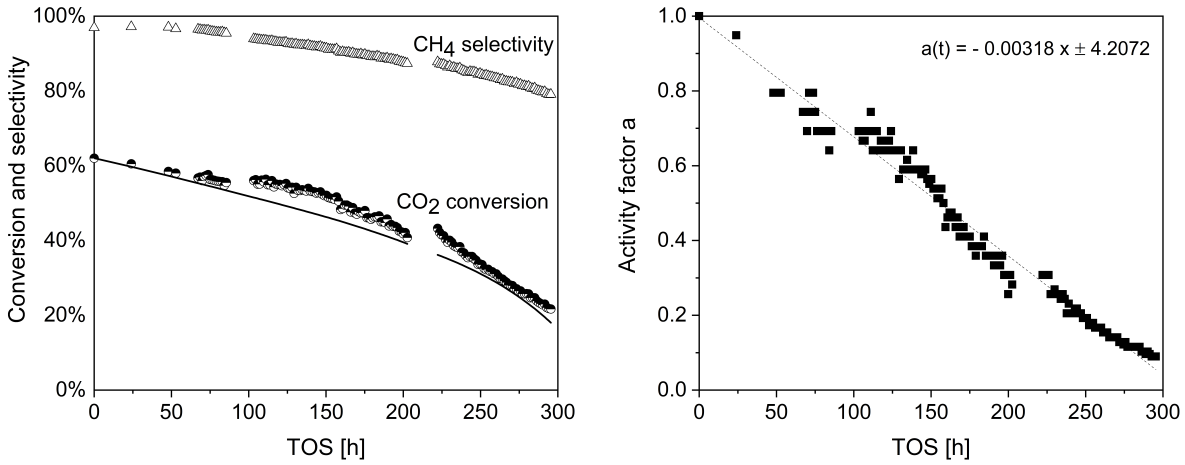

Figure 3.15: Long-term stability test (left), and empirical function for describing the deactivation behavior with the activity factor $a(t)$ for reference conditions (T = 350 °C, p_{abs} = 4 bar and τ_{mod,CO_2} = 0.38 mg min ml^{-1}).

3.3.6 Analysis of the deactivation sources

Since the catalyst expressed a strong activity drop during long-term tests, it was analyzed with various characterization methods to reveal the deactivation sources.
Scanning electron microscope (SEM) imaging (in micrometer dimensions) was not helpful in the detection of a structural or morphology change after the long-term tests. The EDX-SEM imaging also did not prove any hint on carbon or coke formation on the deactivated sample (see Appendix A.5). No apparent trace of crystal structure change in the deactivated catalyst compared to the fresh one was detected by X-ray diffraction (XRD) imaging. These measurements are presented in Appendix A.6. Therefore, transmission electron microscopy (TEM) was exploited to check for changes at the atomic level.
Fig. 3.16 left shows the EFTEM image of a fresh synthesized catalyst, before reduction. The EFTEM map indicates clusters of Fe as well as distinct Fe particles well-dispersed among Ni particles over the whole sample. The diffraction pattern reflected in the SAED (selected area electron diffraction) image shown in Fig. 3.16 right provides further evidence for the presence of Fe particles in the sample.

Fig. 3.17 shows the STEM combined with EDX images of the fresh Ni_3Fe catalyst after reduction. The elemental map for Ni and Fe proves that these two elements are alloyed in the reduced fresh particles. Thus, it can be concluded that the heat treatment associated with the reduction procedure finalizes the alloying process between Ni and Fe. The SAED image in Fig. 3.18 left confirms the presence of alloyed Ni_3Fe particles in the reduced sample. Multiple images from different spots of the sample delivered similar results. In the SAED pattern, nickel oxide (NiO) is also detected which may be formed during TEM sample preparation under air atmosphere. The Ni_3Fe lattice in the SAED image matches the diffraction observed in particles observed by HRTEM (Fig. 3.18 right). No trace of monometallic Fe or iron oxide diffraction patterns were observed in the sample. These results are in accordance with the electron microscopy investigations performed by Mutz et al. [119].

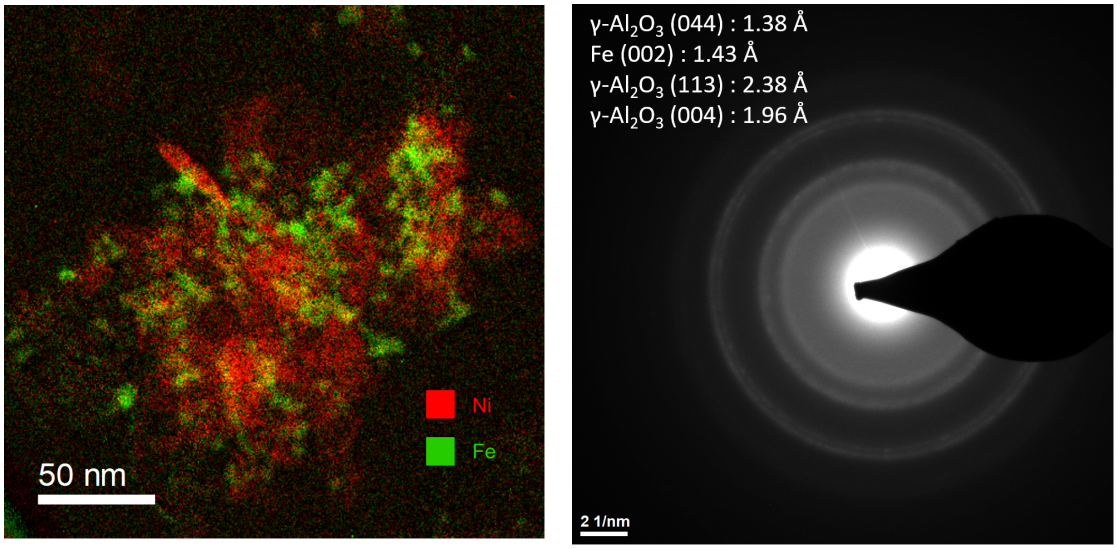

Figure 3.16: Left: EFTEM map of the fresh Ni_3Fe catalyst before reduction. Right: SAED image of the fresh Ni_3Fe catalyst before reduction.

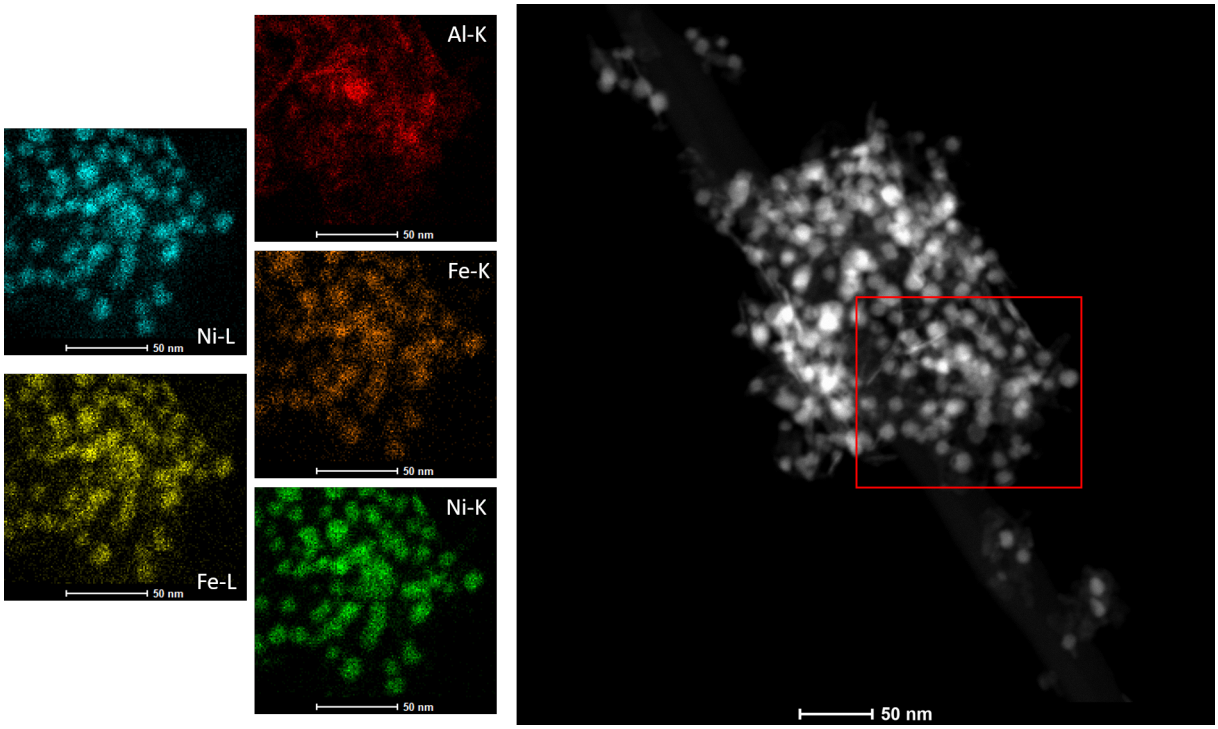

Figure 3.17: STEM image of the freshly reduced Ni_3Fe/γ-Al_2O_3 catalyst and the corresponding elemental map obtained from STEM-EDX spectrum imaging on the marked region.

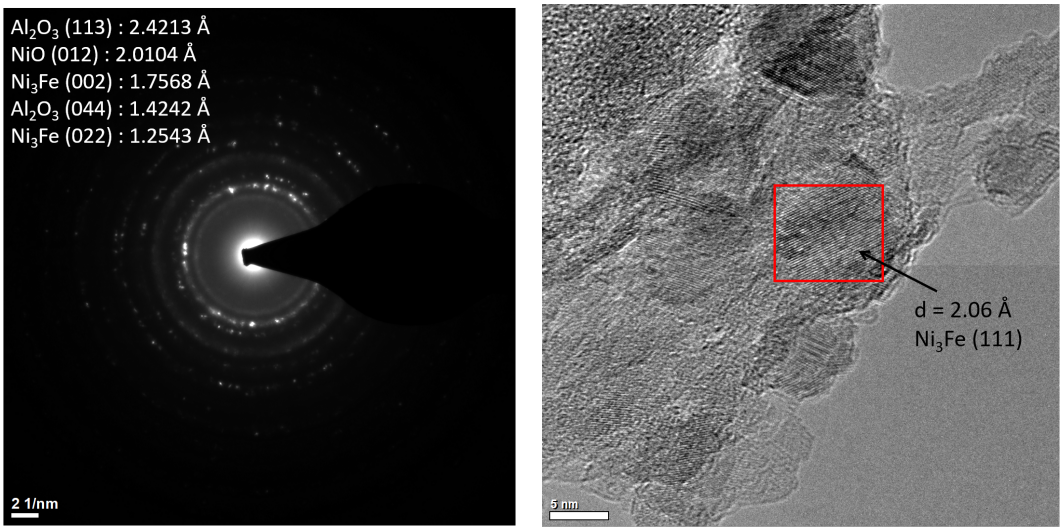

Figure 3.18: SAED image (left) and HRTEM image (right) of the fresh Ni_3Fe catalyst after reduction.

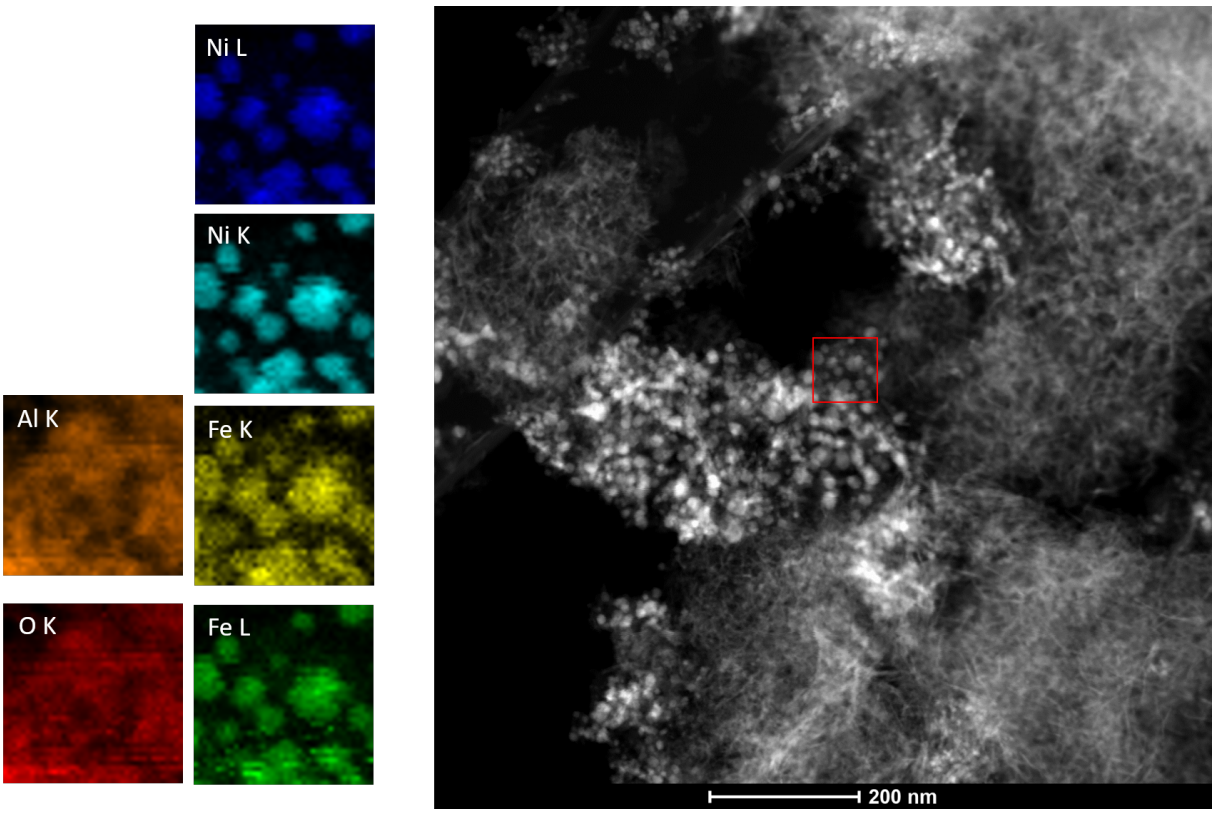

Figure 3.19: STEM image of the deactivated Ni_3Fe/γ-Al_2O_3 catalyst and the corresponding elemental map obtained from STEM-EDX spectrum imaging on the marked region.

Fig. 3.19 shows the STEM-EDX elemental map after long-term tests. The EDX maps illustrate that the alloying between Ni and Fe has not changed after the long-term reaction experiments and no mono-metallic iron element is detectable. The SAED pattern in Fig. 3.20 left illustrates the same rings for the Ni_3Fe catalyst as in the fresh catalyst. Additionally, in the HRTEM image shown in Fig. 3.20 right, the same atomic structure for Ni_3Fe as in the fresh catalyst (Fig. 3.18) is visible. Hence, the catalyst crystal structure did not change after the long-term reaction tests. The same observation was also made by XRD diffraction patterns given in Appendix A.6.

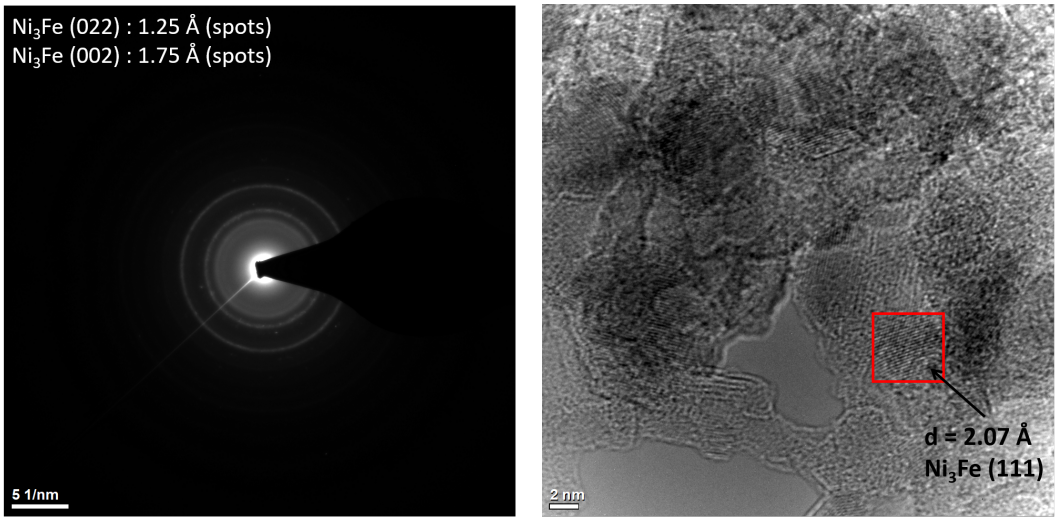

Figure 3.20: SAED image (left) and HRTEM image (right) of the Ni_3Fe catalyst after long-term tests and deactivation.

The most important variations in the catalyst can be deciphered by having a closer look at the STEM images depicted in Fig. 3.17 and 3.19. In the fresh catalyst sample, the needle-like Al_2O_3 support is homogeneously covered with the active material (Fig. 3.17). In contrast, after 300 h reaction treatment, the Al_2O_3 has formed clusters separated from the active phase (Fig. 3.19). Such support and active metal partitioning can have a critical influence on the activity. According to several literature studies, the support plays an important role in the reaction mechanism and assists CO_2 and/or CO splitting and the reaction with adsorbed H atoms (on the Ni surface) [59].

The second valuable information is derived from a comparison of the active phase particle size distribution in the fresh and used sample. Fig. 3.21 demonstrates the particle size distribution determined statistically from multiple STEM images of the Ni_3Fe catalyst before (counted: 269 particles) and after (counted:145 particles) the reaction. Before the reaction, the particle size has a narrow and bell-shaped distribution and is on average between 8-12 nm. This value is larger than the diameter reported by Mutz et al. (3-5 nm) [119]. The first reason for this discrepancy can be that the catalysts are prepared in laboratory scale and are from different batches. Therefore, a certain deviation from one batch to another may be expected. Another factor is the oxidation state. The size of the active metal in the unreduced sample is slightly smaller. Therefore the two batches may have been in different reduction states. Fig. 3.21 displays that the size of the particles after reaction is 1.5 times bigger than that of the fresh catalyst (10±2 nm versus 15±3 nm). This observation is an indication of coalescence of the active metallic phase. Thus,

a reduction of the surface area of the active phase due to sintering is regarded as the major issue leading to deactivation.

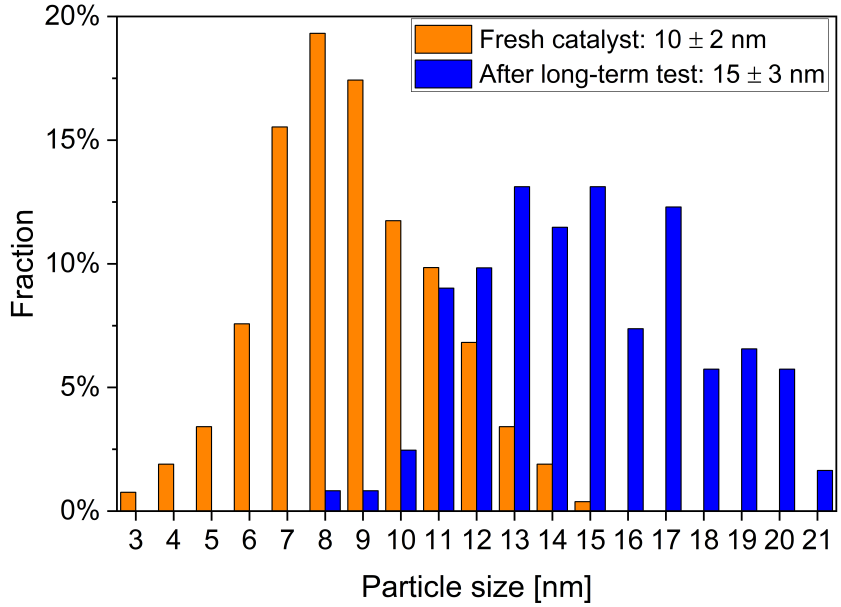

Figure 3.21: Particle size distribution for the Ni_3Fe catalyst before and after long-term tests

3.3.7 Application of the developed kinetic model to a mono-metallic Ni catalyst

The development of a new kinetic model for describing the consecutive pathway of CO_2 methanation on a Ni_3Fe catalyst, stimulates the application of this model to further Ni catalysts, especially mono-metallic systems which are commonly applied. As already mentioned at the beginning of this chapter, two catalyst systems are investigated intensively in this study. The second catalyst of interest is a promoted mono-metallic Ni/γ-Al_2O_3. The characteristics of this catalyst are not further revealed here due to confidentiality reasons.

For investigating the kinetics of this catalyst, 36 measurement points were collected. Tab. 3.9 shows the details of the varied operational conditions. The H_2/CO_2 ratio was kept at 4 in all experimental runs and the feed was diluted with 50% N_2. The catalyst mass is equal to 46 mg and was diluted with γ-Al_2O_3 with the same procedure as in the case of the Ni_3Fe catalyst (dilution ratio of 0.7 to 1, see Sec. 3.1.3).

Table 3.9: Investigated range of operational conditions for kinetic measurements on a promoted mono-metallic Ni catalyst

Exp. no.	Temperature	Pressure	τ_{mod,CO_2}
-	[°C]	[bar]	[N mg min ml^{-1}]
1-6	300	4 and 12.5	0.72, 0.38, 0.16
7-12	325	4 and 12.5	0.72, 0.38, 0.16
13-18	350	4 and 12.5	0.72, 0.38, 0.16
19-24	375	4 and 12.5	0.72, 0.38, 0.16
24-30	400	4 and 12.5	0.72, 0.38, 0.16
30-36	430	4 and 12.5	0.72, 0.38, 0.16

Fig. 3.22 displays the activity comparison between the Ni_3Fe catalyst and the mono-metallic Ni catalyst for two modified contact times of 0.72 and 0.38 mg min ml^{-1} and p_{abs} = 4 bar. As Fig. 3.22 left shows, both catalysts have a very similar activity trend when increasing the temperature. Also for both catalysts, conversion reaches a plateau beyond a temperature of 375 °C. However, it is evident that in the entire temperature window, the Ni_3Fe has a superior activity compared to the mono-metallic Ni catalyst. The same conclusions can be made regarding the CH_4 selectivity, given in Fig. 3.22 right. This means that the kinetic parameter estimates for the Ni_3Fe catalyst cannot be applied for simulating the reactors over this catalyst system. Therefore, the new model was fitted to the 36 data points recorded for the mono-metallic Ni catalyst.

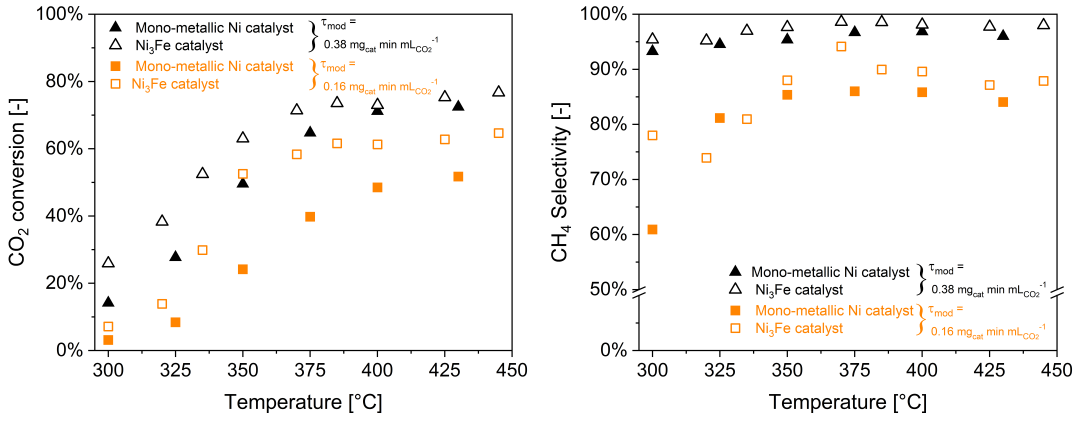

Figure 3.22: Activity comparison between the Ni_3Fe catalyst and the promoted mono-metallic Ni catalyst as a function of temperature for different modified contact times, CO_2 conversion (left), CH_4 selectivity (right), p_{abs} = 4 bar.

The parameters were fitted to experimental data with the same mathematical procedure described in Sec. 3.2.4. For understanding the influence of weighting factors on the results of the parameter estimation, the *RSS* was first defined according to Eq. 3.16 and in a second attempt according to Eq. 3.17. Fig. 3.23 illustrates the parity plots of the CO_2, CO and CH_4 flow rates measured experimentally versus the calculated values with the new LHHW model without weighting factors (corresponding to Eq. 3.16). The parity plot for CO_2 (Fig. 3.23 left) shows that the model has a very good correspondence to the experimental data and all the measured points are within the ±25% range. For the case of CO, the scattering is much higher and the model overestimates CO formation for approximately half of the data points. The parity plot of CH_4 shows an overall good agreement between the model and experiments and except for a few cases, the measured data points are predicted accurately. The R^2_{adj} values for CO_2, CH_4 and CO are 0.97, 0.94 and 0.62, respectively. The *RSS* value is equal to 0.28.

For comparison, the parity plots applying weighting factors during parameter fitting for each data point provided in Tab. 3.6 are displayed in Fig. 3.24. The *RSS* was equal to 0.52. For the case of CO_2 and CH_4, the parity plots are rather identical, and the R^2_{adj} values indicate no apparent improvement in the fit. The small relative error for these two compounds justifies this result. For the case of CO however, the fit became slightly better after applying the weighting factor and the R^2_{adj} improved from 0.62 0.64. Nevertheless, the CO data points show a significant data scattering. This observation validates the assumption that the GC was at its limits for measuring the CO concentrations. The new set of kinetic coefficients estimated for this catalyst using the weighting factors are provided in Tab. 3.10.

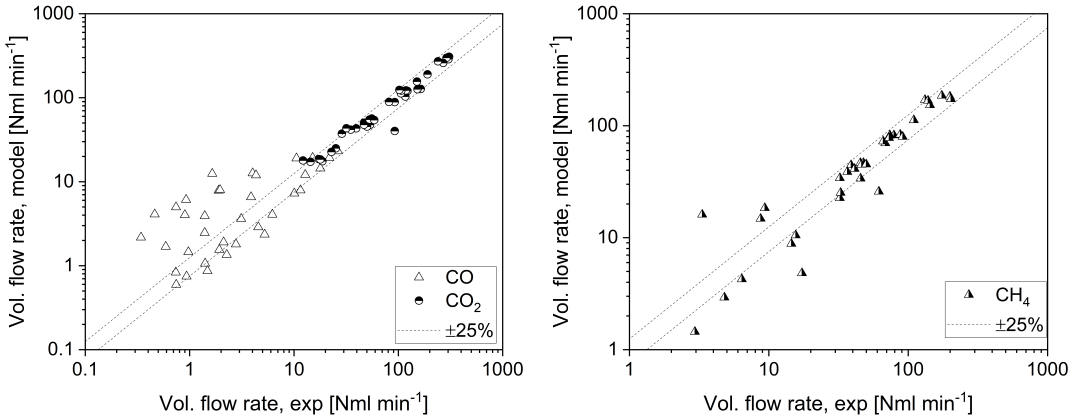

Figure 3.23: Parity plots for comparison of the experimental data for the promoted mono-metallic Ni catalyst to the new LHHW rate model for CO and CO_2 volumetric flows (left), and CH_4 volumetric flow (right) (*RSS* according to Eq. 3.16.)

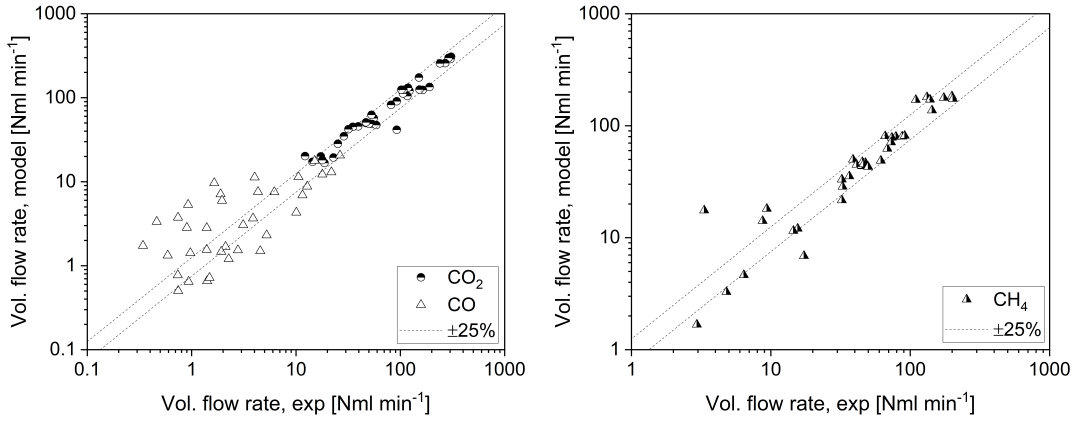

Figure 3.24: Parity plots for comparison of the experimental data for the promoted mono-metallic Ni catalyst to the recommended LHHW rate model for CO and CO_2 volumetric flows (left), and CH_4 volumetric flow (right). Weighting factors were applied during the parameter estimation (*RSS* according to Eq. 3.17).

Table 3.10: Parameter estimates for the rWGS (1) and CO methanation (2) reaction rate models and their corresponding 95% confidence intervals for the promoted mono-metallic Ni catalyst

Parameter	Value	Confidence interval	Unit
$k_{1,555\,k}$	0.081	± 0.038	mol (kg s bar)$^{-1}$
$E_{A,1}$	99.75	± 8.25	kJ mol^{-1}
$k_{2,555\,k}$	1.632	± 0.368	mol (kg s bar$^{1.5}$)$^{-1}$
$E_{A,2}$	117.04	± 23.60	kJ mol^{-1}
$K_{H_2O,555\,k}$	1.012	± 0.236	bar^{-1}
ΔH_{H_2O}	13.84	± 5.58	kJ mol^{-1}

In Tab. 3.11 the correlation matrix for the estimated parameters for the mono-metallic Ni catalyst are provided. Over 73% of the correlation parameters are below 0.5 and show very low interdependence. The rest of the values are between 0.5 and 0.66 which is acceptable and refers to a very moderate correlation between parameter pairs.

Table 3.11: Correlation matrix of the parameters in the suggested model for the promoted mono-metallic Nickel catalyst

	$k_{1,555\,k}$	$k_{2,555\,k}$	$K_{H_2O,555\,k}$	$E_{A,1}$	$E_{A,2}$	ΔH_{H_2O}
$k_{1,555\,k}$	1	-	-	-	-	-
$k_{2,555\,k}$	0.1	1	-	-	-	-
$K_{H_2O,555\,k}$	0.253	-0.514	1	-	-	-
$E_{A,1}$	-0.650	-0.265	0.095	1	-	-
$E_{A,2}$	-0.298	-0.572	-0.069	-0.001	1	-
ΔH_{H_2O}	-0.244	0.128	-0.662	0.209	0.170	1

Finally, a long-term test for duration of 330 hours at reference reaction conditions (T = 350 °C, p_{abs} = 4 bar and τ_{mod,CO_2} = 0.38 mg min ml^{-1}) was carried out. CO_2 conversion, CH_4 selectivity and CO yield as a function of time are depicted in Fig. 3.25. The deactivation behavior is considerably different from the trend observed for Ni_3Fe catalyst (Fig. 3.15). In the case of the mono-metallic Ni catalyst, the activity was much more stable and no sudden drop or exponential deactivation was recognizable. After TOS = 200 h, CO_2 conversion was reduced by about 5%. Methane selectivity showed stochastic variations in the second half of the experiment (TOS = 160-300 h). What must be noted at this point is that in the TOS interval of 150-300 h, due to some technical complications in the setup, the absolute pressure in the reactor was reduced by about 1 bar. During this period the reaction was not terminated. After TOS = 300 h, the pressure could be regulated back to the initially desired level of 4 bar. For this period more data points are plotted for statistical consistency. The final measurements in the reaction time of 300-330 h indicate that only 5% loss in CO_2 conversion after the 330 h TOS is recognizable. The CH_4 selectivity suffers a more severe degradation (about 10%) after this period. The CO yield is consequently increased from 4% in the initial state to 9% after 330 hours of on stream.

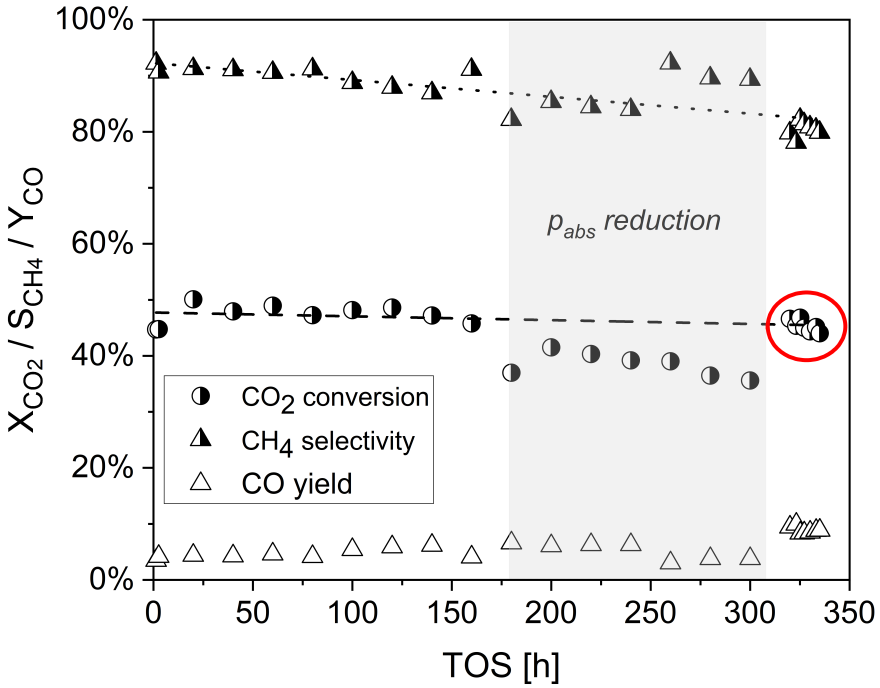

Figure 3.25: Long-term stability test for the promoted mono-metallic Ni catalyst (T = 350 °C, p_{abs} = 4 bar and τ_{mod,CO_2} = 0.38 mg min ml^{-1}).

3.4 Concluding remarks on kinetic studies

The objective of this chapter was the investigation of the CO_2 methanation reaction kinetics in a cross-flow cooled microstructured packed bed reactor using a 17 wt.% Ni_3Fe/γ-Al_2O_3 catalyst. The process parameters of temperature, pressure, contact time, and composition of the reactants were varied. The measured conversion and selectivity were used for evaluation of some representative literature models and the development of a literature-refined model for a consecutive CO_2 methanation pathway. This model offers a lower number of parameters so that the significance of each parameter is highlighted. The reactor model implemented was a 1D PFR non-isothermal pseudohomogeneous model. The modelling of the reaction was carried out based on the LHHW formalism. The mathematical terms were picked systematically based on experimental observations as well as literature results published by Koschany, Kopyscinski and Zhang [61, 149, 150]. The different models were tested and assessed in terms of the sum of least square residuals, confidence intervals of the parameter estimates, correlation matrix and adjusted coefficient of determination. The evaluation of different aspects revealed that the refined model based on two-step CO_2 methanation with direct water adsorption in the inhibition

term provides the smallest sum of least square residuals and the best agreement to the experimental data. In this context, no postulations on the reaction mechanism on Ni_3Fe catalyst can be provided. The validity of the calculated parameter estimates was confirmed by comparing them to relevant literature data.

The selectivity to methane formation was shown to be strongly dependent on temperature and residence time. Shorter residence time and higher temperatures favor CO formation. Especially between 320 °C and 350 °C, the yield of CO increases strongly. This selectivity behavior could be enlightened through describing the methane formation from CO_2 as a two-step reaction: the reverse water gas shift followed by CO methanation. In this regard, CO is the intermediate of the reaction and its abundant yield at higher temperatures and lower residence times was explained by the notably higher activation energy of the reverse water gas shift reaction compared to CO methanation (167 kJ mol^{-1} vs. 61 kJ mol^{-1}) estimated in this work. Stoichiometric variation of the reactants provided proof that the CO_2 concentration has no influence on the rate of CO methanation and that H_2 possibly has a similar order in both reactions. The experiments with CO addition in the feed (with and without CO_2) demonstrated that CO and CO_2 have no retarding effect on the reaction rate. The reaction rate hindrance due to water formation was confirmed experimentally through the addition of water in the feed mixture. It was shown that this effect is rather less dependent on temperature and that the water concentration is the main inhibiting factor. This observation however must be further checked by running further experiments at T > 400 °C, since the model systematically overestimates the rate inhibition at higher temperatures. Further info should help refinement of the inhibition term for approaching the equilibrium at high temperature-regime.

Long-term stability tests for 300 hours on the Ni_3Fe catalyst were recorded which exhibited a different deactivation behavior compared to mono-metallic Ni catalysts applied in the literature. The activity loss in this test was shown to be slow in the beginning, which is favorable for kinetic measurements. Deactivation increased progressively with time on stream which is not optimal for industrial applications. Thus in contrast to its high activity which draws much interest, the long-term performance of this catalyst has a substantial potential for improvement. The reasons behind this deactivation were revealed by transmission electron microscopy. It could be confirmed that sintering and disintegration of the support and the active metal clusters were the major causes of activity loss with time.

In the final step, it was confirmed that the developed model can also be applied for a promoted mono-metallic Ni catalyst. For this purpose, a new set of parameter estimates were determined using kinetic data collected experimentally on this catalyst. Despite its

lower activity, the promoted mono-metallic catalyst showed a solid and stable performance during 330 hours of operation. This suggests that the mono-metallic catalyst is a more promising candidate for industrial applications.

4 Reactor development for decentralized methanation reaction

The compact size along with enhanced heat and mass transfer characteristics of microstructured reactors proposes them as attractive candidates for performing exothermic reactions in decentralized applications. Nonetheless, the assumption of prevailing isothermal conditions is not necessarily fulfilled in microstructured reactors for a reaction like methanation with very fast kinetics.

The PhD project of Michael Belimov was dedicated to the development of a novel microstructured packed bed reactor for the methanation of CO and CO_2 based on specifications prescribed in the MINERVE project. Two reactor prototypes with cooling structure parallel to the catalyst bed were developed [24]. The results of the comprehensive experimental work of Belimov et al. on the first prototype are reported in [205]. The prototype consisted basically of a co-feed of coolant and reactive gases. The tested cooling media were air, steam, and water. They indicated that water entering the cooling zone at the inlet of the reactor led to a reaction blow-out, when the overall heat capacity was reaching the required value. Additional heating cartridges were necessary in order to stabilize the reaction. Thorough investigations led to the second prototype [224], which is examined in the current work. Process analysis is provided with a scale-up of this prototype in [225].

This study engaged with detailed experimental and numerical investigations on the second reactor prototype [224]. Evaporation of pressurized water was the selected cooling mechanism. Evaporation is a highly attractive cooling mechanism due to the high heat transfer coefficient during evaporation and the capability of the fluid to carry substantial quantities of energy through phase change compared to single-phase cooling. Two different Ni-based catalysts were tested and the performance of the reactor under different modes of operation such as start-up and steady-state and varied load and feed composition was analyzed. To assess the reactor behavior, the supply of pressurized water to the cooling structures with varied pressure and in different amounts and distributions between the two inlets of this prototype was investigated. Finally, step changes in the reactor throughput and composition were induced in order to assess the reactor's degree

of stability and response time under transient operating conditions.
The second part of this chapter targets to identify the description of the utilized fixed bed heat-exchanger reactor by taking the essential involving effects into account. For this purpose, a cascade of perfectly mixed CSTRs was implemented for developing a heterogeneous (i.e, considering internal pore diffusion in catalyst) cell model in Matlab®. The modelling results are compared with the experimental data in order to assess the degree of reliability of the model regarding predicting the temperature profile and the product composition.

4.1 Experimental methodology

4.1.1 Microstructured reactor with internal cooling structure

The general reactor concept used in this work is shown in [205, 224] and is illustrated in Fig. 4.1. The microstructured reactor prototype 2 is constructed from austenitic high temperature-resistant alloy (Nicrofer® 3220) to guaranty the reactor endurance in carburizing, oxidizing, and reducing conditions. The reactor prototype has two parallel reaction slits with a length of 100 mm, width of 50 mm and height of 2 mm. The optimization point in contrast to prototype 1 (see [205]) lies in the refined cooling structure. The cooling channels constructed parallel to the catalytic bed comprise 69 rectangular channels of 500 × 500 µm identical to prototype 1. However, in the second prototype, two coolant inlets and one common coolant outlet were constructed. The added second inlet aims to increase the flexibility and potential regarding coolant adjustment. It also helps to cool the hot spot local and adjust the coolant flow rate relative to its position.
In addition, in this prototype, the coolant redirects several times in a serpentine-shaped structure for better fluid distribution. This redirection of the flow helps not only to increase the heat transfer efficiency, but is also in particular advantageous for the evaporative cooling mechanism and the delocalization of the hot spot.
As explained in [24], in between the reaction chambers five holes were manufactured for insertion of heating cartridges. Each heating cartridge was controlled via an adjacent thermocouple, placed in a hole with a diameter of 1 mm. The thermocouples are assigned to **positions 1 to 5**, as depicted in Fig. 4.1. The main task of the heating cartridges is preheating the reactor to the reaction temperature and enabling an in-situ catalyst reduction via a defined temperature program (see Sec. 4.1.3). The symmetrical configuration of the reactor with a cooling channels on the outer wall grants the assumption that ther-

mocouples inserted along the reaction axis measure the maximum temperature in the catalyst bed. This assumption was cross-checked by inserting a K-type thermocouple directly inside the catalyst bed through the reactants inlet (see Sec. 4.2.1). In order to minimize heat losses to the environment, the reactor was placed in an aluminum box filled in with Microtherm Free flow® microporous insulation granules.

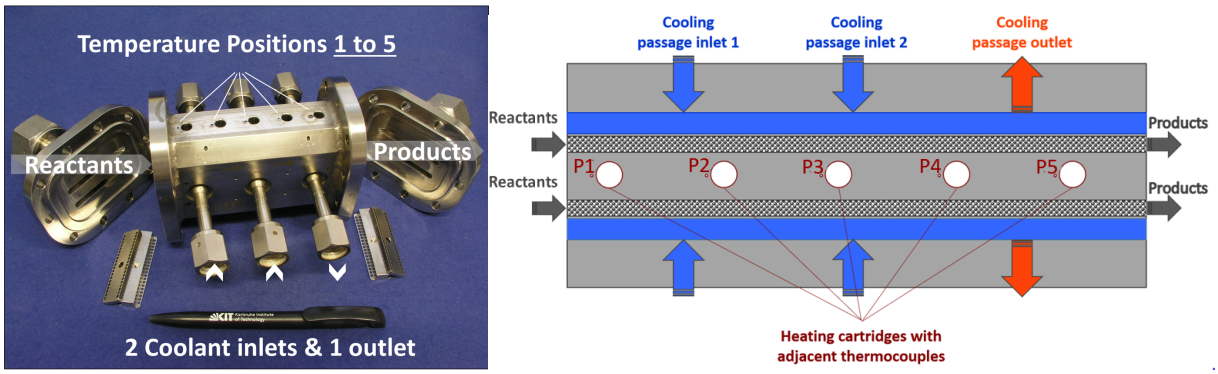

Figure 4.1: Left: The second microstructured reactor prototype with two cooling inlets and one common outlet, right: Schematic cross-sectional view of the reactor

4.1.2 Experimental setup for evaporative cooling methanation

The flow chart of the test rig for methanation experiments with integrated evaporation cooling is shown in Fig. 4.2. The setup can be divided into 4 sections: I. gas supply, II. the microstructured reactor, III. analytics, and IV. the cooling facilities.

I. **Gas supply:** The flows of the gases CO_2, H_2 and N_2 were regulated by mass flow controllers (MKS Instruments). The reactants were preheated before entering the reactor to 300 °C via heating pipelines. The pipes leading the products to the gas chromatograph (GC) were set to 200 °C to avoid water condensation.

II. **Microstructured reactor:** The catalyst inside the reactor was fixed via glass wool together with a perforated metal plate which allows homogeneous flow distribution in the reaction passage. Pressure regulation was done using a Flow-Serve® needle valve. The pressure drop in the bed was measured by means of a pressure difference sensor. The temperature of the reactants at the catalytic bed outlet was measured using a thermocouple inserted in the reactor outlet flange. In addition, a thermocouple measured the temperature directly inside the catalyst bed, inserted through the inlet flange.

III. **Analytics:** The product gas was injected into an online GC from Agilent 6890, equipped with two columns and two detectors; HP-Plot Q and HP-Molesieve. The concentration determination in the GC was done via two detectors; a thermal conductivity detector (TCD) for H_2, N_2 and H_2O analysis and a flame ionization detector (FID) equipped with a Ni catalyst cell for precise CO_2, CO, and CH_4 concentration determination. The data from the online GC was used to calculate CO_2 conversion, selectivity to CH_4 as well as CH_4 yield. A LabView program was applied for recording all the temperature and pressure data continuously throughout the operation.

IV. **Cooling facilities:** Two HPLC pumps from Knauer K-1800 fed the water separately to the cooling passage one and two. The pressure on the coolant side was maintained using a Swagelok back-pressure regulator, a double-ended Swagelok expansion cylinder together with supplying small amounts of N_2 after condensation of the generated steam. The back-pressure regulator cared for a constant pressure at its own inlet (before the device itself) and when the pressure on the cooling channel streamline surpassed that of the setpoint, the excessive flow was released throughout the valve and directed toward the exhaust. The temperature of the cooling water before entering the reactor was set to slightly below its boiling point (2 to 5 K) at the desired pressure. For preheating the water, two sets of micro heat-exchangers built at IMVT with 15 heating cartridges (225 W each), followed by heated pipes were installed. The coolant temperature at the inlet and outlet of the three cooling channels was controlled using thermocouples placed directly inside the inlet or outlet. The generated steam was condensed in a double tube heat exchanger with cold water flowing in the outer tube. The expansion cylinder was emptied between experiments from the condensed and collected water.

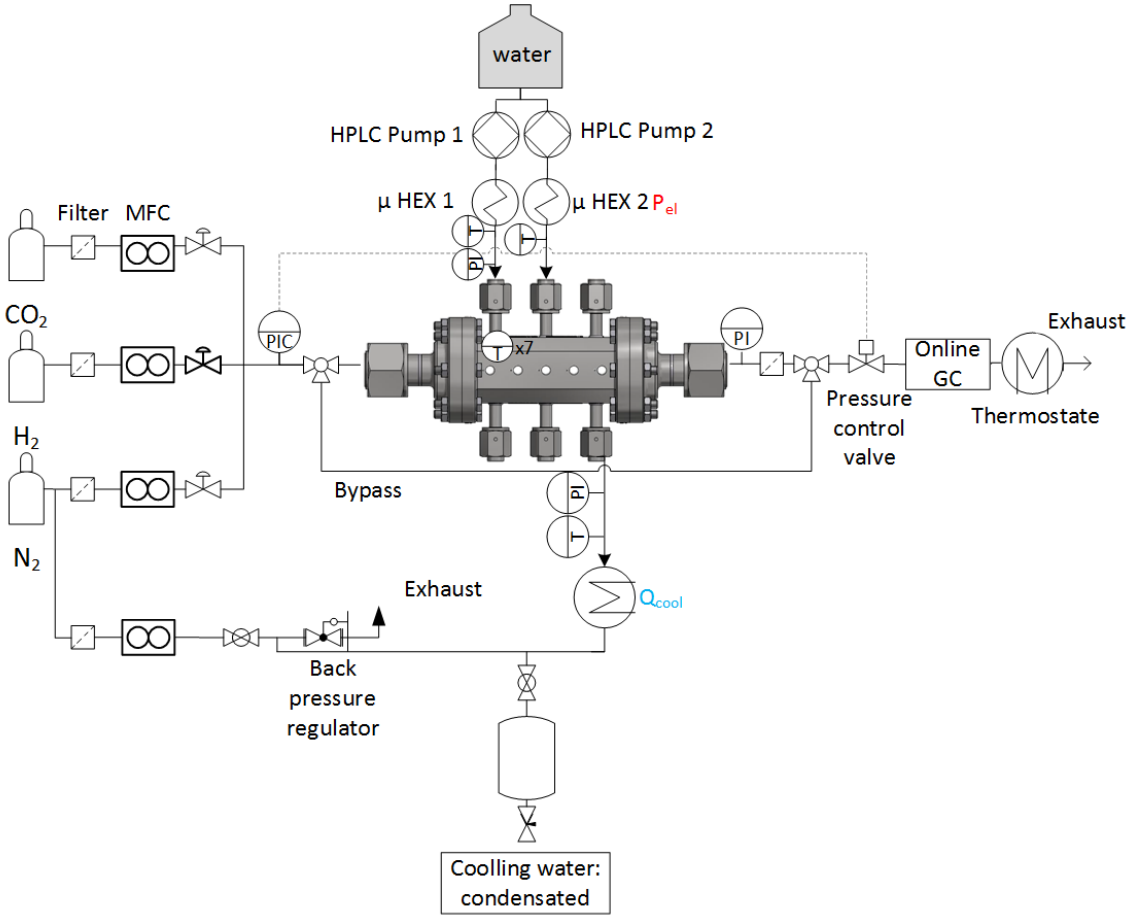

Figure 4.2: Schematic drawing of the evaporation-cooling methanation test rig

4.1.3 Experimental procedure

In all experiments, the reactor was filled with 5 g of catalyst in the particle size of 400-500 µm mixed with 22 g washed, dried and fractioned silicon carbide in 300-400 µm fraction. In order to assure homogeneous distribution of the catalyst and inert SiC while filling the powder mixture in the reactor, the catalyst and SiC were divided into five equally weighted portions and mixed together carefully. The mixed fractions were filled in the reactor successively in order to avoid segregation of the particles due to their different physical properties (e.g. density and particle size). The detailed reactor performance investigations were conducted on the promoted mono-metallic Ni catalyst. In a complementary step, the Ni_3Fe catalyst was filled in the reactor to check for possible changes in the reactor performance provoked by different catalyst activity.
The two catalyst systems were provided in oxidized form and therefore, the first step is the catalyst reduction. The Ni mono-metallic catalyst was reduced online by heating up

to 450 °C with a temperature ramp of 2 K min^{-1} under a mixture of 10% H_2 and N_2 (rest). At 450 °C, the flow was switched to pure H_2 and kept for five more hours. When the reduction procedure was completed, the reactor temperature was set to 300 °C and the reactor was flushed with 1 l min^{-1} (STP) of a mixture of N_2:H_2 (= 1:1). This temperature and gas mixture was preserved in between the experiments and during standby in order to prevent the catalyst from oxidation. The reduction procedure of the Ni_3Fe catalyst can be found in Cha. 3, Sec. 3.1.3.

The reaction was always initiated at 300 °C in the absence of cooling water. The first step was adjusting the flow rate of N_2 which was equal to 5 vol. % in all experimental runs. N_2 acts as an internal standard for product flow rate calculation (see Cha. 3, Sec. 3.2.1). In the next step, the H_2 flow rate was increased gradually until reaching the desired set-point. With inducing CO_2 in the gas mixture the reaction initiated immediately. The water pumps were only started after surpassing a temperature of 370 °C in the hot spot. The range of the studied experimental parameters are demonstrated in Tab. 4.1. The reactor was designed for a maximum absolute pressure of 6 bar (at 450 °C) in the reaction zone. Therefore, the reaction pressure was kept constant at this value during all measurements. The cooling channels were designed for higher pressure, thus the water pressure was raised up to 20 bar.

Table 4.1: Investigated range of operational conditions in the evaporation cooling reactor

Experimental parameter	Studied range
Volumetric flow rate (STP)[l min^{-1}]	10-24
H_2/CO_2 ratio [-]	3-6
Water pressure [bar]	5-20
Water mass flow rate [g min^{-1}]	2.5-15

The reference measurement point had operation parameters of H_2/CO_2 ratio of 4, volumetric flow rate of 21.1 l min^{-1} (STP) and was cooled with water pressure of 10 bar (pre-heated to 180 °C). This reference point was used to identify a possible catalyst deactivation during the experiments. In addition, after under-stoichiometric tests, a reference point was carried out to detect if any irreversible changes have been taken place on the catalyst.

Each experiment was carried out for a minimum of two hours and the product compositi-

on and temperature profiles are reported by averaging the collected data from 30 minutes after reaction start. In sets of experiments, step changes in the feed throughput with constant feed composition as well as step changes in the feed composition at constant flow were executed and the reactor response time with regard to temperature profile development and product composition was monitored.

Considerations on experimental error margins:

Several error sources can affect the laboratory results. For example, the presence of small fractions of vapor or water droplets can affect the start-up behavior of the reactor. The time required for reaction ignition as well as the position of the hot spot can be different when operating the reactor continuously under varied measurement points. This observation was made when repeating a certain experiment for example after a long pause (over weekend) in comparison to running it directly after another test.

For a methanation reactor operating in thermodynamic regime, among other factors, the equilibrium conversion is strongly dependent on temperature level (see Cha. 2, Sec. 2.1). Modest variations in dosed gas ratio alter the product composition. The calibration margins for each mass flow controller were about ± 5% (relative error). This rather high margin was unavoidable due to the wide range of tested flow rates. To study the expected outcome of such a deviation on the product composition, a thermodynamic analysis was performed for three worst-case scenarios corresponding to the reference composition: 1. CO_2 is under-dosed by 5% (CO_2 = 18.05%, H_2/CO_2 = 4.26), 2. CO_2 is over-dosed by 5% (CO_2 = 19.95%, H_2/CO_2 = 3.76) and 3. CO_2 is correctly dosed (CO_2 = 19%, H_2/CO_2 = 4). For all three cases N_2 share was kept constant at 5%.

Fig. 4.3 depicts the bandwidth of CO_2 conversion and CH_4 selectivity in the temperature window of 350-450 °C, which corresponds to the steady-temperature range investigated experimentally. For the case of under-dosing CO_2, CO_2 conversion rises from 95% up to 99% at 350 °C and from 88% to 92% at 450 °C. Overdosing CO_2 by 5% leads to a drop of CO_2 conversion to 90.2% at 350 °C and 83.8% at 450 °C. Fig. 4.3 right shows that methane selectivity is much less sensitive towards CO_2 dosing errors and varies only between 100 to 99.4%.

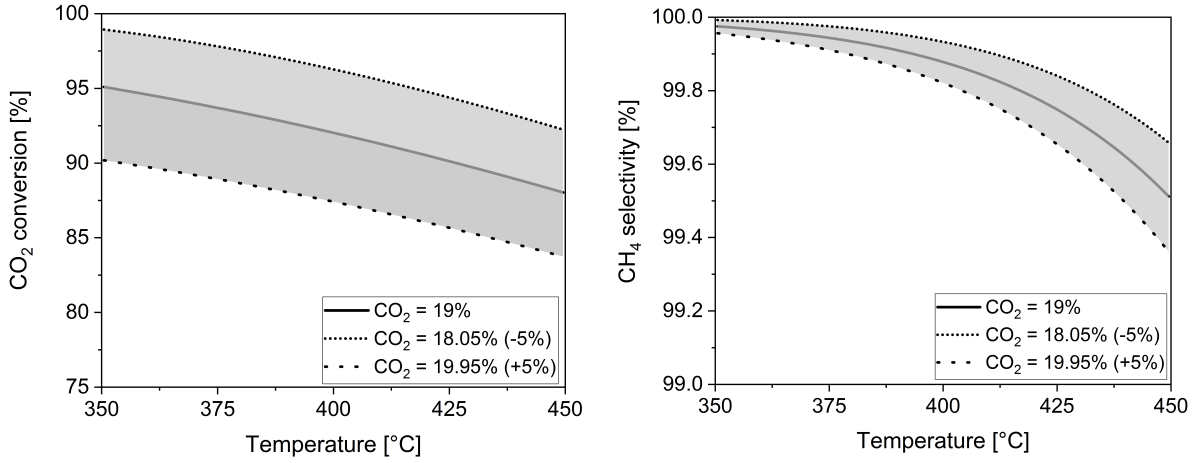

Figure 4.3: Bandwidth of CO_2 conversion (left) and CH_4 selectivity (right) for a 5% deviation of CO_2 dosage in the temperature window of 350-450 °C: 1. CO_2 is under-dosed by 5% (CO_2 = 18.05%, H_2/CO_2 = 4.26), 2. CO_2 is over-dosed by 5% (CO_2 = 19.95%, H_2/CO_2 = 3.76), and 3. CO_2 is correctly dosed (CO_2 = 19%, H_2/CO_2 = 4). Isothermal conditions and infinitely fast kinetics are assumed.

4.2 Results and discussion: experimental

4.2.1 Reactor start-up

The start-up behavior of the reactor and its response time to water coolant dosage was evaluated at the reference measurement point (see Sec. 4.1, $H_2/CO_2 = 4$, $p_w = 10$ bar). In Fig. 4.4, the temperature development along the catalyst bed axis during reactor start-up and until reaching steady-state conditions is presented.

After 30 seconds of dosing CO_2, the temperature starts to rise in the second temperature measurement position, with a clear tendency to form a hot spot in this position only after three minutes. The rate of temperature rise in position 2 is about $10\,\mathrm{K\,min^{-1}}$. This position has the highest growth rate. The slowest temperature increase rate is at position 5 with only $2\,\mathrm{K\,min^{-1}}$. The temperature growth in position 1 is rather different. The heating cartridge in this position continues to consume electricity for around 10 minutes after reaction initiation. After this, the temperature starts to increase in position 1 and reaches an identical value to position 2 within 20 minutes. The temperatures in positions 3 to 5 develop very slowly in comparison. Nevertheless, this is a continuous trend and tends to dwindle the temperature gradient along the bed.

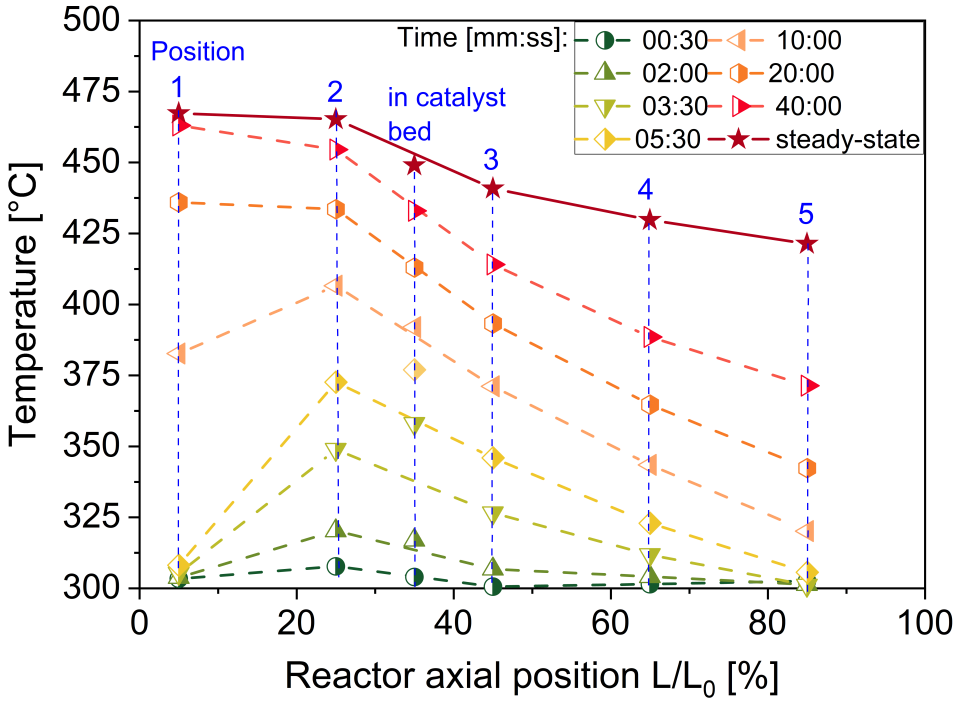

Figure 4.4: Reactor start-up behavior ($\dot{V}_{tot}$ = 21.1 l min^{-1}, H_2/ CO_2 = 4, p_w = 10 bar, $\dot{m}_{w,1}$ = 9.5 g/min and $\dot{m}_{w,2}$ = 1.0 g/min)

The HPLC water pumps were started after about 8 minutes of reaction run time and surpassing 370 °C at the hot spot (see Sec. 4.1.3). In order to avoid reaction blow-out the water flow rates were first set to small values (1-3 g/min) and were increased gradually to keep the hot spot temperature below the desired value of 470 °C. After about 20 minutes, the temperature profile approaches 'quasi steady-state' conditions. Slight manual adjustments in the water flow rate (0.5-1 g/min) were necessary in order to retain the temperature stable and avoid temperature swings above 10 to 15 °C in each position. Observing a continuous drop/rise in a position called for this readjustment in the respective water flow to stabilize the temperature. The steady-state profile in Fig. 4.4 is reached with adjusting 9.5 g/min water in water inlet 1 and 1.0 g/min in water inlet 2. The temperature difference between the first and fifth position in the steady-state condition is about 45 K, and between positions 1 and 3 is about 20 K. Hence, with careful water flow rates control in pressurized evaporation cooling, the typical sharp methanation hot spot is mitigated and a moderate temperature profile can be established along the catalytic bed. Most importantly, the difficulties experienced by Belimov et al. during evaporation cooling in reactor prototype 1 could be overcome in reactor prototype 2: no reaction blow-out or runaway are encountered and the reactor runs in steady-state

without heating.

In order to assure that the temperatures measured from the central metal block are not delayed by the heat conductivity characteristics of the catalyst bed and the high heat capacity of the metal, a thermocouple was inserted directly inside the catalyst bed between positions 2 and 3. Fig. 4.5 left shows the development of the temperature in positions 2 and 3 and in the catalyst bed in the first 10 minutes of reaction. Similar to observations of Belimov et al. [205], the temperature in the catalyst bed in the first 5 minutes is slightly higher than positions 2 and 3. However, the maximum temperature difference is less than 25 K and thus less than the 80 K reported by Belimov et al. under CO/CO_2 conditions. The presence of CO seems to accelerate the hot spot formation. The temperature growth rate in the catalyst bed in the first 5 minutes is 16.8 K min^{-1}, whereas this value for position 2 and 3 is 14.5 K min^{-1}, and 9.2 K min^{-1}, respectively. At the 6^{th} minute, the temperature in position 2 and the catalyst bed overlap, and shortly after the catalyst bed, temperature drops and establishes perfectly in between the temperatures of positions 2 and 3. The temperature growth rate diminishes considerably after dosing coolant water (TOS = 10 min) and reaches 3.0 K min^{-1} for position 2 and the catalyst bed and 2.0 K min^{-1} for position 3.

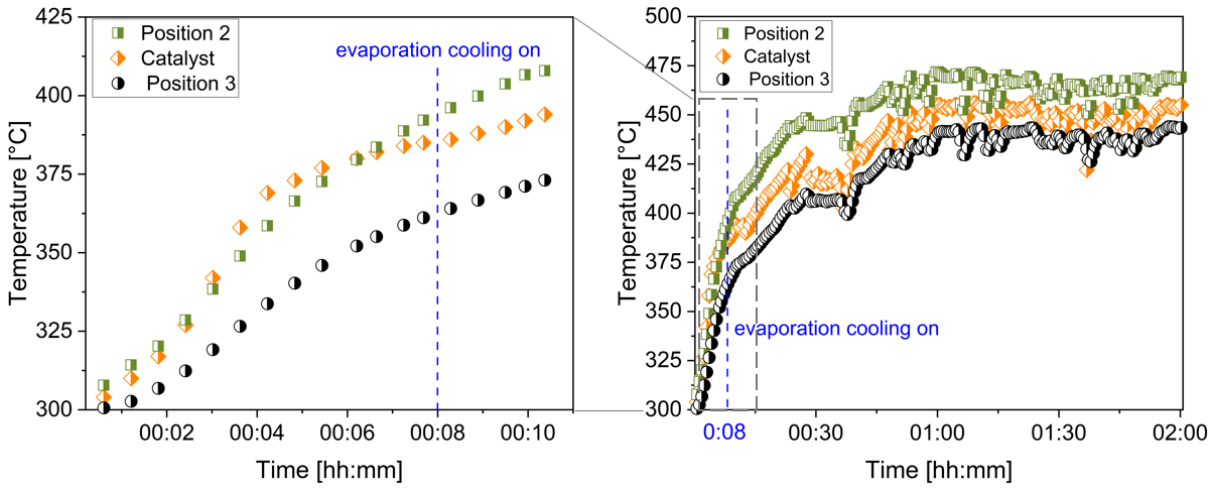

Figure 4.5: Comparison of the temperature development in the catalyst bed and in the metal bulk. Left: The first 10 min of reactor start-up. Right: Two hours of operation ($\dot{V}_{tot}$ = 21.1 l min^{-1}, H_2/CO_2 = 4, p_w = 10 bar, $\dot{m}_{w,1}$ = 9.5 g/min and $\dot{m}_{w,2}$ = 1.0 g/min).

Fig. 4.5 right depicts the temperature development in the three aforementioned positions during two hours of run time. The dynamic nature of the evaporation cooling system is clearly resolved via the scattered temperature measurements throughout time. The

abrupt drops and rises in the temperature may be also a result of HPLC pump pulsations. Additionally, the intensity of these fluctuations depends on operational parameters, e.g. the coolant inlet temperature (i.e. the temperature difference between the reaction side and the cooling side). This issue is discussed in detail in Sec. 4.2.3.

4.2.2 Temperature profile optimization

In the following section, the flexibility regarding temperature regulation and the influence of the water flow rates in each cooling passage on the temperature profile is discussed. The pressure of the water was kept at 10 bar, and the temperature of the water at the reactor inlet was adjusted to 175-180 °C, accordingly. The reactants flow rate and composition were kept at reference conditions (see Sec. 4.1.3). The relevant information which will be discussed in detail in the following is: The cooling passage 1 controls the temperature in positions 1 and 2, further called **front** reactor part. Whereas cooling passage 2 affects temperatures in positions 3 to 5, further called **rear** reactor part.

Temperature manipulation by shifting water flow from water inlet 1 to inlet 2:
From experiment P2-test 1 to experiment P2-test 4, the cooling intensity was gradually shifted from the first to the second water inlet. Tab. 4.2 presents the amount and distribution of water in each cooling channel, the temperature of the steam in the reactor outlet, as well as CO_2 conversion, CH_4 selectivity and yield of CH_4 for the mentioned experiments. In this set of experiments, the temperature of the hot spot at position 2 was constant at 440 °C and temperature in positions 3 to 5 varied (Fig. 4.6 left).
As Fig. 4.6 left indicates, none of the temperature profiles come close to isothermal conditions. In experiment P2-test 1, the coolant was mainly dosed in the cooling inlet 1, and the water flow rate in passage two was set to a minimum value of 1 g min^{-1}. It was observed that by complete elimination of the second pump, the hot spot temperature escalates. Therefore, during all measurements, both pumps were turned on, and the flow of pump 2 was further set to a minimum of $\sim$ 0.5 g min^{-1}.

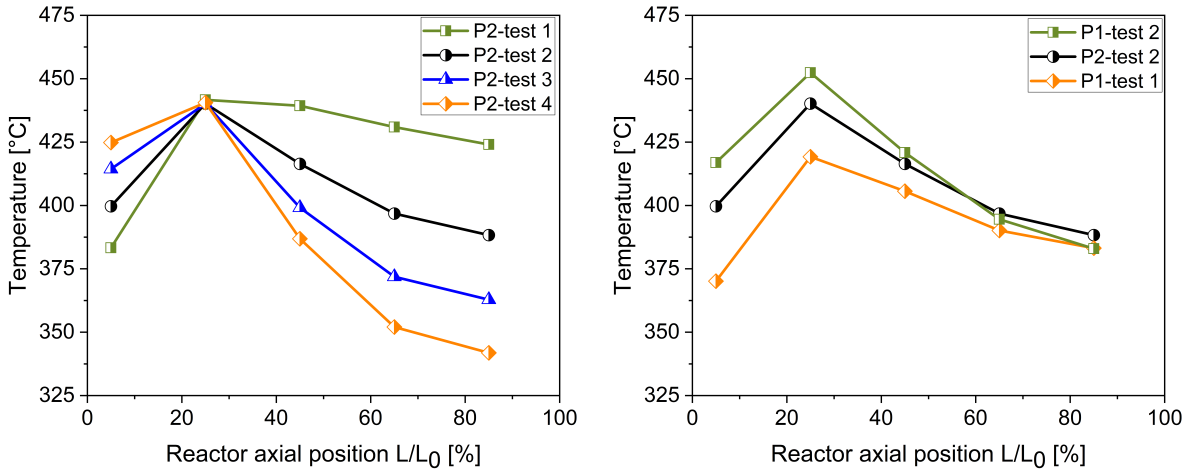

Figure 4.6: Steady-state temperature profiles. Left: rear reactor part experiment, right: front reactor part experiment ($\dot{V}_{tot}$ = 21.1 l min^{-1}, H_2/ CO_2 = 4, p_w = 10 bar, water flow rates according to Tab. 4.2).

Although the total mass flow rate of water was slightly increasing in the P2-test series, it is obvious from experiment P2-test 2, P2-test 3, and P2-test 4 that increasing the coolant in passage 2 and simultaneous decreasing the water flow rate in passage 1 retains the hot spot at the same level. This leads to the conclusion that the water mass flow at inlet 1 has almost no impact on controlling the hot spot at position 2. This is similar to observations of Belimov et al. [205], which conclude that this is most probably due to a heat transfer limitation by the wall thickness separating cooling media and catalyst. The strategy to shift the water flow to inlet 2 is, however, at the expense of increasing the temperature gradient between the front and rear reactor parts.

An interesting observation is that, in experiment P2-test 1, where the coolant flow in the second pump was set to only 1 g min^{-1}, the temperature difference between position 2 and 5 is only 16 K. I.e., when water is applied only in the first 20% of the reactor length, the temperature in the rest of the reactor remains almost constant. This suggests that the water mainly evaporates in the front reactor part, as the reaction is close to equilibrium in all cases at the reactor outlet. This in turn implies that a part of the reactor rear is not used for the reaction. One can assume that the good heat conductivity characteristics of the central metal block also play an important role. The high temperature in the front part of the metal block compared to the rear part results in considerable heat flux. Thus, the metal block compensates for the poor heat conduction and axial gradient in the packed bed.

Table 4.2: Temperature profile optimization experiments: the coolant amount, outlet temperature, reactor performance ($\dot{V}_{tot}$ = 21.1 l min^{-1}, H_2/ CO_2 = 4, p_w = 10 bar)

Experiment label	$\dot{m}_{w,1}$ [g min^{-1}]	$\dot{m}_{w,2}$ [g min^{-1}]	$\Sigma\dot{m}_w$ [g min^{-1}]	$T_{w,outlet}$ [°C]	X_{CO_2} [-]	S_{CH_4} [-]	Y_{CH_4} [-]
P2-test 1	10.5	1.0	11.5	280	92.7%	99.8%	92.6%
P2-test 2	6.2	6.5	12.7	261	93%	99.9%	92.9%
P2-test 3	2.8	10.2	13.0	255	92.3%	99.9%	92.2%
P2-test 4	0.3	12.7	13.0	238	91.0%	99.9%	90.8%
P1-test 1	7.0	6.5	13.5	264	92.3%	99.9%	92.2%
P1-test 2	3.0	8.9	12.0	255	92.3%	99.9%	92.2%

Temperature manipulation of the hot spot:

In this set of experiments, the hot spot temperature was manipulated as far as possible from heat transfer limitation point of view by keeping the flow rate of water at inlet 2 and thus the temperature in the reactor rear near constant. Fig. 4.6 right and Tab. 4.2 exhibit the temperature profile results, water flow rates and product composition, respectively.

During experiment P1-test 1, the coolant amount in passage 2 was kept near the same value as in P2-test 2 and the water flow rate in passage 1 was increased (0.8 g min^{-1}). This increase of the coolant flow led to a 30 K temperature drop in position 1 and 20 K in position 2. The temperature in position 3 also diminished about 10 K, which again shows that coolant in passage 1 has an imprint on the rear section too. Thus, varying the coolant in one passage, without any effect on other reactor parts is impossible.

The lowest possible hot spot temperature, i.e. without blowing out the reaction was 410 °C and was obtained at P1-test 1. At this point, it must be emphasized that this limit is only valid for the current operational parameters. Enhancing the water pressure, i.e., reduction of the temperature gradient between coolant and bed, increasing the load, i.e., increasing the released reaction heat or changing the feed composition would influence the operational limit and can shift this margin to lower or higher temperatures.

The highest hot spot temperature in this experiment series was 455 °C (P1-test 2). In both series it is obvious that the reactor inlet temperature (position 1) is highly responsive to changes in water flow rate and only 1.0 g min^{-1} increase or decrease can create up to 20 K temperature shift.

Remarks on conversion and selectivity by manipulation of reactor temperature:
In a polytropic reactor for CO_2 methanation operating under thermodynamic control, the temperature rise in the inlet supports enhanced reaction rates, whereas the final conversion is dependent on the temperature in the rear part. Governed by thermodynamics, somewhat lower temperatures in the rear section are desired.
In the experiments P2-test 1 to P2-test 4, the conversion lies between 92 to 93%, and having in mind the experimental error, experiment P2-test 4 has the lowest conversion of 91%. Experimental runs of P1-test 1, P1-test 2, and P2-test 2, all display the same conversion degree despite hot spot temperature difference. The lowest conversion of P2-test 4 suggests that providing a high temperature only in the front part and a sharp decrease in the rear part is not optimal in the trade-off between reaction rate and thermodynamics. Comparison of P2-test 4 with other temperature profiles implies that position 3 (or perhaps even position 4) affects this balance. If the temperature in position 3 is above $\sim 400\,°C$, the conversion seems to better approach the thermodynamics. It should be emphasized that this theory could be better resolved via simulations and in reality, it is possible that multiple involving effects lead to a similar conversion at the outlet.
The methane selectivity for all the experimental runs was above 99.8% and does not require any further discussion.
As all points reach high conversion and selectivity, the amount and temperature of the generated steam for electrolysis in the scope of a PtG scheme are interesting. Among all, P2-test 1 has the highest steam temperature, which can be correlated with a lower amount of water dosed, especially in the second passage. However, due to the minimization of the water coolant in channel 2, the possibility of reaction runaway in this operating point imposes some technical challenges. The second highest coolant temperature is found in P1-test 1 with 264 °C. This operational point is also not accredited due to operating on the low-temperature limit of the reactor and was evaluated unstable and prone to reaction blow-out. Therefore, P2-test 2 is selected as the optimal temperature profile with a steam temperature of 261 °C, high CO_2 conversion, and a stable temperature profile.

4.2.3 Coolant pressure variation

The temperature difference between the cooling medium and the reaction chamber is an important factor that can lead to instabilities in the reaction zone if it is set too high. Three pressures of 5, 10 and 20 bar (corresponding to 150 °C, 180 °C and 210 °C) were tested for the water supply. The aim was to reproduce a comparable temperature profile as the one generated in experiment P2-test 2 (see Sec. 4.2.2) by means of water flow rate

adjustment. Fig. 4.7 presents the steady-state temperature profile for these three water pressures. Tab. 4.3 summarizes the water flow rates, steam temperature, and reactor performance. It is observed that for all three pressures, it is very likely to achieve a steady-state operation with an identical CO_2 conversion, see Tab. 4.3. The amount of dosed coolant needed to be reduced by about 1.0 g min^{-1} for every 30 K decrease in the water boiling temperature.

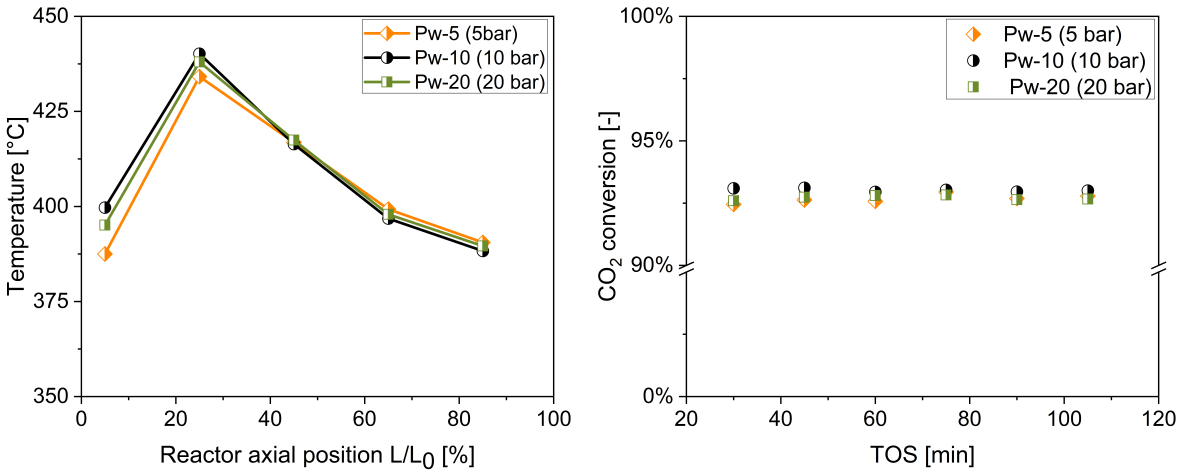

Figure 4.7: Left: Steady-state temperature profiles in varied water pressure. Right: CO_2 conversion for 120 minutes TOS for varied water pressure ($\dot{V}_{tot}$ = 21.1 l min^{-1}, H_2/ CO_2 = 4, water mass flow rates according to Tab. 4.3)

In Sec. 4.2.1 it is mentioned that after reaching steady-state conditions, slight changes in the coolant flow rate are required in order to keep the temperature in the desired range. These adjustments were done manually. In practice, it was confirmed that the intensity of necessary re-adjustments due to temperature instability is correlated to the applied cooling pressure. Fig. 4.8 a-c reports all saved temperature profiles when applying water under 5, 10 and 20 bar, respectively. The profiles were collected after reaching 'quasi steady-state' conditions. The parameter of time is plotted on the x-axis and the measured temperature at each position is plotted separately. This would help to identify whether the fluctuations follow a certain trend with time. It is evident that the most unstable operation belongs to the experiment with 5 bar evaporation pressure. At this pressure, the temperature fluctuates about 5 °C within only 1-2 minutes. This is a continuous trend and no stabilization can be detected throughout the time. The total range of temperature fluctuations at this pressure is about 20 K. The amount of dosed water coolant noted in Tab. 4.3 is the mean dosed water flow rate, plus and minus the range that proved

necessary to counteract the temperature changes.

By increasing the pressure to 10 bar, the fluctuations reduce considerably and temperature at positions 1, 4, and 5 is reasonably constant. The highest fluctuations belong to positions 2 and 3, with a maximum ΔT of 2 °C.

The most stable operation is observed at a coolant pressure of 20 bar, which also required only minor additional adjustments in the coolant (see Tab. 4.3). At this pressure, no abrupt changes at any axial position in temperature are observable. Such behavior is obviously due to the lower temperature difference between the reaction and the coolant and emphasizes the importance of pressurizing the water during evaporation cooling. Base on these observations, the temperature fluctuations due to the ignition/quenching phenomena can be dismissed.

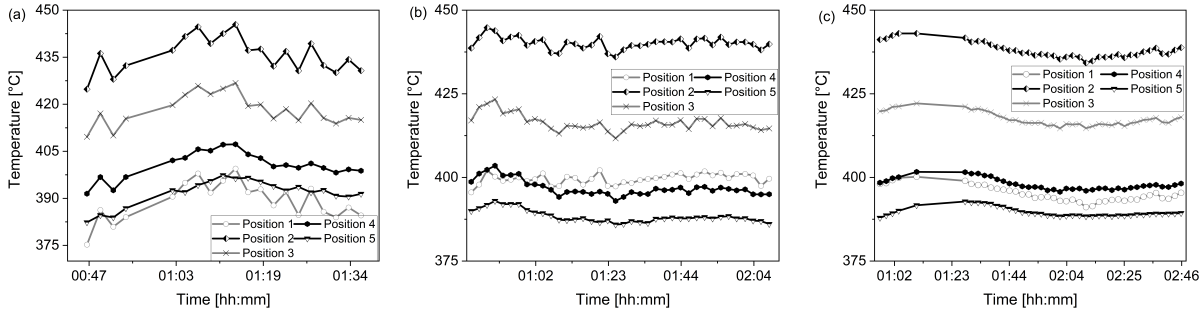

Figure 4.8: a - c: Influence of the water pressure on temperature profile fluctuation. a: 5 bar, b: 10 bar, c: 20 bar ($\dot{V}_{tot}$ = 21.1 l min^{-1}, H_2/ CO_2 = 4, water mass flow rates according to Tab. 4.3).

After all, Fig. 4.7 right indicates that although operating under relatively colder water can impose some practical complexity regarding achieving a stable temperature profile in the reactor, the product has a very stable quality over the complete run-time of 120 minutes for all three coolant pressures. These results are in coherence with the conclusions made in Sec. 4.2.2.

Table 4.3: Water pressure variation experiment: the coolant amount and outlet temperature, reactor performance ($\dot{V}_{tot}$ = 21.1 l min^{-1}, H_2/ CO_2 = 4)

Experiment label	$\dot{m}_{w,1}$ [g min^{-1}]	$\dot{m}_{w,2}$ [g min^{-1}]	$\Sigma\dot{m}_w$ [g min^{-1}]	$T_{w,outlet}$ [°C]	X_{CO_2} [-]	S_{CH_4} [-]	Y_{CH_4} [-]
Pw-5	5.9 ± 0.5	5.7 ± 0.5	11.6	258	92.7%	99.9%	92.6%
Pw-10	6.2 ± 0.2	6.5 ± 0.2	12.7	261	93%	99.9%	92.9%
Pw-20	6.7	7.0 ± 0.1	13.7	271	92.6%	99.9%	92.4%

4.2.4 Load variation

The vol. flow rate of the reactants is varied between 10.6 to 23.7 l min^{-1} (STP), keeping the H_2/CO_2 ratio and the individual partial pressures constant. Tab. 4.4 also shows the dosed coolant in each passage, the temperature of the generated steam, and the conversion of CO_2 as well as the CH_4 selectivity. Fig. 4.9 left displays the steady state temperature profiles for the varied feed flow rate. None of the measurements were disturbed due to reaction blow-out or runaway. The steady-state temperature profiles demonstrated in Fig. 4.9 left confirm that the reactor performs stable in a wide range of throughput. These results prove the enhanced heat management capacity of evaporation cooling and its exceptional controllability compared to other cooling methods (air and steam) applied in the work done by Belimov et al. [205]. The only distinction between different temperature profiles is the shift to higher temperatures in position 1, when the feed flow rate is reduced. This shift may be a consequence of the prolonged residence time of the reactants in the reactor, i.e., near full conversion happens directly in the reactor inlet. Another plausible explanation is that the local cooling effect by the colder feed flow is smaller for a reduced feed flow rate.

Efficient temperature control requires a detailed study of the reaction start-up. During start-up and absence of coolant, the increased heat release at a higher feed flow rate promotes an increase of the hot spot and generates a large gradient along the reactor in a short time. Fig. 4.9 right shows temperature profiles after 4 minutes of dosing CO_2 for the different loads. At higher flow rates, the coolant potential during the start-up must be immediately concentrated in the first passage, while at lower flow rates both passages can be equally started for reaching temperature control. In addition, in lower feed flow rates, the hot spot moves gradually to the front and the coolant must be adapted accordingly. This information is critical during the reactor start-up and dictates the correct sequence

for applying the coolant in order to inhibit reaction blow-out (for low flow rates or partial loads) or runaway (for high flow rates, full load).

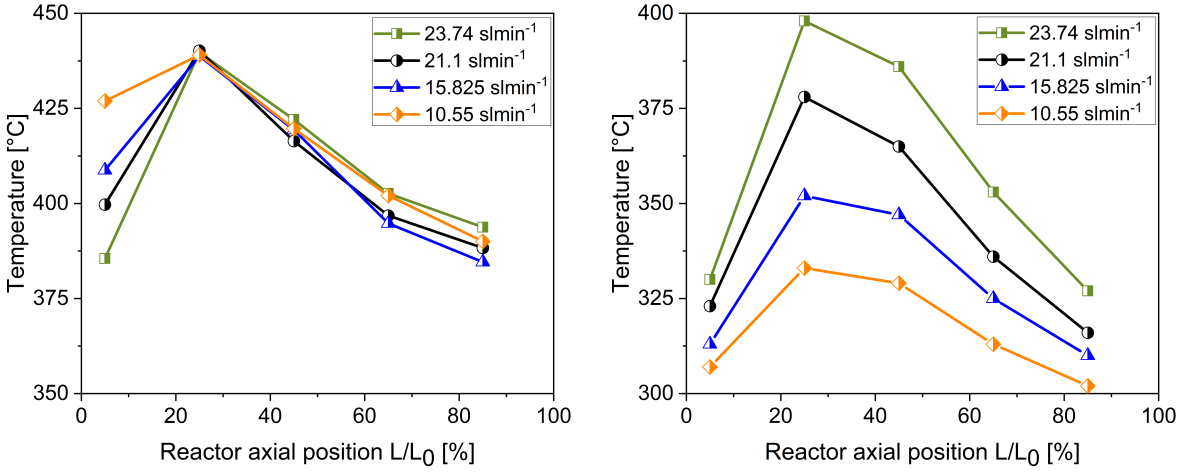

Figure 4.9: Load variation experiment: left: steady-state temperature profile, right: temperature profile after 4 minutes of reaction initiation (H_2/ CO_2 = 4, p_w = 10 bar)

The calculated released reaction heat for this throughput range is equal to 245 to 552 W. The removed heat through water temperature increase of 5 K and subsequent evaporation for the tested reactant flow rate range is about 91-495 W. Considering 30-50 W heat losses as measured by Belimov et al. [205], super-heating of the generated steam can be justified. The outlet temperature of the steam changes from 273 to 215 °C for various loads. The CO_2 conversion for the entire range changes between 92.6 % to 94.1 %. A clear but very modest dependency on throughput is observed, wherewith increasing the residence time in the reactor, more CO_2 is converted. Therefore, kinetics seem to slightly control the reactor performance. The selectivity to CH_4 formation is also constant and close to 100 %.

Table 4.4: Load variation experiment: the coolant amount and outlet temperature, reactor performance (H_2/ CO_2 = 4, p_w = 10 bar)

Throughput STP [l min $^{-1}$]	$\dot{m}_{w,1}$ [g min^{-1}]	$\dot{m}_{w,2}$ [g min^{-1}]	$\Sigma\dot{m}_w$ [g min^{-1}]	$T_{w,outlet}$ [°C]	X_{CO_2} [-]	S_{CH_4} [-]	Y_{CH_4} [-]
23.7	7.1	7.5	14.6	273	92.6%	99.8%	92.5%
21.1	6.2	6.5	12.7	261	93%	99.9%	92.9%
15.8	4.1	3.7	7.8	252	93.3%	99.9%	93.4%
10.6	1.0	1.7	2.7	215	94.1%	99.9%	94.1%

4.2.5 H_2:CO_2 ratio variation

Two scenarios were followed for studying the effect of H_2/CO_2 ratio variation. In the first scenario, the flow rate of CO_2 was kept constant (= 3 l min^{-1}) and the H_2 flow rate is changed in order to change the H_2/CO_2 ratio between 3 and 6. The second scenario was conducted in constant total flow rate (= 15.8 l min^{-1}) and altering the H_2 and CO_2 flow rates to meet the desired reactants ratio. For further details please refer to Tab. 4.5 and 4.6.

$\dot{V}_{CO_2}$ = const. (scenario 1):

Fig. 4.10 left displays the temperature profiles for the experiments with different H_2/CO_2 ratio in constant vol. flow rate of CO_2. No hint on potential limitations of the reactor to control the temperature in different feed compositions was observed. Only marginal temperature profile differences were measured while an increase in total water mass flow was required to control the reaction at an increasing H_2/CO_2 ratio due to increased conversion. In the opposite direction, i.e., by decreasing the H_2 flow rate, the CO_2 conversion diminishes and so does the released reaction heat. Increasing the stoichiometric ratio from 5 to 6 cannot increase the CO_2 conversion any further (already close to 100%) and the unconverted excess of H_2 works in the favour of heat removal. Therefore less water is needed at H_2/CO_2 = 6 and the steam temperature declines.

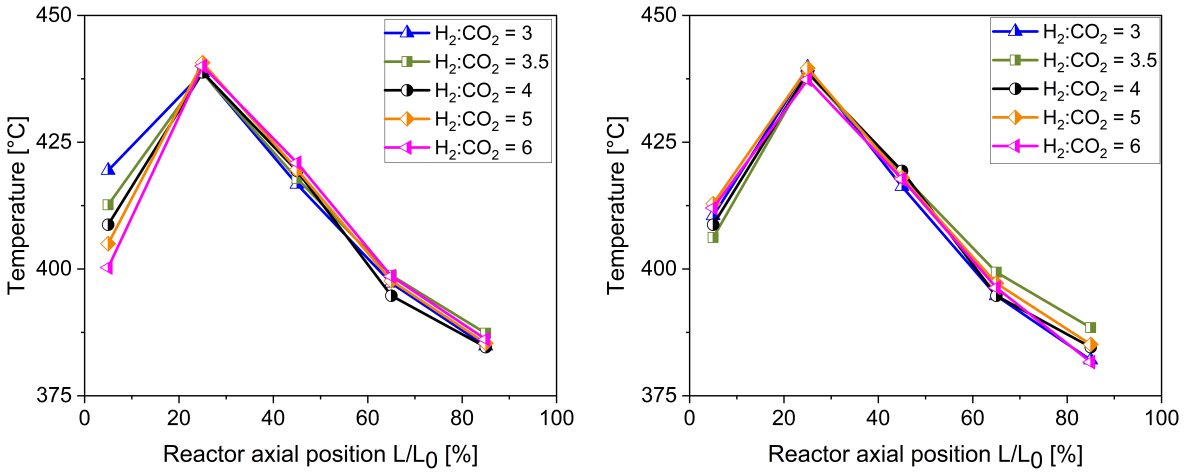

Figure 4.10: Steady-state temperature profiles in H_2/CO_2 ratio variation experiment, left: scenario 1 ($\dot{V}_{CO_2}$ = const. = 3 l min^{-1}), right: scenario 2 ($\dot{V}_{tot}$ = const. = 15.8 l min^{-1})

Table 4.5: The H_2/ CO_2 ratio variation experiment, scenario 1: coolant amount and outlet temperature, total volumetric flow rate and reactor performance ($\dot{V}_{CO_2}$ = const. = 3 l min^{-1}, p_w = 10 bar)

H_2/CO_2 ratio	$\dot{V}_{tot}$ [l min^{-1}]	$\dot{m}_{w,1}$ [g min^{-1}]	$\dot{m}_{w,2}$ [g min^{-1}]	$\Sigma\dot{m}_w$ [g min^{-1}]	$T_{w,outlet}$ [°C]	X_{CO_2} [-]	S_{CH_4} [-]	Y_{CH_4} [-]
3.0	12.7	1.9	2.5	4.4	228	74.4%	99.8%	74.2%
3.5	14.2	3.1	3.0	6.1	240	85.2%	99.8%	85.0%
4.0	15.8	4.1	3.7	7.8	252	93.3%	99.9%	93.1%
5.0	19	3.6	5.0	8.6	250	99.2%	100%	99.2%
6.0	22.2	3.0	5.1	8.1	245	99.7%	100%	99.7%

$\dot{V}_{tot}$ = const. (scenario 2):

Again almost identical temperature profiles were obtained in this series (Fig. 4.10 right). Regarding the applied coolant a different trend can be noticed for scenario 2 in contrast to scenario 1. In the case of keeping the total feed and hydrogen flow constant, the maximum heat release corresponds to the H_2/CO_2 ratio of 4. This is reflected by the maximum amount of cooling water demand in Tab. 4.6. By decreasing the H_2/CO_2 ratio, both the CO_2 conversion and the released heat drop, and therefore less water is demanded. In the opposite direction, the over-stoichiometric ratio increases the CO_2 conversion, but since less CO_2 is dosed, the overall released heat is lower and so less cooling is generated. The direct comparison of the steam temperature in the reactor outlet confirms this claim.

Table 4.6: The H_2/ CO_2 ratio variation experiment, scenario 2: the coolant amount and outlet temperature, CO_2 volumetric flow rate and reactor performance ($\dot{V}_{tot}$ = const. = 15.8 l min^{-1}, p_w = 10 bar)

H_2/CO_2 ratio	$\dot{V}_{CO_2}$ [l min^{-1}]	$\dot{m}_{w,1}$ [g min^{-1}]	$\dot{m}_{w,2}$ [g min^{-1}]	$\Sigma\dot{m}_w$ [g min^{-1}]	$T_{w,outlet}$ [°C]	X_{CO_2} [-]	S_{CH_4} [-]	Y_{CH_4} [-]
3.0	3.8	3.5	3.7	7.2	241	74.4%	99.8%	74.2%
3.5	3.3	3.8	3.6	7.4	250	84.6%	99.8%	84.5%
4.0	3	4.1	3.7	7.8	252	93.3%	99.9%	93.1%
5.0	2.5	2.5	4.0	6.5	240	99.5%	100%	99.5%
6.0	2.1	1.5	2.1	3.6	213	99.9%	100%	99.9%

4.2.6 Measures of reactor stability under transient operation

The solid performance of the reactor in a wide range of operational parameters was a motivation to go one step further and challenge the reactor performance under transient conditions. This aspect receives a great deal of attention with regard to the process scheme the reactor is designed for: dynamically operated PtG plants. Fixed-bed methanation reactors are in fact no good candidates for PtG projects. The heat transfer limitations in a fixed catalytic bed can create serious operational issues due to sudden temperature spark or reaction blow-out when exposed to load or feed composition instabilities.

Several literature studies are dedicated to modelling and simulation of different reactor types for methanation in dynamic operation [226–228]. For instance, dynamic simulations of Li et al. [229] showed that a cooled fixed bed reactor with material and thermal recycling requires up to 1 hour for re-stabilization and reaching steady-state conditions in case of imposing step changes of only 2 mol.% in the CO concentration in the feed. Lately, Fischer et al. [230] introduced a methodology for designing dynamically operated, load flexible wall-cooled fixed bed tubular reactors. In their approach, the most critical aspects for dynamic operation of a CO_2 methanation fixed bed reactor were already taken into account in the design stage.

Experimental work of Matthischke et al. [231] concluded that for having a high CO_2 conversion and temperature regulation in a fixed bed reactor under transient load changes, product recirculation is necessary. They remarked that for effective temperature control, the recirculated product flow rate must be adapted correspondingly. In the research work published by Lefevbre et al. [232] on a three-phase bubble column reactor, step changes in the feed flow velocity caused no fluctuations in the reactor temperature, guaranteed by the good heat removal characteristics of this three-phase methanation reactor. Since

the reactor operation did not approach equilibrium, the transient conditions changed the product quality.
In this section, step changes in the reactor throughput for constant feed composition and step changes in the feed composition in a constant feed flow rate have been exercised. The aim is to assess the reactor response time and possible changes in the product composition under such transient conditions. It is beneficial to point out that in this setup all adjustments were done manually. Whereas, for an industrial plant, the work is being done with an automated control strategy.

4.2.6.1 Load step changes

For load variations, two scenarios were designed and implemented:
The first case is entitled "half-step experiment". Changes made to the gas flow rate are as follows: the test starts with the reference gas flow rate of $21.1\,\mathrm{l\,min^{-1}}$. After 3 GC runs corresponding to 45 minutes of run time, the total flow rate was reduced to $15.8\,\mathrm{l\,min^{-1}}$. The reactor response to the step change was monitored for 45 minutes. Thereafter, the flow rate was decreased further to $10.6\,\mathrm{l\,min^{-1}}$. The same step-change sequence was repeated for altering from 10.6 to 15.8 and afterwards to $21.1\,\mathrm{l\,min^{-1}}$. The step change was initiated 2 minutes after starting the third GC measurement for the previous condition, in order to make sure that there is enough time for the new adjustments made in the feed can be captured by the GC.
The second scenario deals with the so-called "full-step experiment": The feed flow rate was changed from $21.1\,\mathrm{l\,min^{-1}}$ directly to $10.6\,\mathrm{l\,min^{-1}}$ and back. The time interval for executing the changes was the same as in the case of the half-step experiment.

Half-step experiment:
In the following, the influence of inducing a step change in flow rate from 21.1 to $15.8\,\mathrm{l\,min^{-1}}$ and the opposite order is discussed in detail.
The temperature map shown in Fig. 4.11 is generated using the 5 measurement positions along the bed. The profile clarifies the temporal evolution of the temperature throughout the transient conditions. This figure can be divided in 3 sections:

I. The steady-state was achieved about 25 minutes after initiating the reaction.

II. The temperature response to the step change in the feed flow rate and its evolution at $t > 43$ min (switching time).

III. The new steady-state reached for the new parameter set at around 58 min.

Parallel to the temperature map, the water flow rate adjusted to control the sudden temperature changes throughout the time is plotted for a better understanding of the involved effects. Fig. 4.11 left maps the temperature evolution when feed throughput is reduced from 21.1 to 15.8 l min^{-1}. Immediately after the load reduction, the temperature in the hot spot (position 2) drops from 440 to 420 °C. The water mass flow rate is reduced to the value derived in the steady-state load change experiment for 15.8 l min^{-1} to prevent further temperature drop. Although the temperature drop stops, the system does not go back to the initial temperature level (hot spot of 440 °C). Via additional reduction in the coolant amount, the temperature starts to grow again and reaches its initial profile. At this point, the water flow rate must be readjusted again so that no further temperature increase occurs. The time interval which the reactor requires to adapt to the applied changes and evolve toward its initial stage is about 15-20 minutes.
Fig. 4.11 right shows the temporal changes in axial temperature for transient conditions of increasing the flow rate from 15.8 to 21.1 l min^{-1}. After inducing the step in the flow rate, a sudden increase of about 10 K is measured in the hot spot. The water flow rate is adjusted instantly in order to avoid temperature runaway. The reactor reacts rather fast to the coolant modification and after about 5 minutes the temperature starts to diminish. Again, it takes about 15 minutes in total for the reactor to go back to the initial temperature level. During this period also, more water had to be dosed for effective control of the temperature. A maximum increase/decrease of the water flow rate of approximately 1-2 g min^{-1} above/below its steady-state values helped in handling the sudden temperature alterations in transient conditions.

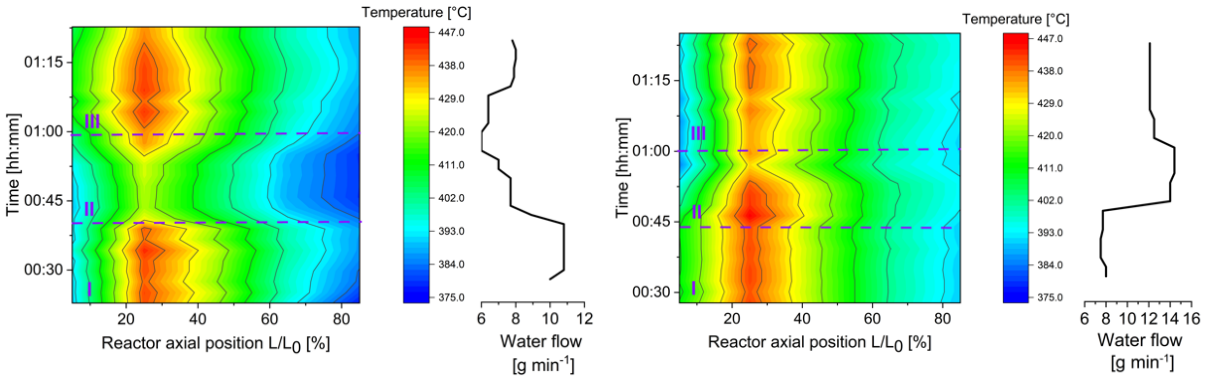

Figure 4.11: Temperature evolution and the total cooling water flow adjusted during half-step change experiments, left: 21.1 to 15.8 l min^{-1}, right: 15.8 to 21.1 l min^{-1} (H_2/ CO_2 = 4, p_w = 10 bar)

Full-step experiment:

Fig. 4.12 left presents the temperature profile when decreasing the feed flow rate to half its initial value from steady-state conditions (from 21.1 to 10.6 l min^{-1}). The temperature of the hot spot drops about 25 K at once. The water flow rate is adjusted quickly after altering the feed throughput to avoid reaction blow-out. The water flow rate, which is cut back in this case, is in total about 2 g min^{-1} less than the value determined for steady-state condition. In a full-step change, it takes roughly 25-30 minutes for the reaction to develop back to its initial stage. Nevertheless, no reaction runaway or blow-out is observed during these transient conditions and the reactor continues to perform without external energy input.

When inducing a step from 10.6 to 21.1 l min^{-1}, a sharp increase in temperature is measured (Fig. 4.12 right). In less than 2 minutes, the hot spot reaches 460 °C. The water flow rate is increased to 16 g min^{-1} to prevent further temperature growth (~ 3 g min^{-1} more than the steady-state value). It takes about 25 minutes for the temperature to gradually diminish and reach the desired steady-state.

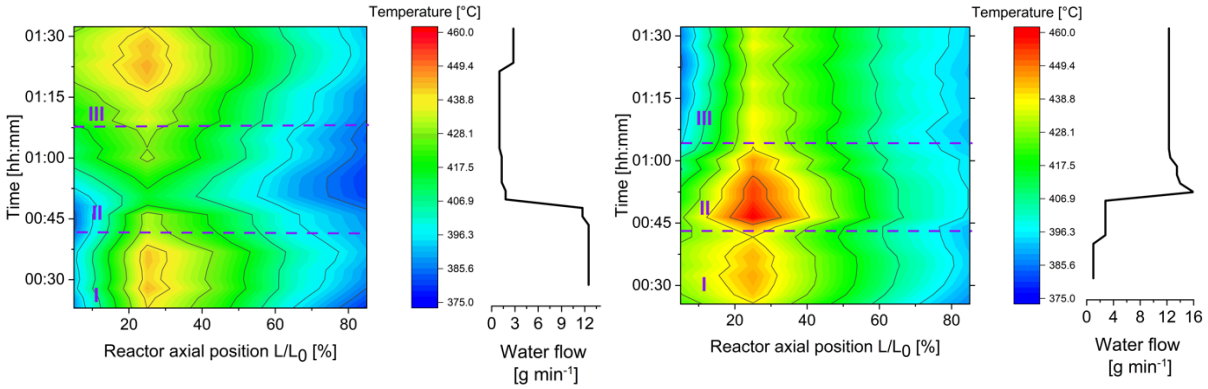

Figure 4.12: Temperature evolution and the total cooling water flow adjusted during full-step change experiments, left: 21.1 to 10.6 l min^{-1}, right: 10.6 to 21.1 l min^{-1} (H_2/ CO_2 = 4, p_w = 10 bar)

What is interesting, after inducing the step change in both cases (half-step and full-step), the temperature changes only marginally in position 1 and positions 3-5. The GC measurements demonstrated in Fig. 4.13 (a) and (b) for both scenarios signify no drastic change in the CO_2 conversion due to transient operation and the measured values certify a consistent performance, which is identical to steady-state experiments (Sec. 4.2.4, Tab. 4.4). The consistency of the temperature in the rear reactor part is a solid reason for constant product composition, as already discussed in Sec. 4.2.2. Although the

GC measurement intervals take long and in an intensive dynamic study, measurement intervals below 5 minutes are desired, one would not expect a dramatic change in the product composition during transient conditions, since the temperature in the rear reactor part is stable and via coolant adjustment, the temperature profile is being controlled appropriately.

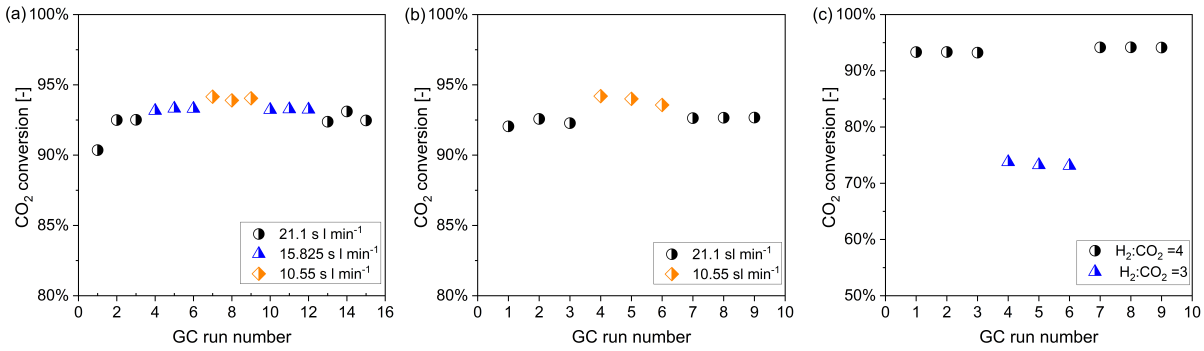

Figure 4.13: CO_2 conversion during step change experiment: (a) half-step change in load, (b) full-step change in load (H_2/CO_2 = 4, p_w = 10 bar), (c) H_2/CO_2 ratio step change ($\dot{V}_{CO_2}$ = const. = 3 l min^{-1}, p_w = 10 bar)

4.2.6.2 H_2/CO_2 step changes

Regarding feed composition, the H_2:CO_2 ratio was varied from 4 to 3 and back to 4 again. The studied case is applied for the assumption of constant CO_2 flow rate. The same procedure was applied as in the load step variation: each parameter was set for 45 minutes with 3 respective GC runs. The measurement started with a H_2/CO_2 ratio of 4 ($\dot{V}_{tot}$ = 15.8 l min^{-1}). Fig. 4.14 left shows that the temperature drops by 10 K after reducing the H_2 flow rate. With water adjustment (decreasing to 4 g min^{-1}) the temperature in position 2 can be controlled perfectly and approaches its original value in less than 10 minutes.

The step change in H_2 flow rate for setting the H_2/CO_2 ratio from 3 to 4 is shown in Fig. 4.14 right. The temperature in the hot spot rises to 450 °C (10 K increase). In this case again in 10 minutes the perturbations could be counteracted with efficient cooling. Fig. 4.13 (c) shows the CO_2 conversion throughout the feed experiment. No changes in the CO_2 conversion during transient operation compared to the steady-state experiments is observable, which certifies the stability of the reactor under transient feed composition.

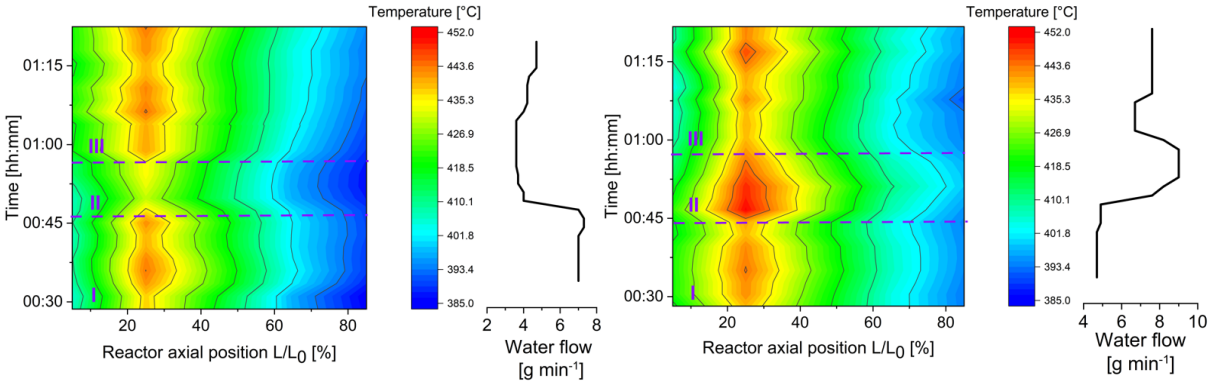

Figure 4.14: Temperature evolution and the total cooling water flow adjusted during H_2/CO_2 step change experiments, left: 4 to 3, right: 3 to 4 ($\dot{V}_{CO_2}$ = const. = 3 l min^{-1}, p_w = 10 bar).

4.2.7 Catalyst variation effect on reactor performance

To this point, the reactor performance under various operating conditions has been discussed in detail for a promoted monometallic Ni catalyst. This section seeks the answer to the question: Does the catalyst activity have any influence on the reactor performance?

For this purpose, the bimetallic Ni_3Fe catalyst was fractionated in the diameter range of 400-500 µm, mixed with SiC and filled in the reactor. The catalyst weight and its weight ratio with regard to the inert SiC were kept consistent as to those applied for the mono-metallic Ni catalyst (see Sec. 4.1.3).

Fig. 4.15 left shows the start-up behavior for the Ni_3Fe catalyst until reaching steady-state. The first positions which undergo temperature growth are positions 2, 3, and 4. This temperature growth happens after only 3 minutes and reaches about 10 K. Referring to Fig. 4.4, it can be realized that in the case of implementing the mono-metallic Ni catalyst, from the moment of reaction initiation, the hot spot is located at position 2. In the case of the Ni_3Fe catalyst, such a clear hot spot at position 2 is detectable after around 7 minutes of reaction. The reaction ignition is moving to the reactor center for this catalyst in the first 5 minutes. The reason for this disparity can be the activity characteristics of the two catalysts (see Cha. 3, Sec. 3.3.7). However, the discrepancy is very small and can also be tangled with some experimental errors, such as the presence of water drops or vapor in some of the reactor channels during start-up, remaining from previous experimental attempts.

After 10 minutes of reaction, the hot spot reaches about 410 °C, which is a good match of what was detected for the mono-metallic catalyst. Fig. 4.15 right displays the steady-state

temperature profile applying the Ni_3Fe catalyst in comparison with the mono-metallic Ni catalyst. The amount of water dosed in steady-state conditions in passages 1 and 2 is equal to 9 and 4.5 g min^{-1}, respectively. For this reason, the P1-test1 experiment, in which in total 13.5 g min^{-1} of water was dosed as well is used for better comparability (see Tab. 4.2). The temperature profiles for both catalysts are very similar and indicate an identical course of the reaction. The CO_2 conversion for this measurement was about 90.5% and the selectivity to methane formation equals 99.8%. For better comparison, the equilibrium CO_2 conversion at position 5 (= 375 °C), which is equal to 93.2% is displayed on the right y-axis [1]. Considering the error margins (clarified in Sec. 4.1.3), the reactor performance for both catalysts is very similar.

The other experiments with changed experimental conditions applying the Ni_3Fe catalyst (total feed flow rate, composition, water pressure, etc.) are not discussed here. The results do not point to any systematic differences compared to the results discussed for the mono-metallic catalyst. Accordingly, the reactor performance for the two different catalyst systems is very much alike and hence the catalytic activity does not affect the reactor operation during both start-up and steady-state.

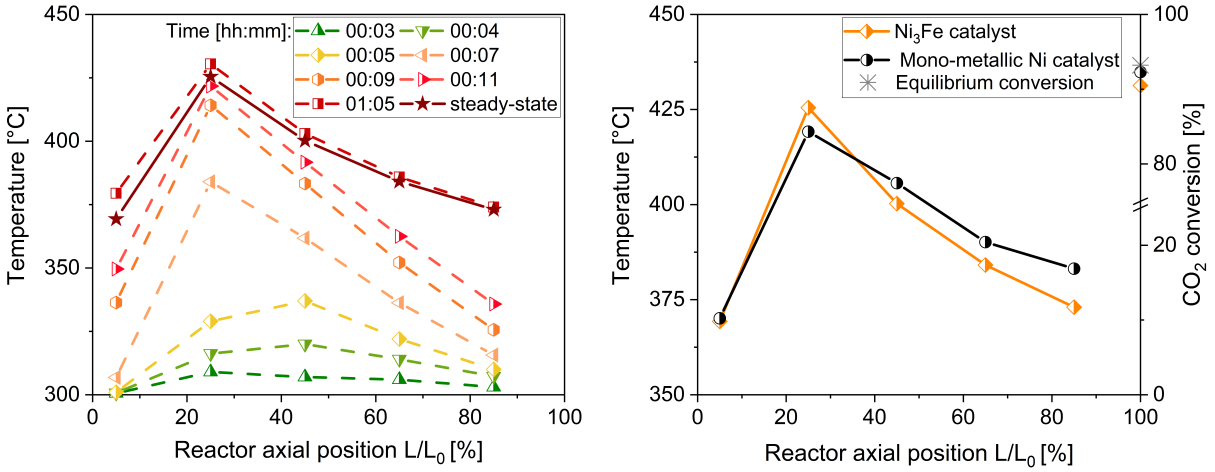

Figure 4.15: left: Reactor start-up behavior for Ni_3Fe catalyst in reference reaction conditions ($\dot{V}_{tot}$ = 21.1 l min^{-1}, H_2/CO_2 ratio = 4, p_w = 10 bar), right: comparison of the steady-state temperature profile between the Ni_3Fe catalyst and the monometallic Ni catalyst for reference reaction conditions

[1] For a more accurate comparison, the temperature of the gases at the reactor outlet (=367 °C) are to be applied. In this case, the equilibrium CO_2 conversion value is equal to 94.1%. Thermodynamic equilibrium value for methane selectivity is equal to 99.96% at this temperature and composition.

4.3 Mathematical methods

4.3.1 Catalytic fixed bed reactor modelling: prologue

Modelling of catalytic reactors helps us to attain deeper insight into the interplay of transport and chemical reactions and their consequences for reactor performance. The two main reactor model categories are pseudo-homogeneous and heterogeneous models. In a pseudo-homogeneous model, the catalyst is entirely accessible by the fluid. If the transport characteristics in the solid and the fluid phase are to be accounted for individually, heterogeneous models must be implemented. Another classification of reactor models is related to 1D, 2D, or 3D profiles of concentration and temperature. Schlereth et al. [233] performed a comparative study on 1D, and 2D pseudo-homogeneous and heterogeneous fixed bed reactor models for methanation of CO_2 with a special focus on thermal runaway triggering operational parameters.
In Cha. 3, the heat and mass transfer balance equations based on a continuous (plug flow) non-isothermal pseudo-homogeneous 1D model are described. The degree of complexity of reactor models can be further increased based on the necessity to include additional effects such as axial and/or radial dispersion and interfacial and/or intraparticle gradients of composition and temperature. The computational time is a decisive factor when increasing the complexity of numerical models. A detailed description of these models and their requirements can be found in textbooks [234].
As given in Cha. 3, the pseudo-homogeneous plug flow reactor model is presented by a system of ordinary differential equations (ODEs). Next to the application of ODEs, the conservation equations in a fixed bed reactor can also be written representing a network of continuously stirred tank reactors (CSTRs). In this approach, a catalytic packed bed reactor is divided into n ideally mixed cells, in which the outlet of each cell serves as the inlet for the next cell. Such model corresponds to a 1D pseudo-homogeneous cell model. The pseudo-homogeneous cell model can be expanded into a heterogeneous model when the diffusion and reaction between the solid and the fluid phase are specified. A 2D cell model is applied by assuming a 2-dimensional network of CSTRs when designating two outlets to each cell. In such a model, the inlet of each cell is specified by its two preceding neighboring cells [234].
The possibility of calculation of the concentration and temperature profiles in a catalytic reactor by means of a cascade of CSTRs was first proposed in 1960 by Deans and Lapidus [235]. The significant advantage of cell models compared to classic continuum models is the simplicity in handling algebraic equations for steady-state conditions (compared

to first and second-order ODEs), and first-order ODEs for transient reaction modelling (compared to PDEs). Despite the inherent physical difference between the cell model and a dispersion model, they come close in relatively low dispersion values ($Bo > 50$). By means of the cell number n, the axial dispersion intensity may be adjusted easily in the cell model (Eq. 4.1 and 4.2) [236].

$$n \approx \frac{Bo}{2} \tag{4.1}$$

$$Bo = \frac{\overline{u}L}{D_{ax}} = Pe_{ax}\frac{L}{d_R} \tag{4.2}$$

The exothermic nature and the fast kinetics of methanation in a scaled-up reactor make the modelling of reactors with a set of ODEs a laborious task due to the stiffness of the problem. In addition, evaporation cooling in spiral-shaped microchannels in the reactor under study has a complex multiphase nature and obliges us to develop special mathematical methods. For these reasons and the numerical concerns mentioned above, a heterogeneous model based on a one-dimensional network of ideally mixed reactors was developed. Special attention is dedicated to the heat transfer phenomena between the catalytic bed and the cooling channel.

4.3.2 Description of the applied reactor model: non-isothermal heterogeneous cell model

The packed bed reactor with a parallel cooling structure was divided into n ideally mixed cells along the axial direction. The model does not consider diffusive mass transport and heat conduction in or against the direction of flow, and the outlet of each cell corresponds to the inlet of the next cell. The interaction between the solid and gas phase is specified via reaction and diffusion relationships. Fig. 4.16 pictures the developed reactor model schematically. The educt components i enter the reactor with inlet concentration of $C_{i,0}$ and after n cells exit with outlet concentration of $C_{i,n}$. The generated reaction heat in each cell is removed via the cooling medium with constant cooling temperature (T_c). The rate of heat transfer is defined via the effective overall heat transfer coefficient k_{eff}. The assumptions taken can be summarized as follows:

- The gas phase is assumed to behave like an ideal gas.
- The energy and mass balances are coupled and solved simultaneously.

- The pressure drop is considered negligible, therefore no momentum balance is solved.
- The conservation equations are solved for the steady-state case.
- The axial mass dispersion and thermal heat conduction (dissipation) are hooked into the model via the number of cells.
- In each cell, the concentration, and temperature of the gas phase are considered to be equal everywhere (the pre-requisite for an ideal CSTR).
- The catalyst is modelled as solid spherical particles. The concentration on the surface of the catalyst is prescribed by diffusion-reaction inside the solid phase.
- The temperature on the surface of the catalyst is prescribed by the thermal conductivity of the catalyst particle and the released reaction heat.
- No external heat and mass transfer resistances are accounted for. Therefore, the conditions (i.e. temperature and concentration) at the surface of the catalyst are identical to those in the bulk phase.

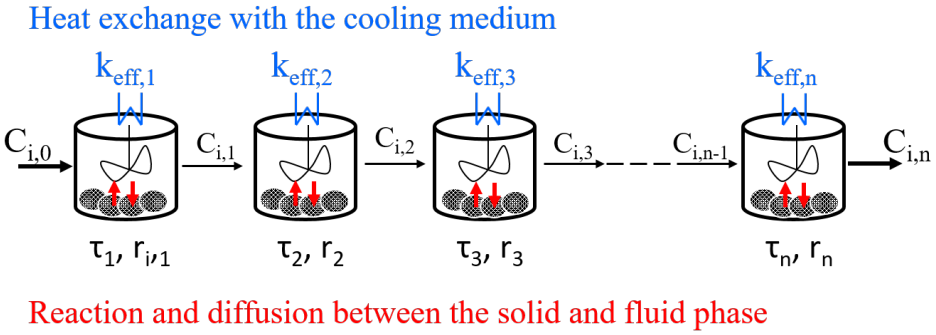

Figure 4.16: Schematic representation of the applied reactor model for the evaporation cooled fixed bed reactor: a 1D network of CSTRs

The mass and energy balance in the solid spherical catalyst pellets can be written as:

$$D_{i,eff}\left(\frac{2}{r}\frac{dC_i}{dr}+\frac{d^2C_i}{dr^2}\right)=\rho_{bed}\cdot R_{m,i}(C_i,T) \tag{4.3}$$

$$\lambda_{eff}\left(\frac{2}{r}\frac{dT}{dr}+\frac{d^2T}{dr^2}\right)=-\rho_{bed}\cdot R_{m,i}(C_i,T)\cdot(-\Delta_R H) \tag{4.4}$$

where $D_{i,eff}$ is the effective diffusivity of species i in the reaction mixture, which was determined using the Bosanquet diffusion model ([220] as part of the handbook [237]). The λ_{eff} represents the effective thermal conductivity in a solid particle. The boundary conditions specify the relationships for transition from the solid into the bulk phase. The first boundary condition imposes symmetry of the concentration and temperature profiles in the center of the catalyst. At the surface of the catalyst, concentration and temperature are equal to the corresponding bulk phase values (Eqs. 4.5 and 4.6).

$$\left.\frac{dC_i}{dr}\right|_{r=0} = 0 \qquad and \qquad C_i\Big|_{r=R} = C_{i,surface} \tag{4.5}$$

$$\left.\frac{dT}{dr}\right|_{r=0} = 0 \qquad and \qquad T\Big|_{r=R} = T_{surface} \tag{4.6}$$

The diffusive molar flux and the heat flux from the catalyst pellets to the gas phase are obtained from the solution of Eqs. 4.3 and 4.4. This leads to:

$$J_M = -D_{i,eff}\frac{dC_i}{dr} \tag{4.7}$$

$$J_H = -\lambda_{eff}\frac{dT}{dr} \tag{4.8}$$

Each cell is modelled as a well-mixed CSTR. The specific heat transfer capacity in each cell is calculated individually based on the temperature and composition of the reactants in the corresponding cell. Therefore the conservation of mass and energy for each cell with a length of Δx and for the bulk phase can be written in the form of the following algebraic equations:

$$u_x \cdot C_{i,x} \cdot A_{cross} + J_M \cdot \Delta S_{cat} = u_{x+dx} \cdot C_{i,x+dx} \cdot A_{cross} \tag{4.9}$$

$$\dot{m} \cdot C_{p,x+dx} \cdot T_{x+dx} - \dot{m} \cdot C_{p,x}T_x + \Delta A_{cool} \cdot k_{eff} \cdot (T_{x+dx} - T_{cool}) = J_H \cdot \Delta S_{cat} \tag{4.10}$$

The parameters ΔA_{cool} and ΔS_{cat} represent the cooling area and catalyst surface area in one control volume respectively. k_{eff} corresponds to the overall heat transfer coefficient. The heat of the reaction is defined as:

$$\dot{Q}_{reac.} = dm_{cat}\sum_j(-\Delta_R H_j) \cdot R_{m,j} \tag{4.11}$$

4.3.3 Determination of the overall heat transfer coefficient

The local overall heat transfer resistance in a cooled fixed bed reactor in general comprises three main terms:

$$\frac{1}{k_{eff}} = \frac{1}{\alpha_{pb}} + \frac{s}{\lambda} + \frac{1}{\alpha_c} \tag{4.12}$$

- The heat transfer coefficient on the packed bed side ($\frac{1}{\alpha_{pb}}$)
- The heat conduction in the separating wall ($\frac{s}{\lambda}$)
- The heat transfer coefficient on the coolant side ($\frac{1}{\alpha_c}$)

The heat conduction in the wall is the simplest term to determine and depends only on the thickness and material of the wall. In contrast, determination of the heat transfer coefficient in the packed bed and in the cooling side require special treatment and will be discussed in detail below.

Heat transfer coefficient on the packed bed side:
In line with heat transfer fundamentals, the heat exchange in a packed bed reactor arises from convection, conduction, and radiation. Determination of the heat transfer coefficient in a bed filled with solid porous particles is a very complicated problem. Lemcoff et al. classify eight various modes for heat transfer in a packed bed [238]. The number of heat transfer coefficients needed depends on the complexity level of the applied reactor model (see Sec. 4.3.1). In chapter three it was shown that one parameter, entitled the overall heat transfer coefficient suffices for the description of the heat transfer in a 1D pseudo-homogeneous model. A 2D heterogeneous model in contrast calls for 7 heat transfer coefficients for proper modelling (radial and axial conductivities and the wall heat transfer coefficient for each phase, and the solid-fluid heat transfer coefficient) [238]. The effective radial and axial heat transfer coefficients and the heat transfer coefficient in the wall are shown to consist of two terms: a static term (non flow dependent) and a dynamic term (flow dependent). There are a number of studies that provide empirical correlations for the estimation of these parameters. An overview of these correlations can be found in references [238, 239].
Depending on the prerequisites of a problem, different approaches can be applied. For a 1D pseudo-homogeneous reactor model, Schlereth et al. estimated the heat transfer in the bed taking two effects into account: a radial heat dispersion term and a term for heat transfer adjacent to the wall. For the implementation of 2D pseudo-homogeneous

reactor models, two approaches were followed. In the first, the so-called α_w model was applied by assuming constant values for the porosity and the dispersion coefficient along the radius. The second model (the Λ model) takes the radial porosity distribution into account via a correlation developed by Giese et al. [240].

Several literature works maintain correlations in terms of one single parameter (α_{pb}) for determining the packed bed heat transfer coefficient. One of the most widely used models was introduced by Gnielinski [241]. In this correlation, a form factor serves for calculation of α_{pb} using the Nusselt number for an over-flowed single particle. The correlation is valid for a wide range of flow conditions (for spherical particles: 10^{-1} <Re< 10^4 and 0.6 <Pr< 10^4). The packed bed heat transfer for the applied reactor in this study was calculated applying this correlation for the reference reaction conditions at inlet, outlet and an average state. For these three points α_{pb} is equal to 4700 W m^{-2} K^{-1}, 2300 W m^{-2} K^{-1} and 3500 W m^{-2} K^{-1}, respectively. It is important to remark that according to VDI Heat Atlas, the Nu numbers for the flows with Pe numbers below 500-1000 are strongly overestimated. Since the estimated Pe number in this work for the reference reaction condition falls below the noted limit ($\approx$ 200), the model might show some inaccuracy and the estimated heat transfer coefficient values must be handled with care.

De Wasch and Froment [242] provided a linear relationship between the Nu and Re numbers and included a static term (valid for 30 <Re< 10^3). Leva's correlation allows calculation of α_{pb} for a reaction mixture being heated up or cooled down. By applying this correlation, the influence of the Pe number and the form of the tube can be neglected (for $\frac{d_t}{d_h} > 10$). The estimated value for α_{pb} using this correlation is about 410 W m^{-2} K^{-1}. However, the Re number for the current problem is not within the validated range for this correlation (valid for 250 <Re< 3000). In addition, calculation of the hydraulic diameter based on the available generic equation ($d_h = \frac{4A}{P}$) is rather speculative and invalid for laminar flows [241]. Some further works done for 1D heat transfer coefficient estimation in packed beds are delivered by Li and Finlayson [243], Dixon [244] and others.

Despite the rich literature studies on the calculation of heat transfer coefficients for various flow conditions and bed geometries, the application of each of these models is always accompanied by a considerable degree of uncertainty. This uncertainty becomes perceivable when comparing the values estimated from different researchers, especially at low Re numbers. Different sources of errors can be counted responsible, such as experimental errors and applying different data evaluation methods.

Heat transfer coefficient on the cooling side:

As already stated, the evaporation experiments carried out by Belimov et al. [205] in the first reactor prototype ended up with either reaction blow-out or runaway. Comprehending the fundamental differences between the two prototypes during evaporation is vital for proper modelling of the reactor. The central question to answer is how the reaction blow-out problem is fixed in the second reactor prototype.

Fig. 4.17 displays a cross-sectional view of the second reactor prototype and the stacking design of the microfabricated plates. This figure shows that via stacking 3 microfabricated foils on top of each other, the cooling fluid is redirected 3 times before streaming in the main channel adjacent to the reaction bed. During the reaction, it is expected that the water gradually evaporates throughout the spiral channels. In this way, the indirect heat exchange at the reactor inlet is retarded. Therefore, despite the utilization of the high water evaporation enthalpy, the effective temperature difference between the cooling and reaction passage is reduced. This information is decisive for the search for a suitable evaporation heat transfer model since no empirical model is developed and validated for such complex geometry.

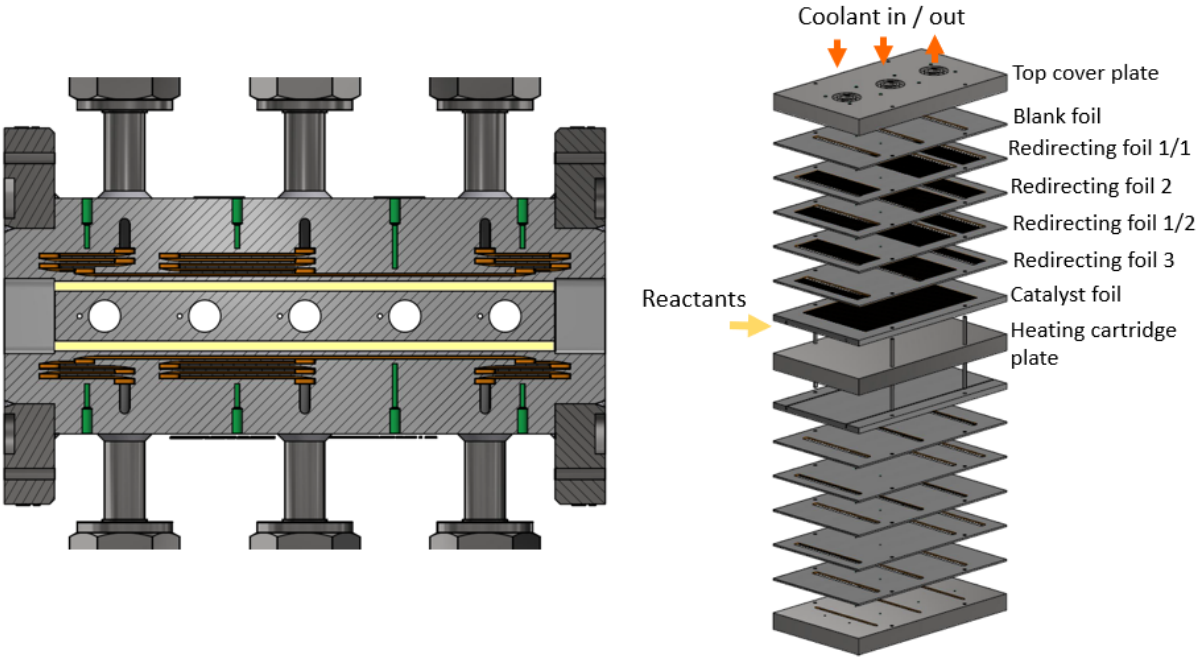

Figure 4.17: Left: cross sectional view of the microstructured reactor prototype two. Right: the stacking strcuture

In line with experimental data, the coolant leaving the reactor is in superheated state. This proposes that the heat transfer in the rear part of the reactor is drastically poor compared to the inlet. In addition during evaporation, the vapor fraction changes between 0 to 1, which has a notable influence on the heat transfer efficiency. Hence, the heat transfer coefficient must be capable of reflecting the local heat transfer changes of evaporation.
Despite being intensively studied, the collection of heat transfer data during an evaporation process is a challenging task. Various works report unstable experimental conditions throughout their measurements, which votes for speculative results and wide uncertainty regions. In addition, the varied range of the heat flux, mass flow rates, and fluid type (water or diverse refrigerants) in these studies makes it difficult to acknowledge them as generic relationships [245]. An overview of the developed correlations for estimation of evaporation heat transfer coefficient in micro and minichannels based on the type of applied fluid, channel diameter, and the experimental conditions is accessible in [245].
Among the 40 research works surveyed, only three of the models are established for predicting local heat transfer coefficients of water evaporation. The model developed by Steinke and Kandlikar [246] provides one of the most popular correlations, which is valid over a large range of heat flux ($\dot{Q}$ = 5-930 kW m^{-2}). The model is composed of two terms: 1. the nucleate boiling and 2. the convective boiling term. The authors recommend that for flows with Re < 100, only the nucleate boiling term is to be applied. Unfortunately, the model is being validated for much higher flow rates and a different microchannel geometry compared to this work (G = 157-1782 kg m^{-2} s^{-1}, d_h = 0.2 mm, water inlet temperature = 22 °C, atmospheric outlet pressure) and delivers huge heat transfer coefficients (20-100 100 kW m^{-2} K^{-1}). The same problem applies to the two remaining studies [247, 248].
Based on these learnings, literature correlations are of little use here. According to Eq. 4.12, accounting a value of 20 kW m^{-2} K^{-1} for the cooling side implies that the overall heat transfer is only controlled by the packed bed side. To appraise such assumption, the temperature profile and CO_2 conversion in the reactor for the reference reaction condition and a coolant pressure of 10 bar (boiling temperature = 180 °C) when keeping the k_{eff} constant are presented and discussed in the following.
The axial temperature profiles and CO_2 conversions for the reference reaction conditions (see Tab. 4.7) and three exemplary overall heat transfer coefficients (k_{eff} = 300, 350 and 370 W m^{-2} K^{-1} each assumed constant along the reactor) are drawn in Fig. 4.18. Higher values of k_{eff} resulted in reaction blow-out directly at the inlet. The simulated temperature profile in Fig. 4.18 left suggests that by increasing the k_{eff}, the hot spot moves obviously away from the inlet and its intensity declines sharply (from 566 to 516 °C). However,

irrespective of the applied k_{eff}, the reaction completely turns off after 50% of the reactor length and approaches the coolant temperature (180 °C).
Fig. 4.18 right shows that lower k_{eff} (higher hot spot temperature), is in favour of the CO_2 conversion and enhances the initial consumption rate. However, since all three cases have the same temperature degree in the rear reactor part, their conversions approach an analogous value (78%).

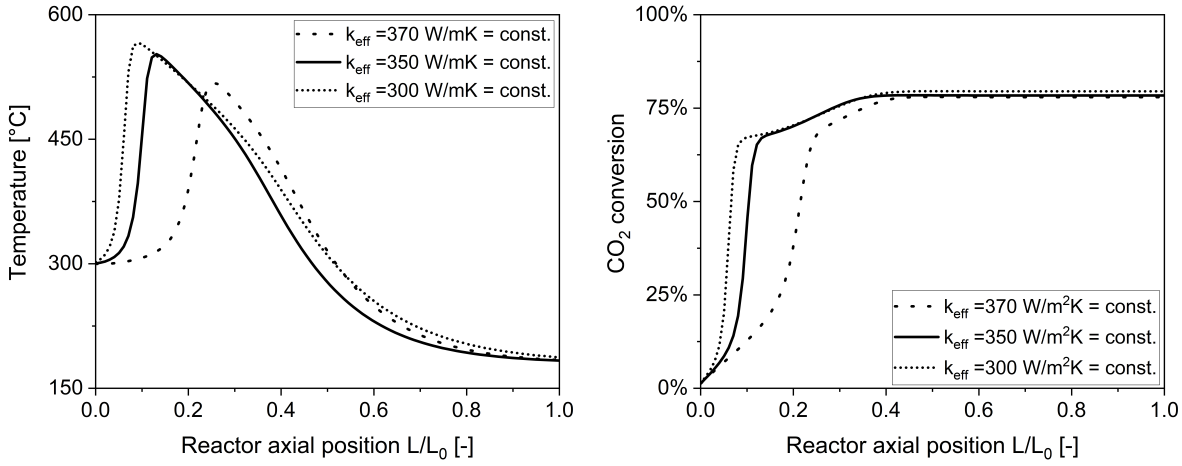

Figure 4.18: Temperature (left) and CO_2 conversion (right) axial profile for constant overall heat transfer coefficients and reference reaction condition ($\dot{V}_{tot}$ = 21 l min^{-1}, p_{abs} = 6 bar, T_c = 180 °C, $\dot{m}_w$ = 12.5 g min^{-1})

These results and the explanations given before lead us to the conclusion that the assumption of a constant k_{eff} for the current reactor system has three major problems:

1. It is experimentally approved that by small increases in the coolant flow rate, the temperature in the reactor goes through vast changes. An uncontrolled increase in the water flow leads eventually to reaction blow-out.

2. Since the coolant leaves the reactor in super-heated state with very low heat transfer capacity, the heat transfer must be controlled for an unknown length by the cooling channel.

3. The developed correlations are only valid for straight and parallel microchannels. Whereas here water flows into several serpentine-shaped microchannels. The design of the serpentine microchannels serves not only to reduce the heat transfer intensity but also to delocalize the evaporation zone. This mechanism guarantees a stable

operation for a range of water flow rate values and allows the reaction side to adapt itself to the removed heat intensity steadily.

Hence, for a strictly correct and precise mathematical description of the heat exchange process, every microchannel plate must be taken into account individually with a new boundary condition, prescribed from the previous one. Adding the fact that the reactor is designed with three coolant inlets, results in a massive computational effort.
For these reasons, a different and simplified strategy for pragmatic estimation of the overall heat transfer coefficient was followed. The overall heat transfer coefficient introduced in Eq. 4.12 can be calculated having the heat duty of the system, the area of the heat exchange and the temperature difference between the two reactor zones, as the following equation holds:

$$\dot{Q} = k_{eff} A_{cool} (T(x) - T_c) \tag{4.13}$$

For simplicity, the temperature of the coolant (T_c) was assumed to remain constant along the channel and equal to the saturation temperature at the respective pressure. For the approximation of the axial temperature profile in the reactor, 6 measurement points were used: the temperature at the entrance (pre-heating temperature), 4 temperature measurement positions (positions 2 to 5) and the reactor outlet temperature (see Sec. 4.1). A cubic spline function was used for interpolation of the temperature in each cell, based on these experimental axial temperature points. This estimated temperature was inserted as $T(x)$ in Eq. 4.13.

4.3.4 Numerical procedure

The 1D representation of the material and heat balance in the catalyst particles (Eq. 4.3 and 4.4) is a boundary value problem which was solved via the `bvp4c` routine in Matlab®. The catalyst was discretized in 50 grid points.
As already discussed in Sec. 4.3.1, the number of reactor cells can be estimated via the Bodenstein number (Eq. 4.1). The Bodenstein number is dependent on the axial Peclet number (Eq. 4.2). For calculation of the Pe_{ax} for gas phase flows in packed bed reactors, the book chemische Reaktionstechnik recommends an empirical diagram. Having the values for Reynolds and Schmidt number ($Re_p \cdot Sc$), the Pe_{ax} and its uncertainty range can be identified [236]. Based on this calculation method, the estimated Pe_{ax} for this study ranges between 3-4. Therefore the number of cells can vary between 75 to 100. For enhancing the computational effort (lowering the problem stiffness), the upper margin of 100 CSTR cells was used. The effective heat transfer coefficient profiles when using

a smaller number of cells are also presented for understanding the effect of the number of CSTRs on this estimated value.
For cubic spline interpolation of the axial temperature profiles in the reactor based on experimental data points, the Matlab function `csapi` was used as the standard case. The starting temperature in all measurements was constrained to 300 °C. The function `fnval` was implemented for evaluating the computed values from the temperature fit for each cell.

4.4 Results and discussion: Modelling

This section presents the results of modelling the heat-exchanger microstructured reactor via a heterogeneous 1D cell model. The modelling results are discussed in detail for one reference point concerning the temperature and concentration profile in the bulk and in the catalyst. Tab. 4.7 presents the experimental parameters for this reference point and the catalyst specifications. The catalyst pore diameter and porosity were measured via N_2 sorption analysis using the method of Barrett, Joyner, and Halenda (BJH). The catalyst tortuosity was estimated applying the correlation provided in [249]. The reaction kinetic model used is taken from the developed model presented in Cha. 3.
Fig. 4.19 displays the effective heat transfer coefficient (k_{eff}) in axial direction for each CSTR cell and at reference reaction conditions. The location of water injection for two inlets and the outlet is depicted via a band since after entering the reactor, water is being redirected several times through microchannels before flowing in the cooling passage parallel to the reaction channel (see Fig. 4.17). For cooling inlet 1, water flows in at $L/L_0 = 0.15$ and is redirected in the bandwidth $0 < L/L_0 < 0.15$. Water is injected at $L/L_0 = 0.5$ through the second cooling inlet and flows back and forth between $0.2 < L/L_0 < 0.5$. The outlet cooling channel covers $0.85 < L/L_0 < 100$.
The calculated profile for k_{eff} can be explained with the nature of evaporation cooling implemented for fast and exothermic methanation. The heat transfer coefficient through the wall (λ/s) is about $1.78 \times 10^4\,\mathrm{W\,m^{-2}\,K^{-1}}$ and is considerably higher than $3500\,\mathrm{W\,m^{-2}\,K^{-1}}$, which is estimated for the packed bed (see Sec. 4.3.3). Therefore, s/λ cannot be the limiting heat transfer resistance. The heat transfer coefficient in the first CSTR (inlet) is about $75\,\mathrm{W\,m^{-2}\,K^{-1}}$, which increases sharply to $330\,\mathrm{W\,m^{-2}\,K^{-1}}$ already in the second cell.
In the first cell, liquid water enters the reactor and thus k_{eff} is low. Along the reactor, the reaction rate increases exponentially due to the temperature and the cooling water starts to

Table 4.7: The constant and reference model parameters values

Parameter	unit	value
Absolute pressure of the reaction zone (p_{abs})	[bar]	6
Mass of the catalyst (m_{cat})	[kg]	0.005
Catalyst diameter (d_{cat})	[µm]	450
Catalyst pore diameter (d_{pore})	[nm]	10
Catalyst packed bed density (ρ_{cat})	[kg m^{-3}]	890
Catalyst porosity (ϵ_{cat})	-	0.64
Catalyst tortousity (τ_{cat})	-	4
Catalyst heat conductivity (λ_{eff})	[W m^{-1} K^{-1}]	0.3
Bed porosity (ϕ_{bed})		0.36
Feed flow rate ($\dot{V}_{tot}$)	[NL min^{-1}]	21.1
H_2/CO_2 ratio	-	4
N_2 molar ratio (y_{N_2})	-	0.052
Feed temperature (T_{in})	[°C]	300
Coolant temperature (T_c)	[°C]	180
Coolant flow rate ($\dot{m}_{cool}$)	[g/min]	12.5

evaporate, leading to very high k_{eff} values. The high evaporation heat transfer coefficient shifts the heat transfer resistance to the packed bed side shortly. The maximum value of k_{eff} reaches 883 W m^{-2} K^{-1} and is located at L/L$_0$ = 6%. During evaporation, the vapor fraction on the cooling side grows which leads to a gradual reduction of the heat transfer coefficient within some cells. At L/L$_0$ ≈ 40%, the decreasing slope of k_{eff} changes and increases slightly, most likely due to water entering the reactor from the second coolant inlet. But since the peak of the reaction rate is already surpassed and the coolant is a mixture of water and vapor, the k_{eff} value does not change significantly. Afterwards, k_{eff} continues to decline with a mild slope to a minimum value of 30 W m^{-2} K^{-1}. In this region, steam is superheated and heat transfer resistance is dominated by the cooling side. At L/L$_0$ = 80%, the k_{eff} starts to increase gradually again. Redirection of the superheated steam through the cooling passage outlet and the turbulence created in serpentine-shaped microchannels is most probably the reason for this observation.

In order to understand the effect of CSTR cell numbers on the heat transfer coefficient, the axial k_{eff} value for 50 and 75 CSTRs are depicted in Fig. 4.20 left and right, respectively. The CSTR number of 50 however led to reaction blow-out and the calculated values for axial temperature when using 50 cells were well below reaction temperature (i.e., 300 °C). By reducing the number of CSTRs, the k_{eff} value in the first cell increases to

310 W m^{-2} K^{-1} for 50 CSTRs and to 159 W m^{-2} K^{-1} when dividing the reactor in 75 well-mixed cells. From mathematical view, the higher temperature difference between the reaction and the cooling side ($T(x)$ and T_c in Eq. 4.13) before reaching the temperature peak, when reducing the number of CSTRs explains the higher overall heat transfer coefficient value in the first cell. This however apparently overlooks axial mixing and does not deliver a proper description for heat transfer coefficient.

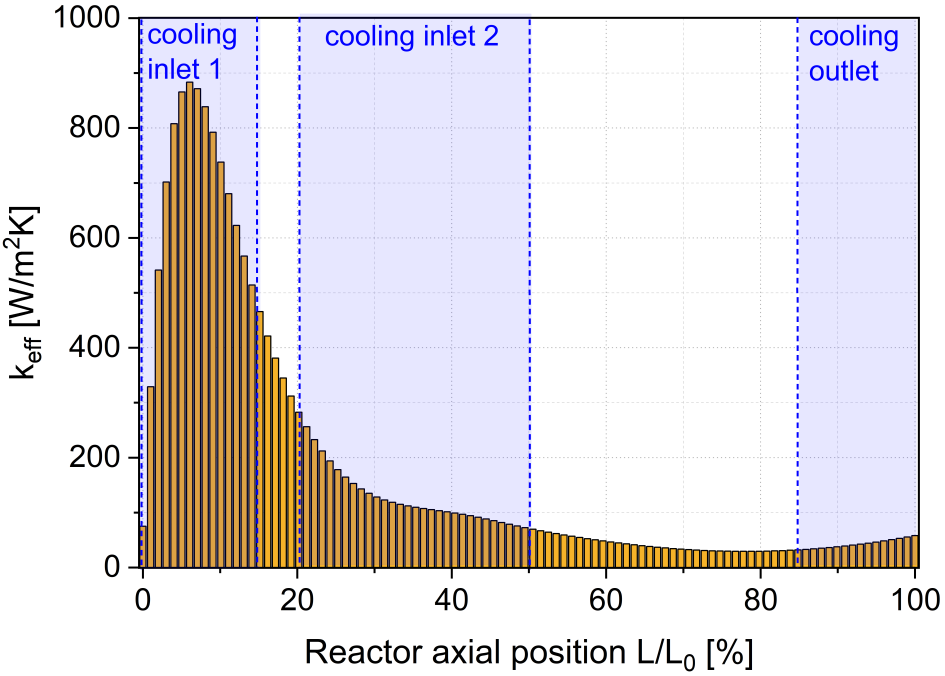

Figure 4.19: The calculated effective heat transfer coefficient for 100 CSTRs along the catalyst bed axis at reference reaction conditions.

The maximum value for the k_{eff} in the three studied cases are rather similar and reduces slightly with decreasing the CSTRs. The k_{eff} peak position is consistent in all three cases (at L/L$_0$ = 6%, maximum k_{eff} is 829 W m^{-2} K^{-1} for 50 CSTRs, 865 W m^{-2} K^{-1} for 75 cells and 883 W m^{-2} K^{-1} for 100 cells). These results confirm that the estimation of the number of axial CSTRs using the Bodenstein number and the criteria described in Sec. 4.3.1 (75 to 100 CSTRs) delivers reliable data. The temperature profile did not show a distinct change when using 75 or 100 cells. Since reducing the number of cells is tangled with problem stiffness and higher computation time, 100 CSTRs were chosen as the optimum value.

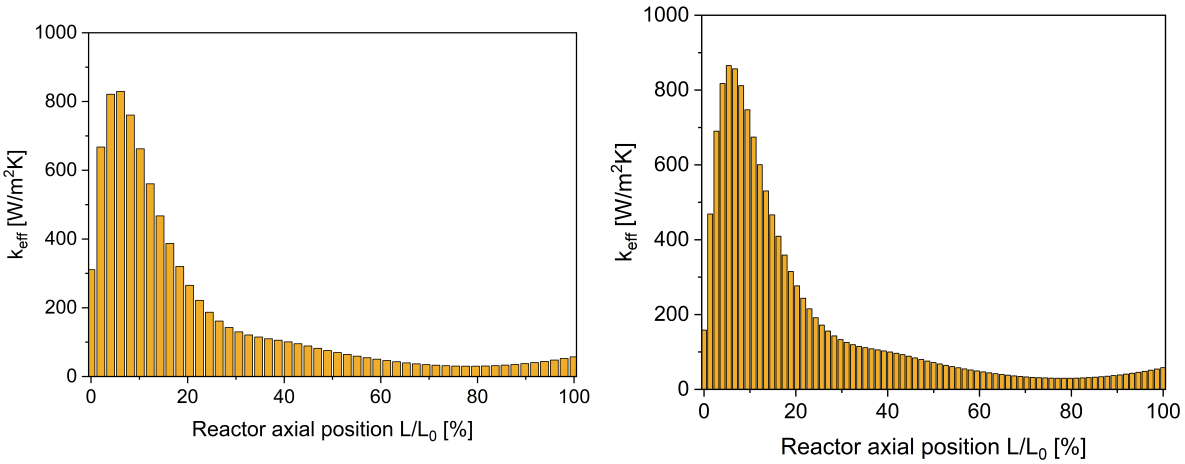

Figure 4.20: The calculated effective heat transfer coefficient for (left) 50 CSTRs, (right) 75 CSTRs along the catalyst bed axis at reference reaction conditions.

The k_{eff} profile for experiments with cooling water at 5 bar and 20 bar are displayed in Fig. 4.21. The k_{eff} value in the first cell for both cases is rather close and is below 100 W m^{-2} K^{-1} and is near to the reference point provided in Fig. 4.19. The overall k_{eff} profile shape is very similar when changing the water pressure and is accompanied with a sharp peak, followed by a gradual decline. The marginal peak in the k_{eff} at around L/L$_0$ = 40% and the k_{eff} increase toward the outlet is detectable in these two cases as well.
The main noticeable variation in k_{eff} when changing the water cooling pressure is the maximum k_{eff} value. This value is equal to 752 W m^{-2} K^{-1} for operation with 5 bar cooling water and 1038 W m^{-2} K^{-1} for cooling water applied at 20 bar. The reference case operated at 10 bar, locates in the middle of this spectra (max. k_{eff} = 883 W m^{-2} K^{-1}). Having a closer look at Eq. 4.13 indicates that when an identical heat exchange value ($\dot{Q}$), heat transfer area and similar temperature profile ($T(x)$, see Fig. 4.7) are granted, the k_{eff} value grows by increasing the coolant temperature T_c. This relationship justifies the trend observed for k_{eff} peak value calculated for the three studied water pressures. Finally, the k_{eff} value for all studied cases, was always estimated to be below 3500 W m^{-2} K^{-1}, applying Gnielinski correlation [241]. Therefore, it is confirmed that this correlation delivers realistic values for approximation of the packed bed heat transfer coefficient for the reactor system and reaction conditions used in this study.

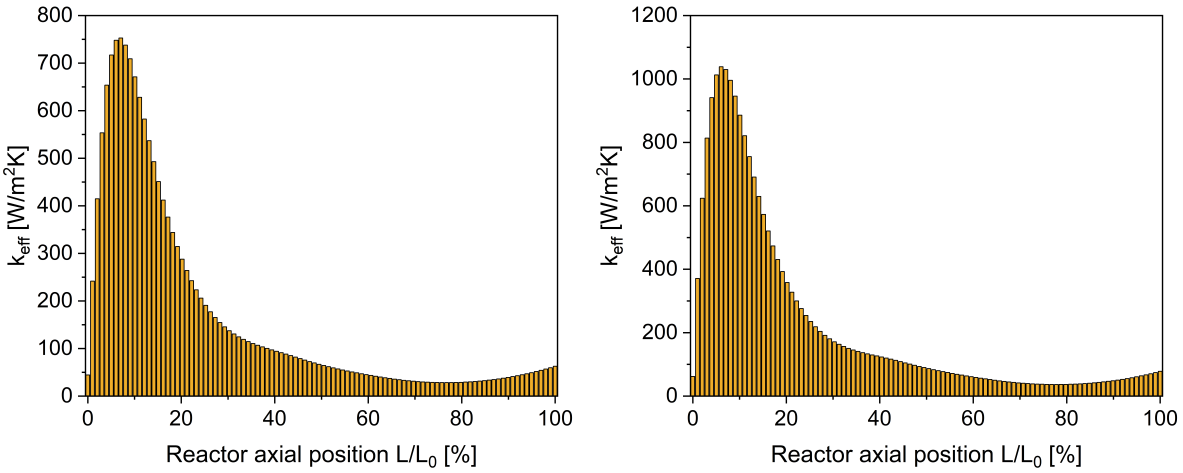

Figure 4.21: The calculated effective heat transfer coefficient along the catalyst bed axis for (left) cooling water pressure of 5 bar, (right) cooling water pressure of 20 bar at reference reaction conditions.

Fig. 4.22 left depicts the modelled axial temperature profile in the gas phase (reactants), the catalyst surface and catalyst center for the reference case in comparison with the experimental temperature profile, portrayed with dots (for reference experiment: P2-test 2 in Sec. 4.2.2). The comparison reveals that the implemented reactor modelling methodology almost perfectly fits the experimental temperature profile. The position of the hot spot, and the moderate course of temperature decline after the maximum are modelled precisely. The experimentally measured temperature at position 1 slightly surpasses the modelled temperature profile. This can be related to the fact that during the experiment and at steady-state conditions, the reactor body temperature and thus the inlet temperature (temperature at reactor axial position = 0) is higher than the 300 °C that is used in the numerical modelling. Therefore, a very sharp and prompt increase of temperature from position zero to position 1 followed by a gradual decline is numerically irrelevant. However, since no other information on the temperature at position zero was available, the feed temperature (300 °C) was applied as inlet temperature for the numerical studies. Fig. 4.22 right provides a magnified view of the catalyst center and gas-phase temperatures. As the model assumptions impose (see Sec. 4.3), the temperature on the surface and bulk are identical. The maximum over temperature in the catalyst center occurs at the reactor entrance where the kinetics are extremely fast and is about 5 K. After L/L_0 = 30%, the intraparticle temperature difference drops to below 1 K. To conclude, it is confirmed that the reaction is not limited by intraparticle heat transfer due to the small size of the catalyst particles.

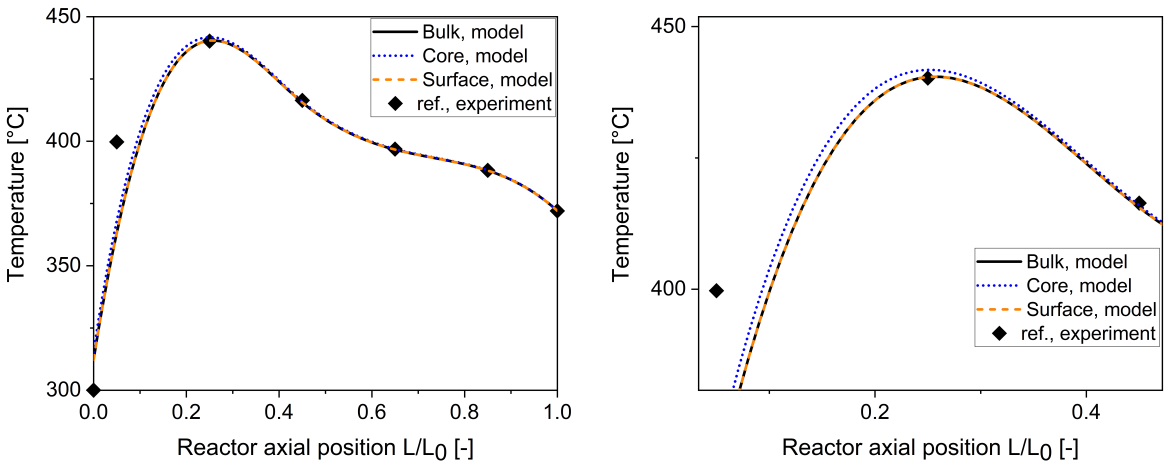

Figure 4.22: Left: temperature development in the bulk phase, the catalyst center and catalyst surface as predicted by the model. Comparison with experimental temperature data for the reference data point. Right: magnified view of the hot spot temperature at the catalyst center, surface and bulk phase.

The axial concentrations of CO_2, CH_4 and CO on the external catalyst surface and in the center is depicted in Fig. 4.23 left. The catalyst particles show strong concentration gradients, especially in the first half of the reactor, where the reaction is fast. CO_2 shows the highest diffusion limitation. This is due to the fact that CO_2 has the lowest diffusion coefficient among all (after CO_2, CH_4 has the lowest diffusion coefficient). In the first cell, the CO_2 concentration in the particle core is about 50% of the surface value. The CO_2 concentration drops during the temperature increase, in which the catalyst core starves from CO_2. The ratio of the CO_2 concentration in the core compared to the surface reaches 23% at its minimum. After the initial heat release, the CO_2 concentration in the catalyst core starts growing again and approaches the surface values gradually. The highest core to surface concentration ratio for CO_2 is about 94%.

In the case of methane, the catalyst core concentration is always higher than that on the surface. The concentration of CH_4 in the core and on the surface is continuously growing. The minimum surface to core ratio for methane is experienced in the first cell (5.4%). This value increases to 99.3% in the last cell.

CO which is the intermediate product of CO_2 methanation has a different trend. In the first 3 cells, the CO concentration in the core surpasses that on the surface. Afterwards, the catalyst core has a constant concentration all along the reactor axis. The surface CO concentration on the other hand after exceeding that in the core goes through a maximum (at the hot spot), which degrades and flattens until the end of the reactor.

Modelled CO_2 conversion, CH_4 selectivity and CO yield axial profiles are presented in

Fig. 4.23 right. CO_2 conversion increases with a sharp slope in the temperature increase region; which is approximately the first 20% of the reactor inlet length (3.4% CO_2 converted in 1% of the bed length). After the hot spot, the CO_2 conversion rate reduces to 0.2% for 1% of the bed length in the rest of the reactor. The predicted CO_2 conversion in the outlet is equal to 84% and falls slightly behind the experimentally measured value of 90%-92% (≈6%). This CO_2 conversion underestimation at higher operating temperatures by the kinetics has already been discussed in Cha. 3, Sec. 3.3.2. Since the applied kinetic model describes a consecutive pathway for CH_4 formation, the yield of CO increases shortly after the inlet (max. 8%). Such CO yield peak in the gas phase was discussed in Cha. 3 both experimentally and via the model (see Sec. 3.3.4.4). At the same location where CO experiences a maximum, the methane selectivity drops. After this peak, the CO yield dwindles to 0.4% and the methane selectivity reaches 99.5%. Identical values were measured during the experiment for both CO yield and CH_4 selectivity. Therefore, the model provides an accurate prediction of product distribution.

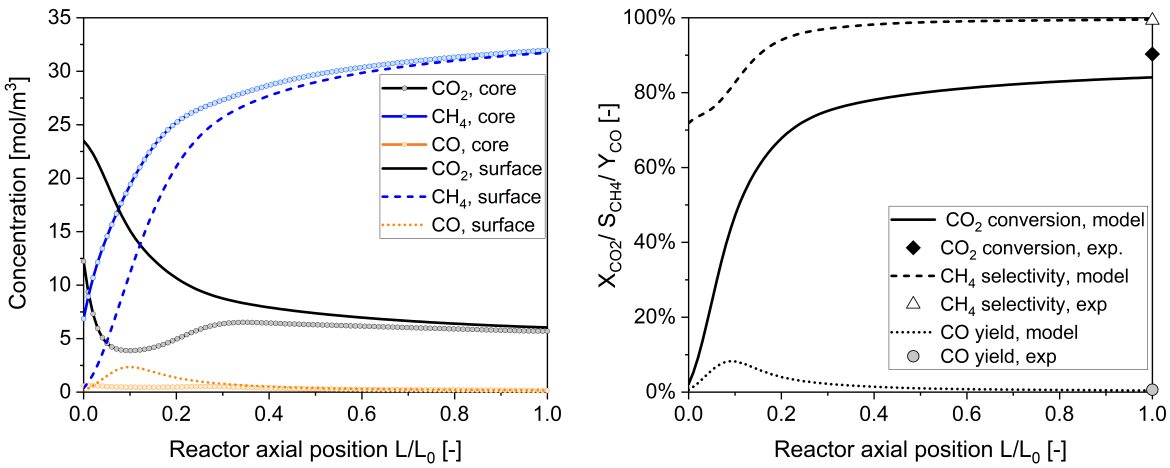

Figure 4.23: Left: axial concentration profile for CO_2, CH_4 and CO in the core and catalyst surface. Right: axial CO_2 conversion, CH_4 selectivity and CO yield according to the model and comparison to the experimental data (measured at reactor outlet).

4.5 Concluding remarks

The aim of this chapter was a detailed investigation of the application of the evaporation cooling mechanism for catalytic methanation reaction of CO_2 and H_2 on a Ni catalyst. This mechanism is shown to be highly efficient by means of a newly developed micro-structured heat-exchanger reactor that allows high reactants conversion in a single stage.

This is especially desired in a PtG process scheme and for decentralized applications. The exothermic energy generated through methane formation is perfectly utilized via steam generation, which can be further applied in a steam electrolyzer.
The implemented reactor cooling structure is modified compared to the first prototype, examined by Belimov et al. [205]. The second reactor prototype comprises two cooling inlets. This allows the enhanced local heat removal and prevention of reaction blow-out caused by excessive cooling. The utilization of pressurized water enables operation without external energy input. The temperature has a polytropic development along the reactor axis and is well-below 500 °C. The hot spot is moderated and can be tuned via smart cooling adjustment, which is a harsh task in most fixed bed reactors. It was shown that the temperature in different axial positions can be superbly regulated via altering the water distribution in the two passages. The manipulation of the temperature profile via two coolant inlets showed that the hot spot degree between 415-455 °C has no influence on CO_2 conversion degree. However, when the temperature in the rear reactor part (positions 3-5) is lower than 400 °C, the conversion may be limited by the reaction kinetics. It was also confirmed that the reactor performs stable under a wide range of coolant pressures. However, lower water pressures impose a certain degree of complexity due to frequent temperature fluctuations in the catalyst bed.
A wide range of reaction throughput and compositions were studied that also endorsed promising reactor performance under the tested conditions. Finally, the temperature profile evolution and product perturbation under transient load and feed composition were monitored. The step changes showed that under transient conditions in the inlet feed flow rate, the reactor requires a maximum time of 30 minutes for re-stabilization and regulating towards its initial temperature level. This is indeed granted by the smart coolant adaptation. No changes in the quality of the product was measured under the performed experiments.
The objective of the second part of this chapter was numerical modelling of the heat-exchanger reactor by means of a 1D heterogeneous (i.e., considering internal pore diffusion) cell model in Matlab. It was demonstrated that the description of the overall heat transfer coefficient is the major hurdle in the way of simulating the temperature profile and thus the reactor performance. The heat transfer coefficient was calculated for each CSTR cell through interpolation of the axial temperature with the help of experimental data. The axial heat transfer coefficient provided valuable information on the course of evaporation heat exchange. Comparison to the experimental data showed that the developed model can predict the concentration in the output and the axial temperature profile accurately.

5 Microstructured reactor scale-up and characterization

In line with energy transition goals illuminated in Cha. 1, a large-scale research infrastructure for studying the interaction among different elements of a sustainable energy system was launched by the Helmholtz Association. Energy Lab 2.0, kicked off at KIT in the year 2014, serves to address important aspects of the massive integration of renewable energy sources into the power grid and further into the energy system [1]. The main challenges of such an energy system are investigated by considering connections between all sectors starting from renewable power generation and distribution, energy storage, energy conversion, and finally consumption. These studies serve to pave the transition path to renewable energies and provide a unique and deep understanding of these systems. In this context, three forms of energy storage are proposed: electrochemical (lithium-ion and redox-flow batteries), thermal (high-temperature energy storage), and chemical (gas and fuels generation).

As declared in Cha. 1, PtG is one of the attractive energy storage pathways due to the existing infrastructure for methane. In Energy Lab 2.0, in cooperation with Engler-Bunte-Institute (EBI-KIT) a container-based pilot plant for methanation was built and put into operation. CO_2 and H_2 source is to be directly from the air and from an electrolyzer, respectively, and are supplied from storage tanks which could be filled with CO_2 and H_2. The container-based plant was developed for two novel methanation reactor concepts: a slurry bubble column reactor designed by EBI-KIT and two parallel microstructured reactors designed by IMVT-KIT. The present chapter provides a brief overview of the microstructured reactor applied, the evaporation cooling system and the start-up procedure for methane generation in the microstructured reactor.

At this point, it is worthwhile to mention that due to the time constraints instructed by the project Kopernikus P2X, the design of the 100 kW reactor had to be already finalized, before the results presented in chapters 3 and 4 were thoroughly collected and it was not possible to fully implement the insights achieved in this study for reactor scale-up.

[1] https://www.elab2.kit.edu/. Last accessed: 18.4.2021

5.1 Scaled-up microstructured reactor

The microstructured reactor prototype presented in Cha. 4 was scaled up with a factor of 28 (taking both blocks into account). Fig. 5.1 shows the two scaled-up methanation reactors for generation of 100 kW methane all together. For this purpose, an internal as well as external numbering up strategy, was implemented. For the internal numbering up, in a reactor prototype, the number of parallel catalyst slits was increased to 22. In this respect, 16 slits kept their dimensions as in the lab prototype investigated in Cha. 4; and the depth of 6 slits was increased from 2 mm to 4 mm. With raising the reaction channel height, the contact time in the respective channel increases compared to a single 2 mm-height channel. However, for every pair of 2 mm-height channel, one 4 mm-height channel is foreseen. The amount of catalyst filled in a 4 mm-height channel was kept equal to a 2 mm-height channel pair and identical to that filled in the lab prototype (5 g). Hence, in total, the same amount of reacting gases are processed in these two-channel arrangements. The channel height in laminar flow regimes and in microstructured reactors is associated with the characteristic reaction length and influences the heat transfer time constant and diffusion time constant (see Cha. 2, Sec. 2.6.2). Therefore, increasing this parameter is expected to directly affect the reaction progress and reactor performance. The information acquired will be used for scale-up designs of the next methanation prototypes.

The co-flow cooling concept via two inlets and one common outlet was applied here consistently. Also pre-heating the reactor or reduction of the catalyst is regulated by means of electrical heating cartridges. The detailed information on the reactor design and the arrangement and geometry of the microchannels may not be disclosed here due to a filed patent application.

In both reactors together, 140 g catalyst was filled. The feed flow rate for a full load operation was equal to $50\,m^3\,h^{-1}$ (at NTP) and at stoichiometric H_2/CO_2 ratio (CO_2 = $10\,m^3\,h^{-1}$, H_2 = $40\,m^3\,h^{-1}$). Thus, the contact time is kept in the same range as to that in the lab prototype ($0.35\,m^3\,h^{-1}\,g^{-1}_{catalyst}$). For a partial load operation, the flow rate of CO_2 and H_2 were reduced to $5\,m^3\,h^{-1}$ and $20\,m^3\,h^{-1}$ respectively, diluted with $10\,m^3\,h^{-1}$ N_2 (all at NTP).

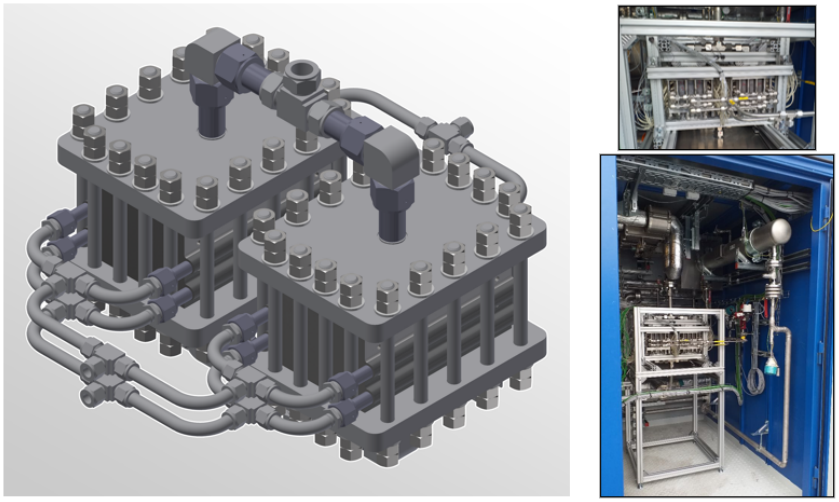

Figure 5.1: Left: Rendering of the scaled-up methanation unit, right: the assembled scaled-up methanation unit in Energy Lab 2.0 container-based plant

5.2 Methanation setup in Energy Lab 2.0

The simplified setup with regard to the high-pressure cooling mechanism is shown in Fig. 5.2. Unlike the strategy implemented in the lab prototype reactor (see Cha. 4, Sec. 4.1.1), here the water coolant flows in a closed circuit. As Fig. 5.2 shows, water is pressurized via dosing N_2 up to the desired cooling pressure (in standard case 20 bar). After the pump, the water is heated electrically. The pressure and temperature of the water are controlled after the pump and the heater, respectively. The water flow divides between the first and second cooling inlet by means of a control valve. Two thermocouples are inserted adjacent to the catalyst bed. The first thermocouple is placed close to the reactor inlet. The position of the other thermocouple corresponds to the expected hotspot position, i.e., position 2 (see Sec. 4.2.1). However, unlike the lab reactor where the amount of water in each cooling channel was regulated manually, here the hotspot degree dictates when the control valve is to be opened, so that water flows in the second cooling inlet too (an automated cooling strategy). Thus, at the beginning of the reaction and before reaching the given hotspot, water only flows in the first cooling inlet. This controlling temperature is defined by the operator.

After the reactor, the generated steam is directed into a heat exchanger where it condensates back into water below 70 °C and accumulates in the water tank.

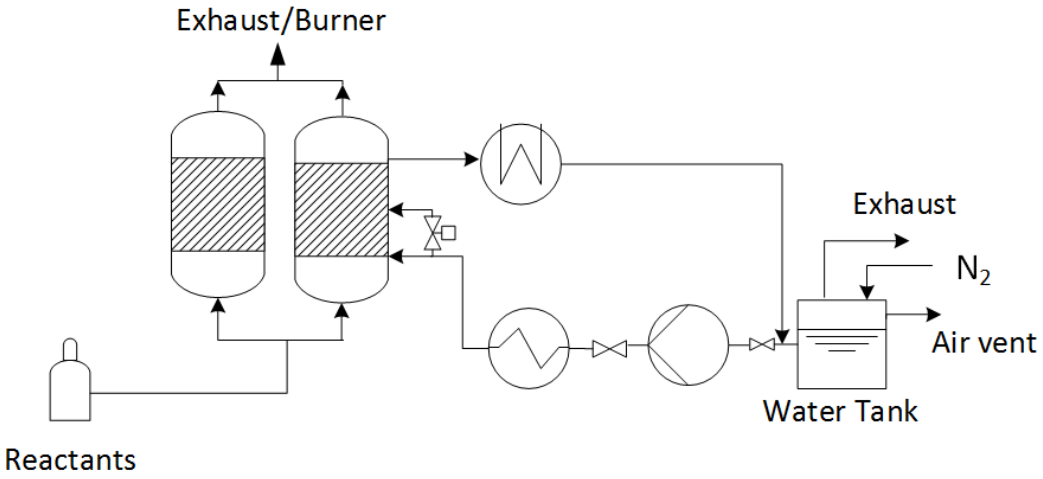

Figure 5.2: The process flow sheet of evaporation cooling in Energy Lab 2.0

5.3 Trial operation

In the following, a short description of the steps carried out for taking the reactor into operation is provided.

Testing the microreactor with N_2:
The first step is verification of the process components. For this purpose, the pressure in the water tank is set to 20 bar. The water pump must be set to 80% of its output performance. The electrical heater after the water pump increases the water temperature to 180 °C and the temperature of the water at the reactor inlet is screened regularly. After water adjustment, a N_2 flow of 5 $m^3\,h^{-1}$ (STP) is dosed in the reactor and the reactor temperature is increased to 350 °C in 50 K steps (controlled via heating cartridges). During this period, the behavior of both reactors regarding temperature uniformity and stability is monitored.

Catalyst reduction:
The second step is reducing the catalyst. For this purpose, a H_2:N_2 flow of 1:1 (= 7.5 $m^3\,h^{-1}$) is adjusted. The reactor temperature was increased with a ramp of 3 K min^{-1} to 400 °C and kept for 3 hours at this temperature. After completion of the catalyst reduction, the reactor temperature was reduced to room temperature and N_2 was filled in

the reactor for standby periods.

Trial operation of the microreactors unit:

The trial operation of the methanation microreactor unit aimed to verify that all the setup components function properly. Both reactors were operated without isolation. Before starting the reaction, it must be approved that the entire water loop is filled with water, the water tank is half full and the valves leading the water to the reactor are open and functional. The water-Glycol media for condensation of the steam after the reactor must be regulated.

For starting the reactor operation, the flow rates of CO_2, H_2 and N_2 were set to 5, 20 and 10 $m^3\,h^{-1}$ respectively (50% of the full reactor load).

During the first trial operation, several issues were detected which require detailed inspection and trouble-shooting. For one, the temperature in one of the microreactors failed to reach the target value of 350 °C uniformly along the bed (especially at the inlet). This sluggish temperature regulation hindered the proper reaction initiation in this reactor and the heating cartridges continued delivering electricity after dosing CO_2. Towards the middle of the reactor, the heating cartridges turned off, but no typical methanation temperature rise was observed, most probably due to the cold reactor inlet. This poor temperature regulation can have several reasons. For one, the thermocouples at the reactor inlet must be thoroughly checked, since a cold reactor inlet hinders the reaction initiation.

Another reason can be the different pressure drop on the cooling channel side for two microreactors. The coolant flow in both reactors is regulated via a common control valve and thus the water flow will be always higher in one reactor compared to the other. As experimental measurements and simulations in Cha. 4 demonstrated, the reactor works stably under a restricted water flow range, and surpassing the limits leads to reaction blow-out. For future works, in the first place, the full functionality of all electrical heating cartridges is to be approved. After this step, a uniform temperature along the reactor must be guaranteed. In case after these steps, the same problem re-occurred, an independent (i.e., isolated) operation of each microreactor is recommended to investigate the reactor performance.

The second microreactor did not show any issues with temperature regulation and a uniform temperature in all positions was achieved. Therefore, in contrast to the first microreactor, after initial temperature regulation, the reaction initiation followed smoothly. However, this reactor suffered from operational instability, which prevented long-term

experimentation. In this reactor, although the hotspot reached over 420 °C and the temperature growth showed a typical methanation behavior, the reaction was blown out after a short while of dosing water. The reason behind this reaction blow-out is suspected to be the currently applied cooling strategy.
The major share of the coolant flows through the cooling inlet one. The coolant in the second inlet is regulated by the control valve, which allows a fraction of the total water flow to pass into the second inlet. This strategy leads to over-cooling the reaction directly in the front reactor part. As already described earlier, excessive cooling leads to turning the reaction off instantaneously. Increasing the peak temperature to 450 °C, at which the control valve opens up did not help to solve the issue. Increasing the reactants flow rates (CO_2 to 7.5 $m^3\,h^{-1}$ and H_2 to 30 $m^3\,h^{-1}$) led to reaction runaway and a hotspot above 500 °C.
Based on these observations, refining the cooling strategy before running a second experimental campaign must be carefully assessed. One possibility is switching the position of the control valve to the first inlet. As described in Sec. 4.2.1, during start-up the coolant was always dosed firstly in the second cooling inlet. Temperature stabilization in the reactor front demands more time and only after a significant temperature increase in the inlet ($\approx$ 70 K) the coolant in the first channel is dosed to avoid such reaction blow-out. With this modification, during start-up, water would flow mainly in the rear reactor part, in which also the reaction triggers first (see Cha. 4, Sec. 4.2.1). When the reaction is established in the entire length of the reactor and temperature sparks in the front part, the control valve opens and takes part in controlling the hotspot temperature. Another solution that would assist in a safe reactor start-up is implementing two independent pumps or two control valves for regulating the temperature in each cooling inlet with an automatic control procedure.

Due to time constraints imposed on the PhD study and the shared methanation plant in Energy Lab 2.0 with KIT-EBI, executing the suggested adaptations and a second experimental attempt was not feasible during this work.
As described in Cha. 4, the heat transfer during evaporation cooling cannot be predicted quantitatively and temperature profile data are essential for simulation of the reactor. Due to the lack of experimental data on the temperature profile, no prognosis regarding the reactor performance via simulations can be accomplished. Since the scale-up reactor design and the methanation plant in Energy Lab 2.0 were concluded without the knowledge obtained through this doctoral study, at this point no concrete conclusions

on the performance of this methanation plant, the necessity of developing a new coolant regulation strategy, flow distribution control or design of new microstructured reactor prototypes can be provided.

6 Summary and outlook

The catalytic methanation reaction of carbon dioxide and hydrogen was investigated thoroughly in this work. This reaction was introduced as one of the remarkable schemes for the storage of surplus generated renewable energy. The current research work introduces microstructured reactors as promising candidates in reactions with high heat and mass transfer requirements and demonstrates their impressive technical maturity.

In chapter three, the kinetics of CO_2 and H_2 reaction on a $Ni_3Fe/\gamma\text{-}Al_2O_3$ catalyst under high temperature and pressures and in a microstructured packed bed reactor and applying a non-isothermal 1D pseudo-homogeneous plug-flow reactor model were studied in detail. Measurement of conversion and selectivity in short residence times in a wide parameter range helped to unfold several important aspects of this reaction. It was shown that the intermediate CO formation is a missing key point in literature. In addition, most of the literature kinetic models do need a high number of model parameters. A refined kinetic model was developed based on literature-based knowledge from both CO methanation and direct CO_2 methanation models and experimentally obtained information. The kinetic model describes methane generation from CO_2 as a two-step reaction with reverse water-gas-shift (rWGS) reaction as the first step, followed by CO methanation. The CH_4 selectivity was confirmed to be dependent on the reaction temperature and contact time in the reactor. Shorter residence time and higher temperatures favor the formation of CO. This behavior could be resolved via inspecting the activation energy of the two consecutive reactions: $167\,kJ\,mol^{-1}$ for rWGS versus $61\,kJ\,mol^{-1}$ for CO methanation. Hence, at higher temperatures, the first reaction has a higher rate compared to the second step. The numerical and experimental analysis showed that water is the only inhibiting factor for the reaction rate. Also, this inhibition is merely temperature-dependent and the partial pressure of water in the reaction mixture is the decisive rate inhibiting parameter. Based on this information, the number of kinetic model parameters could be reduced to 6, which has multiple numerical advantages. This improvement was made sensible with the assistance of statistical methods.

Despite superior activity and selectivity of the applied Ni_3Fe catalyst and its stable activity in the first 50 hours of operation, long-term stability tests revealed that this catalyst

experiences a strong loss of activity. The course of the deactivation course differs from known trends from literature but could be evaluated and interpreted by means of simple mathematical expressions. Detailed transmission electron microscopy measurements disclosed that separation of the particles from the Al_2O_3 support and active metal particle size growth, i.e., by sintering were the main reasons for the deactivation. Finally, the developed rate model was applied for a Ni-Al_2O_3 catalyst and a new set of parameters, were estimated for this catalyst. This second catalyst showed slightly lower activity, but better stability. Thus, it was chosen as the main catalyst of interest for pilot testing associated with long operational hours.

the development of an efficient and compact reactor concept for one-step methanation with sufficiently high conversion was the subject of the fourth chapter. The heat exchanger-reactor applied includes a microstructured cooling channel parallel to the slit-form catalytic bed. The two channels, i.e., reaction and cooling are separated with a wall. The reactor has two cooling inlet passages and a common outlet. High-pressure evaporation of water was selected as the cooling mechanism of interest. The experimental measurements showed that the start-up phase takes approximately 20 minutes. The reaction proceeded without external electricity input after this period. Coolant adjustment (e.g. amount and pressure) allowed for a temperature profile optimization and certified the superior performance and high stability of the reactor over a wide operational range. Additionally, the feed flow and composition variation confirmed that the reactor operated in the thermodynamic regime. The temperature profile proved to be adaptable by means of coolant adjustment in the studied window. As a result of the conformable adjustment of the temperature profile, the product composition varied only a little for different contact times. Nevertheless, the start-up strategy which is a crucial step for efficient performance was highly dependent on these operational parameters and must be obeyed strictly.

Step changes on the feed flow rate and composition were carried out which proved that the reactor has a very good response time, and in the worst-case scenario, within 30 minutes the induced transient conditions can be neutralized via coolant adjustment. Finally, the Ni_3Fe catalyst used for kinetic studies was applied to demonstrate the independent reactor performance when using different catalysts. Similar temperature profiles and CO_2 conversion degrees were obtained which assured this claim.

A non-isothermal 1D heterogeneous reactor model based on *n* ideally mixed CSTRs was successfully constructed in Matlab. It was shown that assigning a constant heat transfer coefficient leads to either reaction blow-out or runaway (numerically). The complex nature of evaporation cooling and lack of empirical equations for estimating the local heat transfer coefficient during evaporation in the conditions of interest was identified

as the bottleneck for the prediction of the polytropic temperature profile and reactor performance. Therefore, the overall heat transfer coefficient along the reactor axis was calculated by means of a cubic spline function, interpolating the temperature from experimental measurement points. In this method, the measured axial temperature profile was applied for the calculation of the overall heat transfer coefficient for every single CSTR cell. Applying this strategy, the temperature profile and composition were simulated with very good correspondence to the experimental measurements. The computed coefficient facilitated a deeper understanding of the involved phenomena during evaporation cooling. These results explain why water evaporation and generation of superheated steam is the optimal cooling strategy for methanation and prevention of hot spots and reaching high reactants conversion. The packed bed heat transfer coefficient was identified as the main heat removal resistance in the first 20% of the reactor where the water starts to evaporate. The value of the heat transfer coefficient determined by simulation was shown to be in coherence with a packed bed heat transfer coefficient estimated via literature correlations.
Finally, the packed bed microstructured reactor prototype was scaled up for generation of 100 kW methane applying internal and external numbering-up method. Evaporation cooling of high-pressure water was integrated into a container-based experimental setup in the Energy Lab 2.0 in KIT. Throughout the first operation, the functionality of the main process components was examined. Several technical issues hindered a stable reactor operation. Further trouble-shooting and detailed reactor performance tests in the course of current work were not possible due to time limitations.

Because of restraints in time and resources, various interesting aspects of CO_2 methanation remain open, which can be subject to further research. For future studies, some potential investigation areas can be counted:

1. Applying spatial concentration and temperature measurement methods in a proper reactor (e.g. a reactor accessible via optical windows, a capillary reactor, or a reactor with tap positions) the kinetics of CO_2 methanation in the view of intermediate formation could be studied in more detail. Additional concentration and temperature data could be applied to further validate/improve the consecutive description of CO_2 methanation.
2. By means of optical measurement methods such as diffuse reflectance infrared Fourier transform spectroscopy (DRIFTS) the formed surface species may be detected.

How such measurements could assist in finding out the deactivation mechanism and treating it, can be the subject of an intensive research project.

3. The microstructured reactor with evaporation cooling mechanism can be examined further through intensive dynamic tests. In this respect, an experimental campaign is to be taken into action with temporal changes in the feed flow rate and composition to check for instabilities in the product concentration in short time intervals. This information would indicate the limitations of the current prototype and can be a clue for the next reactor generations.

4. Development of a relationship for calculation of the heat transfer coefficient in the evaporation cooled reactor without using the experimental temperature data would support predicting the reactor output for arbitrary reaction conditions. The experimental setup for examining the evaporation cooling mechanism in the microstructured reactor can be modified in order to collect more temperature data on the coolant or the catalyst side, recording the vapor fraction in the cooling outlet or along the coolant passage. The information are beneficial for improving and verifying the numerical description of the evaporation phenomena.

5. An experimental campaign must be arranged for testing the scaled-up microstructured reactor in the Energy Lab 2.0. This know-how would support future activities for pilot plant or industrial scales of methanation in microreactors in reactor design as well as process control level.

A Appendix

A.1 Experimental plan for kinetic studies on the Ni_3Fe catalyst

Table A.1: Experimental plan for kinetic studies on the Ni_3Fe catalyst.

Varied parameter	constant parameter
Reference and long term test	T=350 °C, p =4 bar τ_{mod,CO_2} = 0.38 mg min ml^{-1} H_2/CO_2=4, y_{N_2}= 0.5
Temperature T = 300, 320, 335, 350, 370, 385, 400, 425, 450 °C	τ_{mod,CO_2} = 0.16, 0.38 and 0.72 mg min ml^{-1} p = 4 bar and 12.5 bar
Pressure p = 4, 7, 10, 12.5, 15, 18 bar	T = 300 °C, τ_{mod,CO_2} = 0.72 mg min ml^{-1} T = 350 °C, τ_{mod,CO_2} = 0.38 mg min ml^{-1} T = 400 °C, τ_{mod,CO_2} = 0.16 mg min ml^{-1}
Residence time τ_{mod,CO_2} = 0.72, 0.52, 0.38, 0.31, 0.24, 0.16, 0.09 mg min ml^{-1}	T = 300, 350, 400 °C p = 4 and 12.5 bar
Stoichiometry, H_2/CO_2 = 2-8 Set 1: p_{CO_2} = const. = 1.6 bar Set 2: p_{H_2} = const. = 0.4 bar	T = 350 °C τ_{mod,CO_2} = 0.38 mg min ml^{-1}
CO addition in feed (T=350 °C) $\dot{V}_{CO}$= 0, 3, 6, 12 ml min^{-1}, each with $\dot{V}_{CO_2}$ = 125 ml min^{-1} and without dosing CO_2 in feed	$\dot{V}_{tot}$= 1250 ml min^{-1} $\dot{V}_{H_2}$ = 500 ml min^{-1} $\dot{V}_{N_2}$ = rest
CO_2 addition in feed (T=350 °C) $\dot{V}_{CO_2}$ = 0, 31, 63, 125 ml min^{-1}, each with $\dot{V}_{CO}$ = 6 ml min^{-1} and without CO in the feed	$\dot{V}_{tot}$ = 1250 ml min^{-1} $\dot{V}_{H_2}$ = 500 ml min^{-1} $\dot{V}_{N_2}$ = rest
H_2O addition in the feed (T=350 °C) y_{H_2O}= 0, 2.5, 10, 15, 25 %, y_{N_2}= 50 %- y_{H_2O}	$\dot{V}_{tot}$ = 1250 ml min^{-1}

A.2 Estimation of mass- and heat transfer limitation

In order to assess if the reaction rate data collected in chapter 3 are falsified, the possibility of internal and/or external mass- and heat transfer limitations in the catalytic bed were calculated. The applied criteria are listed and formulated as the following:

Internal mass diffusion limitation, Weisz-Prater criterion [250]

$$\Phi = (\frac{n+1}{2}) \frac{R^{obs.}_{v,CO_2} (\frac{6}{d_p})^2}{D_{mix,eff} C_{CO_2,s}} < 0.08 \tag{A.1}$$

External mass transfer limitation, Carberry number defined via Mears criterion [251]:

$$Ca = \frac{R^{obs.}_{V,CO_2}}{k_G C_{CO_2,bulk} (\frac{6}{d_p})} < \frac{0.05}{n} \tag{A.2}$$

Intraparticle heat transfer limitation (heat transfer limitations inside the catalyst particle), Anderson criterion [252]:

$$\Delta T_{particle} = \frac{R^{obs.}_{V,CO_2} |\Delta_R H_{reac.}| d_p^2}{60 \lambda_p} < \frac{0.05 R T^2_{bulk}}{E_A} \tag{A.3}$$

External heat transfer limitation, via Mears crietreion [251]:

$$\Delta T_{film} = \frac{R^{obs.}_{v,CO_2} |\Delta_R H_{reac.}| d_p}{6 \alpha_p} < \frac{0.05 R T^2_{bulk}}{E_A} \tag{A.4}$$

A.3 Effective diffusion coefficient

The effective diffusion coefficient of the mixture ($D_{mix,eff}$) was estimated considering both molecular diffusion and Knudson diffusion.

$$D_{i,Knudson} = \frac{2}{3} \bar{r} \sqrt{\frac{8RT}{\pi M_i}} \tag{A.5}$$

The molecular diffusion (bulk diffusivity, $D_{i,j}$) for the binary mixture of components i and j was calculated via:

$$D_{i,j} = \frac{3.2 \times 10^{-11} T^{1.75} \sqrt{\frac{1}{M_i} + \frac{1}{M_j}}}{p_{abs.} \left\{ (\sum \nu)_i^{\frac{1}{3}} + (\sum \nu)_j^{\frac{1}{3}} \right\}^2} \tag{A.6}$$

Therefore, the effective diffusion coefficient in the catalyst pellet was estimated via the Bosanquet relationship [220]

$$D_{i,eff} = \frac{\phi_{cat}}{\tau_{cat}} \frac{1}{\frac{1}{D_{i,Knudson}} + \frac{1}{D_{i,mix.}}} \tag{A.7}$$

A.4 Newly fitted parameters for literature kinetic models

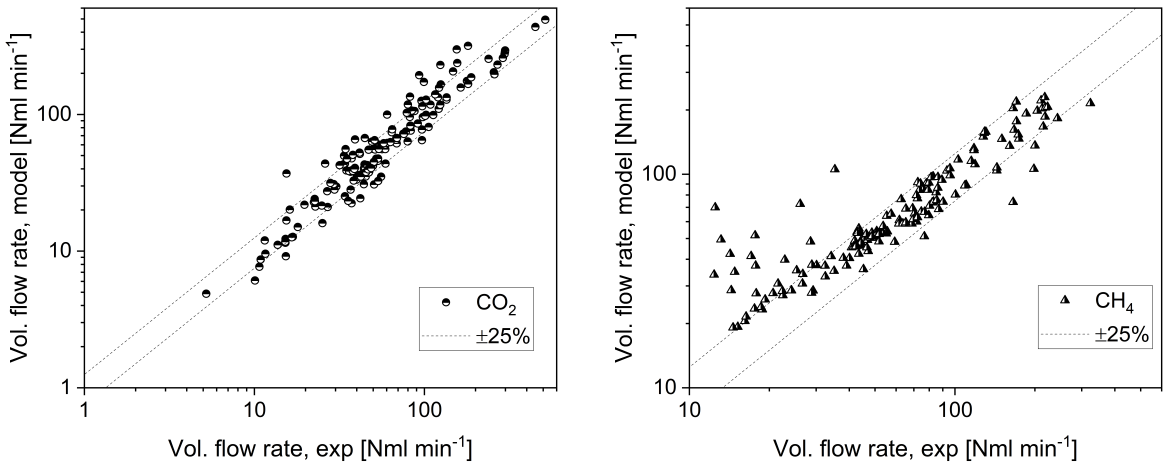

Figure A.1: Parity plots for comparison of the experimental data to the fitted literature rate model proposed by Koschany et al. [61] for CO_2 volumetric flows (left), and CH_4 volumetric flow (right).

Table A.2: The estimated parameters for the literature kinetic model developed by Koschany et al. [61] based on experimental data collected in this work on a Ni_3Fe catalyst.

Parameter	Value	Unit
$k_{0,\ 555\ K}$	0.884 ± 0.15	$mol(kg\ s\ bar)^{-1}$
E_A	77.5 ± 9.37	$kJ\,mol^{-1}$
$K_{OH,\ 555\ K}$	1.05 ± 1.02	$mol(kg\ s\ bar^{1.5})^{-1}$
ΔH_{OH}	22.4 ± 20.40	$kJ\,mol^{-1}$
$K_{H_2,555\ k}$	0.276 ± 0.09	bar^{-1}
ΔH_{H_2}	-6.2 ± 0.43	$kJ\,mol^{-1}$
$K_{mix,555\ k}$	0.923 ± 0.09	bar^{-1}
ΔH_{mix}	-9.99 ± 1.14	$kJ\,mol^{-1}$

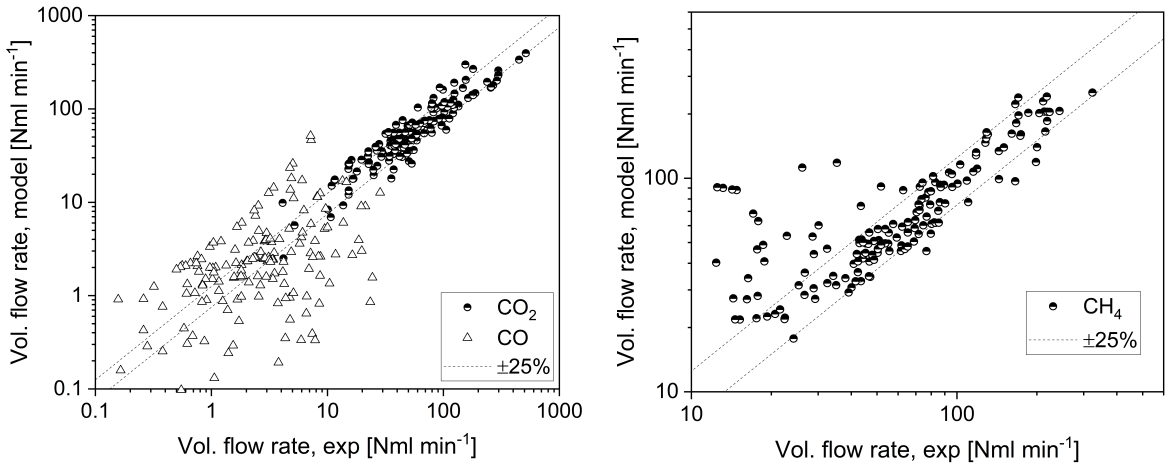

Figure A.2: Parity plots for comparison of the experimental data to the fitted literature rate model proposed by Kopyscinski et al. [149] for CO and CO_2 volumetric flows (left), and CH_4 volumetric flow (right).

Table A.3: The estimated parameters for the literature kinetic model developed by Kopyschinski et al. [149] based on experimental data collected in this work on a Ni_3Fe catalyst.

Parameter	Value
$\ln(k_{1,\,T_{ref}})$	2.79
$\ln(k_{OH,\,T_{ref}})$	2.61
$\ln(k_{C,\,T_{ref}})$	1.15
$\ln(k_{2,\,T_{ref}})$	9.76
$E_{A1}/(RT_{ref})$	10.26
$\Delta H_{OH}/(RT_{ref})$	-3.87
$\Delta H_{C}/(RT_{ref})$	4.88
$E_{A2}/(RT_{ref})$	0.15
$\ln(k_{\alpha,\,T_{ref}})$	1.12
$\Delta H_{\alpha,\,T_{ref}}/(RT_{ref})$	-3.02

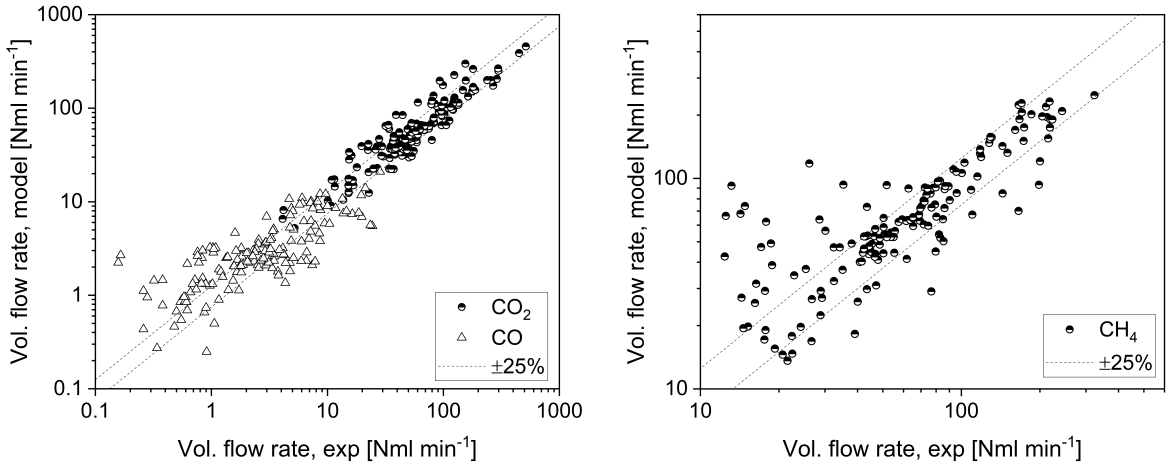

Figure A.3: Parity plots for comparison of the experimental data to the fitted literature rate model proposed by Zhang et al. [150] for CO and CO_2 volumetric flows (left), and CH_4 volumetric flow (right).

Table A.4: The estimated parameters for the literature kinetic model developed by Zhang et al. [150] based on experimental data collected in this work on a Ni_3Fe catalyst.

Parameter	Value	Unit
k_1	3.71×10^{17}	mol $Pa^{0.5}$ $kg^{-1}s^{-1}$
k_2	5.43	mol kg^{-1} Pa^{-1} s^{-1}
K_{CO}	8.23×10^{-14}	Pa^{-1}
K_{H_2}	6.12×10^{-14}	Pa^{-1}
K_{CH_4}	6.65×10^{-9}	Pa^{-1}
K_{H_2O}	$1.77\ 6.12 \times 10^{-5}$	Pa^{-1}
E_1	240.10	kJ mol^{-1}
E_2	67.13	kJ mol^{-1}
ΔH_{CO}	-70.65	kJ mol^{-1}
ΔH_{H_2}	-82.90	kJ mol^{-1}
ΔH_{CH_4}	-38.28	kJ mol^{-1}
ΔH_{H_2O}	88.68	kJ mol^{-1}

A.5 SEM images of the Ni_3Fe catalyst

A field emission electron probe micronanalyzer (EPMA) JXA-8530F was utilized to examine the morphology of the catalyst particles before and after deactivation.

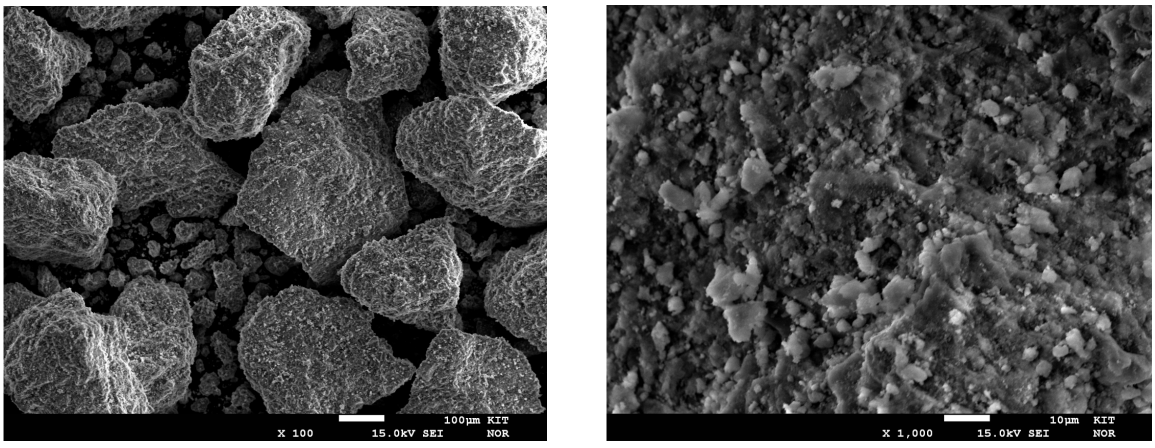

Figure A.4: SEM images of the fresh Ni_3Fe catalyst, left: × 100 magnification, right: × 1000 magnification.

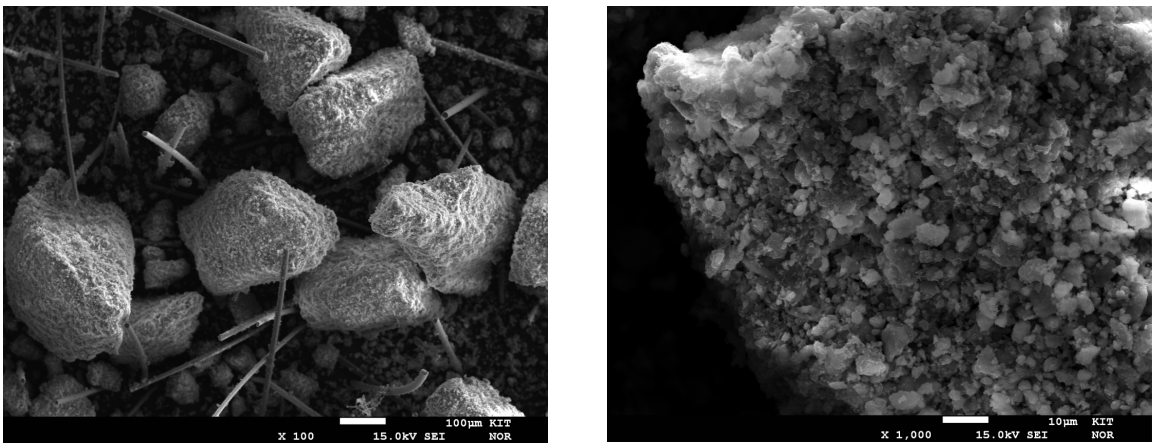

Figure A.5: SEM images of the Ni_3Fe catalyst after 300 hours TOS, left: × 100 magnification, right: × 1000 magnification.

Table A.5: EDX measurements revealing the composition of the fresh Ni_3Fe catalyst

Atom%	Average	Standard deviation	Tolerance (+/-)
C	4.2	1.5	2.9
O	59.1	4.6	5.9
Al	28.3	3.0	5.2
Fe	1.9	0.5	0.6
Ni	6.5	1.8	2.0

Table A.6: EDX measurements revealing the composition of the Ni_3Fe catalyst after deactivation

Atom%	Average	Standard deviation	Tolerance (+/-)
C	4.2 / 4.5	0.3 / 1.1	0.3 / 1.1
O	63.5 / 53.0	1.2 / 1.0	1.2 / 1.0
Al	32.0 / 33.2	0.9 / 0.1	0.9 / 0.1
Si	0.2	0.0	0.0
Fe	0.1 / 2.8	0.0 / 0.6	0.0 / 0.6
Ni	0.2 / 6.3	0.0 / 0.9	0.0 / 0.9

A.6 XRD pattern of the Ni_3Fe catalyst

The Ni_3Fe catalyst was characterized by X-ray diffraction (XRD), before and after long-term tests for 300 hours (see Cha. 3, Sec. 3.3.5). The measurements were carried out at Institute of Functional Interfaces (IFG-KIT). Fig. A.6 presents the results of XRD characterization of the fresh and deactivated catalyst sample. Measurements were conducted applying CuKa1,2 radiation of 0.15419 nm with a Bruker D8 Advance diffractometer equipped with a Si-strip detector (PSD Lynxeye) in theta-theta geometry and a variable divergence slit on the primary side. The diffractograms were recorded over an angular range of 2theta= 20-80 °, with a step width of 2theta=0.015° and 84 s per step.

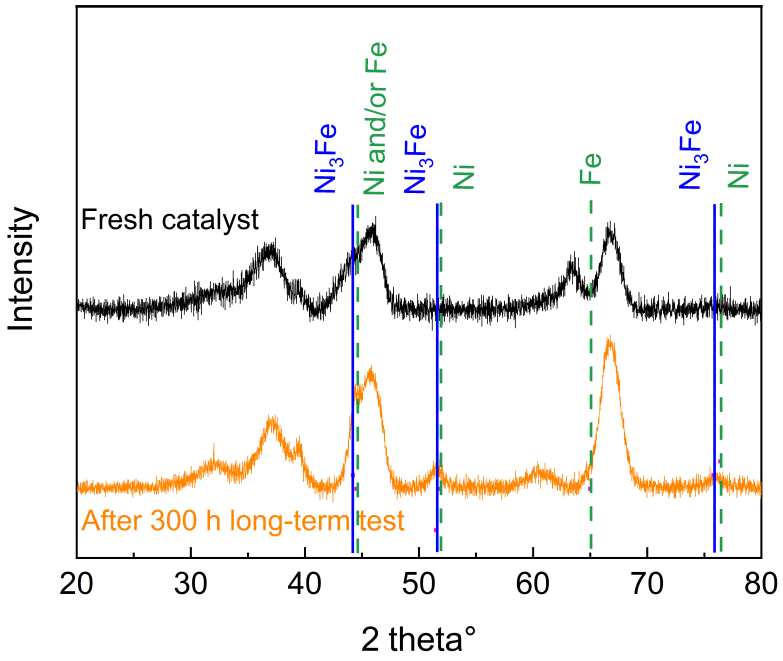

Figure A.6: Diffractogram of Ni_3Fe catalyst prepared by the author, interpreted using the data provided in [119].

References

[1] H. Grassl, *Was stimmt? Klimawandel: Die wichtigsten Antworten*. Freiburg: Herder, 2007.

[2] H. Washington and J. Cook, *Climate change denial: Heads in the sand*. London: Earthscan, 2011.

[3] IPCC, "Climate change 2014: Synthesis report: Contribution of working groups i, ii and iii to the fifth assessment report of the intergovernmental panel on climate change [core writing team, r.k. pachauri and l.a. meyer (eds.)]," IPCC, 2014, Geneva, Switzerland, 151 pp.

[4] N. Nuttall, "Historic paris agreement on climate change: 195 nations set path to keep temperature rise well below 2 degrees celsius: (https://unfccc.int/news/finale-cop21)," 13.12.2015, last accessed: 06.02.2020.

[5] United Nations Environment Programme, "The emissions gap report 2019," 2019.

[6] V. Quaschning, *Erneuerbare Energien und Klimaschutz: Hintergründe, Technik und Planung, Ökonomie und Ökologie, Energiewende*. München: Hanser, 4., überarbeitete und erweiterte auflage ed., 2018.

[7] B. Wehrmann, "Renewables overtake fossil fuels in germany's annual power production for first time: (https://www.cleanenergywire.org/news/renewables-overtake-fossil-fuels-germanys-annual-power-production-first-time)," 02.12.2019, last accessed: 02.03.2020.

[8] B. Benrath, "Tut deutschland genug gegen den klimawandel? (https://www.faz.net/aktuell/wirtschaft/schneller-schlau/tut-deutschland-genug-gegen-den-klimawandel-16227147.html)," 10.06.2019, last accessed: 13.03.2020.

[9] M. Sterner and I. Stadler, *Energiespeicher - Bedarf, Technologien, Integration*. Berlin, Heidelberg: Springer Berlin Heidelberg, 2017.

[10] M. Lehner, R. Tichler, H. Steinmüller, and M. Koppe, *Power-to-Gas: Technology and Business Models*. Cham: Springer International Publishing, 2014.

[11] H. Hesse, M. Schimpe, D. Kucevic, and A. Jossen, "Lithium-ion battery storage for the grid—a review of stationary battery storage system design tailored for applications in modern power grids," *Energies*, vol. 10, no. 12, p. 2107, 2017.

[12] P. Breeze, *Power Generation Technologies*. Elsevier, 2019.

[13] G. Centi and S. Perathoner, eds., *Green carbon dioxide: Advances in CO2 utilization*. Hoboken, New Jersey: Wiley, 2014.

[14] D. Stolten and V. Scherer, eds., *Transition to renewable energy systems*. Weinheim: Wiley-VCH Verlag GmbH & Co. KGaA, 2013.

[15] R. van Basshuysen, *Natural Gas and Renewable Methane for Powertrains*. Cham: Springer International Publishing, 2016.

[16] M. Götz, J. Lefebvre, F. Mörs, A. McDaniel Koch, F. Graf, S. Bajohr, R. Reimert, and T. Kolb, "Renewable power-to-gas: A technological and economic review," *Renewable Energy*, vol. 85, pp. 1371–1390, 2016.

[17] J. Wettengel, "Power-to-gas: Fix for all problems or simply too expensive? (https://www.cleanenergywire.org/factsheets/power-gas-fix-all-problems-or-simply-too-expensive)," 20.06.2018, last accessed: 04.03.2020.

[18] Sabatier, P., Senderens, J. B., "New methane synthesis," *C. R. Acad. Sci. Paris*, vol. 314, p. 514, 1902.

[19] S. Fendt, A. Tremel, M. Gaderer, and H. Spliethoff, "The potential of small-scale sng production from biomass gasification," *Biomass Conversion and Biorefinery*, vol. 2, no. 3, pp. 275–283, 2012.

[20] S. Rönsch and M. Kaltschmitt, "Bio-sng production — concepts and their assessment," *Biomass Conversion and Biorefinery*, vol. 2, no. 4, pp. 285–296, 2012.

[21] J. Kopyscinski, T. J. Schildhauer, and S. M. Biollaz, "Production of synthetic natural gas (sng) from coal and dry biomass – a technology review from 1950 to 2009," *Fuel*, vol. 89, no. 8, pp. 1763–1783, 2010.

[22] R. Gautam and W. D. Deider, "Computation of phase and chemical equilibrium: Part i. local and constrained minima in gibbs free energy," *AIChE Journal*, vol. 25, no. 6, pp. 991–999, 1979.

[23] J. Gao, Y. Wang, Y. Ping, D. Hu, G. Xu, F. Gu, and F. Su, "A thermodynamic analysis of methanation reactions of carbon oxides for the production of synthetic natural gas," *RSC Advances*, vol. 2, no. 6, p. 2358, 2012.

[24] M. Belimov, *Methane production from co-electrolysis products applying a microchannel reactor*. Karlsruhe: PhD Thesis, Karlsruher Institut für Technologie (KIT), 2020.

[25] K. Altfeld and D. Pinchebeck, "Admissible hydrogen concentrations in natural gas systems," *Gas Energy*, vol. 3, 2013.

[26] F. Fischer, H. Tropsch, and P. Dilthey, "Reduction of carbon monoxide to methane in the presence of various metals," *Brennstoff-chemie*, vol. 265, no. 6, 1925.

[27] M. A. Vannice, "The catalytic synthesis of hydrocarbons from h2/co mixtures over the group viii metals: Ii. the kinetics of the methanation reaction over supported metals," *Journal of Catalysis*, vol. 37, pp. 462–473, 1975.

[28] M. A. Vannice and R. L. Garten, "Metal-support effects on the activity and selectivity of ni catalysts in co/h2 synthesis reactions," *Journal of Catalysis*, vol. 56, pp. 236–248, 1979.

[29] G. A. Mills and F. W. Steffgen, "Catalytic methanation," *Catalysis Reviews*, vol. 8, no. 1, pp. 159–210, 1974.

[30] X. Su, J. Xu, B. Liang, H. Duan, B. Hou, and Y. Huang, "Catalytic carbon dioxide hydrogenation to methane: A review of recent studies," *Journal of Energy Chemistry*, vol. 25, no. 4, pp. 553–565, 2016.

[31] S. Li and J. Gong, "Strategies for improving the performance and stability of ni-based catalysts for reforming reactions," *Chemical Society reviews*, vol. 43, no. 21, pp. 7245–7256, 2014.

[32] J. Gao, Q. Liu, F. Gu, B. Liu, Z. Zhong, and F. Su, "Recent advances in methanation catalysts for the production of synthetic natural gas," *RSC Advances*, vol. 5, no. 29, pp. 22759–22776, 2015.

[33] M. A. A. Aziz, A. A. Jalil, S. Triwahyono, and A. Ahmad, "Co2 methanation over heterogeneous catalysts: recent progress and future prospects," *Green Chemistry*, vol. 17, no. 5, pp. 2647–2663, 2015.

[34] P. Frontera, A. Macario, M. Ferraro, and P. Antonucci, "Supported catalysts for co2 methanation: A review," *Catalysts*, vol. 7, no. 12, p. 59, 2017.

[35] S. Rönsch, J. Schneider, S. Matthischke, M. Schlüter, M. Götz, J. Lefebvre, P. Prabhakaran, and S. Bajohr, "Review on methanation – from fundamentals to current projects," *Fuel*, vol. 166, pp. 276–296, 2016.

[36] W. Wang, S. Wang, X. Ma, and J. Gong, "Recent advances in catalytic hydrogenation of carbon dioxide," *Chemical Society reviews*, vol. 40, no. 7, pp. 3703–3727, 2011.

[37] W. Li, H. Wang, X. Jiang, J. Zhu, Z. Liu, X. Guo, and C. Song, "A short review of recent advances in co2 hydrogenation to hydrocarbons over heterogeneous catalysts," *RSC Advances*, vol. 8, no. 14, pp. 7651–7669, 2018.

[38] K. Ghaib, K. Nitz, and F.-Z. Ben-Fares, "Chemical methanation of co2: a review," *ChemBioEng Reviews*, vol. 3, no. 6, pp. 266–275, 2016.

[39] S. Z. Ozdogan, P. D. Gochis, and J. L. Falconer, "Carbon and carbon monoxide hydrogenation on nickel: Support effects," *Journal of Catalysis*, vol. 83, no. 2, pp. 257–266, 1983.

[40] X. Yan, Y. Liu, B. Zhao, Z. Wang, Y. Wang, and C.-j. Liu, "Methanation over ni/sio2: Effect of the catalyst preparation methodologies," *International Journal of Hydrogen Energy*, vol. 38, no. 5, pp. 2283–2291, 2013.

[41] G. Garbarino, D. Bellotti, P. Riani, L. Magistri, and G. Busca, "Methanation of carbon dioxide on ru/al2o3 and ni/al2o3 catalysts at atmospheric pressure: Catalysts activation, behaviour and stability," *International Journal of Hydrogen Energy*, vol. 40, no. 30, pp. 9171–9182, 2015.

[42] A. Quindimil, U. De-La-Torre, B. Pereda-Ayo, A. Davó-Quiñonero, E. Bailón-García, D. Lozano-Castelló, J. A. González-Marcos, A. Bueno-López, and J. R. González-Velasco, "Effect of metal loading on the co2 methanation: A comparison between alumina supported ni and ru catalysts," *Catalysis Today*, 2019.

[43] J. Cored, A. García-Ortiz, S. Iborra, M. J. Climent, L. Liu, C.-H. Chuang, T.-S. Chan, C. Escudero, P. Concepción, and A. Corma, "Hydrothermal synthesis of ruthenium nanoparticles with a metallic core and a ruthenium carbide shell for low-temperature activation of co2 to methane," *Journal of the American Chemical Society*, vol. 141, no. 49, pp. 19304–19311, 2019.

[44] A. Muñoz-Murillo, L. M. Martínez T., M. I. Domínguez, J. A. Odriozola, and M. A. Centeno, "Selective co methanation with structured ruo2/al2o3 catalysts," *Applied Catalysis B: Environmental*, vol. 236, pp. 420–427, 2018.

[45] J. B. Powell and S. H. Langer, "Low-temperature methanation and fischer-tropsch activity over supported ruthenium, nickel, and cobalt catalysts," *Journal of Catalysis*, vol. 94, no. 2, pp. 566–569, 1985.

[46] C. H. Bartholomew, "Mechanisms of catalyst deactivation," *Applied Catalysis A: General*, vol. 212, pp. 17–60, 2001.

[47] B. Mutz, *Methanation of CO_2: Insight into deactivation mechanisms and catalyst stability under dynamic reaction conditions*. PhD Thesis, Karlsruher Institut für Technologie (KIT), 2017.

[48] D. C. Gardner and C. H. Bartholomew, "Kinetics of carbon deposition during methanation of carbon monoxide," *Ind. Eng. Chem*, vol. 20, pp. 80–87, 1981.

[49] K. V. Craig and C. H. Bartholomew, "Hydrogenation of carbon dioxide on group viii metals: Iii, effects of support on activity/selectivity and adsorption properties of nickel," *Applied Catalysis*, vol. 7, no. 2, pp. 169–177, 1983.

[50] C. H. Bartholomew, "Effects of support on the kinetics of carbon hydrogenation on nickel," *Journal of Catalysis*, vol. 91, no. 1, pp. 78–84, 1985.

[51] H. Liu, X. Zou, X. Wang, X. Lu, and W. Ding, "Effect of ceo2 addition on ni/al2o3 catalysts for methanation of carbon dioxide with hydrogen," *Journal of Natural Gas Chemistry*, vol. 21, no. 6, pp. 703–707, 2012.

[52] S. Hwang, U. G. Hong, J. Lee, J. H. Baik, D. J. Koh, H. Lim, and I. K. Song, "Methanation of carbon dioxide over mesoporous nickel–m–alumina (m = fe, zr, ni, y, and mg) xerogel catalysts: Effect of second metal," *Catalysis Letters*, vol. 142, no. 7, pp. 860–868, 2012.

[53] D. Hu, J. Gao, Y. Ping, L. Jia, P. Gunawan, Z. Zhong, G. Xu, F. Gu, and F. Su, "Enhanced investigation of co methanation over ni/al2o3 catalysts for synthetic natural gas production," *Industrial & Engineering Chemistry Research*, vol. 51, no. 13, pp. 4875–4886, 2012.

[54] G. Zhang, T. Sun, J. Peng, S. Wang, and S. Wang, "A comparison of ni/sic and ni/al2o3 catalyzed total methanation for production of synthetic natural gas," *Applied Catalysis A: General*, vol. 462-463, pp. 75–81, 2013.

[55] J. Gao, C. Jia, J. Li, M. Zhang, F. Gu, G. Xu, Z. Zhong, and F. Su, "Ni/al2o3 catalysts for co methanation: Effect of al2o3 supports calcined at different temperatures," *Journal of Energy Chemistry*, vol. 22, no. 6, pp. 919–927, 2013.

[56] J. Barrientos, M. Lualdi, M. Boutonnet, and S. Järås, "Deactivation of supported nickel catalysts during co methanation," *Applied Catalysis A: General*, vol. 486, pp. 143–149, 2014.

[57] G. Garbarino, P. Riani, L. Magistri, and G. Busca, "A study of the methanation of carbon dioxide on ni/al2o3 catalysts at atmospheric pressure," *International Journal of Hydrogen Energy*, vol. 39, no. 22, pp. 11557–11565, 2014.

[58] Y. Li, Q. Zhang, R. Chai, G. Zhao, Y. Liu, Y. Lu, and F. Cao, "Ni-al2o3/ni-foam catalyst with enhanced heat transfer for hydrogenation of co2 to methane," *AIChE Journal*, vol. 61, no. 12, pp. 4323–4331, 2015.

[59] H. Muroyama, Y. Tsuda, T. Asakoshi, H. Masitah, T. Okanishi, T. Matsui, and K. Eguchi, "Carbon dioxide methanation over ni catalysts supported on various metal oxides," *Journal of Catalysis*, vol. 343, pp. 178–184, 2016.

[60] Y. Li, Q. Zhang, R. Chai, G. Zhao, F. Cao, Y. Liu, and Y. Lu, "Metal-foam-structured ni–al2o3 catalysts: Wet chemical etching preparation and syngas methanation performance," *Applied Catalysis A: General*, vol. 510, pp. 216–226, 2016.

[61] F. Koschany, D. Schlereth, and O. Hinrichsen, "On the kinetics of the methanation of carbon dioxide on coprecipitated ni al(o)x," *Applied Catalysis B: Environmental*, vol. 181, pp. 504–516, 2016.

[62] A. Lechkar, A. Barroso Bogeat, G. Blanco, J. M. Pintado, and M. Soussi el Begrani, "Methanation of carbon dioxide over ceria-praseodymia promoted ni-alumina catalysts. influence of metal loading, promoter composition and alumina modifier," *Fuel*, vol. 234, pp. 1401–1413, 2018.

[63] V. Middelkoop, A. Vamvakeros, D. de Wit, S. D. Jacques, S. Danaci, C. Jacquot, Y. de Vos, D. Matras, S. W. Price, and A. M. Beale, "3d printed ni/al2o3 based catalysts for co2 methanation - a comparative and operando xrd-ct study," *Journal of CO2 Utilization*, vol. 33, pp. 478–487, 2019.

[64] D. Beierlein, D. Häussermann, M. Pfeifer, T. Schwarz, K. Stöwe, Y. Traa, and E. Klemm, "Is the co2 methanation on highly loaded ni-al2o3 catalysts really structure-sensitive?," *Applied Catalysis B: Environmental*, vol. 247, pp. 200–219, 2019.

[65] J. N. Dew, R. R. White, and C. M. Sliepcevich, "Hydrogenation of carbon dioxide on nickel-kieselguhr catalyst," *Industrial and Engineering Chemistry*, vol. 47, no. 1, pp. 140–146, 1955.

[66] J. L. Falconer and E. Zagli, "Adsorption and methanation of carbon dioxide on a nickel/silica catalyst," *Journal of Catalysis*, vol. 62, no. 2, pp. 280–285, 1980.

[67] G. D. Weatherbee and C. H. Bartholomew, "Hydrogenation of co2 on group viii metals: Ii. kinetics and mechanism of co2 hydrogenation on nickel," *Journal of Catalysis*, vol. 77, pp. 460–472, 1982.

[68] X. ZHANG, W.-j. SUN, and W. Chu, "Effect of glow discharge plasma treatment on the performance of ni/sio2 catalyst in co2 methanation," *Journal of Fuel Chemistry and Technology*, vol. 41, no. 1, pp. 96–101, 2013.

[69] X. Chen, J. Jin, G. Sha, C. Li, B. Zhang, D. Su, C. T. Williams, and C. Liang, "Silicon–nickel intermetallic compounds supported on silica as a highly efficient catalyst for co methanation," *Catal. Sci. Technol.*, vol. 4, no. 1, pp. 53–61, 2014.

[70] M. Guo and G. Lu, "The effect of impregnation strategy on structural characters and co2 methanation properties over mgo modified ni/sio2 catalysts," *Catalysis Communications*, vol. 54, pp. 55–60, 2014.

[71] M. Aziz, A. A. Jalil, S. Triwahyono, and M. Saad, "Co2 methanation over ni-promoted mesostructured silica nanoparticles: Influence of ni loading and water vapor on activity and response surface methodology studies," *Chemical Engineering Journal*, vol. 260, pp. 757–764, 2015.

[72] R.-P. Ye, W. Gong, Z. Sun, Q. Sheng, X. Shi, T. Wang, Y. Yao, J. J. Razink, L. Lin, Z. Zhou, H. Adidharma, J. Tang, M. Fan, and Y.-G. Yao, "Enhanced stability of ni/sio2 catalyst for co2 methanation: Derived from nickel phyllosilicate with strong metal-support interactions," *Energy*, vol. 188, p. 116059, 2019.

[73] J. B. Branco, P. E. Brito, and A. C. Ferreira, "Methanation of co2 over nickel-lanthanide bimetallic oxides supported on silica," *Chemical Engineering Journal*, vol. 380, p. 122465, 2020.

[74] J. Liu, C. Li, F. Wang, S. He, H. Chen, Y. Zhao, M. Wei, D. G. Evans, and X. Duan, "Enhanced low-temperature activity of co2 methanation over highly-dispersed ni/tio2 catalyst," *Catal. Sci. Technol.*, vol. 3, no. 10, p. 2627, 2013.

[75] V. M. Shinde and G. Madras, "Co methanation toward the production of synthetic natural gas over highly active ni/tio2 catalyst," *AIChE Journal*, vol. 60, no. 3, pp. 1027–1035, 2014.

[76] C. Schild, A. Wokaun, R. A. Koeppel, and A. Baiker, "Carbon dioxide hydrogenation over nickel/zirconia catalysts from amorphous precursors: on the mechanism of methane formation," *J. Phys. Chem. (The Journal of Physical Chemistry)*, vol. 95, pp. 6341–6346, 1991.

[77] N. Perkas, G. Amirian, Z. Zhong, J. Teo, Y. Gofer, and A. Gedanken, "Methanation of carbon dioxide on ni catalysts on mmsoporous zro2 doped with rare earth oxides," *Catalysis Letters*, vol. 130, no. 3-4, pp. 455–462, 2009.

[78] A. Chen, T. Miyao, K. Higashiyama, and M. Watanabe, "High catalytic performance of mesoporous zirconia supported nickel catalysts for selective co methanation," *Catal. Sci. Technol.*, vol. 4, no. 8, pp. 2508–2511, 2014.

[79] H. Takano, H. Shinomiya, K. Izumiya, N. Kumagai, H. Habazaki, and K. Hashimoto, "Co2 methanation of ni catalysts supported on tetragonal zro2 doped with ca2+ and ni2+ ions," *International Journal of Hydrogen Energy*, vol. 40, no. 26, pp. 8347–8355, 2015.

[80] C. Guo, Y. Wu, H. Qin, and J. Zhang, "Co methanation over zro2/al2o3 supported ni catalysts: A comprehensive study," *Fuel Processing Technology*, vol. 124, pp. 61–69, 2014.

[81] J. Ren, X. Qin, J.-Z. Yang, Z.-F. Qin, H.-L. Guo, J.-Y. Lin, and Z. Li, "Methanation of carbon dioxide over ni–m/zro2 (m=fe, co, cu) catalysts: Effect of addition of a second metal," *Fuel Processing Technology*, vol. 137, pp. 204–211, 2015.

[82] X. Jia, N. Rui, X. Zhang, X. Hu, and C.-j. Liu, "Ni/zro2 by dielectric barrier discharge plasma decomposition with improved activity and enhanced coke resistance for co methanation," *Catalysis Today*, vol. 334, pp. 215–222, 2019.

[83] S. Tada, T. Shimizu, H. Kameyama, T. Haneda, and R. Kikuchi, "Ni/ceo2 catalysts with high co2 methanation activity and high ch4 selectivity at low temperatures," *International Journal of Hydrogen Energy*, vol. 37, no. 7, pp. 5527–5531, 2012.

[84] P. U. Aldana, F. Ocampo, K. Kobl, B. Louis, F. Thibault-Starzyk, M. Daturi, P. Bazin, S. Thomas, and A. C. Roger, "Catalytic co2 valorization into ch4 on ni-based ceria-zirconia. reaction mechanism by operando ir spectroscopy," *Catalysis Today*, vol. 215, pp. 201–207, 2013.

[85] G. Zhou, H. Liu, K. Cui, H. Xie, Z. Jiao, G. Zhang, K. Xiong, and X. Zheng, "Methanation of carbon dioxide over ni/ceo2 catalysts: Effects of support ceo2 structure," *International Journal of Hydrogen Energy*, vol. 42, no. 25, pp. 16108–16117, 2017.

[86] L. Atzori, M. G. Cutrufello, D. Meloni, R. Monaci, C. Cannas, D. Gazzoli, M. F. Sini, P. Deiana, and E. Rombi, "Co2 methanation on hard-templated ni/ceo2 mixed oxides," *International Journal of Hydrogen Energy*, vol. 42, no. 32, pp. 20689–20702, 2017.

[87] S. M. Lee, Y. H. Lee, D. H. Moon, J. Y. Ahn, D. D. Nguyen, S. W. Chang, and S. S. Kim, "Reaction mechanism and catalytic impact of ni/ceo2-x catalyst for low-temperature co2 methanation," *Industrial & Engineering Chemistry Research*, 2019.

[88] E. Marconi, S. Tuti, and I. Luisetto, "Structure-sensitivity of co2 methanation over nanostructured ni supported on ceo2 nanorods," *Catalysts*, vol. 9, no. 4, p. 375, 2019.

[89] C. Italiano, J. Llorca, L. Pino, M. Ferraro, V. Antonucci, and A. Vita, "Co and co2 methanation over ni catalysts supported on ceo2, al2o3 and y2o3 oxides," *Applied Catalysis B: Environmental*, vol. 264, p. 118494, 2020.

[90] F. Ocampo, B. Louis, L. Kiwi-Minsker, and A.-C. Roger, "Effect of ce/zr composition and noble metal promotion on nickel based cexzr1−xo2 catalysts for carbon dioxide methanation," *Applied Catalysis A: General*, vol. 392, no. 1-2, pp. 36–44, 2011.

[91] Q. Pan, J. Peng, T. Sun, D. Gao, S. Wang, and S. Wang, "Co2 methanation on ni/ce0.5 zr0.5o2 catalysts for the production of synthetic natural gas," *Fuel Processing Technology*, vol. 123, pp. 166–171, 2014.

[92] M. Boaro, S. Colussi, and A. Trovarelli, "Ceria-based materials in hydrogenation and reforming reactions for co2 valorization," *Frontiers in chemistry*, vol. 7, p. 28, 2019.

[93] L. Atzori, E. Rombi, D. Meloni, R. Monaci, M. F. Sini, and M. G. Cutrufello, "Nanostructured ni/ceo_2-zro_2 catalysts for co_2 conversion into synthetic natural gas," *Journal of nanoscience and nanotechnology*, vol. 19, no. 6, pp. 3269–3276, 2019.

[94] L. Atzori, E. Rombi, D. Meloni, M. F. Sini, R. Monaci, and M. G. Cutrufello, "Co and co2 co-methanation on ni/ceo2-zro2 soft-templated catalysts," *Catalysts*, vol. 9, no. 5, p. 415, 2019.

[95] W. L. Vrijburg, J. W. A. van Helden, A. Parastaev, E. Groeneveld, E. A. Pidko, and E. J. M. Hensen, "Ceria–zirconia encapsulated ni nanoparticles for co2 methanation," *Catal. Sci. Technol.*, vol. 9, no. 18, pp. 5001–5010, 2019.

[96] L. He, Q. Lin, Y. Liu, and Y. Huang, "Unique catalysis of ni-al hydrotalcite derived catalyst in co2 methanation: cooperative effect between ni nanoparticles and a basic support," *Journal of Energy Chemistry*, vol. 23, no. 5, pp. 587–592, 2014.

[97] S. Abate, K. Barbera, E. Giglio, F. Deorsola, S. Bensaid, S. Perathoner, R. Pirone, and G. Centi, "Synthesis, characterization, and activity pattern of ni–al hydrotalcite catalysts in co2 methanation," *Industrial & Engineering Chemistry Research*, vol. 55, no. 30, pp. 8299–8308, 2016.

[98] D. Wierzbicki, R. Debek, M. Motak, T. Grzybek, M. E. Gálvez, and P. Da Costa, "Novel ni-la-hydrotalcite derived catalysts for co2 methanation," *Catalysis Communications*, vol. 83, pp. 5–8, 2016.

[99] C. V. Miguel, M. A. Soria, A. Mendes, and L. M. Madeira, "A sorptive reactor for co2 capture and conversion to renewable methane," *Chemical Engineering Journal*, vol. 322, pp. 590–602, 2017.

[100] K. Stangeland, D. Kalai, H. Li, and Z. Yu, "Co2 methanation: The effect of catalysts and reaction conditions," *Energy Procedia*, vol. 105, pp. 2022–2027, 2017.

[101] F. Vidal Vázquez, J. Kihlman, A. Mylvaganam, P. Simell, M.-L. Koskinen-Soivi, and V. Alopaeus, "Modeling of nickel-based hydrotalcite catalyst coated on heat exchanger reactors for co2 methanation," *Chemical Engineering Journal*, vol. 349, pp. 694–707, 2018.

[102] J. Zhang, Z. Xin, X. Meng, Y. Lv, and M. Tao, "Effect of moo3 on the heat resistant performances of nickel based mcm-41 methanation catalysts," *Fuel*, vol. 116, pp. 25–33, 2014.

[103] H. L. Rotgerink, R. Paalman, J. G. van Ommen, and J. Ross, "Studies on the promotion of nickel—alumina coprecipitated catalysts," *Applied Catalysis*, vol. 45, no. 2, pp. 257–280, 1988.

[104] H. Qin, C. Guo, Y. Wu, and J. Zhang, "Effect of la2o3 promoter on nio/al2o3 catalyst in co methanation," *Korean Journal of Chemical Engineering*, vol. 31, no. 7, pp. 1168–1173, 2014.

[105] M.-T. Fan, K.-P. Miao, J.-D. Lin, H.-B. Zhang, and D.-W. Liao, "Mg-al oxide supported ni catalysts with enhanced stability for efficient synthetic natural gas from syngas," *Applied Surface Science*, vol. 307, pp. 682–688, 2014.

[106] Z. Li, L. Bian, Q. Zhu, and W. Wang, "Ni-based catalyst derived from ni/mg/al hydrotalcite-like compounds and its activity in the methanation of carbon monoxide," *Kinetics and Catalysis*, vol. 55, no. 2, pp. 217–223, 2014.

[107] Q. Liu, F. Gu, X. Lu, Y. Liu, H. Li, Z. Zhong, G. Xu, and F. Su, "Enhanced catalytic performances of ni/al2o3 catalyst via addition of v2o3 for co methanation," *Applied Catalysis A: General*, vol. 488, pp. 37–47, 2014.

[108] H. Y. Kim, H. M. Lee, and J.-N. Park, "Bifunctional mechanism of co2 methanation on pd-mgo/sio2 catalyst: Independent roles of mgo and pd on co2 methanation," *The Journal of Physical Chemistry C*, vol. 114, no. 15, pp. 7128–7131, 2010.

[109] J. Liu, J. Yu, F. Su, and G. Xu, "Intercorrelation of structure and performance of ni–mg/al2o3 catalysts prepared with different methods for syngas methanation," *Catal. Sci. Technol.*, vol. 4, no. 2, pp. 472–481, 2014.

[110] Q. Liu, J. Gao, M. Zhang, H. Li, F. Gu, G. Xu, Z. Zhong, and F. Su, "Highly active and stable ni/gamma-al2o3 catalysts selectively deposited with ceo 2 for co methanation," *RSC Adv*, vol. 4, no. 31, pp. 16094–16103, 2014.

[111] H. Zhu, R. Razzaq, C. Li, Y. Muhmmad, and S. Zhang, "Catalytic methanation of carbon dioxide by active oxygen material cexzr1−xo2 supported ni-co bimetallic nanocatalysts," *AIChE Journal*, vol. 59, no. 7, pp. 2567–2576, 2013.

[112] S. Hwang, J. Lee, U. G. Hong, J. H. Baik, D. J. Koh, H. Lim, and I. K. Song, "Methanation of carbon dioxide over mesoporous ni–fe–ru–al2o3 xerogel catalysts: Effect of ruthenium content," *Journal of Industrial and Engineering Chemistry*, vol. 19, no. 2, pp. 698–703, 2013.

[113] F. Lange, U. Armbruster, and A. Martin, "Heterogeneously-catalyzed hydrogenation of carbon dioxide to methane using runi bimetallic catalysts," *Energy Technology*, vol. 3, no. 1, pp. 55–62, 2015.

[114] C. Yuan, N. Yao, X. Wang, J. Wang, D. Lv, and X. Li, "The sio2 supported bimetallic ni–ru particles: A good sulfur-tolerant catalyst for methanation reaction," *Chemical Engineering Journal*, vol. 260, pp. 1–10, 2015.

[115] W. Zhen, B. Li, G. Lu, and J. Ma, "Enhancing catalytic activity and stability for co2 methanation on ni@mof-5 via control of active species dispersion," *Chemical communications (Cambridge, England)*, vol. 51, no. 9, pp. 1728–1731, 2015.

[116] S.-H. Kang, J.-H. Ryu, J.-H. Kim, S.-J. Seo, Y.-D. Yoo, P. S. Sai Prasad, H.-J. Lim, and C.-D. Byun, "Co-methanation of co and co2 on the nix-fe1−x /al2o3 catalysts; effect of fe contents," *Korean Journal of Chemical Engineering*, vol. 28, no. 12, pp. 2282–2286, 2011.

[117] D. Pandey and G. Deo, "Promotional effects in alumina and silica supported bimetallic ni–fe catalysts during co2 hydrogenation," *Journal of Molecular Catalysis A: Chemical*, vol. 382, pp. 23–30, 2014.

[118] A. L. Kustov, A. M. Frey, K. E. Larsen, T. Johannessen, J. K. Nørskov, and C. H. Christensen, "Co methanation over supported bimetallic ni–fe catalysts:

From computational studies towards catalyst optimization," *Applied Catalysis A: General*, vol. 320, pp. 98–104, 2007.

[119] B. Mutz, M. Belimov, W. Wang, P. Sprenger, M.-A. Serrer, Di Wang, P. Pfeifer, W. Kleist, and J.-D. Grunwaldt, "Potential of an alumina-supported ni3fe catalyst in the methanation of co2: Impact of alloy formation on activity and stability," *ACS Catalysis*, vol. 7, no. 10, pp. 6802–6814, 2017.

[120] M.-A. Serrer, K. F. Kalz, E. SaraÒ«i, H. Lichtenberg, and J.-D. Grunwaldt, "Role of iron on the structure and stability of ni3.2fe/al2o3 during dynamic co 2 methanation for p2x applications," *ChemCatChem*, vol. 11, no. 20, pp. 5018–5021, 2019.

[121] J. K. Nørskov, T. Bligaard, J. Rossmeisl, and C. H. Christensen, "Towards the computational design of solid catalysts," *Nature chemistry*, vol. 1, no. 1, pp. 37–46, 2009.

[122] D. E. Peebles, D. W. Goodman, and J. M. White, "Methanation of carbon dioxide on ni(100) and the effects of surface modifiers," *The Journal of Physical Chemistry C*, vol. 87, pp. 4378–4387, 1983.

[123] S.-i. Fujita, H. Terunuma, M. Nakamura, and N. Takezawa, "Mechanisms of methanation of co and co2 over ni," *The Journal of Physical Chemistry C*, vol. 30, pp. 1146–1151, 1991.

[124] S.-i. Fujita, M. Nakamura, T. Doi, and N. Takezawa, "Mechanisms of methanation of carbon dioxide and carbon monoxide over nickel/alumina catalysts," *Applied Catalysis A: General*, vol. 104, no. 87-100, 1993.

[125] S.-J. Choe, H.-J. Kang, S.-J. Kim, S.-B. Park, D.-H. Park, and D.-S. Huh, "Adsorbed carbon formation and carbon hydrogenation for co 2 methanation on the ni(111) surface: Ased-mo study," *Bulletin of the Korean Chemical Society*, vol. 26, no. 11, pp. 1682–1688, 2005.

[126] J. Ren, H. Guo, J. Yang, Z. Qin, J. Lin, and Z. Li, "Insights into the mechanisms of co2 methanation on ni(111) surfaces by density functional theory," *Applied Surface Science*, vol. 351, pp. 504–516, 2015.

[127] J. Wambach, G. Illing, and H.-J. Freund, "Co2 activation and reaction with hydrogen on ni(110): formate formation," *Chemical Physics Letters*, vol. 184, no. 1-3, pp. 239–244, 1991.

[128] P. Bothra, G. Periyasamy, and S. K. Pati, "Methane formation from the hydrogenation of carbon dioxide on ni(110) surface–a density functional theoretical study,"

Physical chemistry chemical physics : PCCP, vol. 15, no. 15, pp. 5701–5706, 2013.

[129] Q. Pan, J. Peng, S. Wang, and S. Wang, "In situ ftir spectroscopic study of the co2 methanation mechanism on ni/ce0.5zr0.5o2," *Catal. Sci. Technol.*, vol. 4, no. 2, pp. 502–509, 2014.

[130] Q. Pan, J. Peng, T. Sun, S. Wang, and S. Wang, "Insight into the reaction route of co2 methanation: Promotion effect of medium basic sites," *Catalysis Communications*, vol. 45, pp. 74–78, 2014.

[131] A. Westermann, B. Azambre, M. C. Bacariza, I. Graça, M. F. Ribeiro, J. M. Lopes, and C. Henriques, "Insight into co2 methanation mechanism over niusy zeolites: An operando ir study," *Applied Catalysis B: Environmental*, vol. 174-175, pp. 120–125, 2015.

[132] M. Araki and V. Ponec, "Methanation of carbon monoxide on nickel and nickel-copper alloys," *Journal of Catalysis*, vol. 44, pp. 439–448, 1976.

[133] H. H. Madden and G. Ertl, "Decomposition of carbon monoxide on a (110) nickel surface," *Surface Science*, vol. 35, pp. 211–226, 1973.

[134] D. W. Goodman, R. D. Kelley, T. E. Madey, and J. T. Yates, JR., "Kinetics of the hydrogenation of co over a single crystal nickel catalyst," *Journal of Catalysis*, vol. 63, no. 1, pp. 226–234, 1980.

[135] I. Alstrup, "On the kinetics of co methanation on nickel surfaces," *Journal of Catalysis*, vol. 151, no. 1, pp. 216–225, 1995.

[136] M. P. Andersson, F. Abild-Pedersen, I. N. Remediakis, T. Bligaard, G. Jones, J. Engbæk, O. Lytken, S. Horch, J. H. Nielsen, and J. Sehested, "Structure sensitivity of the methanation reaction: H2-induced co dissociation on nickel surfaces," *Journal of Catalysis*, vol. 255, no. 1, pp. 6–19, 2008.

[137] J. L. C. Fajín, J. R. B. Gomes, and M. N. D. S. Cordeiro, "Mechanistic study of carbon monoxide methanation over pure and rhodium- or ruthenium-doped nickel catalysts," *The Journal of Physical Chemistry C*, vol. 119, no. 29, pp. 16537–16551, 2015.

[138] Y. Wang, Y. Su, M. Zhu, and L. Kang, "Mechanism of co methanation on the ni4/gamma-al2o3 and ni3fe/gamma-al2o3 catalysts: A density functional theory study," *International Journal of Hydrogen Energy*, vol. 40, no. 29, pp. 8864–8876, 2015.

[139] C. Zhi, Q. Wang, B. Wang, D. Li, and R. Zhang, "Insight into the mechanism of methane synthesis from syngas on a ni(111) surface: a theoretical study," *RSC Advances*, vol. 5, no. 82, pp. 66742–66756, 2015.

[140] Jan Kopyscinski, *Production of synthetic natural gas in a fluidized bed reactor: Understanding the hydrodynamic, mass transfer, and kinetic effects*. Zurich: ETH Zurich, 2010.

[141] B. Miao, S. S. K. Ma, X. Wang, H. Su, and S. H. Chan, "Catalysis mechanisms of co2 and co methanation," *Catalysis Science & Technology*, vol. 6, no. 12, pp. 4048–4058, 2016.

[142] K. Jalama, "Carbon dioxide hydrogenation over nickel-, ruthenium-, and copper-based catalysts: Review of kinetics and mechanism," *Catalysis Reviews*, vol. 59, no. 2, pp. 95–164, 2017.

[143] C. Vogt, E. Groeneveld, G. Kamsma, M. Nachtegaal, L. Lu, C. J. Kiely, P. H. Berben, F. Meirer, and B. M. Weckhuysen, "Unravelling structure sensitivity in co2 hydrogenation over nickel," *Nature Catalysis*, vol. 1, no. 2, pp. 127–134, 2018.

[144] H. C. Wu, Y. C. Chang, J. H. Wu, J. H. Lin, I. K. Lin, and C. S. Chen, "Methanation of co2 and reverse water gas shift reactions on ni/sico2 catalysts: the influence of particle size on selectivity and reaction pathway," *Catalysis Science & Technology*, vol. 5, no. 8, pp. 4154–4163, 2015.

[145] G. G. Binder and R. R. White, "Synthesis of methane from carbon dioxide and hydrogen," *Chemical Engineering Progress*, vol. 46, pp. 563–574, 1950.

[146] J. Klose and M. Baerns, "Kinetics of the methanation of carbon monoxide on an alumina-supported nickel catalyst," *Journal of Catalysis*, vol. 85, pp. 105–116, 1984.

[147] J. Xu and G. F. Froment, "Methane steam reforming, methanation and water-gas shift: I. intrinsic kinetics," *Aiche Journal*, vol. 35, no. 1, pp. 88–96, 1989.

[148] O. A. Hougen and K. M. Watson, "Solid catalysts and reaction rates," *Ind. Eng. Chem*, vol. 43, no. 5, pp. 529–541, 1943.

[149] J. Kopyscinski, T. J. Schildhauer, F. Vogel, S. M. Biollaz, and A. Wokaun, "Applying spatially resolved concentration and temperature measurements in a catalytic plate reactor for the kinetic study of co methanation," *Journal of Catalysis*, vol. 271, no. 2, pp. 262–279, 2010.

[150] J. Zhang, N. Fatah, S. Capela, Y. Kara, O. Guerrini, and A. Y. Khodakov, "Kinetic investigation of carbon monoxide hydrogenation under realistic conditions of methanation of biomass derived syngas," *Fuel*, vol. 111, pp. 845–854, 2013.

[151] J. R. Rostrup-Nielsen, K. Pedersen, and J. Sehested, "High temperature methanationsintering and structure sensitivity," *Applied Catalysis A: General*, vol. 330, pp. 134–138, 2007.

[152] M. Bailera, P. Lisbona, L. M. Romeo, and S. Espatolero, "Power to gas projects review: Lab, pilot and demo plants for storing renewable energy and co2," *Renewable and Sustainable Energy Reviews*, vol. 69, pp. 292–312, 2017.

[153] D. L. Trimm, "The formation and removal of coke from nickel catalyst," *Catalysis Reviews*, vol. 16, no. 1, pp. 155–189, 1977.

[154] D. L. Trimm, "Catalyst design for reduced coking," *Applied Catalysis*, vol. 5, no. 3, pp. 263–290, 1983.

[155] D. L. Trimm, "Catalysts for the control of coking during steam reforming," *Catalysis Today*, vol. 49, pp. 3–10, 1999.

[156] J. G. McCarty and H. Wise, "Hydrogenation of surface carbon on alumina-supported nickel," *Journal of Catalysis*, vol. 54, no. 3, pp. 406–416, 1979.

[157] P. Forzatti and L. Lietti, "Catalyst deactivation," *Catalysis Today*, vol. 52, pp. 165–181, 1999.

[158] P. Munnik, M. E. Z. Velthoen, P. E. de Jongh, K. P. de Jong, and C. J. Gommes, "Nanoparticle growth in supported nickel catalysts during methanation reaction-larger is better," *Angewandte Chemie*, vol. 126, no. 36, pp. 9647–9651, 2014.

[159] C. H. Bartholomew and W. L. Sorensen, "Sintering kinetics of silica- and alumina-supported nickel in hydrogen atmosphere," *Journal of Catalysis*, vol. 81, pp. 131–141, 1983.

[160] R. M. Ravenelle, J. R. Copeland, W.-G. Kim, J. C. Crittenden, and C. Sievers, "Structural changes of gamma-al2o3 -supported catalysts in hot liquid water," *ACS Catalysis*, vol. 1, no. 5, pp. 552–561, 2011.

[161] G. W. Huber, J. W. Shabaker, and J. A. Dumesic, "Raney ni-sn catalyst for h2 production from biomass-derived hydrocarbons," *Science (New York, N.Y.)*, vol. 300, no. 5628, pp. 2075–2077, 2003.

[162] D. Li, Y. Nakagawa, and K. Tomishige, "Methane reforming to synthesis gas over ni catalysts modified with noble metals," *Applied Catalysis A: General*, vol. 408, no. 1, pp. 1–24, 2011.

[163] S. Li and J. Gong, "Strategies for improving the performance and stability of ni-based catalysts for reforming reactions," *Chemical Society reviews*, vol. 43, no. 21, pp. 7245–7256, 2014.

[164] H. Harms, B. Höhlein, and A. Skov, "Methanisierung kohlenmonoxidreicher gase beim energie-transport," *Chemie Ingenieur Technik*, vol. 52, no. 6, pp. 504–515, 1980.

[165] J. H. Jensen, J. M. Poulsen, and N. U. Andersen, "From coal to clean energy," *Nitrogen+Syngas*, vol. 310, pp. 34–38, 2011.

[166] Y.-L. Kao, P.-H. Lee, Y.-T. Tseng, I.-L. Chien, and J. D. Ward, "Design, control and comparison of fixed-bed methanation reactor systems for the production of substitute natural gas," *Journal of the Taiwan Institute of Chemical Engineers*, vol. 45, no. 5, pp. 2346–2357, 2014.

[167] L. Romano, F. Ruggeri, and R. Marx, "Sng production from coal: A possible solution to energy demand," *Energy Procedia*, vol. 45, pp. 1330–1336, 2014.

[168] J. Kopyscinski, T. J. Schildhauer, and S. M. Biollaz, "Methanation in a fluidized bed reactor with high initial co partial pressure: Part i—experimental investigation of hydrodynamics, mass transfer effects, and carbon deposition," *Chemical Engineering Science*, vol. 66, no. 5, pp. 924–934, 2011.

[169] M. Rüdisüli, T. J. Schildhauer, S. M. Biollaz, and J. R. van Ommen, "Scale-up of bubbling fluidized bed reactors — a review," *Powder Technology*, vol. 217, pp. 21–38, 2012.

[170] J. Li, L. Zhou, P. Li, Q. Zhu, J. Gao, F. Gu, and F. Su, "Enhanced fluidized bed methanation over a ni/al2o3 catalyst for production of synthetic natural gas," *Chemical Engineering Journal*, vol. 219, pp. 183–189, 2013.

[171] M. Götz, *Methanisierung im Dreiphasen-Reaktor*. KIT, 2014.

[172] Jonathan Lefebvre, Manuel Götz, Siegfried Bajohr, Rainer Reimert, and Thomas Kolb, "Improvement of three-phase methanation reactor performance for steady-state and transient operation," *Fuel Processing Technology*, vol. 132, pp. 83–90, 2015.

[173] C. Fukuhara, K. Hayakawa, Y. Suzuki, W. Kawasaki, and R. Watanabe, "A novel nickel-based structured catalyst for co 2 methanation: A honeycomb-type ni/ceo 2 catalyst to transform greenhouse gas into useful resources," *Applied Catalysis A: General*, vol. 532, pp. 12–18, 2017.

[174] P. Biegger, F. Kirchbacher, A. Medved, M. Miltner, M. Lehner, and M. Harasek, "Development of honeycomb methanation catalyst and its application in power to gas systems," *Energies*, vol. 11, no. 7, p. 1679, 2018.

[175] D. Schollenberger, S. Bajohr, M. Gruber, R. Reimert, and T. Kolb, "Scale-up of innovative honeycomb reactors for power-to-gas applications - the project store&go," *Chemie-ingenieur-technik*, vol. 90, no. 5, pp. 696–702, 2018.

[176] A. Vita, C. Italiano, L. Pino, P. Frontera, M. Ferraro, and V. Antonucci, "Activity and stability of powder and monolith-coated ni/gdc catalysts for co2 methanation," *Applied Catalysis B: Environmental*, vol. 226, pp. 384–395, 2018.

[177] S. Razza, T. Heidig, E. Bianchi, G. Groppi, W. Schwieger, E. Tronconi, and H. Freund, "Heat transfer performance of structured catalytic reactors packed with metal foam supports: Influence of wall coupling," *Catalysis Today*, vol. 273, pp. 187–195, 2016.

[178] M. Frey, T. Romero, A.-C. Roger, and D. Edouard, "Open cell foam catalysts for co2 methanation: Presentation of coating procedures and in situ exothermicity reaction study by infrared thermography," *Catalysis Today*, vol. 273, pp. 83–90, 2016.

[179] O. Görke, P. Pfeifer, and K. Schubert, "Highly selective methanation by the use of a microchannel reactor," *Catalysis Today*, vol. 110, no. 1-2, pp. 132–139, 2005.

[180] K. P. Brooks, J. Hu, H. Zhu, and R. J. Kee, "Methanation of carbon dioxide by hydrogen reduction using the sabatier process in microchannel reactors," *Chemical Engineering Science*, vol. 62, no. 4, pp. 1161–1170, 2007.

[181] Z. Liu, B. Chu, X. Zhai, Y. Jin, and Y. Cheng, "Total methanation of syngas to synthetic natural gas over ni catalyst in a micro-channel reactor," *Fuel*, vol. 95, pp. 599–605, 2012.

[182] N. Engelbrecht, S. Chiuta, R. C. Everson, H. W. Neomagus, and D. G. Bessarabov, "Experimentation and cfd modelling of a microchannel reactor for carbon dioxide methanation," *Chemical Engineering Journal*, vol. 313, pp. 847–857, 2017.

[183] Michael Neubert, Alexander Hauser, Babak Pourhossein, Marius Dillig, and Juergen Karl, "Experimental evaluation of a heat pipe cooled structured reactor as part of a two-stage catalytic methanation process in power-to-gas applications," *Applied Energy*, vol. 229, pp. 289–298, 2018.

[184] S. Pérez, J. J. Aragón, I. Peciña, and E. J. Garcia-Suarez, "Enhanced co2 methanation by new microstructured reactor concept and design," *Topics in Catalysis*, vol. 62, no. 5-6, pp. 518–523, 2019.

[185] A. Alarcón, J. Guilera, and T. Andreu, "Co2 conversion to synthetic natural gas: Reactor design over ni–ce/al2o3 catalyst," *Chemical Engineering Research and Design*, vol. 140, pp. 155–165, 2018.

[186] E. Giglio, F. A. Deorsola, M. Gruber, S. R. Harth, E. A. Morosanu, D. Trimis, S. Bensaid, and R. Pirone, "Power-to-gas through high temperature electrolysis and carbon dioxide methanation: Reactor design and process modeling," *Industrial & Engineering Chemistry Research*, vol. 57, no. 11, pp. 4007–4018, 2018.

[187] H. Ohya, J. Fun, H. Kawamura, K. Itoh, H. Ohashi, M. Aihara, S. Tanisho, and Y. Negishi, "Methanation of carbon dioxide by using membrane reactor integrated with water vapor permselective membrane and its analysis," *Journal of Membrane Science*, vol. 131, pp. 237–247, 1997.

[188] J. Witte, A. Kunz, S. M. Biollaz, and T. J. Schildhauer, "Direct catalytic methanation of biogas – part ii: Techno-economic process assessment and feasibility reflections," *Energy Conversion and Management*, vol. 178, pp. 26–43, 2018.

[189] J. Witte, J. Settino, S. M. Biollaz, and T. J. Schildhauer, "Direct catalytic methanation of biogas – part i: New insights into biomethane production using rate-based modelling and detailed process analysis," *Energy Conversion and Management*, vol. 171, pp. 750–768, 2018.

[190] B. Lee, H. Lee, S. Kim, H.-S. Cho, W.-C. Cho, B.-H. Jeon, C.-H. Kim, and H. Lim, "Quantification of economic uncertainty for synthetic natural gas production in a h2o permeable membrane reactor as simultaneous power-to-gas and co2 utilization technologies," *Energy*, vol. 182, pp. 1058–1068, 2019.

[191] R. Currie, M. W. Fowler, and D. S. Simakov, "Catalytic membrane reactor for co2 hydrogenation using renewable streams: Model-based feasibility analysis," *Chemical Engineering Journal*, vol. 372, pp. 1240–1252, 2019.

[192] A. Borgschulte, N. Gallandat, B. Probst, R. Suter, E. Callini, D. Ferri, Y. Arroyo, R. Erni, H. Geerlings, and A. Züttel, "Sorption enhanced co2 methanation," *Physical chemistry chemical physics : PCCP*, vol. 15, no. 24, pp. 9620–9625, 2013.

[193] S. Walspurger, G. D. Elzinga, J. W. Dijkstra, M. Sarić, and W. G. Haije, "Sorption enhanced methanation for substitute natural gas production: Experimental results

and thermodynamic considerations," *Chemical Engineering Journal*, vol. 242, pp. 379–386, 2014.

[194] E. Jwa, S. B. Lee, H. W. Lee, and Y. S. Mok, "Plasma-assisted catalytic methanation of co and co2 over ni–zeolite catalysts," *Fuel Processing Technology*, vol. 108, pp. 89–93, 2013.

[195] R. Dittmeyer, T. Boeltken, P. Piermartini, M. Selinsek, M. Loewert, F. Dallmann, H. Kreuder, M. Cholewa, A. Wunsch, M. Belimov, S. Farsi, and P. Pfeifer, "Micro and micro membrane reactors for advanced applications in chemical energy conversion," *Current Opinion in Chemical Engineering*, vol. 17, pp. 108–125, 2017.

[196] A. I. Stankiewicz and J. A. Moulijn, "Process intensification: Transforming chemical engineering," *Chemical Engineering Progress*, vol. 96, no. 1, pp. 22–34, 2000.

[197] C. Ramshaw, "The incentive for process intensification," *Proceedings, 1st Intl. Conf. Proc. Intensif. for Chem. Ind.*, vol. 18, 1995.

[198] V. Hessel, S. Hardt, and H. Löwe, *Chemical micro process engineering*. Weinheim: Wiley-VCH, 2005.

[199] M. N. Kashid, A. Renken, and L. Kiwi-Minsker, *Microstructured devices for chemical processing*. Weinheim: Wiley-VCH, 2015.

[200] N. Kockmann, *Transport phenomena in micro process engineering*. Heat and mass transfer, Berlin and New York: Springer, 2008.

[201] H. Herwig and A. Moschallski, *Wärmeübertragung*. Wiesbaden: Springer Fachmedien Wiesbaden, 2019.

[202] H. Bakhtiary-Davijany, F. Hayer, X. K. Phan, R. Myrstad, H. J. Venvik, P. Pfeifer, and A. Holmen, "Characteristics of an integrated micro packed bed reactor-heat exchanger for methanol synthesis from syngas," *Chemical Engineering Journal*, vol. 167, no. 2-3, pp. 496–503, 2011.

[203] F. Hayer, H. Bakhtiary-Davijany, R. Myrstad, A. Holmen, P. Pfeifer, and H. J. Venvik, "Synthesis of dimethyl ether from syngas in a microchannel reactor—simulation and experimental study," *Chemical Engineering Journal*, vol. 167, no. 2-3, pp. 610–615, 2011.

[204] R. Myrstad, S. Eri, P. Pfeifer, E. Rytter, and A. Holmen, "Fischer–tropsch synthesis in a microstructured reactor," *Catalysis Today*, vol. 147, pp. S301–S304, 2009.

[205] M. Belimov, D. Metzger, and P. Pfeifer, "On the temperature control in a microstructured packed bed reactor for methanation of co/co 2 mixtures," *AIChE Journal*, vol. 63, no. 1, pp. 120–129, 2017.

[206] R. Berger, "Eurokin spreadsheet on requirements for measurement of intrinsic kinetics in the gas-solid fixed-bed reactor," 2012.

[207] C. H. Bartholomew and R. J. Farrauto, *Fundamentals of industrial catalytic processes*. Hoboken, NJ: Wiley-Interscience, 2. ed. ed., 2010.

[208] S. Tauro, *One-step Synthesis of Dimethyl Ether Using Microreactors*. Shaker Verlag GmbH, 2014.

[209] J. Nocedal and S. J. Wright, *Numerical optimization*. New York, NY: Springer, 2000.

[210] L. F. Shampine and M. W. Reichelt, "The matlab ode suite," *SIAM Journal on Scientific Computing*, vol. 18, no. 1, pp. 1–22, 1997.

[211] E. Emagbetere, O. O. Oluwole, and T. A. Salau, "Comparative study of matlab ode solvers for the korakianitis and shi model," *Bulletin of Mathematical Sciences and Applications*, vol. 19, pp. 31–44, 2017.

[212] G. Schwarz, "Estimating the dimension of a model," *the Annals of Statistics*, vol. 6, no. 2, pp. 461–464, 1978.

[213] H. Akaike, "A new look at the statistical model identification," *IEEE Transactions on Automatic Control*, vol. 19, no. 6, pp. 716–723, 1974.

[214] D. C. Montgomery, *Design and analysis of experiments*. Hoboken NJ: John Wiley & Sons Inc, 8 ed., 2013.

[215] C. A. Callaghan, *Kinetics and catalysis of the water-gas-shift reaction: A microkinetic and graph theoretic approach*. WORCESTER POLYTECHNIC INSTITUTE, 2006.

[216] M. Swickrath and M. Anderson, "The development of models for carbon dioxide reduction technologies for spacecraft air revitalization," *American Institute of Aeronautics and Astronautics*, 2012.

[217] R. E. Hayes, W. J. Thomas, and K. E. Hayes, "A study of the nickel-catalyzed methanation reaction," *Journal of Catalysis*, vol. 92, no. 2, pp. 312–326, 1985.

[218] C. Wheeler, A. Jhalani, E. J. Klein, S. Tummala, and L. D. Schmidt, "The water–gas-shift reaction at short contact times," *Journal of Catalysis*, vol. 223, no. 1, pp. 191–199, 2004.

[219] R. J. Byron Smith, M. Loganathan, and M. S. Shantha, "A review of the water gas shift reaction kinetics," *International Journal of Chemical Reactor Engineering*, vol. 8, 2010.

[220] R. Dittmeyer and G. Emig, "Simultaneous heat and mass transfer and chemical reaction," in *Handbook of heterogeneous catalysis* (G. Ertl, ed.), Weinheim and Chichester: Wiley-VCH, 2008.

[221] S. A. Theofanidis, V. V. Galvita, H. Poelman, and G. B. Marin, "Enhanced carbon-resistant dry reforming fe-ni catalyst: Role of fe," *ACS Catalysis*, vol. 5, no. 5, pp. 3028–3039, 2015.

[222] A. Winkler and K. D. Rendulic, "Adsorption kinetics for hydrogen adsorption on nickel and coadsorption of hydrogen and oxygen," *Surface Science*, vol. 18, pp. 19–31, 1982.

[223] F. B. Koschany, *Experimentelle Studien zur Methanisierung von CO2 auf Nickel-katalysatoren*. München: Universitätsbibliothek der TU München, 2016.

[224] P. Pfeifer and M. Belimov, "Microreactor and process control for methanation: Microreactors, e.g. miniaturised or microfabricated reactors," Patent Nr.: DE102016110498A1, KIT, 2017.

[225] J. Guilera, T. Boeltken, F. Timm, I. Mallol, A. Alarcón, and T. Andreu, "Pushing the limits of sng process intensification: High ghsv operation at pilot scale," *ACS Sustainable Chemistry & Engineering*, vol. 8, no. 22, pp. 8409–8418, 2020.

[226] J. Bremer, K. H. G. Rätze, and K. Sundmacher, "Co2 methanation: Optimal start-up control of a fixed-bed reactor for power-to-gas applications," *AIChE Journal*, vol. 63, no. 1, pp. 23–31, 2017.

[227] A. El Sibai, L. K. Rihko Struckmann, and K. Sundmacher, "Model-based optimal sabatier reactor design for power-to-gas applications," *Energy Technology*, vol. 5, no. 6, pp. 911–921, 2017.

[228] R. Güttel, "Study of unsteady-state operation of methanation by modeling and simulation," *Chemical Engineering & Technology*, vol. 83, no. 11, pp. n/a–n/a, 2013.

[229] X. Li, B. Yang, and Y. Zhang, "Dynamics and control study on the low temperature methanation reactor with mass and heat recycle," *Journal of Process Control*, vol. 23, no. 10, pp. 1360–1370, 2013.

[230] K. L. Fischer and H. Freund, "On the optimal design of load flexible fixed bed reactors: Integration of dynamics into the design problem," *Chemical Engineering Journal*, vol. 393, p. 124722, 2020.

[231] S. Matthischke, R. Krüger, S. Rönsch, and R. Güttel, "Unsteady-state methanation of carbon dioxide in a fixed-bed recycle reactor — experimental results for transient flow rate ramps," *Fuel Processing Technology*, vol. 153, pp. 87–93, 2016.

[232] J. Lefebvre, M. Götz, S. Bajohr, R. Reimert, and T. Kolb, "Improvement of three-phase methanation reactor performance for steady-state and transient operation," *Fuel Processing Technology*, vol. 132, pp. 83–90, 2015.

[233] D. Schlereth and O. Hinrichsen, "A fixed-bed reactor modeling study on the methanation of co2," *Chemical Engineering Research and Design*, vol. 92, no. 4, pp. 702–712, 2014.

[234] G. F. Froment, J. de Wilde, and K. B. Bischoff, *Chemical reactor analysis and design*. Hoboken N.J.: Wiley, 3rd ed. ed., 2011.

[235] H. A. Deans and L. Lapidus, "A computational model for predicting and correlating the behavior of fixed–bed reactors: I. derivation of model for non-reactive systems," *Aiche Journal*, vol. 6, no. 4, pp. 656–663, 1960.

[236] M. Baerns, H. Hofmann, and A. Renken, eds., *Lehrbuch der technischen Chemie*. Stuttgart: Thieme, 2., durchges. aufl. ed., 1992.

[237] G. Ertl, ed., *Handbook of heterogeneous catalysis*. Weinheim and Chichester: Wiley-VCH, 2nd, completely rev. and enl. ed. ed., 2008.

[238] N. Lemcoff, S. I. Pereira Duarte, and O. M. Martinez, "Heat transfer in packed beds," *Reviews in Chemical Engineering*, vol. 6, no. 4, pp. 229–292, 1990.

[239] A. A. Iordanidis, *Mathematical modeling of catalytic fixed bed reactors*. Enschede: Twente University Press, op. 2002.

[240] M. Giese, *Stroemung in poroesen Medien unter Beruecksichtigung effektiver Viskositaeten.* PhD Thesis, TU München, 1998.

[241] Verein Deutscher Ingenieure VDI-Gesellschaft Verfahrenstechnik und Chemieingeneurwesen, ed., *VDI-Wärmeatlas*. Springer Reference, Berlin: Springer Vieweg, 11., bearb. und erw. aufl. ed., 2013.

[242] A. P. de Wasch and G. F. Froment, "Heat transfer in packed beds," *Chemical Engineering Science*, vol. 27, no. 3, pp. 567–576, 1972.

[243] Li, Chi-Hsiung, Finlayson, B. A., "Heat transfer in packed beds- a reevaluation," *Chemical Engineering Science*, vol. 32, pp. 1055–1066, 1977.

[244] A. G. Dixon, "Wall and particle-shape effects on heat transfer in packed beds," *Chemical Engineering Communications*, vol. 71, no. 1, pp. 217–237, 1988.

[245] S. G. Kandlikar, *Heat transfer and fluid flow in minichannels and microchannels*. Amsterdam: Elsevier, 1. ed. ed., 2006.

[246] M. E. Steinke and S. G. Kanlikar, "An experimental investigation of flow boiling characteristics of water in parallel microchannels," *Transactions of the ASME*, vol. 126, pp. 518–526, 2004.

[247] W. Yu, D. M. France, M. W. Wambsganss, and J. R. Hull, "Two-phase pressure drop, boiling heat transfer, and critical heat flux to water in a small-diameter horizontal tube," *International Journal of Multiphase Flow*, vol. 28, pp. 927–941, 2002.

[248] W. Qu and I. Mudawar, "Flow boiling heat transfer in two-phase micro-channel heat sinks—-i. experimental investigation and assessment of correlation methods," *International Journal of Heat and Mass Transfer*, vol. 46, no. 15, pp. 2755–2771, 2003.

[249] A. Jess and P. Wasserscheid, *Chemical Technology : An Integral Textbook*. Weinheim: Wiley-VCH, 2013.

[250] P. B. Weisz and C. D. Prater, "Interpretation of measurements in experimental catalysis," *Advances in Catalysis*, vol. 6, pp. 143–196, 1954.

[251] D. E. Mears, "Tests for transport limitations in experimental catalytic reactors," *Industrial & Engineering Chemistry Process Design and Development*, vol. 10, no. 4, pp. 541–547, 1971.

[252] J. B. Anderson, "A criterion for isothermal behaviour of a catalyst pellet," *Chemical Engineering Science*, 1963.

[253] V. Quaschning, *Regenerative Energiesysteme: Technologie, Berechnung, Simulation*. München: Hanser, 3. aufl., [überarb. und aktualisiert] ed., 2003.

Parts of this dissertation have already been published in:

- S. Farsi, W. Olbrich, P. Pfeifer, R. Dittmeyer, A consecutive methanation scheme for conversion of CO_2 - a study on Ni_3Fe catalyst in a short-contact time micro packed bed reactor, *Chemical Engineering Journal*, vol. 388, p. 124233, 2020.
- S. Farsi, S. Liang, P. Pfeifer, R. Dittmeyer, Application of evaporation cooling in a microstructured packed bed reactor for decentralized CO_2 methanation, *International Journal of Hydrogen Energy*, vol. 46, issue 38, pp. 19971-19987, 2021.